2018

REVERSE INSULATOR DIELECTROPHORESIS: UTILIZING DROPLET MICROENVIRONMENTS FOR DISCERNING MOLECULAR EXPRESSIONS ON CELL SURFACES

Jeana Collins
jeanac@mtu.edu

REVERSE INSULATOR DIELECTROPHORESIS: UTILIZING DROPLET MICROENVIRONMENTS FOR DISCERNING MOLECULAR EXPRESSIONS ON CELL SURFACES

By

Jeana L. Collins

A DISSERTATION

Submitted in partial fulfillment of the requirements for the degree of

DOCTOR OF PHILOSOPHY

In Chemical Engineering

MICHIGAN TECHNOLOGICAL UNIVERSITY

2018

© 2018 Jeana L. Collins

This dissertation has been approved in partial fulfillment of the requirements for the Degree of DOCTOR OF PHILOSOPHY in Chemical Engineering.

Department of Chemical Engineering

Dissertation Advisor: *Adrienne R. Minerick*

Committee Member: *Rebecca Ong*

Committee Member: *Faith Morrison*

Committee Member: *Gowtham S*

Department Chair: *Pradeep K. Agrawal*

Table of Contents

List of figures

List of tables

Preface

Published Material:

Four chapters in this dissertation are published materials. The content in Chapter 6, Effects of Additives on Droplet Size and Stability in a Microfluidic T-junction Device, is part of a planned publication. The content in Chapter 7, Introduction to a new, novel dielectrophoretic technique, Reverse Insulator Dielectrophoresis (riDEP), is also part of a planned publication. Chapter 8, Electrical and chemical characterizations of hafnium (IV) oxide films for biological lab-on-a-chip devices, has been published in the journal Thin Solid Films. Chapter 9, Microdevice replication and design using a water-based acrylic polymer emulsion, has been submitted to the ACS Journal of Education and is under review.

Collaborative Projects:

Chapters 8 and 9 were both collaborative projects. Chapter 8: The microfabrication and characterization experiments were completed by myself, Zhichao Wang, Nupur Bihari, Hector Moncada Hernandez, Sanaz Habibi, and Chito Kendrick. Simulations were completed by myself and Hector Moncada Hernandez. Adrienne Minerick and Paul Bergstrom provided guidance on experiments, analysis, and writing throughout the process. I wrote the majority of the manuscript, and Adrienne Minerick and I completed the majority of the edits. Chapter 9: Anna Nelson helped complete the profilometry characterizations and wrote the code for analyzing the profilometry data. Anna Nelson also read through the manuscript and provided edits.

Acknowledgements

If you think an advanced degree is something that someone earns on their own, I would tell you that you are incorrect. In my experience, there is a vast system of support that is necessary when undertaking such a large task. Family, friends, and colleagues helped build the stable, intertwining structure that housed my brain throughout this process. I am not sure there are words to describe how thankful I am to everyone, but I will try.

My family has supported me, even when I moved across Lake Superior to pursue a degree in something that they knew nothing about. I read somewhere recently that talking to your mom releases the same endorphins as getting a hug- well mom, thank you for all of the endorphins during our daily phone calls. You are always there to listen to the good, the bad, and the ugly. Dad, thank you for listening, for visiting, and for fixing the little things. You are always there and that means the world to me. Jenny- you know exactly what I have been going through and your insight into this process, even though it was different for the two of us, has helped me put things into perspective. Jamie- thank you for being there for me, you really are my second mom. Brennen- you are my rock. How you have put up with me and my stress through the past six years is amazing (I am tearing up thinking about it). On a bad day, I come home, see you, and start crying. And you let me. You let me show you all of my emotions no matter how ridiculous they are and you help me find my way back to happy.

During the first few years of my degree I relied on my family for support. That all changed with 47° North. The dance community here has saved me; being able to get back in touch with my passion for dance has made my life much less stressful. Thank you Allison Mills, Annelise Doll, Robin Lieburn, Sylvia Schourek, Amanda Rasner, Krista Empey, Cynthia May Drake, and Shannon Nulf, you are all so inspirational. I can't wait to start the next chapter of my life with you all there.

I would like to thank Dr. Adrienne Minerick, my advisor. You have been a mentor in research, in teaching, in life. Thank you for the opportunity to work in your lab, it has been a wonderful experience. Getting a Ph.D. is not just about the final product, it is about the journey getting there. The journey that you lead your students on is a worthwhile journey. You teach us to work hard, to endure, to persevere, to be proud, to work as a team, and to have fun.

To the members of μM.D.-ERL: Dr. Adrienne Minerick has created a research group that is respective and supportive of one another. The comradery that I have experienced is amazing. Everyone helps each other when they can, whether it is reading a manuscript, helping fix a microdevice, bouncing around ideas about their research, or providing a ride home. I was always able to count on my fellow researchers for support.

I would like to thank my co-authors Dr. Adrienne Minerick, Dr. Paul Bergstrom, Sanaz Habibi, Dr. Hector Moncada Hernandez, Dr. Chito Kendrick, Dr. Zhichao Wang, and

Nupur Bihari for all of the hard work and collaboration during the hafnium work. It was a pleasure to work with such a talented group of individuals.

I would like to thank my undergraduate students. The first group that I would like to thank is the students that I mentored as they worked on their own project; Eliot Nagler, Katherine Massa, Ashley Fox, Hien Nguyen, Jacqueline Harms, Pennie Winters, Madison Diehl, Anna Nelson, and Logan McMillan. Working with you all helped me grow as a researcher, a teacher, and a mentor. The second group that I would like to thank is the students that directly helped me with my project; Anna Nelson, for your profilometry measurements and analysis for the WBAPE project; Jessika Rogers, for your help asking for figure permissions; Trevor Pitcel, for your help with extracting raw data from videos; and Stefan RhodeHumphries, for your help editing.

I would like to thank my committee members for the help, the insightful questions, and the guidance through this process; Dr. Julie King, Dr. Rebecca Ong, Dr. Gowtham Shankara (G), and Dr. Faith Morrison. I would like to give a special thanks to G for the help and guidance on supercomputing.

Last, but definitely not least, I would like to thank the Department of Chemical Engineering at Michigan Tech. This department was very supportive throughout the process of working on my degree. Thank you for the financial support. The opportunity to be a graduate teaching assistant for multiple classes allowed me to gain skills as a teacher, giving me the best possible preparation for teaching at the collegiate level. Taana Kalliainen, Alexis Snell, and Sue Niemi- thank you for all the help with paperwork and organization, you all are the glue that holds the department together. Julie King- thank you for my very first teaching assistant position and all of the advice over the years. Tony Rogers- thank you for the opportunity to be your teaching assistant, for your guidance, for your mentorship, and for your support.

Only with the help of all of you was I able to complete this dissertation. Thank you so much!

Abstract

Lab-on-a-chip (LOC) technologies enable the development of portable analysis devices that use small sample and reagent volumes, allow for multiple unit operations, and couple with detectors to achieve high resolution and sensitivity, while having small footprints, low cost, short analysis times, and portability. Droplet microfluidics is a subset of LOCs with the unique benefit of enabling parallel analysis since each droplet can be utilized as an isolated microenvironment. This work explored adaptation of droplet microfluidics into a unique, previously unexplored application where the water/oil interface was harnessed to bend electric field lines within individual droplets for insulator dielectrophoretic (iDEP) characterizations. iDEP polarizes particles/cells within non-uniform electric fields shaped by insulating geometries. We termed this unique combination of droplet microfluidics and iDEP reverse insulator dielectrophoresis (riDEP). This riDEP approach has the potential to protect cell samples from unwanted sample-electrode interactions and decrease the number of required experiments for dielectrophoretic characterization by ~80% by harnessing the parallelization power of droplet microfluidics. Future research opportunities are discussed that could improve this reduction further to 93%.

A microfluidic device was designed where aqueous-in-oil droplets were generated in a microchannel T-junction and packed into a microchamber. Reproducible droplets were achieved at the T-junction and were stable over long time periods in the microchamber using Krytox FSH 157 surfactant in the continuous oil FC-40 phase and isotonic salts and dextrose solutions as the dispersed aqueous phase. Surfactant, salts, and dextrose interact at the droplet interface influencing interfacial tension and droplet stability. Results provide foundational knowledge for engineering stable bio- and electro-compatible droplet microfluidic platforms.

Electrodes were added to the microdevice to apply an electric field across the droplet packed chamber and explore riDEP responses. Operating windows for droplet stability were shown to depend on surfactant concentration in the oil phase and aqueous phase conductivity, where different voltage/frequency combinations resulted in either stable droplets or electrocoalescence. Experimental results provided a stability map for strategical applied electric field selection to avoid adverse droplet morphological changes while inducing riDEP. Within the microdevice, both polystyrene beads and red blood cells demonstrated weak dielectrophoretic responses, as evidenced by pearl-chain formation, confirming the preliminary feasibility of riDEP as a potential characterization technique.

Two additional side projects included an alternative approach to isolate electrode surface reactions from the cell suspension via a hafnium oxide film over the electrodes. In addition, a commercially prevalent water-based polymer emulsion was found to adequately duplicate microchannel and microchamber features such that it could be used for microdevice replication.

1 Introduction

1.1 Introduction and Outline

In recent years, technology miniaturization has become a prominent research interest that has increased access to data by the average member of society. Micro-total analysis systems (μTAS) were introduced in the 1980s with the idea of miniaturizing multiple analytical process steps and combining them into a single flow system [15]. Since then (μTAS), microelectromechanical systems (MEMS) [16], and Lab-on-a-chip (LOC) devices have provided a means for researchers to develop analysis systems that require small (microliter) sample and reagent sizes; allow for multiple unit operations including separations, dilutions, concentrations, and mixing; and incorporate detectors with high resolution and sensitivity, while having a small footprint, low cost, short analysis times, and portability [17-26].

As a subset of sought-after LOC device applications, medical microdevices are emerging technologies that enable portable, low cost, sensitive, selective, less invasive, and fast measurements and manipulations for medical diagnostics and treatment management. Droplet microfluidics, one technology used in LOCs and medical microdevices, has become well established over the last decade. The ability to generate monodisperse droplets where each droplet acts as its own isolated microenvironment allows for flexible, high throughput kinetics, analytical chemistry, and biological cell manipulations within portable microdevices [27-29]. Another key advantage of droplet microfluidics is the ability for parallel experimentation that allows multiplexation of multiple microenvironment experiments into one.

Electrokinetic tools are also widely utilized in μTAS and LOC applications because they have the ability to selectively focus [30], separate [31], or transport molecules [32], bioparticles [33], cells [34], or droplets [35]. The use of electric fields to manipulate and reproducibly distinguish charged cells, proteins, DNA, and other molecules has substantially impacted knowledge of fundamental biological processes [36]. A valuable technique for cell/particle characterization within microfluidic platforms is dielectrophoresis (DEP). Dielectrophoresis is a powerful electrokinetic tool because it can polarize any particle/cell based on its insulative and charge storage characteristics. Although there are many advantages to DEP characterizations, there are disadvantages, including unwanted sample-electrode ion interactions and the number of experiments required to obtain a single particle or cell's dielectric spectra. Insulator dielectrophoresis (iDEP), a subset of DEP, addresses the unwanted sample-electrode interactions by using solid, insulating obstacles or protrusions into fluid channels to alter electric field path lines, thus creating spatially variant electric field gradients that can be used to manipulate and separate polarizable particles or cells. DEP is highly dependent upon the media conditions, and while each individual media condition gives property classes, testing at multiple media conditions is necessary to calculate cell/particle dielectric properties. Traditional approaches utilize one media condition to generate a single DEP

curve/spectrum across a large range of frequencies. It can take months to accurately generate one DEP curve.

1.2 Reverse Insulator Dielectrophoresis

This dissertation systematically explores a novel approach that combines iDEP with droplet microfluidics to harness iDEP's advantageous separation between samples and electrodes with the multiplexing abilities of droplet microfluidics. This approach is novel within our lab, and we have termed this technique 'reverse insulator dielectrophoresis' (riDEP) because the electric field is being generated within the droplets instead of around insulating geometries. Droplets were generated in a T-junction microfluidic device with an aqueous dispersed phase (electrically conductive) and a continuous oil phase (electrically insulative) and then packed into a microchamber. Due to the droplet to droplet proximity of the insulative/conductive fluids, the fluid interfaces shape a spatially non-uniform electric field within the droplets packed into the microchamber. This work explored not only the formation of those non-uniform fields but also the polarization of dielectric particles/cells within the droplets. Established polystyrene bead and red blood cell DEP published data were used to benchmark this technique.

A novel, new dielectrophoresis technique termed 'reverse insulator DEP' was systematically explored. riDEP combines principles of droplet microfluidics and insulator dielectrophoresis to create a microdevice for parallel characterization of particles/cells that protect the samples from unwanted sample-electrode interactions via utilization of droplet microfluidics. The use of droplet interfaces to shape non-uniform electric fields needed for DEP characterizations is novel and is presented for the first time within this dissertation. First, a device was designed and prototyped to generate aqueous-in-oil droplets in a T-junction and subsequently collect them in a microfluidic chamber. Each droplet served as an isolated microenvironment that acted as its own experiment. This allowed completion of simultaneous replicate trials of the same sample solution. Independent repeat experiments were also completed. Surfactants were investigated to optimize the stabilization of the entire droplet microfluidic system, resulting in monodispersed, non-coalescing droplets. Parallel electrodes were designed to fit on the opposite walls of the microfluidic chamber within which droplets were packed. The oil surrounding each droplet acted as an insulator, shaping a nonuniform electric field within each conductive aqueous droplet. Electric field characteristics (applied voltage, DC, AC, frequency) could be tuned based on the droplets and their packing within the microchamber. Close, ordered packing was found to be important for riDEP for the electric field to be able to divert around the oil and traverse through the narrowest interfacial distance from aqueous droplet to aqueous droplet; further, the ordered droplet packing enabled a consistent electric field gradient within each droplet. This riDEP microdevice was explored by utilizing knowledge from previous work completed by µM.D.-ERL on the ABO-Rh blood typing system to test the viability of the riDEP technique.

1.3 Dissertation Objectives and Aims

The first objective of this project was to experimentally generate monodisperse droplets, 100-200 µm in diameter, and pack them into a microfluidic chamber. This objective was broken down into two main aims, one engineering based and one science-based. The first aim (engineering) was to design, fabricate, and prototype a microfluidic device for stable droplet generation and packing within a chamber. The goal in implementing a droplet system was to enable parallelization of experiments to increase experimental throughput, as shown in Figure 1.1. The second aim (science) was to study the effect of additives on the droplet formation and stability in the microfluidic system. Dielectrophoretic responses of particles and cells are highly dependent on media conditions, which means varied amounts of salt ions, as well as dextrose in the aqueous phase to achieve a range of DEP spectra for the characterization of particles/cells while maintaining solution isotonicity. The second aim of objective one systematically studied how surfactant concentration, salt concentration, dextrose concentration, and the combination of salt and dextrose affected the generated droplet size and stability. Chapters 4 and 6 present the results from objective one.
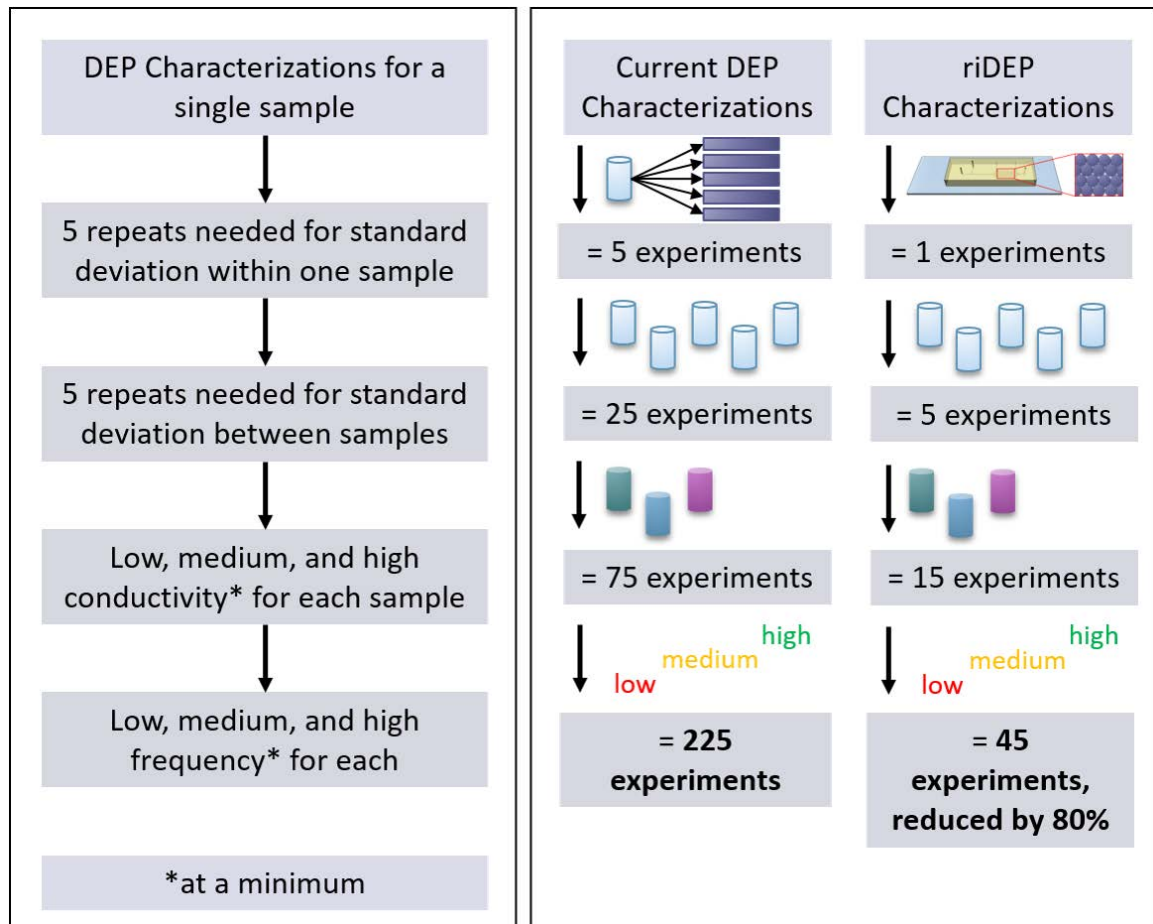
Figure 1-1. The potential impact of the new technique, riDEP, on reducing the amount of time needed to complete experiments by up to 80%.

The second objective of this project was to explore reverse insulator dielectrophoresis within droplets. This objective was broken down into three main aims, one engineering based and two science-based. The first aim (engineering) of objective two was to design and implement parallel electrodes within the microchamber of the microfluidic device. The second aim (science) was to study the effect of an applied electric field on droplet stability because it was important for the droplets to remain intact for the parallelization of DEP experiments within droplets. The third aim (science) was to seed particles/cells into the droplets to explore riDEP performance for cell characterizations. Chapter 7 presents the results of objective two.

The third objective was to use simulations to inform experimental matrices and to compare to experimental results in order to more fully understand the underlying physics behind the droplet behaviors. Chapter 5 presents the set up and results of three types of COMSOL simulations: droplet generation in a T-junction, shaping non-uniform electric fields within droplets, and dielectrophoretic responses within droplets. This work was completed in tandem with objectives one and two.

As mentioned previously, a disadvantage of traditional dielectrophoresis includes unwanted sample-electrode ion interactions. The insulative nature of riDEP prevents direct contact between the aqueous microenvironments and the electrode. In addition, a second technique for isolating experimental samples from electrodes to prevent unwanted sample-electrode interactions was explored. The strategy was electrode passivation via a thin non-reactive film of hafnium oxide. For some experimental configurations, droplet microfluidics may not be possible, so hafnium oxide was explored and characterized as a material to physically isolate samples from electrodes while still allowing the electric field to penetrate into the samples. Chapter 8 presents hafnium oxide as an alternative method for eliminating unwanted sample-electrode interactions.

All microchannel and microchamber designs within this work relied on microfabrication of high-aspect ratio features. Microfabrication of high-aspect ratio features is challenging and can result in features losing adhesion to master silicon wafers after only two or three elastomer castings over the wafer. Chapter 9 presents the creative use of Puffy Paint, a water-based polymer emulsion as a tool to replicate microfluidic features without compromising the original master silicon wafer.

The future work from this project is to further multiplex experiments. This goal is broken down into two main aims, one engineering, and one science. The first aim (engineering) of objective three involves designing and modeling microdevices with microfluidic tree structures. Simultaneous investigation of multiple experimental conditions is possible by adding branching or tree structures to the microdevice design. The second aim (science) of objective three would be to study the riDEP responses for two or more experimental conditions (additional aqueous phase conductivities, etc.) simultaneously. Chapter 10 presents the results of future work. Chapter 11 presents the key findings and conclusions from all objectives and analysis.

2 Project Background/Literature Review

2.1 Droplet Microfluidics

The following sections discuss the applications of droplet microfluidics; methods and applications for droplet handling techniques including fusion/fission/mixing and sorting/trapping; droplet formation techniques; and the role of surfactants.

2.1.1 Applications and Advantages of Droplet Microfluidics

The first microfluidic technique utilized in this work is droplet microfluidics. Droplet microfluidics utilizes the capability of monodisperse droplet formation and manipulation within a microfluidic device. The use of microfluidic structures to generate droplets began in the 1950s when Skeggs used air bubbles to separate an aqueous stream [37] but exploded in the early 2000s after the seminal work of S. Anna, which investigated the physics involved in droplet generation [38-41].

Droplet microfluidics is a growing field, due to the numerous applications that encompass a range of fields of study. A range of techniques are used to achieve specific tasks. These techniques include fission, fusion, mixing, sorting, trapping, as well as formation. The high throughput possible in droplet microfluidics provides a platform for biological and chemical research [37]. Along with high throughput, parallel analysis allows applications including large-scale polymerase chain reaction (PCR) and cell culturing techniques to be completed [37, 42].

By adjusting the upstream composition, drug discovery, protein crystallization, and enzymatic assays are possible [13, 28, 29, 37]. Other applications include irregular particles, double emulsions, hollow microcapsules, microbubbles, single cell analysis, synthesis of biomolecules, drug delivery, therapeutics, biomedical imaging, diagnostic testing, and others [28, 29, 37, 42-49]. These applications come from the ability of droplets to mimic micro reactors such that reactions and molecular processes can be observed in greater time and spatial resolution. Complex fluids can also be used in droplet microfluidics, including liquid crystals, lipids, polymeric solutions, and most relevant to the work described herein, surfactants [50]. Phase changes within droplet microfluidics have also been investigated due to the need for gels or solids in many biomedical applications. One way to achieve a phase change is by ultra violet (UV) light. UV light initiates polymerization of soluble particles into solid particles and activates photo initiators which cause monomers to link and solidify [29]. Use of chemical agents and solvent evaporation/extraction can also achieve the phase change from liquid to solid [29]. Other applications that use emulsions include foods, personal care products, and topical delivery of drugs [38, 51]. Simple Boolean logic functions have been performed via droplet microfluidics, making microfluidic computer chips feasible [29]. When droplets come to a branch in the channels, the path they take is governed by the number of droplets already in the two branches, resulting in a complex sequence of choices that

can be reversed [52]. *In this dissertation we present droplet microfluidics for applications in diagnostics, harnessing many of the advantages of droplet microfluidics including targetable size, monodispersity, isolation, minimum cross-contamination, and their ability to be neatly packed within a chamber.*

One of the key challenges in continuous flow microfluidics is that as the number of parallel experiments increases, the size of the device increases almost linearly [29]. Droplet microfluidics is one effective method of addressing this challenge. In droplet microfluidics, the complexity and size of the device do not have to increase to increase the number of parallel experiments. Droplet microfluidics can generate non-spherical, yet monodispersed, droplets due to physical confinement in the channels. This is difficult to achieve on a macro scale because droplets are formed by agitating a mixture of two or more immiscible fluids [29]. This results in polydispersed droplets, where the size and number of droplets produced vary considerably. Droplet microfluidics controls the formation of each droplet and can reproduce uniform droplets within the nano- to micro-meter diameter range [29] with only a 1-10 % dispersity [28, 53, 54]. Each droplet can contain its own experiment, allowing for parallel experimentation within the same device. This results in increased throughput, scalability, and the ease of collecting large data sets. Other advantages of droplet microfluidics include monodisperse droplets, independent control, and high surface area to volume ratios [29].

Each droplet acts as its own isolated microenvironment, which is an attribute extensively leveraged in this research. Droplets can also exist on a scale relevant to biological conditions [37]; this work focused on droplets on the order of 100-200 microns in diameter to enable numerous particles/cells on the order of 5-10 microns in diameter to be seeded within the monodispersed droplets. Homogeneous controlled conditions, such as external temperature and humidity, are present in droplet microfluidics, which makes droplets ideal chemical reactors [55] or cell chambers [56]. Droplets provide miniaturization and compartmentalization of pico- to micro-liter volumes with high throughput device configurations [28, 37, 55], which leads to low consumption of reagents, cells, and samples. The high surface area to volume ratio results in faster reaction times, as short as a few milliseconds [55], due to shorter diffusion distances as well as faster heat and mass transfer [14, 29].

Isolated chambers, separated by the immiscible carrier fluid [28], are advantageous due to stable reaction conditions, parallel reactions, batch and continuous capabilities, no cross contamination, no dilution, control over evaporation, and high throughput possibilities [28, 37, 57]. Reactions can also be followed in time by imaging at different positions in the microfluidic chip. The effect of initial concentration on the overall yield and kinetics is of interest in the field of reaction kinetics. Chemical composition at any point along the channel can be determined using methods such as Raman spectroscopy [58], which allows whole kinetic mapping to be completed [55]. Other methods of content characterization include in situ fluorescence microscopy, in situ electrochemical detection, secondary mass spectroscopy, and secondary electrophoresis [28]. Table 2.1

compares attributes of droplet microfluidics for chemical reactors and for the electrokinetic microenvironments in this work.

Table 2-1. Comparison of attributes of droplet microfluidics for chemical reactions and electrokinetic microenvironments.

Attribute	Chemical reactors	Electrokinetic microenvironments (this work)
Ability to adjust upstream composition	Concentration dependent kinetics	Media dependent responses
Isolated microenvironment	Does not have to be stationary	
	Minimal cross contamination	
	Parallel experimentation	
	High throughput	
	Fewer evaporation effects	
Scale relevant to biological conditions	Mimic biological reactions and molecular processes	
	Small sample requirements	
Uniform size distribution	Reproducibility	
Homogeneous controlled conditions	Reproducibility	
	Parallel experimentation	

2.1.2 On-Chip Droplet Manipulation Techniques

One of the advantages of droplet microfluidics is the ability to manipulate the droplets by sorting, trapping, fission, fusion, and mixing. Droplet sorting is important for the separation of specific droplets of interest. Droplets can be sorted based on size using only channel geometry where smaller side channels will take smaller droplets as the larger droplets flow through the main channel [29]. Dielectrophoresis (DEP), magnetophoresis, and electrowetting-on-dielectrics (EWOD) can be used to sort droplets based on contents [28]. Using DEP to sort droplets based on the contents should not be confused with the research presented herein; performing DEP characterizations on particles/cells seeded within the droplets. The first uses the electric fields to manipulate the whole droplet while the second uses DEP to manipulate particles within individual droplets. DEP and magnetophoresis sort whole droplets by using an electric or a magnetic field. Under the field conditions, droplets will behave differently and move toward either the high or low field regions based on the whole droplet's dielectric properties [59]. Fluorescence-activated separation is capable of separating 2000 droplets per second by optically detecting specific droplets and using either valves or lasers to "push" the desired droplets
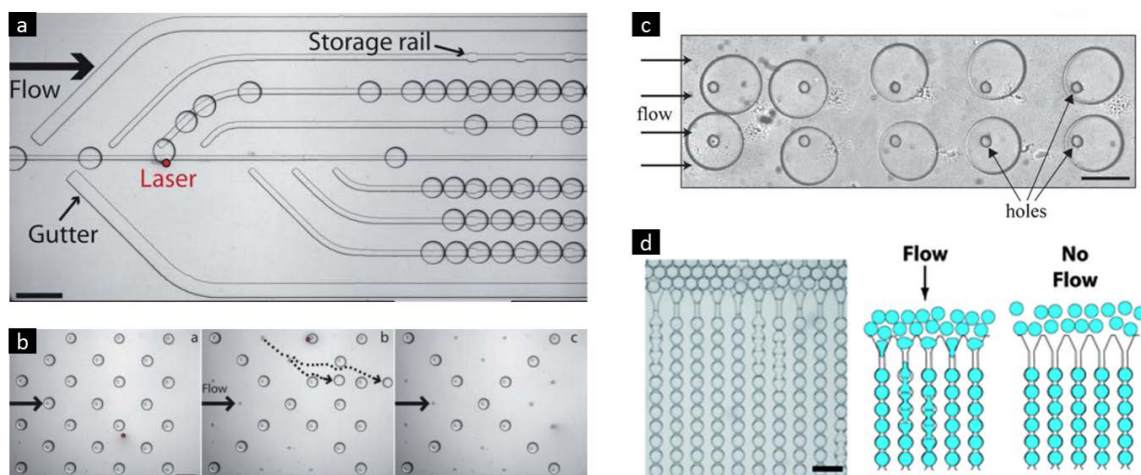
Figure 2-1. (a) and (b) Droplet sorting via laser force [2] , droplet trapping via (c) surface patterning [8] and (d) dropspots [12].

into a separate channel [28]. Other methods include surface acoustic waves and laser-induced localized heating which alter the interfacial tension [28]. Abbyad et al. utilized focused laser heating and surface patterning for moving droplets in a specific manner [2, 8]. The localized heating from the laser causes a pushing force due to the change in density from the temperature shift, and the surface pattering causes a force due to a change in surface tension as shown in Figure 2.1.

A change in surface tension can not only be used for droplet sorting but droplet trapping as well, as shown in Figure 2.1. Droplet trapping can be beneficial for increasing residence time. Normally, microdevices have a residence time of only seconds to minutes, but many reaction or cell culturing circumstances require several hours or days [28]. The simplest way to increase residence time is to increase the length of the channel. Other methods that require less space on a microdevice include reservoirs, drop spots, and surface patterning. A disadvantage to reservoirs is that the original generation order of droplets is lost [43, 60]. Drop spots create arrays of round chambers connected with narrow constrictions that will hold one droplet each [12, 57]. The drop spots investigated by Schmitz et al. could trap thousands of droplets for time-lapse studies and allowed for droplet recovery. Surface patterning is a trapping technique that uses grooves in the device to hold a droplet in place or to guide a droplet to a specific location by altering the surface tension of the droplet, (essentially allowing the droplets to take the path of least resistance) [2, 8]. Surface patterning can, in some cases, retain droplet generation order.

Droplet fission is another droplet manipulation technique used in droplet microfluidics. It can scale up the number of parallel experiments by splitting previously formed droplets. Droplet fission can also be used to control the concentration of the droplets' contents. Passive splitting geometries include T-junctions, branching channels, and channel obstructions [5, 29, 37]. Abate et al. used the branching channels of a microfluidic tree structure for faster droplet generation by splitting larger droplets at each branch down to the desired droplet size, as shown in Figure 2.2a [5]. Asymmetrical droplets are possible

by altering the lengths of the branching channels [28]. Active methods of droplet fission include electrical, magnetic, and thermal methods [37]. EWOD alters the interfacial tension, and thermal methods alter both the interfacial tension and viscosity since both properties are temperature dependent [29].

As droplet fission has advantages, droplet fusion does as well. Many reactions require reactants to be kept separate until the correct conditions or have multiple steps that require the addition of reagents at specific times [28, 56, 61]. Droplet microfluidics can keep reactants in individual droplets, and then fuse them together at a prescribed time. Droplet fission can be utilized to combine the contents within a droplet. Electrical, magnetic, thermal, optical, and chemical methods can achieve active fusion [11, 29, 37]. Some examples of achieving droplet fusion via electrical coalescence can be seen in Figure 2.2b [11]. The channel geometry can achieve passive fusion, where collision, film drainage, and film rupture occur [11, 29, 37].

Droplet contents need to be well mixed to facilitate chemical reactions. Due to the nature of laminar flow and the length scale in which droplet microfluidics occurs, diffusion times are very long [28, 37]. To overcome slow diffusion, active and passive mixing methods have been researched. Droplets being sandwiched between or laying on top of electrodes can facilitate active mixing. An advantage to electric methods is that mixing can occur in a confined space [29], however, electrodes require at least one extra layer of fabrication. Um et al. demonstrated droplets of varying concentrations being passively achieved by first splitting droplets of two concentrations and then fusing different numbers of the smaller droplets of the two concentrations together and passively mixing them using channel geometry, as shown in Figure 2.2c [13]. An effective passive method
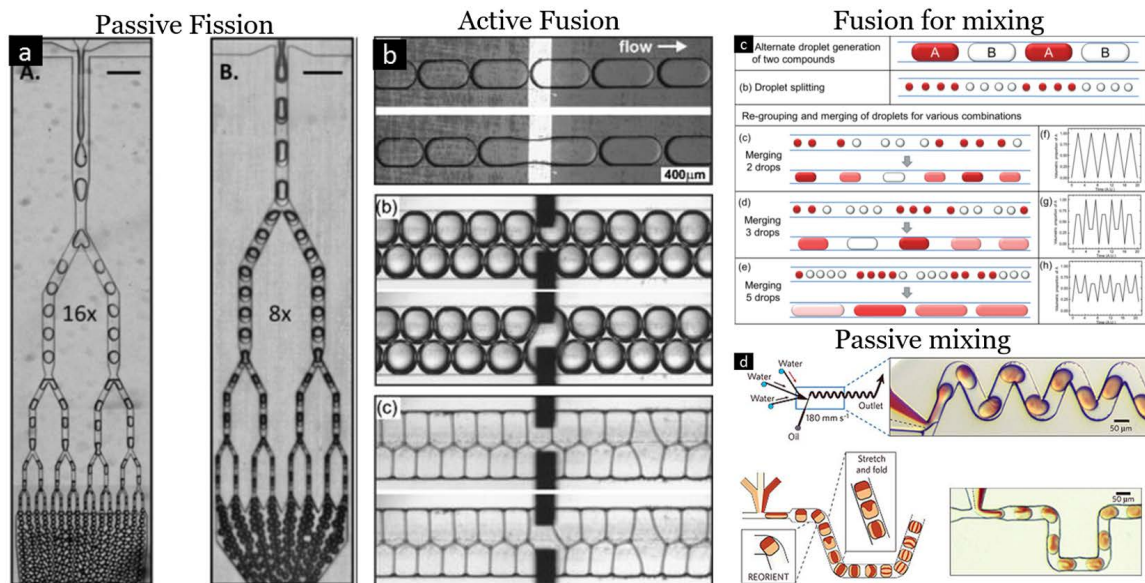
Figure 2-2. Examples of (a) passive droplet fission using tree structures [5] , (b) active droplet fusion using electric fields [11] , (c) droplet fission for mixing droplets of varied concentration [13] , and (d) mixing within droplets via channel geometry [14].

is to have long winding channels, as shown in Figure 2.2d [14]. Recirculation flows within the droplets are caused by the shear interaction of the channel wall with the droplet interface. This mixes the contents or two halves of the droplet, but diffusion governs mixing between the two halves. Long winding channels overcome this by making the recirculation flows uneven [28]. Disadvantages of this are that it takes significant space, pressure drops for fluid flow, and time. However, with strategic geometry designs, complete mixing can be achieved in milliseconds [28].

2.1.3 Methods and Theory of Droplet Formation

Droplet manipulation has many advantages, but first requires the generation of droplets. "Top-down" generation occurs by direct agitation. This turbulence-enhanced generation provides little control over individual droplets [28, 38] and results in an undesirable broad size distribution [29, 62]. "Bottom-up" methods control the formation of individual droplets. There are both active and passive forms of droplet generation within the "bottom-up" category. Active forms of droplet generation include DEP and EWOD which both use electric means to generate droplets. DEP can pull electrically neutral droplets out of a reservoir on the microdevice [29]. EWOD uses an electric field to manipulate the interfacial tension between the surface and the droplet. The advantages of EWOD are that it is compact and does not require external pumps [29]. Other active generation methods for droplet generation include centrifugal [63], thermal capillary valving via a laser [64], and pneumatic microvalving [65].

Passive means of droplet generation consist of two or more immiscible fluids and laminar fluid flow. Common geometries for passive droplet generation include flow-focusing, co-flowing, Y-junction, and T-junction geometries [29, 37, 66]. T-junctions form droplets by intersecting the dispersed phase in a channel perpendicular to the continuous phase, as shown in Figure 2.3a. With a large enough flow rate [37] the dispersed phase elongates as it enters the main continuous phase channel until the shear force and pressure gradient formed pinching off droplets at the junction [29]. *Due to the multiple advantages and high presence in literature, the work presented here utilized the T-junction geometry.*

T-junctions, the most common droplet generation geometry, are adaptable to a wide range of velocities and pressures and are useful in chemical reactions and cell encapsulations [44, 67-70]. Y-junction and K-junction (not shown in Figure 2.3) are variations of the T-junction geometry, using angled channels instead of the 90-degree channels [71]. Flow-focusing forces both the dispersed and the continuous phase through a smaller orifice. Droplets are broken off downstream [28, 29, 57, 60, 72-75]. In flow-focusing geometry, as the flow rate increases, production rate increases and droplet size decreases [28, 29]. Figure 2.3c shows the set-up for flow-focusing geometry. Co-flowing geometries use a smaller channel such as a capillary within a larger channel to break-off droplets [51].

Droplet formation is governed by the Capillary number (Ca), Equation 2.1, where η is the continuous phase viscosity, v is the continuous phase velocity, and γ is the interfacial
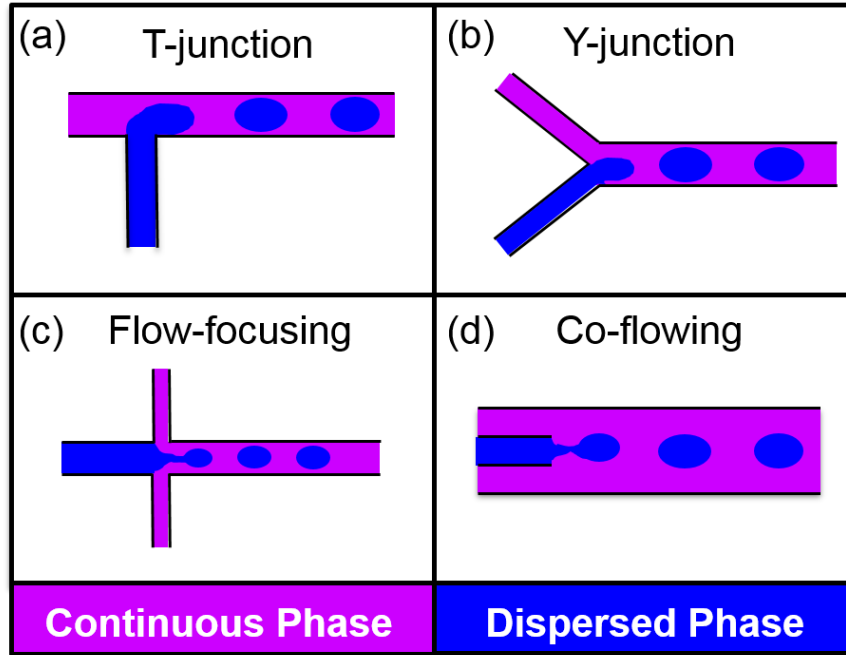
Figure 2-3. Schematics showing droplet break-up in (a) T-junction, (b) Y-junction, (c) flow-focusing, and (d) co-flowing geometries.

tension [29]. For a Capillary number less than 10^{-2}, interfacial forces dominate over viscous forces and the ratio of the volumetric flow rates of the two phases govern droplet breakup [37] and above 0.1 the main influencer is the competition between shearing effect from the continuous phase and the interfacial tension [76].

$$Ca = \frac{\eta v}{\gamma} \qquad 2.1$$

There is a competition between the viscous and capillary forces in a T-junction [55]. Viscous forces tend to draw fluid along the channel, and capillary forces tend to reduce the total interface between two fluids by forming droplets. Joanicot et al. found droplet size to be comparable with the channel width [55]. It can be concluded that droplet size depends on the type of geometry used to generate the droplets [40, 55]. A variety of models/simulations for the prediction of droplet break-up in a T-junction have been developed [68, 69, 77].

2.1.4 Material Properties, Geometry, and Flow Rate Effects on Droplet Generation

Different droplet formation geometries have demonstrated different regimes of droplet formation [40, 54, 66, 69, 77-79]. Droplet breakup regimes are analogous to flow regimes. As the Reynolds number increases, the fluid flow goes from laminar, to transition, to turbulent. Similarly, as the Capillary number increases, droplet breakup goes from squeezing, to dripping, to jetting [40, 80]. Figure 2.4 shows examples of each
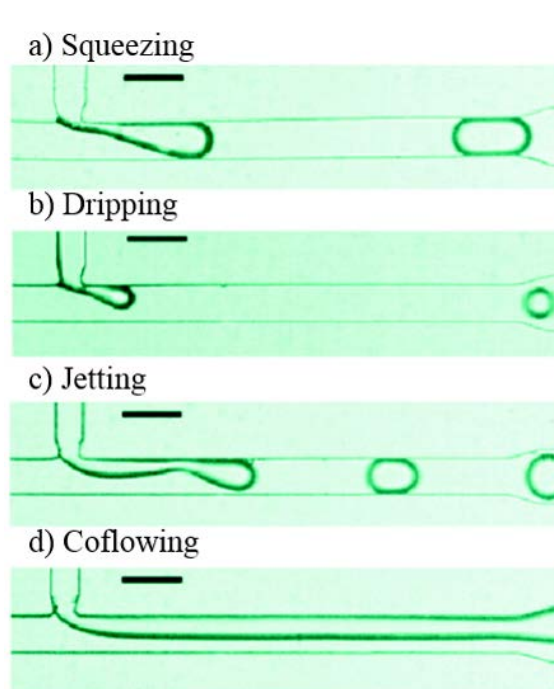
Figure 2-4. Droplet break-up regimes; a) squeezing, b) dripping, c) jetting, and d) coflowing [1].

droplet breakup regime. Droplet formation in the squeezing regime, with a Capillary number less than 10^{-2} [40, 78], is governed by pressure buildup upstream whereby the dispersed phase extends into the flow of the continuous phase squeezing the neck and pinching off a droplet [80]. An increase in Capillary number decreases the size of the droplets and an increase in flow rate or channel depth increases the droplet length. In the jetting regime, with a Capillary number greater than 0.1 [40, 78], droplets experience a combination of end pinching and capillary wave instabilities [80]. Thread formation, common in flow-focusing devices, is where thread formation occurs in which a primary droplet forms and then pulls a thin thread of the dispersed phase behind it. Interfacial tension then causes the thread to breakup into small, uniform droplets that are orders of magnitude smaller than the primary droplet [39-41].

As previously mentioned, the geometry and flow rates within a device affect the formation of droplets. Surface properties are also important to consider for droplet generation [28, 74, 81]. How droplet formation occurs depends on the wetting conditions of the microdevice walls. Poly(dimethylsiloxane), or PDMS, is one of the most common materials used in the fabrication of droplet microfluidic devices. Advantageous properties of PDMS include ease of use, mechanical/chemical stability, biocompatibility, and low cost [82, 83]. A disadvantage of PDMS is that swelling and deformation can occur within the device in the presence of organic solvents [29]. Other materials, with a higher solvent resistance, such as glass, silicon, and thiolene are used to eliminate this challenge [29]. Glass can be either hydrophobic or hydrophilic, but the fabrication of glass devices is time-consuming and costly [28]. Flow-focusing and co-flowing geometries alleviate

some surface problems due to the continuous phase shielding the dispersed phase [62]. Roberts et al. investigated surface properties for both water-in-oil and oil-in-water droplets, showing that the contact angle between the fluids and the channel affect droplet production [74]. *For this work, PDMS was used with a compatible fluorinated oil and glass microscope slides that were treated to become hydrophobic before running experiments.*

Controlling how droplets are generated can be very important depending on the application. It is important that the size, shape, and monodispersity are controlled while the droplets form. For drug delivery and biosensing, well-defined volumes and compositions are necessary to achieve the correct dosing and manufacturing. Further, the biological and chemical properties of microparticles are strongly affected by the size and morphology [29]. For example, as droplet size decreases the ratio of surface area to volume increases. For an application such as drug delivery, a decrease in droplet size would lead to a higher drug release rate due to the decreased amount of transport necessary. *Uniformity and size are important to this project because of how they pack within the microfluidic chamber, and Chapters 4 and 5 discuss the implications of poor uniformity and packing. Chapter 4 presents investigations into materials and experminetal set-up which play important roles in droplet size determination [29].*

2.2 Surfactants for Control of Droplet Uniformity/Size/Stability in Droplet Microfluidics

The use of surfactants can be very advantageous in microfluidic devices, as discussed in the following sections.

2.2.1 Introduction to Surfactants

As previously mentioned in Section 2.1.4, it is important to be able to control droplet generation. One way to aid in this control is to add a surfactant into the system. Traditionally, a wide range of applications use surfacants including motor oils, pharmaceuticals, cleaning/laundry detergents, petroleum drilling muds, and ore beneficiation floatation agents [84]. More recently surfactants are being used in technologies including microelectronics, viral research, and biotechnology. The term surfactant comes from **surf**ace-**act**ive **age**nt. Surfactants have an amphipathic structure; a lyophobic group that has little attraction to the solvent and a lyophilic group with a strong attraction to the solvent. The hydrophobic group is generally a long chain hydrocarbon residue, but it can also be a halogenated or oxygenated hydrocarbon or siloxane chain. The hydrophilic group is an ionic or highly polar group and is also sometimes referred to as the surface active portion [84].

There are four classifications of the surface active portion based on the charge; nonionic has no apparent ionic charge, zwitterionic has both positive and negative charges, cationic has a positive charge, and anionic has a negative charge. Because of their nature,

there are many different surfactants available and can be chosen based on the specific application. Table 2.2 contains a list of surfactants and their applications in microdevices. *This work focuses on surfactants for the application of stabilizing emulsions within a microdevice for biological/medical applications. After testing multiple surfactants (discussed in Chapter 4), Krytox 157 FSH (perfluoroalkyl polyether carboxylic acid), an anionic surfactant was chosen to aid in system stabilization.*

2.2.2 Surfactants in Microfluidics

Surfactants play a major role in emulsions because the phase boundary area is very large with respect to the volume. This means that a substantial fraction of the total mass present is at the boundaries [84]. In most microfluidic applications they reduce the interfacial tension, aiding in droplet breakup and stability [76, 85]. At low concentrations, surfactants can absorb to surfaces and interfaces. The desired outcome is usually a decrease in surface/interfacial tension, although some applications desire an increase. This is done using the nature of interfacial tension, the interfacial free energy per unit area, by decreasing the interfacial energy we are decreasing the minimum amount of work required to create an interface, thus stabilizing droplet formation [84]. Due to the amphiphilic nature of surfactant molecules, in an immiscible aqueous/oil solution, they are attracted to the fluid interface, with the hydrophobic portion of the molecule going to the oil phase and the hydrophilic portion of the molecule going to the aqueous phase [85]. This layer of molecules at the interface of each droplet acts as a repulsive barrier helping the droplets resist coalescence [86, 87].

The Gibbs adsorption isotherm describes the decrease in surface tension for dilute solutions (Equation 2.2), where γ is the surface tension, c the surfactant concentration, Γ the surface concentration, R the gas constant, and T the temperature [85].

$$\Gamma = -\frac{C}{RT}\frac{d\gamma}{dC} \qquad 2.2$$

The surfactant concentration is important in this equation due to the nature of surfactants. As the concentration of surfactants increase, there comes a point when the molecules come together to form micelles. This point is referred to as the critical micelle concentration (CMC). The CMC also corresponds to the limiting interfacial tension achievable since the interface is homogenously covered maintaining constant interfacial tension [88]. Above the CMC, surfactant molecules have to dissociate from the micelles to diffuse to the interface between the aqueous and oil phases [76].

In addition, droplet size and time to collision with other droplets also affects coalescence due to kinetic mechanisms of surfactant adsorption. Adsorption/desorption surfactant interface kinetics dominate in smaller droplets, while diffusion dominates in larger droplets. The more time droplets have between formation and collision, the more time the surfactant molecules have to diffuse to the aqueous/oil interface.

14

Table 2-2. Surfactants and uses in literature

Solubility	Surfactant	Dissolved Phase	Concentration Used	Bio-compatible*	Ref.
oil	Krytox 157 FSL	HFE-7500	2 % (w/w)	-	[89]
		FC40	0.5% (w/w)	-	[2]
	PFPE-PEG /PEG based	HFE-7500	2% (w/w)	✓	[90]
		HFE-7500	0.5% (w/w)	✓	[91]
		FC40	0.5% (w/w)	✓	[92]
		FC40 or R (Raindance Technologies)	1.8% (w/w)	✓	[47]
		FC40	0.01% (w/w)	-	[2]
		FC-3283 (3M)	2% (w/w)	-	[93]
	DMP-PFPE	FC40	0.5% (w/w)	✓	[8, 92]
	Span80	hexadecane	2% (w/w)	-	[94, 95]
		hexadecane	>cmc=0.02wt% (HLB=4.3)	-	[96]
		Decane, tetradecane, and hexadecane	-	-	[29]
	PGPR 90	Benzyl benzoate and SO (1:1 v/v)	2-5 % (w/v)	-	[72]
	PFO	FC-40	9:1 (oil:surfactant)	-	[79]
	Span80 and Tween20	Mineral oil	0-10% (w/w)	-	[76]
water	SDS	0.01 M fluorescein sodium salt in DI water	>cmc=0.2 wt% (HLB=40)	-	[96]
		Milli-Q water	0.03, 0.15, 0.25, 1.5, 3.0% (w/w)	-	[71]
		deionized water	0.001-1.0% (w/w)	-	[97]
		water	8 mM	-	[98]
		water	-	-	[29]
		water	0.5-4.0 wt%	-	[76]
	Tween80	0.01 M fluorescein sodium salt in DI water	>cmc=0.1 wt% (HLB=15)	-	[96]
	Tween20	water	-	-	[29]
		water	6-18 wt%	-	[76]
	Synperonic PEF108	Milli-Q water	0.025, 0.25, 1.25, 5.0% (w/w)	-	[71]
	Phospholipids	water	-	-	[29]
	Pluronic F-127	5-10 % (w/v) glycerol aqueous solution	1% (w/v)	-	[72]
	octaethylene glycol monododecyl ether	deionized water	2.5*cmc (cmc=100μM)	-	[40]

* key: - not mentioned ✓ biocompatible

Not only can surfactants increase the ease of formation and stability of droplets, but they can also aid biocompatibility [40, 47, 62, 87, 99, 100]. *Biocompatibility is important for this project because we are completing particle/cell characterization, which requires the cells to stay alive.* Other applications in medical microdevices that require biocompatibility include applications such as polymerase chain reaction (PCR), cell culturing, and single cell analysis [28, 29, 37]. The addition of surfactants can prevent the adsorption of biomolecules at the aqueous/oil interface [47]. Surfactants can be tailored to a system by strategically choosing a molecule, changing the head or tail group, or even just by having other molecules present in the solution. By simply changing the head group from a carboxylic acid to polyethylene glycol (PEG), there is an improvement in biocompatibility [47]. The interaction between a carboxylated perfluoropolyether from a surfactant head group and a heterocyclic, nitrogenous base in a fluorous solvent or a primary amine can create a similar biocompatible effect [87]. Table 2.2 contains a list of oil phase/aqueous phase/surfactant combinations that have been used in droplet microfluidic applications.
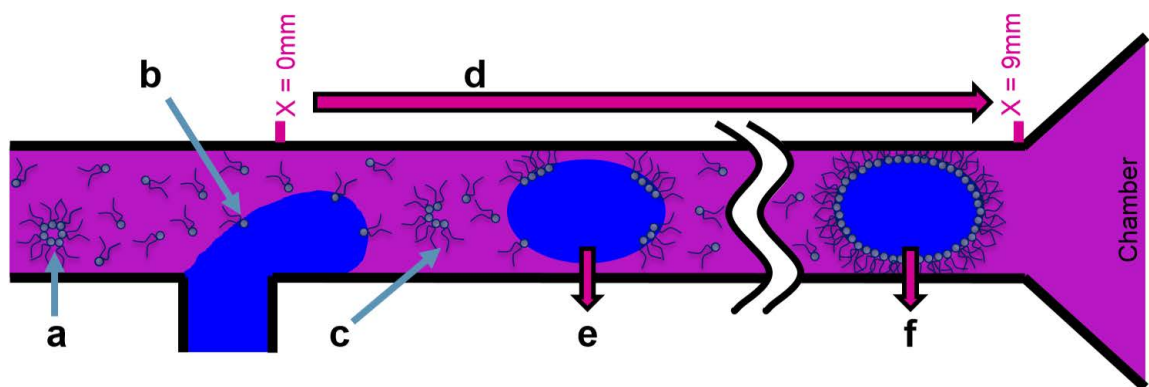
Figure 2-5. Mechanisms of surfactant transport for droplet microfluidics. a) micelle: self-assembly of surfactant molecules, b) surfactant molecules transport to the interface, c) micelle molecules must diffuse apart in order for the molecules to transport to a droplet interface, d) a longer channel length allows more time for diffusion to the interface, e) partially coated droplet = not stable = coalescence, e) fully coated droplet = stable = very little coalescence.

2.3 Electrokinetic Particle/Cell Characterization via Dielectrophoresis

The following sections detail particle/cell characterizations.

2.3.1 Current Methods of Particle/Cell Characterizations (Advantages and Disadvantages)

As mentioned in the introduction, this work utilized two microfluidic techniques. So far droplet microfluidics has been introduced. The second portion of this project was related

to particle/cell characterization. There are many methods of particle/cell characterization. One method is flow cytometry and microscopy imaging, which detect markers that require fluorescent labeling [101]. Another method, magnetophoresis, uses magnetic nanoparticles for characterization and separation [102]. Electrokinetic methods, such as electrorotation, electrical impedance spectroscopy, and dielectrophoresis provide label-free methods of characterization [101]. Electrokinetics are discussed further in the following sections on dielectrophoresis and insulator dielectrophoresis.

2.3.2 Previous μM.D.-ERL research for Characterizing Polystyrene Beads and Red Blood Cells

μM.D.-ERL has completed a multitude of experiments for characterizing new device designs by using polystyrene beads (PS) and red blood cells (RBC). To characterize a new device, it is desirable to verify DEP responses of particles with ideal behavior. Before adding complex particles/cells into a system, many researchers benchmarked new dielectrophoretic devices using polystyrene beads [103-109]. Polystyrene beads are highly uniform, behave ideally in many systems, and come in a large variety of sizes. Prior Minerick lab research has explored the dielectrophoretic behavior of 6 μm polystyrene beads and experimentally quantified the DEP response of all eight blood types (A+, B+, AB+, O+, A-, B-, AB-, and O-). The ABO-Rh blood typing system is the
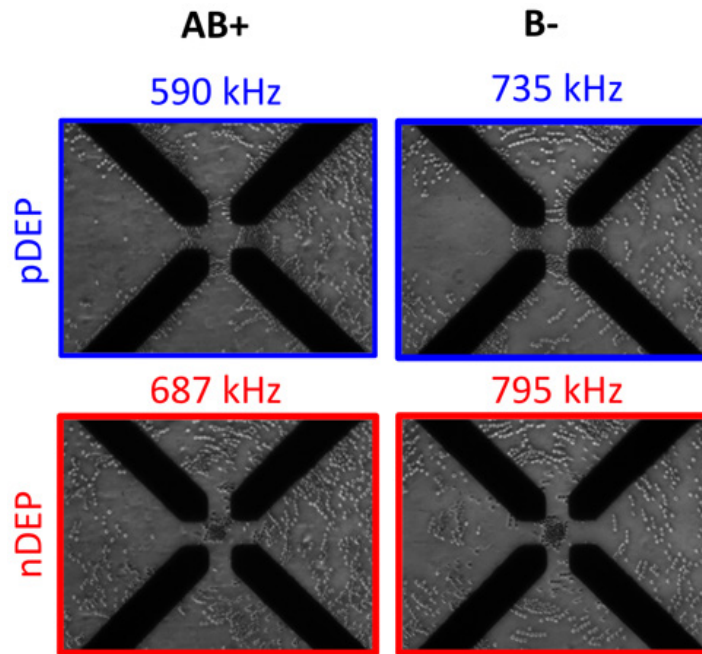
Figure 2-6. Native AB+ and B- red blood cells in 0.1 S/m dextrose buffer and subjected to a 2.5 V_{pp} AC signal swept from 100 kHz to 1.9 MHz over 400 seconds. Both AB+ and B- experience p DEP and nDEP, although the range differs. This demonstrates differences in cell motion by ABO antigen expression on red blood cell membranes. Figure courtesy of μM.D.-ERL researchers K. Leonard and H. Moncada Hernandez.

dominant antigen classification system for RBCs characterized by antigen polysaccharides expressed on the membrane surface, a transmembrane protein, and plasma antibodies [110, 111].

RBC membranes [112-120] are essentially non-conducting [121-125], vary from 50 to 90 nm thick depending on exerted force [114], and are the reason RBCs exhibit a low electrical conductivity (they behave as a dielectric) [34, 123]. In contrast, RBC interiors are conductive [125-127] and how conductive they are varies with hemoglobin and cytoplasm molecules [125, 128, 129]. RBCs have a biconcave shape, ranging from 6 to 8 μm in diameter and 0.5 μm (center) to 2 μm (edge) in thickness. RBCs vary dynamically in response to solvent conditions, pH, tonicity, and temperature [127]. Blood cell molecular expression varies by person; ABO-Rh type dominates its classification based on antigen polysaccharides expressed on the membrane surface and plasma antibodies [112, 113].

Prior μM.D.-ERL research quantified cell movement in a batch DEP device, shown in Figure 2.6 [36, 130, 131], interrogated insulator DEP blood cell deflection at a microfluidic bifurcation in a continuous DEP device [132], and demonstrated that ABO-Rh expression shifts cross-over frequencies. The cross-over frequency is the frequency at which there is zero cell motion in the transition between movement up the electric field gradient to movement down the electric field gradient or vice versa. Lastly, systematic experiments and automated intensity profile analysis revealed that ABO-Rh expression alters the entire cell dielectrophoretic frequency spectra. These experiments were completed batch-wise consuming considerable resources and person-hours. *The use of droplet microfluidics flowing into a DEP chamber allows simultaneous completion of multiple experiments. With the established red blood cell typing database, the reliability and reproducibility of reverse-insulator dielectrophoresis (riDEP), was explored, as discussed in Chapter 7.*

2.3.3 Other Cell/Particle Systems

There is a wide range of particle/cell systems that can be characterized via dielectrophoretic techniques. DEP characterizations have been completed for biological cells [24, 33, 133-142], whole blood [127, 128, 143-158], erythrocytes (RBCs) [31, 36, 121, 125, 126, 130-132, 147, 149, 152, 154, 156, 157, 159-178], leukocytes [148, 179-187], and peripheral blood [188, 189]. As mentioned, previous μM.D.-ERL work has shown ABO-Rh blood typing using DEP [131, 132, 190, 191]. A change in cholesterol level changes human RBC morphology [192]. High cholesterol alters human RBC membrane thickness, sickle cell anemia changes human RBC shape [193], stem cells change shape/size/properties as they differentiate into their different progeny [194, 195], and more. *The new electrokinetic technique presented in this dissertation, riDEP, takes the field of medical microdevices one step closer to being able to characterize particle/cell systems without requiring any labeling/alterations to the particles/cells and with minimal sample volume and time required.*

2.4 Dielectrophoresis

Dielectrophoresis, the characterization method used for this work, is discussed in the following sections.

2.4.1 Background: Electrokinetics to Dielectrophoresis

Electrokinetics is the use of electric fields to induce motion. Three of the most common types of electrokinetics are electrophoresis, isoelectric focusing, and dielectrophoresis. Electrophoresis is the migration of charged objects within a solution when under the influence of an electric field. Both the size and charge density of the object contribute to the migration speed. Isoelectric focusing is object migration in pH gradients to its iso-pH (iso-electric) point. Amphoteric molecules (proteins, amino acids) can act as an acid or a base, either donating or accepting a proton. In isoelectric focusing, an electric field is applied across a channel. Amphoteric molecules will move toward the cathode when in acidic conditions and toward the anode when in basic conditions. There is a point where the electrophoretic force will become zero, and the amphoteric molecule will no longer move. This occurs at the isoelectric point where the molecule's charge is neutral. Dielectrophoresis is object motion due to its electrical properties in non-uniform electric fields. The electrical permittivity and conductivity of the object and the surrounding solutions determine the direction of motion either up or down the electric field gradient. These electrical properties along with the size of the object and the magnitude of the electric field also determine the size of the dielectrophoretic force experienced. Other types of electrokinetics include electroendosmosis, electrolysis, and capillary electrophoresis. All of these techniques can be applied to aspects of particle/cell characterization and separation. *In this dissertation, dielectrophoresis (DEP) was chosen as a particle/cell characterization technique due to its versatile, fast, noninvasive, and nondestructive qualities [132].*

2.4.2 Applications/Advantages of Dielectrophoresis for Particle/Cell Characterization

Dielectrophoresis is a fast, noninvasive, and nondestructive technique for the manipulation/characterization of bioparticles such as yeast, cancer, stem, and blood cells [132]. Dielectrophoresis has many practical applications in the fields of engineering, medicine, atmospheric sciences, space explorations, industry, life sciences, and more [196]. In the field of life science, manipulation of particles is important for diagnostic and clinical applications. Disease detection, separation of cancerous from normal cells, separation of living from dead bacteria, and ABO-Rh human blood typing are examples of the applications of DEP in the life sciences [4].

Advantages to using DEP for particle manipulation include instrumentation simplicity, favorable scaling effects, and label-free operation. Another key advantage is that, unlike electrophoresis, DEP is applicable to any polarizable particle or cell, even those with no

net charge. Depending on the size and electrical properties of both the suspending medium and the particles, both positive and negative forces can be induced by DEP. DEP microdevices can integrate sample injection, sample preparation, and analysis including trapping, concentration, separation, focusing, and characterization within a single device [197]. For biological applications specifically, benefits of DEP microdevices include small samples, minimal waste, low costs, high-resolution separation and detection, and short analysis times [197].

DEP uses the spatial gradient of a non-uniform electric field to induce a particle dipole and thus cause particle movement up or down the electric field gradient [196]. Particle size, shape, and electrical properties as well as suspending media properties, and the frequency of the electric field influence the DEP force [132, 198]. DEP force, Equation 2.3, also depends on the sign and magnitude of the Clausius-Mossotti factor (f_{CM}), $K(\omega)$ shown in Equation 2.4. The complex permittivities ($\tilde{\varepsilon}_i$) are calculated using the relative permittivities (ε_i), the conductivities (σ_i), and the angular frequency (ω) as shown in Equation 2.5. For a f_{CM} greater than zero, particles are attracted to the electric field maxima (positive DEP, p-DEP) and for a f_{CM} less than zero, the particles are attracted to the electric field minima (negative DEP, n-DEP) [196].

$$\langle \bar{F}_{dep}(t) \rangle = 2\pi \varepsilon_m r^3 \mathrm{Re}[K(\omega)] \nabla |\bar{E}_{rms}|^2 \qquad 2.3$$

$$K(\omega) = \frac{\tilde{\varepsilon}_p - \tilde{\varepsilon}_m}{\tilde{\varepsilon}_p + 2\tilde{\varepsilon}_m} \qquad 2.4$$

$$\tilde{\varepsilon}_i = \varepsilon_i \varepsilon_0 - \frac{j\sigma}{\omega} \qquad 2.5$$

Dielectrophoretic force is influenced by particle size, electric properties of the particles and the suspending medium, and the electric field frequency and amplitude [132, 198]. This allows DEP to characterize particles/cells based on their size, membrane/cytoplasm permittivities and conductivities, and shape characteristics [36, 130, 132, 133, 159]. This is advantageous over linear electrophoresis, which can only characterize particles/cells by size and surface charge [34, 199, 200]. Electrokinetic characterization results are dependent upon the supporting media conditions. Therefore a different DEP spectra curve is needed for each media condition, such as conductivity. Until recently, each point on the DEP spectra needed a separate experiment at a different frequency. Previous µM.D.-ERL research overcame this by implementing a frequency sweep, allowing multiple frequencies to be combined into one experiment [201]. The time and sample requirements for generating DEP spectra for different media conditions limit the practicality of using DEP characterizations for medical diagnostics. *The new riDEP technique presented herein takes one step closer to overcoming this limitation. The utility of the new electrokinetic technique presented was benchmarked against known data.*

2.4.3 Formation of Non-Uniform Electric Fields

Dielectrophoresis can be completed using either direct current (DC) or alternating current (AC) fields [196, 202]. In DC-DEP non-uniform electric fields are created by the device geometry. Common geometries include parallel or interdigitated, castellated, oblique, curved, quadrupole, microwell, matrix, extruded, top–bottom patterned, and side-wall patterned, which can be seen in Figure 2.7 (all except side-wall patterned) [7]. An advantage to using DC-DEP is that the f_{CM} is dependent on the electrical conductivities of the particles and the suspending medium as shown in Equation 2.3. Living cells are weakly conductive. The electric field drops across the cell membrane causing the f_{CM} to be negative, allowing the DEP motion of cells to be modeled by n-DEP [196]. Due to their complexity, electric and physical properties of the cytoplasm, cellular and nuclear membranes affect the DEP response of living cells [198]. The high voltages necessary to generate sufficient DEP force can cause Joule heating effects inside the channel [196].
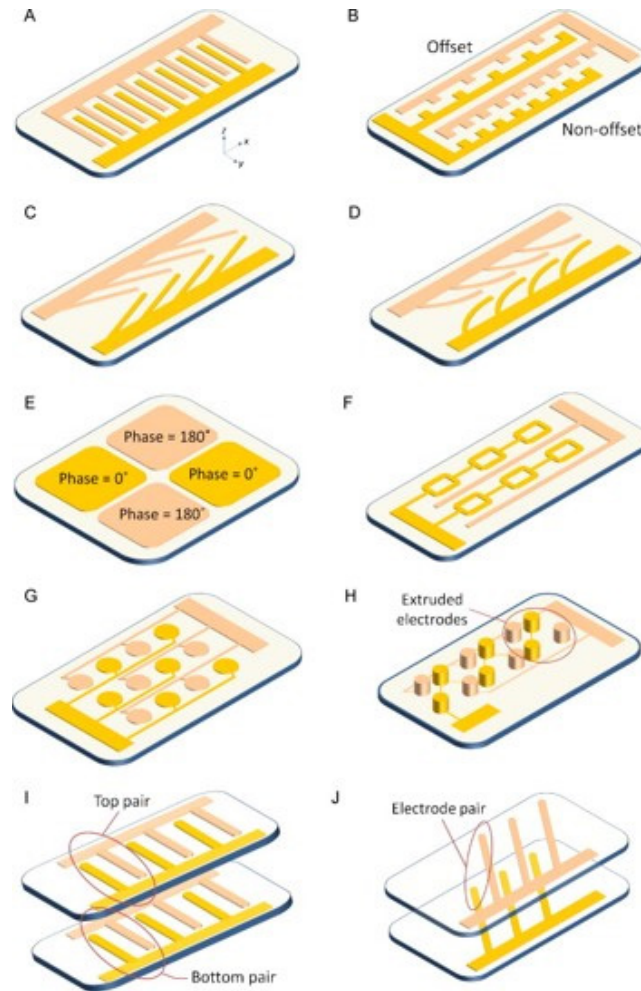
Figure 2-7. Schematics of common DEP geometries. (a) parallel or interdigitated, (b) castellated, (c) oblique, (d) curved, (e) quadrupole, (f) microwell, (g) matrix, (h) extruded, and (i) top–bottom patterned [7].

Joule heating effects are unwanted due to the temperature increase associated with them. An increase in temperature can cause a disturbance in the operation of the device due to bubble formation or changes in cell viability and physiology, even cell death [196].

In AC-DEP, the non-uniform electric fields are generated by an embedded electrode array [203]. Fabrication of such electrode arrays is complex, expensive, and time-consuming. This makes AC-DEP devices less economically feasible as system scale increase [196]. The f_{CM} for AC-DEP is dependent not only on the electrical conductivities of the particles and the suspending medium but also the permittivities [196]. A disadvantage to AC-DEP is that there may be a disturbance in the operation of the device due to fouling of the electrodes. An advantage of AC-DEP over DC-DEP is the prevention of Joule heating by using low voltages [196]. *The work presented herein eliminates some of the complexity of the electrode designs due to the electric field gradient being formed by the droplet interfaces instead of the electrode configuration.*

2.4.4 2D versus 3D Electrodes

Two types of electrodes for DEP experiments have been presented in the literature, two-dimensional (planar) and three dimensional (3D). Planar electrodes are more common than 3D electrodes due to microfabrication complexity and cost [204]. Planar electrodes require fewer steps, time, and materials for microfabrication. However, 3D electrodes can provide a more effective electric field, and many researchers are finding cheaper, alternative methods for fabrication such as alternating layers of conductive (aluminum foil) and insulative (epoxy resin) materials and drilling a well through them [205], spacing wires using Scotch tape [206], weaving stainless steel wires with polyester yarn cloth [207], using deep reaction ion etching for silicon electrodes [9], Using a base layer
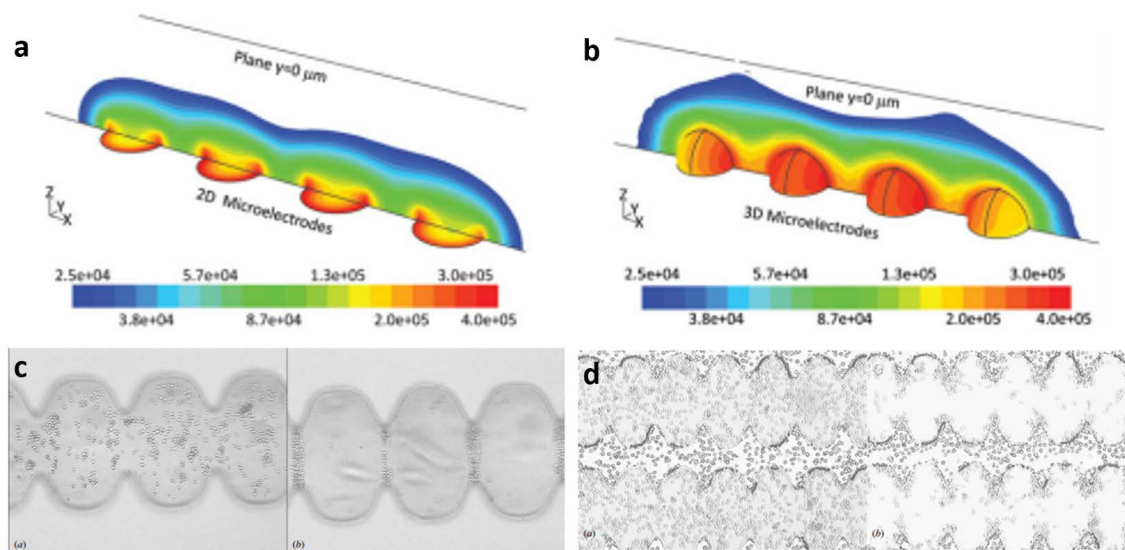
Figure 2-8. Simulation comparison of 2D (a) and 3D (b) electrodes [3]. Experimental comparison of 2D (c) and 3D (d) electrodes [9].

(such as silicon or photoresist) to form the 3D structure before metal deposition [3, 208], carbonizing photoresist structures [209-211], and electroplating [212].

With planar electrodes, the distance up into the chamber that the electric field traverses is limited [3]. With 3D electrodes, the electric field can be present throughout the entire chamber. A simulation comparison [3] and an experimental comparison [9] are shown in Figure 2.8. *For riDEP, three-dimensional electrodes are necessary to get the electric field close enough to the droplet interface to traverse through the droplets.*

2.5 Insulator Dielectrophoresis

2.5.1 Advantages

For the new DEP technique that we are presenting herein droplets shape the electric field instead of electrodes. This is similar to insulator dielectrophoresis, although in a reversed fashion. Insulator dielectrophoresis (iDEP) is a subset of DEP that shapes the electric field lines by adding insulator geometries within the microfluidics. There are many advantages to utilizing insulator dielectrophoresis, including the ability to trap and sort particles/cells, fouling reduction, reduced cost of materials and fabrication [4, 132, 196, 202]. Using trapping and streaming for particle/cell separation is very common in insulator dielectrophoresis, but due to the batch nature of the work presented here trapping and streaming are not discussed. One key iDEP advantage is the ability to create a device tailored to a particular task. Obstructing features positioned within channel or chamber geometries can achieve trapping or sorting [4]. A wide variety of materials and geometries may be utilized with iDEP allowing devices to be more specific to a certain
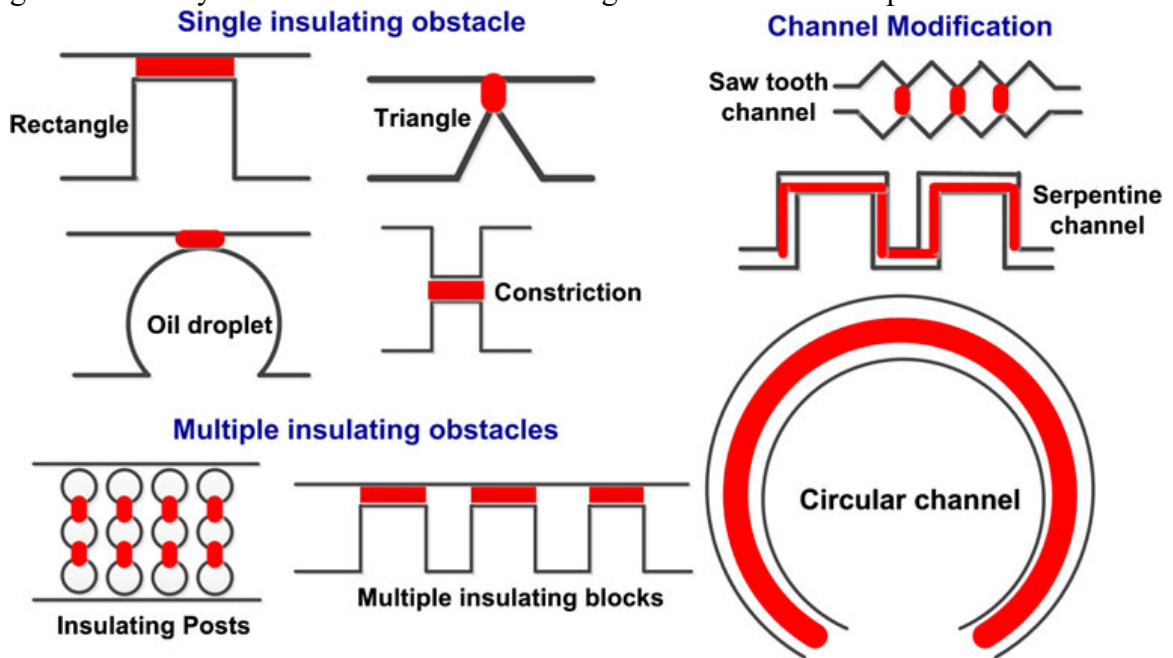
Figure 2-9. Schematics showing common iDEP geometries [4].

task or more general for a variety of tasks. Another advantage of using insulating features over complex electrode arrays when shaping electric fields is that they do not foul as electrodes do [202].

Srivastava et al. compiled common insulating geometries showing where the particles undergo the maximum effect under DC fields, shown in Figure 2.9 [4]. The cost of iDEP fabrication is reduced from electrode DEP because microfabricated iDEP devices use only a single material and two remotely positioned electrodes [202]. Only having two electrodes is beneficial because it decreases electrode complexity and reduces material costs. Remotely positioned electrodes also render the device more electrochemically inert [196].

Gallo-Villanueva et al. utilized the insulating post geometry in their experiments. Three geometry variables were studied; insulating post diameter, size of the gaps between posts, and the number of gaps. Along with COMSOL simulations, the experiments showed that device geometry has an important effect [203]. Experiments completed by Srivastava et al. observed DEP forces by varying medium conductivity, particle size, and field strength [132]. Results of these experiments show promise to accurately predicting particle paths and designing effective devices for trapping and sorting. In this dissertation, we present a new method of insulator dielectrophoresis that is essentially the reverse of traditional iDEP. Instead of having solid insulating features shape the electric field, we show how the electric field can be shaped within isolated droplets by the surrounding insulative oil.

Streaming and trapping are the two iDEP regimes observed during continuous flow experimentation. Cell/particle characterization and separation can be achieved by using streaming/trapping. This can be achieve by applying electric fields of different magnitude/frequency. Both regimes have a large dependence on the device geometry, the most common being an array of posts [213]. Streaming occurs when the dielectrophoretic force acting upon a cell/particle is less than the other forces (such as forces from fluid flow). Trapping occurs when the dielectrophoretic force is stronger than the other forces acting on a cell/particle.

 In combination streaming and trapping can be used to separate particles based on size, shape, or electric properties such as polarizability and charge [197]. Experiments conducted by Baylon-Cardiel et. al. showed an increase in DEP force with an increase in applied electric field, an increase with an increase in suspended medium conductivity, and a decrease with an increase in pH [214]. These results are consistent with theory and simulation. An increase in the suspended medium conductivity yields lower electroosmotic flow. A decrease in the suspended medium pH also yields lower electroosmotic flow. With lower electroosmotic flow particle immobilization is easier [214]. Trapping occurs when the dielectrophoretic forces overcome the electrokinetic forces.

In both trapping and streaming the diffusive forces are weaker than both the electrokinetic and dielectrophoretic forces [202]. Experiments and simulations completed

by Camacho et. al. demonstrate large agreement. This implies that the theory is reflected in the experiments for both regimes [215]. Trapping can be used to concentrate a sample by immobilizing the target particles as they enter the system [197]. This is done by using a high electric field to trap the particles and after sufficient time switch to a low electric field to allow the release of the now concentrated particles [213]. Streaming can also be used to concentrate particles but in a continuous fashion. By using an electric field that is lower than that required for trapping and high enough to cause particle movement within the fluid, particles can be concentrated in a stream [213]. Figure 2.10 shows an example of using a combination of trapping and streaming in order to separate live (blue) and dead (red) THP-1 cells [137]. *When utilizing droplet microfluidics, where each droplet is its own isolated environment, use streaming and trapping cannot be used. For these types of applications, hafnium oxide use as a physical barrier between samples and electrodes was investigated as an alternative to riDEP and is presented in Chapter 8.*

2.5.2 DC vs. AC vs. DC-Offset AC for iDEP

Traditionally iDEP is conducted using a DC electric field [216]. This is advantageous over the traditional AC field used for DEP due to single material fabrication, reduced fouling, and remote electrodes [4]. Srivastava et al. presented a comprehensive review of DC-iDEP applications. Disadvantages of DC-iDEP include high DC voltages needed and joule heating which can affect the viability and physiology of cells [216]. Joule heating causes a rise in temperature of the fluid and then forms a temperature gradient throughout the device by thermal diffusion [217]. This can cause adverse effects such as the reduction of the ability to trap and focus particles [217]. By introducing an AC component to the electric field three key benefits are observed; contribution to the dielectrophoretic force acting on the particles, suppressed electroosmotic flow, and no electrophoretic motion [216]. Experiments conducted by Lewpiriyawong et al. using DC-offset AC iDEP to observe the electrokinetics concentration of particles and cells by negative iDEP showed a reduction in the DC field component and the Joule heating [216].

2.5.3 Electrocoalescence

The riDEP microdevice presented in this dissertation used the continuous oil phase around the droplets as an insulator, shaping a non-uniform electric field to within each droplet. A possible challenge when combining dielectrophoresis with droplet generation is that electric fields can impact the droplet interface itself, thus influencing droplet transport, deformation, fission, and fusion of droplets within microdevices [28, 29, 35, 37, 218]. There have been numerous studies on droplet deformation in a uniform electric field, including a handful in non-uniform electric fields [218]. Coalescence occurs when the electric field destabilizes the thin film between droplets [85] and has been shown to depend on the materials present in the two phases [11, 85, 219, 220]. Operating conditions must be carefully chosen to avoid splitting and coalescence. Research has shown that electrocoalescence depends on the materials present in both phases [11, 85,
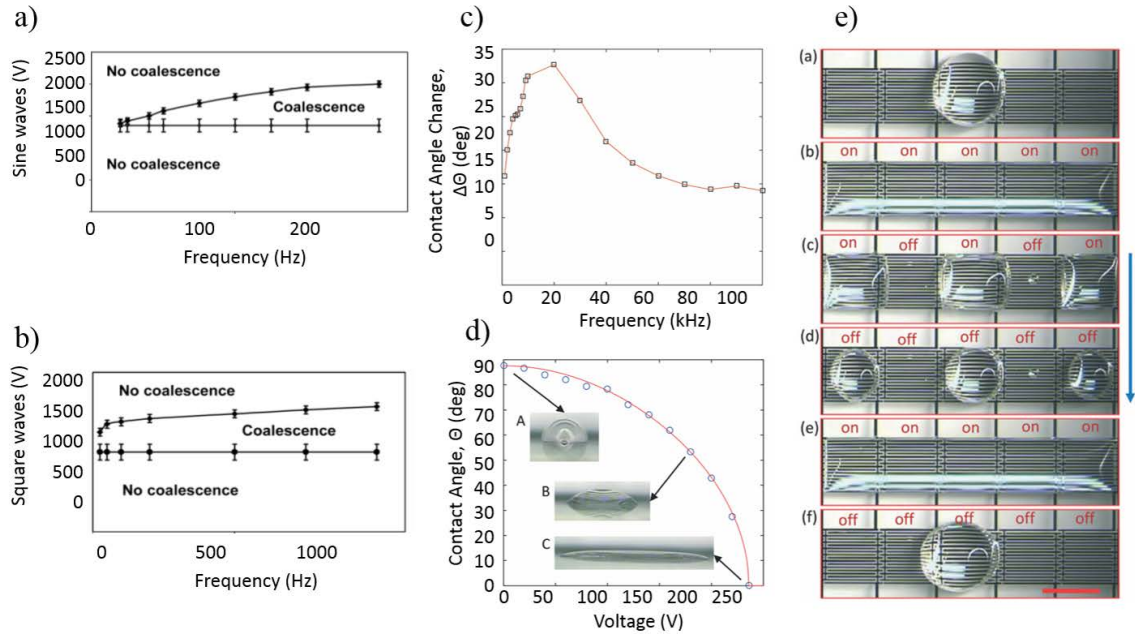
Figure 2-10. Droplet coalescence phase diagrams for (a) sine and (b) square waves [6]. Contact angle dependence on (c) frequency and (d) voltage, along with (e) the utilization of electric field induced contact angle change to enable droplet fusion and fission [10].

219, 220]. *Experiments for this dissertation had multiple aqueous phases with multiple salts and dextrose additives and continuous phases with multiple surfactants as additives.* Phase diagrams exist for droplet coalescence in a static fluid and AC fields as a function of frequency [6, 220]. This type of data illustrated that electric fields can achieve electric field effects within the droplets without destabilizing the interface between droplets [6, 11, 219, 220]. Figure 2.10 a and b show the coalescence of two droplets in a static fluid for both sine and square wave AC field as a function of frequency [6]. The effects of voltage and frequency on contact angle have also been studied and used to target droplet fusion and fission, as shown in Figure 2.10 c, d, and e [10]. *These examples of previous research provided the means to reduce the range of experimental parameters investigated. Correct experimental conditions to reduce fluid shear and control droplet coalescence in applied electric fields were found via a systematic study of the effects of the applied voltage on droplet destabilization, presented in Chapter 7.*

2.6 Conclusions

One of the key limitations to current DEP devices is the amount of time it takes to generate DEP curves. This project aimed to eliminate this by implementing parallel experimentation. This was accomplished by using droplet microfluidics, which provided isolated microenvironments to multiplex the number of experiments. An electric field was applied across the chamber resulting in non-uniform electric fields within each droplet that can be used for DEP interrogations.

Research shows that droplet microfluidics can control the formation of droplets within the nano-micrometer diameter range with high monodispersity that act as isolated microreactors [28, 29]. This work used T-junctions due to their high presence in the field, adaptability to a wide range of velocities and pressures, and useful in chemical reactions and cell encapsulations [44, 67-70]. Surfactants can be tailored to a specific purpose in a system, such as increasing droplet stability or biocompatibility [31, 67, 112, 131, 191, 198]. Krytox FSH 157 was chosen herein, for its high molecular weight and similarity to a biocompatible surfactant (which was not chosen due to cost), to form a layer of molecules at the interface of each droplet to act as a repulsive barrier helping the droplets resist coalescence [86, 87]. Multiple works showed that the droplets formed can be packed within a larger microfluidic chamber [43, 60].

In this dissertation, dielectrophoresis (DEP) was chosen as a particle/cell characterization technique due to its versatile, fast, noninvasive, and nondestructive qualities [132]. An electric field was applied across the microfluidic chamber shaping a non-uniform electric field within each droplet. Previous research showed that the presence of an electric field destabilizes the film between droplets [11, 85, 218]. Therefore, operating conditions were carefully chosen to avoid splitting and coalescence. The non-uniform electric field shaped within each droplet can be used for dielectrophoretic characterizations. Before adding complex particles/cells into a system, many researchers benchmarked new dielectrophoretic devices using polystyrene beads [103-108]. Prior Minerick lab research explored the dielectrophoretic behavior of 6 μm polystyrene beads and experimentally quantified the DEP response of all eight blood types (A+, B+, AB+, O+, A-, B-, AB-, and O-). Both polystyrene beads and the ABO-Rh blood typing system were used to test the viability of the reverse insulator dielectrophoretic technique.

3   Materials and Methods

3.1   Microdevice Fabrication

This section describes, in detail, the fabrication processes used for device fabrication.

3.1.1   Fluidic Layer

Microdevices used for this work were microfabricated in the Michigan Technological University's Microfabrication Facility (MFF) by customized soft lithography techniques [221, 222]. Entrance to the MFF required safety training on all hazards that were or could be present. To gain qualification to use any piece of equipment, a series of at least three watches and three hands-on followed by a qualification exam were completed. This ensured safe and proper use of the different types of equipment and chemicals present. Devices consisted of either a fluidic layer or an electrode layer with a fluidic layer, both with a standard microscope slide as the substrate. Poly-dimethyl siloxane (PDMS), a clear polymer, was used for the fluidic layers. The clear PDMS and glass slide allowed optical observations and measurements. A master silicon wafer was microfabricated and used for making castings of the PDMS fluidic layers. The desired fluidics were designed/drawn in AutoCAD (AutoDesk Inc, San Rafael, CA). They were translated into a film mask by either sending to Output City (Bandon, OR) or by hand in the dark room of the MFF. In the dark room, an AutoCAD file was transferred to a transparency using a laser photoplotter and standard development techniques.

To get the desired features from the film to a silicon master wafer, the clean room of the MFF was used. SU-8 processing information [223], along with literature [224] and μM.D.-ERL personnel experience informed the fabrication recipes used. Throughout the project, multiple recipes were utilized. The different recipes were used to either improve the outcome of the microfabrication or target a different thickness. Table 3.1 documents these recipes. There were three main parts in the process of adding features to the silicon master wafer; cleaning, photoresist crosslinking, and feature development. The following three paragraphs discuss the details and reasoning behind each step of the process.

Cleaning: A 4-inch silicon wafer was sonicated in acetone for 5 minutes, followed by isopropyl alcohol (IPA) for 5 minutes then deionized (DI) water for 5 minutes. The wafer was immediately rinsed with DI water to ensure removal of all contaminated solvents before the wafer had a chance to dry, reducing the chance of leaving contaminants on the wafer. The wafer was dried via nitrogen. A second cleaning step was completed to ensure no contaminants were deposited during the drying process. This step was completed on the polymer spin station (Laurell, North Wales, PA). First, the polymer spin station was set up for the desired two-step spin cycle. For the SU-8 2025 and 2035 recipes, the wafer was placed on the spin coater and secured via vacuum. During the spin cycle, the silicon wafer was cleaned by rinsing with acetone, to remove any organic impurities, followed by isopropyl alcohol (IPA), to remove the contaminated acetone. The silicon wafer was

Table 3-1. SU-8 recipes used to target different structure thicknesses

Desired Thickness	70 µm	70 µm	70 µm	120 µm	75 µm
Photoresist	SU-8 2025	SU-8 2025	SU-8 2025	SU-8 2035	SU-8 2075
Cleaning	Acetone, IPA on spin coater	Acetone, IPA on spin coater	Acetone, IPA on spin coater	Acetone, IPA on spin coater	Sonicate in acetone, IPA, and DI water, 5 min each Heat at 150°C, 30 min, slowly cool
Additional preparation steps	none	65°C, 1 min	65°C, 5 min	none	HDMS adhesion promoter 3000 rpm, 600 rpm/s, 30 sec, Heat at 150°C, 1 min, slowly cool
Spin Conditions	800 rpm, 100 rpm/s, 15 sec 1750 rpm, 300 rpm/s, 30 sec	750 rpm, 100 rpm/s, 15 sec 1500 rpm, 300 rpm/s, 30 sec	500 rpm, 100 rpm/s, 10 sec 1250 rpm, 300 rpm/s, 45 sec Relax 5 min	500 rpm, 100 rpm/s, 10 sec 1000 rpm, 300 rpm/s, 45 sec	500 rpm, 10 rpm/s, 55 sec 3000 rpm, 150 rpm/s, 47 sec Relax 20 minutes
Prebake	65°C, 6 min 95°C, 12 min	65°C, 3 min 95°C, 6 min	65°C, 3 min 95°C, 8 min, slowly cool	65°C, 5 min 95°C, 25 min, slowly cool	65°C, 10 min 95°C, 25 min, slowly cool
Exposure	10 sec	20 sec	196.5 mJ/cm^2	240 mJ/cm^2	196.5 mJ/cm^2
Postbake	65°C, 4 min 95°C, 7 min	65°C, 6 min 95°C, 12 min	65°C, 2 min 95°C, 7 min Cool 30 min	65°C, 6 min 95°C, 12 min	65°C, 5 min 95°C, 25 min, cool 30 minutes
Development	SU-8 developer 10 min	SU-8 developer 7 min	SU-8 developer 3 min	SU-8 developer 7-10 min	SU-8 developer 3 min
Hardbake	none	none	80°C, 30 min Slowly cool	none	none

placed on a hot plate at 65 °C for 5 minutes to remove any volatiles. For the SU-8 2075 recipe, the wafer was placed on a hotplate at 65 °C for 20 minutes directly after the rinsing with DI water post sonication cleaning. The heating of the wafer post cleaning ensured that the substrate was dry, which aided in the success of the proceeding steps.

Photoresist coating: The wafer was secured back onto the spin coater to undergo the spin cycle a second time. For the second spin cycle, 4 ml of the negative photoresist, SU-8 (MicroChem, Westborough, MA), was placed on the wafer. The first step of the spin cycle spread the SU-8 out over the entire wafer and the second step of the spin cycle targeted the desired thickness of the SU-8 layer. After the spin cycle was complete, the wafer was removed, set on a flat surface, and allowed to relax for 5 minutes to minimize edge beading. While the wafer relaxed, the polymer spin station was thoroughly cleaned. Chemical gloves were worn, and the chemical hood sash was kept as low as possible for protection against the chemicals used for cleaning. First, acetone was used to remove the SU-8 and then IPA was used to ensure all SU-8 and acetone were removed. The SU-8, acetone, and IPA were sent down the drain in the polymer spin station into a waste collection tank to later be properly disposed of by university safety personnel. The tank was checked before each use to ensure that there would be no possibility of overflow/chemical spill.

Photoresist crosslinking: The silicon wafer was then pre-baked to evaporate any solvents present on the wafer and densify the photoresist layer. The wafer was slowly cooled to room temperature to avoid any temperature shock to the substrate and photoresist layer. The wafer was carefully slid off of the hotplate onto a pad of cleaning wipes that would allow the wafer to cool without any thermal shock. To see if the pre-bake was sufficient the wafer was placed back on the 95 °C hot plate [223]. If wrinkles appeared the wafer was kept on the hot plate until they disappeared and was then cooled back down to room temperature. This was repeated until wrinkles no longer appeared in the SU-8 layer. The wafer was allowed to relax as the EVG 620 Aligner (EVG, Austria) was turned on and set up for exposure. The desired thickness determined the optimal exposure dose. To achieve the correct dosage, the intensity of the UV lamp within the aligner was measured and an amount of time for exposure was calculated using Equation 3.1.

$$Dose = Intensity * Time \qquad 3.1$$

The intensity and uniformity of the UV lamp were measured using a five-point measurement system. UV protective safety glasses were worn during the measurements to prevent any possible eye damage from the UV lamp. The resulting intensity was used in Equation 3.1 along with the desired dose to calculate the correct exposure time. Over time the intensity of the UV lamp decreases, so it was checked each time to ensure proper exposure. The software was set-up for a top-down, soft contact process. The mask was inspected to ensure that it was particle free. If anything was present on the mask, it was cleaned using nitrogen. If nitrogen was not effective a cloth swab was used with acetone and IPA followed by rinsing with DI water and drying with nitrogen. Before the mask

was loaded it was "dusted" using a pressurized stream of nitrogen. The mask was loaded with the emulsion side down to ensure that the desired features were as close to the substrate as possible during processing, followed by the wafer, and the process allowed to run. While the process ran, users faced away from the equipment to ensure that they weren't exposing their eyes to high doses of UV light, which can be damaging. During UV exposure, the formation of a strong acid occurs in the areas exposed. A check to ensure correct exposure time was if the latent image of the features were visible in the first 5-15 seconds of the post-bake [223]. If no image had appeared after a minute into the post-bake the photoresist was under-exposed. During the post-bake, an acid-catalyzed, thermally driven epoxy crosslinking occurred in areas that underwent UV exposure. Once the post-bake was completed the wafer was slowly cooled to room temperature and then allowed to relax for 30 minutes to relieve any residual stresses present in the photoresist.

Feature Development: The wafer was then ready for development. It was placed in the SU-8 developer (MicroChem, Westborough, MA) and gently agitated to improve the development of the higher aspect ratio features [223]. Every two minutes the wafer was removed from the developer and rinsed with IPA and then re-submerged in the developer. The development was complete when the white film was no longer generated when rinsing with IPA. After development was complete, the wafer was rinsed with deionized water and dried using nitrogen. A hard bake was completed to help ensure the photoresist features were fully cross-linked and would be permanent on the silicon wafer [223]. The wafer was then gradually cooled to room temperature to avoid any deformation of the
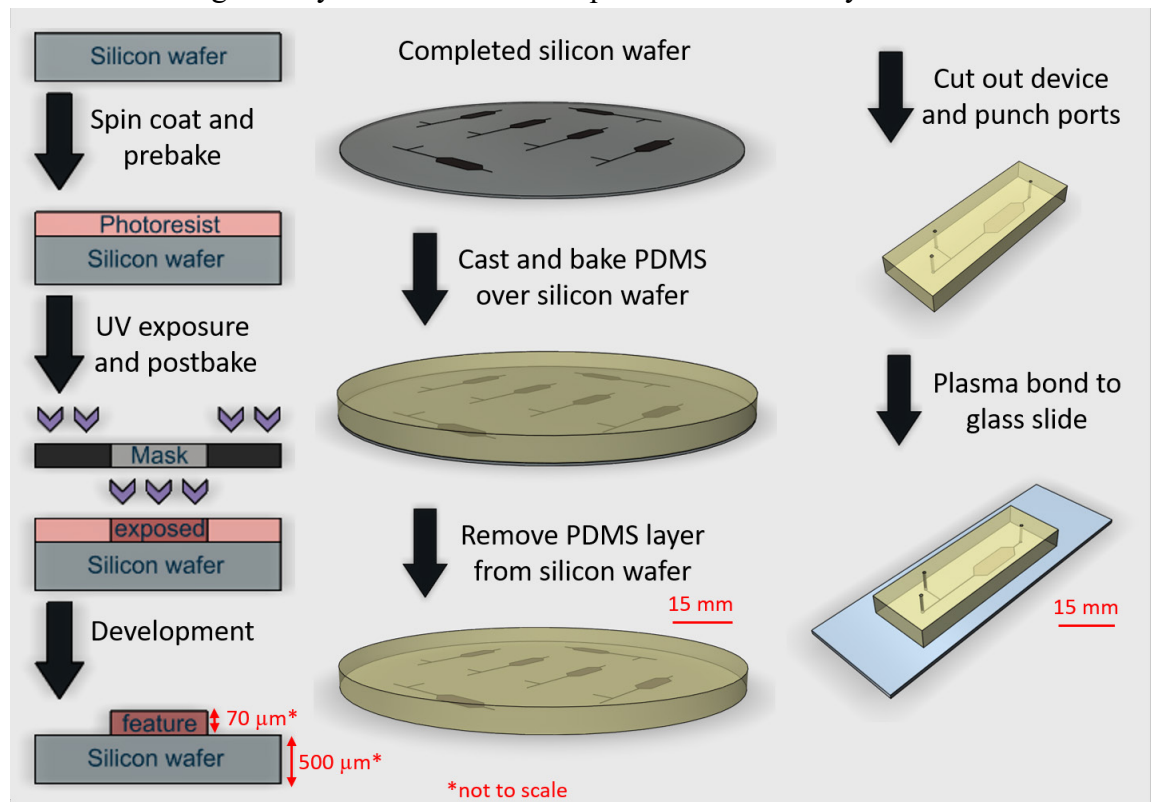
Figure 3-1. Flow diagram of microfabrication process.

features [224]. As the wafer cooled, the chemicals and containers used for the development were properly disposed of and cleaned according to the MFF facility safety manual. The developer and IPA were sent down the drain of a second spin station to another waste collection tank. Each container was rinsed in triplicate with DI water, which was also sent down the drain to the waste collection tank. As with the other collection tank, the level in the tank was checked before each use to ensure that there was no chance of overflow/chemical spill. If the tank was close to the allowable fill line, MFF management was contacted. Figure 3.1 shows the process flow of fabricating a silicon wafer via soft lithography, along with an image of a completed master wafer.

Fluidic layer casting and bonding: The silicon master wafer could then be used for a casting of the fluidic layer. Foil was carefully placed around the wafer to form a structure to contain the PDMS during the casting. A base/curing agent combination (Sylgard 184, Dow Corning, Auburn MI) was used to get the desired PDMS properties. A 10/1 ratio of base to curing agent was well mixed, and vacuum was applied to remove any air bubbles generated during the mixing process. It was carefully poured over the silicon master wafer and placed in an oven at 70 °C for 4 hours. The silicon master wafer was removed from the oven. The foil was carefully removed, and the PDMS layer slowly peeled off. A scalpel was used to cut out each feature. Ports were then punched at the inlets and outlets using a 360-micron biopsy punch (Harris Uni-core, Sigma Aldrich, St. Louis, MO). The PDMS layer was bonded to a glass slide via air plasma (Harrick Plasma). A clean glass slide and the desired feature were placed in the plasma chamber with the sides that were to come in contact facing up. The system was pumped down for 4 minutes and then exposed to generated plasma with medium radio frequency (RF) for 60 seconds. The PDMS layer and the glass slide were immediately pushed together and placed in the oven at 70 °C for 24 hours. Over time the strength of the RF weakened and the system was pumped down for 3 minutes and then exposed to generated plasma with high RF for 75 seconds. This increase in the time and strength of the plasma treatment helped maintain the strength of the bond resulting from the plasma treatment.

3.1.2 Electrode Layer

Dielectrophoretic experiments used 50-micron platinum wire (Goodfellow, Coraopolis, PA) for electrodes. 360-micron holes were punched in all four corners in the microfluidic chamber. The 50 μm platinum wire was pulled through the holes to form two parallel electrodes. Uncured PDMS was placed at the top of each hole to make a watertight seal. The PDMS with the electrodes were cleaned with Scotch tape® and bonded to a glass slide as described in Section 3.1.1.

Addition of external electrodes: To connect the platinum electrodes to an external electric field source (AC generator, Agilent, Santa Clara, CA) silver conductive epoxy (MGChemicals, Surrey, B.C., Canada) was used to bond copper wires to the platinum wires as shown in Figure 3.2. The copper wires (22 GA Gauge AWG 2, local hardware store) were connected to alligator clips attached to the ground and potential; the copper
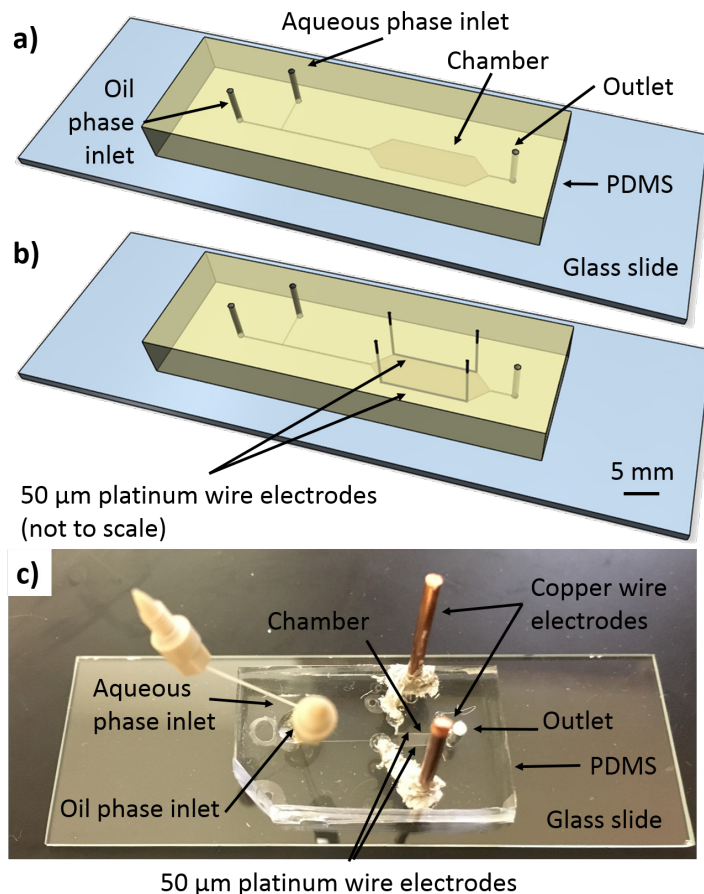
Figure 3-2. Three dimensional representations of a completed microdevice a) without and b) with electrodes. 50 micron platinum wire electrodes were positioned on either side of the chamber allowing an electric field to be applied across the chamber. c) Picture of real, completed microdevice on a 25 x 75 mm glass slide.

wires provided a stronger connection than the fragile platinum wire alone. The silver conductive epoxy was a two-part mixture that was combined and well mixed in equal proportions. The epoxy was placed around the copper wire on the seed layer. The microdevice was then placed in the oven at 70°C overnight to allow the epoxy to cure.

3.2 Solution Preparation

3.2.1 Continuous phase: oil and surfactant

Silicone oil: Preliminary experiments were completed with materials readily available in the lab that are also present in the literature. Sodium dodecyl sulfate (SDS) and Triton X-100 are two surfactants, and silicone oil is an oil phase that are commonly used in droplet microfluidics [29, 71, 76, 96-98]. SDS (Sigma Aldrich, St. Louis, MO) and Triton X-100 (Sigma Aldrich, St. Louis, MO) were added to the water and silicone oil, respectively, to make solutions ranging from 0 to 10 w/w% and 0 to 1.0 w/w%, respectively. These

concentration ranges were determined based on the critical micelle concentrations of the two surfactants; 0.25 w/w% for SDS, and 0.016 w/w% for Triton X-100 [225].

FC-40: After completing preliminary experiments investigating stability it was determined that a surfactant with a higher molecular weight might provide a more stable system (See Chapter 4). Since the project required a change in material, at the same time research into biocompatibility was completed to account for both stability and biocompatibility concerns. A fluorinated oil, FC-40 (3M, Maplewood, MN) was chosen as the oil phase and perfluoropolyether carboxylic acid, Krytox FSH 157 (DuPont, Wilmington, DE), was chosen as the surfactant. Krytox or perfluoropolyether carboxylic acid is an anionic surfactant that contains a perfluoropolyether tail and a carboxylic acid head. Although itself it not truly biocompatible, Krytox contains the same tail group and a similar head group to a biocompatible surfactant [47]. This study used Krytox over a commercially available biocompatible surfactant (Ran BioTechnologies, Beverly, MA) due to the large cost difference. Krytox was added to the FC-40 to make solutions with concentrations ranging from 0.33 mM to 2.35 mM.

3.2.2 Aqueous phase: different conductivities, dextrose only, salt only, particles

Due to the desired dielectrophoretic experiments, it was paramount that the aqueous phase was isotonic to protect the cells seeded within. Epure water (Millipore, Billerica, MA) was used as an aqueous phase throughout the project. It was used not only to ensure that the fluidics were working properly and for cleaning the microdevices but also as a control to aid in determining the chemistry and physics of the system. Multiple phosphate buffer saline (PBS) solutions were used to explore the effect of conductivity on the results. The PBS solutions were comprised of epure water, a salt stock (containing 1.1696 grams NaCl, 2.7223 grams KH_2PO_4, and 3.4961 grams K_2HPO_4), and dextrose (Sigma Aldrich, St. Louis, MO). Conductivities of 0.0000055 S/m (epure water), 0.05 S/m, 0.1 S/m, 0.5 S/m, and 1.0 S/m were used for this project. These solutions were also broken down into their separate components for the stability study to investigate not only the effect of conductivity but also the individual effects of dextrose and salt stock on the stability of the system. Table 3.2 details the recipes for each of these solutions.

Particles: Polystyrene beads (Spherotech, Lake Forest, IL) ranging from 3 to 9 microns were added into the aqueous dispersed phase. These were used to explore the dielectrophoretic capabilities of the new riDEP technique and compare the results with other dielectrophoretic techniques in the literature. Red blood cells were also seeded into the aqueous dispersed phase to compare riDEP with previous work completed by µM.D.-ERL. A phlebotomist collected blood from a donor into EDTA Becton Dickinson vacutainers, following IRB approved protocols. The red blood cells were separated from the rest of the blood by centrifugation at 132 relative centrifugal force (rcf) for 10 minutes. The packed RBCs were re-suspended in the desired aqueous phase, for each conductivity. Chapter 7 presents the results of the polystyrene bead and RBC experiments.

Table 3-2. Amounts of each component in each aqueous phase solution

Control Solution	Epure Water (ml)	Salt Stock (µl)	Dextrose (g)
Epure water	20.000	0.0	0.0000
0.960 mM	24.976	24.0	0.0000
2.616 mM	24.935	65.4	0.0000
13.892 mM	24.653	347.2	0.0000
24.122 mM	24.397	603.0	0.0000
Dextrose-only Solutions	Epure Water (ml)	Salt Stock (µl)	Dextrose (g)
58.837 mM	25.000	0.0	0.2650
161.108 mM	25.000	0.0	0.7256
273.845 mM	25.000	0.0	1.2334
290.404 mM	25.000	0.0	1.3080
Conductivity Solution	Epure Water (ml)	Salt Stock (µl)	Dextrose (g)
0.05 S/m	24.976	24.0	1.3080
0.1 S/m	24.935	65.4	1.2334
0.5 S/m	24.653	347.2	0.7256
1.0 S/m	24.397	603.0	0.2650

3.3 Device set-up: equipment uses and settings

Device pretreatment: Two pretreatment steps were completed to aid in the successful flow through the device. The first step was to ensure hydrophobic channels (detailed in Appendix A). Rain-X®, a commercially available glass water repellent, was flushed through the microdevice. The microdevice was kept at room temperature until the Rain-X was completely evaporated. The microdevice was generally treated at the end of the work so that it would be ready for experiments the following morning. The second step ensured that the surfactant concentration with the oil solutions did not go to the solid-liquid interface at the channel walls. Filling the device with the desired surfactant/oil solution and allowing it to sit for ~one hour before experiments allowed the surfactant time to reach equilibrium in solution as well as at the solid-liquid interface minimizing interference during experiments.

Experimental setup: The microdevice was loaded onto the stage of an SVM340 synchronized video microscope (Labsmith, Livermore, CA). Each side of the microdevice was taped onto the stage to prevent movement during experiments. The aqueous and oil solutions were loaded into the syringe pumps. For early experiments, the aqueous and oil solutions were loaded into a two mL HPLC vial and pulled through a 360 micron capillary into microsyringe pumps (LabSmith). Before use, the syringe pumps were flushed with Epure water to check their functionality. The solutions were then withdrawn at 0.5 µl/min to avoid the formation of a vacuum within the pump. When the pumps were full, the capillaries were switched with a longer set and connected to the microdevice via T-connectors (Labsmith).
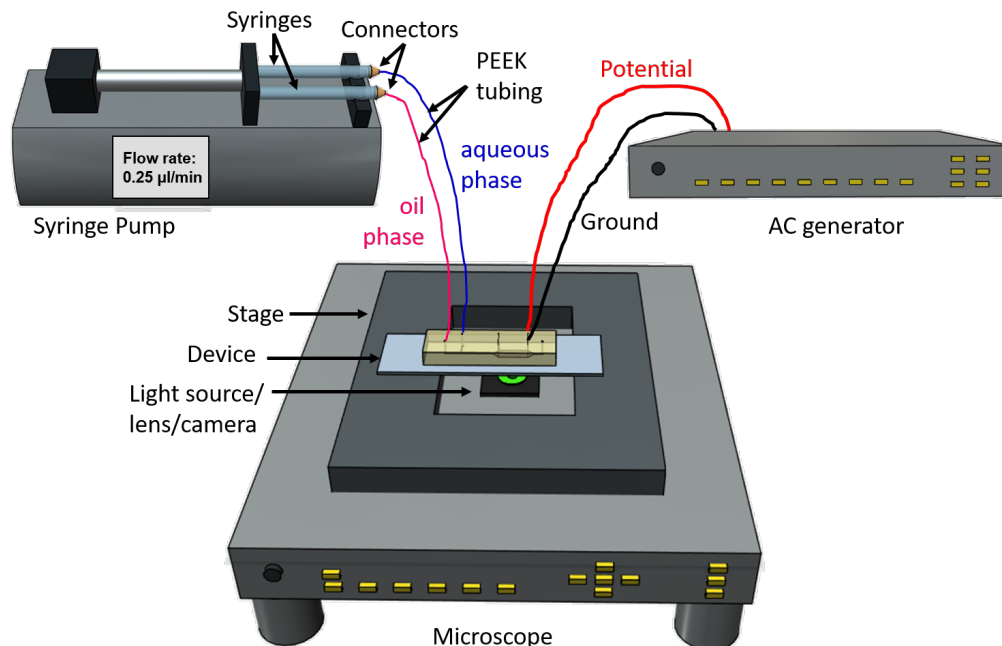
Figure 3-3. Experimental set-up. A syringe pump infused both the continuous oil and the dispersed aqueous phase into the microdevice. The microdevice was mounted on a Labsmith microscope for visual observation and recording. A ground and potential were applied via a high voltage sequencer.

For the remaining experiments, a Harvard Apparatus syringe pump (Harvard Apparatus, Holliston, MA) was utilized for pumping to reduce the polydispersity of the droplets (detailed in Chapter 4) as well as the time needed to load the pump. Both the aqueous and oil solutions were withdrawn into three mL syringes (Becton Dickinson, Franklin Lakes, NJ) and loaded onto the syringe pump. The syringes were connected to the device via 360 micron PEEK tubing (Labsmith) and t-connectors. The microscope was then turned on, and the brightness, contrast, and focus were adjusted to the ideal settings for observing/recording the experiments at 4x magnification. The solutions were then infused into the device for 10 minutes to allow the system to reach steady state before beginning experiments (data for reaching steady state shown in Chapter 4). For the dielectrophoretic experiments, an AC generator was used to apply an electric field across the chamber. The applied voltage ranged from 1 to 10 volts, and the applied frequency ranged from 100 to 1000 kHz. Figure 3.3 shows the experimental set-up.

3.4 Video/Data Analysis: imaging software and analysis techniques

Experiments were observed and recorded using the UScope software (Labsmith). The collected data was then analyzed using ImageJ, a free image analysis program from the National Institute of Health [226]. Droplet size analysis at generation, droplet monodispersity at generation, droplet generation regime, and droplet stability in the

chamber entrance are presented in Chapter 6, and electrical stability and dielectrophoretic responses are presented in Chapter 7.

3.5 Modeling methods: COMSOL, Computing Cluster

Computing: Superior and Portage, high-performance computing infrastructure at Michigan Technological University, were used in obtaining results presented in this dissertation. Superior has 92 compute nodes, each with 16 CPU cores and 64 GB of RAM, providing 30 TFLOPS. Portage is a smaller version of Superior with 3 TFLOPS of CPU. Preliminary, simple COMSOL simulations of droplet generation took 50+ hours to reach completion. Due to this large amount of time, a comparison was made between the same simulation run on a normal Michigan Tech computer and on Portage, a supercomputing cluster. The simulation took one-tenth the time to run on Portage (50 hours on a normal computer vs. 5 hours on Portage). These resources allowed multiple simulations to be run simultaneously and in a much shorter amount of time. 145 simulations, taking 9,679 CPU hours (749 wall hours) were run on Portage and 49 simulations, taking 887 CPU hours (132 wall hours), were run on Superior. On average, 8 processors were used per simulation. The number of processors, wall time, CPU time, and memory for the largest simulations run on Superior are presented in Table 3.3, all simulation times and memory can be found in Appendix B. Chapter 5 describes the details of the simulations.

Table 3-3. Number of processors, wall time, CPU time, and memory for the most memory intensive COMSOL simulations run on Superior.

NPROC	Wall Time	CPU Time	Memory (GB)
6	98:36:11	606:46:31	5.37
8	0:01:48	0:14:58	6.00
13	3:07:42	40:21:27	6.05
9	0:02:27	0:20:57	6.71
15	0:57:05	14:38:13	6.71
4	0:09:24	0:34:16	19.14
8	1:26:58	11:27:43	24.30
4	0:10:27	0:38:50	24.65
8	1:56:55	15:46:18	25.08
8	2:05:25	16:04:47	29.82
9	1:40:22	14:42:03	30.70
8	3:02:28	23:31:07	31.50
8	1:55:53	15:32:56	32.81
7	3:04:27	21:53:22	36.01
8	13:53:25	104:47:30	50.89

4 System Stabilization

4.1 Introduction

4.1.1 Applications

Droplet microfluidics is a growing research field due to the numerous microscale applications that encompass a range of fields from biotechnology (drug delivery and biosensing) to particulate synthesis. The high throughput possible in droplet microfluidics provides a platform for biological and chemical research [37]. Along with the high throughput, parallel analysis of the microenvironments allows large-scale polymerase chain reaction (PCR) and cell culturing techniques to be completed [37, 42]. By adjusting the upstream composition, drug discovery, protein crystallization, and enzymatic assays are possible [13, 28, 29, 37]. Other current applications include irregular particles, double emulsions, hollow microcapsules, microbubbles, single cell analysis, synthesis of biomolecules, drug delivery, therapeutics, biomedical imaging, and diagnostic testing [28, 29, 37, 42-49].

4.1.2 Advantages

Each droplet acts as its own isolated microenvironment, on a scale relevant to biological conditions [37]. These isolated chambers, caused by the separation from the immiscible carrier fluid [28], are advantageous because the droplets enable a) relatively stable reaction conditions, b) the ability to run reactions in parallel, c) non-stationary reactions (e.g., reactions progressing along with droplet flow, d) no cross contamination, e) no dilution, f) control over evaporation, and g) high throughput possibilities [28, 37, 57]. These isolated microenvironments are key to riDEP because they eliminate direct contact between samples and electrodes, thus preventing unwanted sample-electrode interactions. The ability to reproducibly generate uniform droplets within the nano- to micro-meter diameter range [29] is also advantageous; however achieving stable, monodisperse droplets can be challenging. If the interfacial tension is too low, some droplets will coalesce together forming larger droplets and increasing polydispersity, and if it is too high, some droplets will split, forming smaller droplets and increasing polydispersity. The interfacial tension is dependent on properties of the two phases as well as any additives/surfactants present in each phase that transport to the interface between the phases.

4.1.3 Purpose and Motivation

The monodispersity, size, and shape of the droplets formed is important for many applications, especially drug delivery and biosensing, where well-defined volumes and compositions are necessary to achieve the correct concentration. Further, the biological and chemical properties of microparticles are strongly affected by droplet size and

morphology [29]. Droplet size is affected by device geometry, material viscosity, interfacial tension, the use of surfactants, surface/fluid hydrophobicity or hydrophilicity, and pump stability, and flow rate. [29]. For this work, T-junction devices with two inlets, one for each phase, a junction where the two inlet channels combine into a single channel, and a chamber downstream were used. The devices were constructed with poly(dimethylsiloxane) (PDMS) and glass microscope slides. An example of a device is shown in Figure 4.1.

This chapter describes the process of optimizing all of the aforementioned materials and experimental conditions used for the bulk of the research in this dissertation. Parameters were highly informed by literature, but some required specific tuning to the resources available in the research lab. The materials were optimized for ideal droplet interfacial tension including the oil and surfactant combination and the microdevice treatment for obtaining hydrophobic channels. Experimental conditions, including the type of pump
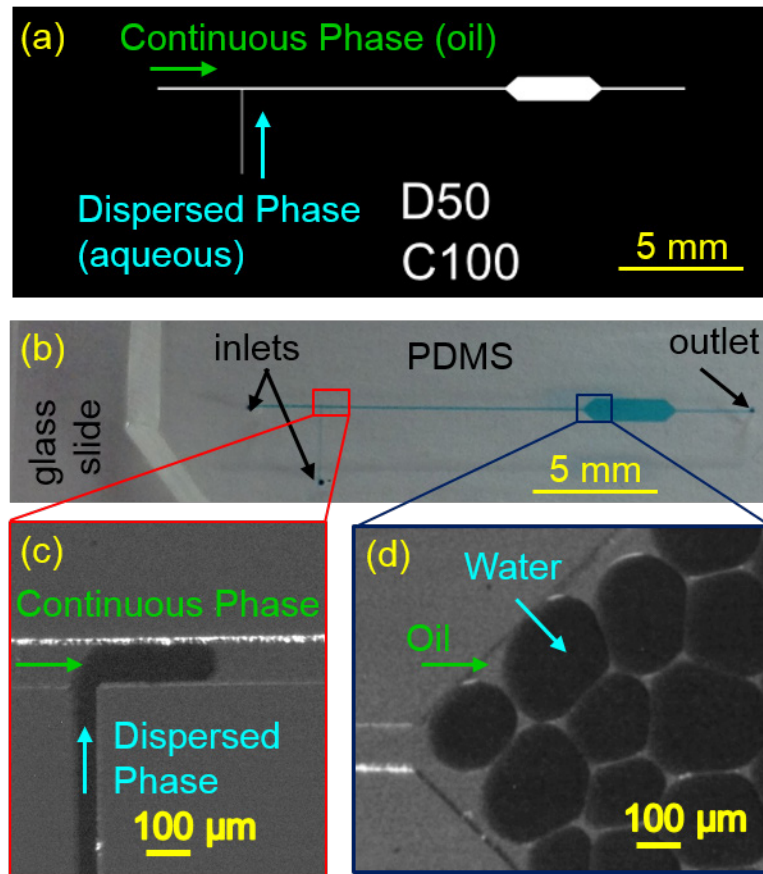
Figure 4-1. Design (a), realization (b), and operational images of a T-junction microdevice used to generate aqueous droplets in 0.125% Krytox 157 FSH in FC-40. a and b) Inlet flow rates are controlled by independent syringe pumps, while droplets are collected in the tapered chamber. c) T-junction droplet pinching at 1.0 µl/min and 0.15 µl/min flow rates for the continuous and dispersed phases, respectively. d) Stable droplets packed into chamber region. Larger droplets are from coalescence, which is being controlled via surfactants.

and capillary length, utilized impacted droplet generation and were optimized to minimize droplet size variation. The background, materials and methods, and results of each optimization are discussed in the remainder of this chapter.

4.1.4 Surfactants

Surfactants can benefit microfluidic systems in a variety of ways; increasing the ease of formation, lowering interfacial tension, hindering coalescence, maintaining wetting conditions, as well as controlling biocompatibility [40, 62, 99, 100]. Surfactants are **surf**ace-**act**ive **agents** that have an amphipathic structure, both a hydrophobic group and a hydrophilic group are present in the molecule. At low concentrations, in an immiscible aqueous/oil solution, they readily migrate to the interface between fluids, which decreases the interfacial tension, thus stabilizing the interface. Within the context of the microfluidic system in this research, the surfactants stabilize the droplet interface against coalescence [85]. The Gibbs adsorption isotherm for dilute solutions decribes the decrease in surface tension, $\Gamma = -\frac{c}{RT}\frac{d\gamma}{dc}$, where γ is the interfacial tension, c is the surfactant concentration, Γ is the surface concentration, R is the gas constant, and T is the temperature [84, 85]. When combined with the Laplace Pressure, $\gamma = \frac{d\Delta P}{4}$, this can be separated, integrated, and rearranged to show a natural log dependence of concentration on droplet size, as shown in Equations 4.1-4.3 where b is the constant of integration.

$$\Gamma = -\frac{c\Delta P}{4RT}\frac{\partial d}{\partial c} \qquad 4.1$$

$$\frac{1}{c}\partial c = -\frac{\Delta P}{4\Gamma RT}\partial d \qquad 4.2$$

$$d = -\frac{4\Gamma RT}{\Delta P}\ln c - \frac{4\Gamma RT}{\Delta P}b \qquad 4.3$$

Two readily available surfactants with differing properties, ionic sodium dodecyl sulfate (SDS) and non-ionic Triton X-100, were investigated. A large operating window of stability was desired because a wide range of dispersed phases, with additives known to alter interactions at the interface, were used in this work. The results of the investigation led to the purchase and experimentation of a higher molecular weight surfactant, Krytox FSH 157. Krytox was chosen for its high molecular weight and its similarity to a biocompatible surfactant (which was not chosen due to cost, ~$1.25/g versus ~$550/g), to form a layer of molecules at the interface of each droplet and act as a repulsive barrier helping the droplets resist coalescence [86, 87].

4.1.5 Hydrophobicity

Channel wall properties can affect droplet microfluidic systems [74, 227] including how droplets are generated and ease of droplet motion within microfluidic device channels

and chambers. Different materials have been used both for fabrication and for altering the natural surface properties of a material to control wettability and other flow characteristics including materials, surface treatments, and surfactants. It is very common to see microscale PDMS fluidic features bonded onto glass microscope slides to form closed channels, chambers, and other fluidic components. The PDMS is hydrophobic, and the glass is hydrophilic. Sealing PDMS fluidics on top of a PDMS layer has been demonstrated to achieve uniform wettability on all surface/liquid interfaces within the device [67, 228, 229]. In work by Thompson, et al., a double-sided adhesive tape was used instead of plasma bonding for sealing PDMS to the glass with the benefit of achieving hydrophobicity on all interior surfaces [230].

Surfaces of microfluidic features can also be treated to shift the phobicity of materials. For example, when PDMS is treated with oxygen plasma, bonded methyl groups are released and replaced with silonal groups [231]. This results in the PDMS becoming more hydrophilic after treatment. The attribute is time-dependent with hydrophilicity declining as surface rearrangements occur, over the course of ~30 minutes returning to the native hydrophobic state [232]. However, if kept in contact with water or another polar organic solvent, the PDMS can be kept hydrophilic indefinitely [233]. In this work, the continuous phase was the oil phase, so hydrophobic surfaces were desirable for increased wettability.

Since surfactants also migrate to liquid/solid interfaces, they can be utilized to alter the charge and/or hydrophobicity of microfluidic features within microchannels. Multiple research groups use chemical compounds, such as Rain-X [79], Aquapel [47, 79, 109], octadecyltrichlorosilane [74], and photoreactive sol-gels [234] for altering naturally hydrophilic glass to be hydrophobic for optimal droplet generation and stability. Thus, in this work, the use of different bonding conditions and Rain-X were investigated.

4.1.6 Pump Effects

Passive droplet breakup in microfluidic channels can greatly increase the monodispersity of droplets as compared to active droplet breakup as discussed in Chapter 2 Section 2.1.3. Syringe pumps are commonly used in droplet microfluidics to precisely and independently deliver the continuous fluid and the fluid dispersed into droplets. However, the pumps used can affect the monodispersity [53]. Droplet generation causes intrinsic velocity fluctuations during the break-off process for both syringe pump-driven and applied pressure-driven methods [53]. Syringe pumps also experience pressure fluctuations due to mechanical oscillations [53, 228, 235-237]. In addition to fluctuations caused by the generation method, factors including channel material and droplet generation rate can also affect droplet polydispersity [53]. PDMS, a soft polymer, was used to fabricate channels, as it is a common material used in microfluidics and softer materials have been shown to reduce polydispersity [53, 229, 238]. Longer, flexible tubing has also been shown to decrease polydispersity from syringe pump-driven flow. In this work, two lengths of tubing droplets were tested and compared using Labsmith

syringe pumps with the goal of generating reproducible monodispersed droplets. Two types of syringe pumps Labsmith and Harvard Apparatus, were also tested and compared.

4.2 Materials and Methods

4.2.1 Surfactants

To understand droplet coalescence and polydispersity, a parametric study on surfactants was initiated. First, sodium dodecyl sulfate (SDS), an ionic surfactant (MW=288.38), was investigated with concentrations from 0 to 10 w/w% in the aqueous dispersed phase. After investigating the surfactant concentrations in the dispersed phase, surfactant in the continuous oil phase was investigated. Triton X-100, a non-ionic surfactant (MW=647) was added to silicone oil (Sigma Aldrich, St. Louis, MO) at concentrations ranging from 0 to 1.0 w/w%. These surfactant concentrations were chosen to cover a range that included the critical micelle concentrations, CMC, of ~0.25 w/w% and ~0.016 w/w% for SDS and Triton X-100, respectively [225]. Larger molecule surfactants, with longer tails, have demonstrated long term stability, even in large droplets [47]. For this reason, an anionic surfactant Krytox FSH 157 (MW=7000-7500) was investigated at concentrations ranging from 0.125 to 0.76 w/w%, with FC-40, a fluorinated carbon oil, as the continuous phase.

A microfluidic device consisting of an aqueous phase inlet, continuous phase inlet, T-junction, large chamber, and a single outlet was used for this study, as shown in Figure 4.1. Aqueous-in-oil droplet generation (Figure 4.1 a and b) was achieved passively via the T-junction in the device geometry and observed optically as shown in Figure 4.1 c. Two microsyringe pumps (Labsmith, Livermore, CA) independently controlled the flow rates of the continuous and dispersed phases. SDS experiments were completed in device 1, with 200 µm and 100 µm channel widths and 2.5 µl/min and 0.5 µl/min flow rates for the continuous and dispersed phases, respectively. Triton X-100 experiments were completed in device 2, with 300 µm and 200 µm channel widths and 3.0 µl/min and 1.5 µl/min flow rates for the continuous and dispersed phases, respectively. Both devices were 70 µm in height. Since the dimensions were different for the two devices, flow rates were chosen so that the overall velocity entering the chamber was the same at 2.5×10^5 µm/min. The Krytox experiments were completed in device 3, with 100 µm and 50 µm channel widths and 1.0 µl/min and 0.5 µl/min flow rates for the continuous and dispersed phases, respectively. Note that this was an exploratory study until a system was located (device dimensions as well as materials) with broad stability for the conductivity research in future chapters. As structured, trends were discerned, but not rigorous quantitative comparisons.

The droplets generated at the T-junction traversed down the channel and packed into the chamber, as shown in Figure 4.1 d. Droplet size and stability were measured optically upon entrance to the chamber. A Labsmith microscope and corresponding Uscope software were used to record videos at 30 fps of experiments under 4x bright field

magnification. ImageJ software [226] was used to extract still images and analyze droplet size and coalescence behaviors. Droplet areas were translated to an effective droplet diameter by converting the area from pixels squared to square microns. The effective diameter, in microns, was calculated using Equation 4.1 where d_h was the effective droplet diameter, A was the cross-sectional area, and H was the chamber height (70 μm). Depending on droplet volumes generated and the device dimensions, both spherical and disc-like droplets were possible. Equation 4.2 was used for spherical droplets and Equation 4.3 was used for disc-like droplets. Droplets were assumed spherical if the observed diameter was less than the chamber height and disc-like if the diameter was greater than the chamber height.

$$d_h = \sqrt{\frac{4}{\pi} A} \qquad 4.2$$

$$d_h = \sqrt[3]{\frac{6}{\pi} A \cdot H} \qquad 4.3$$

The effective droplet diameters were averaged to obtain an average effective droplet diameter (with standard deviation) for each parameter condition. The monodispersity and reproducibility within a single experiment (repeats), as well as a set of independent experiments (replicates), were investigated. Coalescence was measured for each experiment to quantify droplet stability. The percent of primary droplets that coalesce within the first 1000 μm of the chamber were measured, then experiments were averaged and compared using statistical techniques similar to those with the effective droplet diameter analysis.

4.2.2 Hydrophobicity

Four methods of increasing device hydrophobicity were investigated; 1) air plasma bonding followed by 24 hours in a 70°C oven, 2) air plasma bonding followed by 45 seconds at 120°C, 3) air plasma bonding followed by 24 hours in a 70°C oven followed by surfactant treatment by filling the device with pure Rain-X and allowing it to evaporate overnight, and 4) sealing the PDMS fluidics to the glass slide via double-sided tape (Scotch, 3M, Maplewood, MN). Hydrophobicity was determined by visual observation of how the aqueous phase interacted with the device walls. Experiments were recorded at the T-junction, where the aqueous and oil phases met. Poor hydrophobicity resulted in the aqueous phase being attracted to the device walls, and good hydrophobicity resulted in the aqueous phase being repelled by the device walls. The latter resulted in very clear droplet formation.

4.2.3 Pump Effects

A comparison between two lengths of 360-micron diameter PEEK capillaries (Labsmith) was made to determine if polydispersity could be decreased by lengthening the distance between the two Labsmith pumps and the microdevice. Two lengths were tested, 20 cm and 40 cm. A comparison of two pumps, a Labsmith micro syringe pump and a Harvard Apparatus, was also quantified for droplet quality and consistency. The same device, device 3, was used with both pumps. For the Labsmith, flow rates of 1.0 µl/min and 0.5 µl/min for the continuous and dispersed phase flow rates, respectively were used. For the Harvard Apparatus, 0.5 µl/min was used for both phases. A single pump was used for both phases, so the flowrates for each phase were equal. Both comparisons, between capillary length and between pump types, were made by looking at the polydispersity of the droplets. Droplet polydispersity was measured as described in Section 4.2.1. Note that the flow rate was changed from 0.5 µl/min to 0.25 µl/min for Chapter 6 for ease of visibility.

Data regarding the effect of different surfactants, surface treatments, and pumping setups was collected via bright field microscopy. To ascertain surfactant efficacy, data was compiled as a function of surfactant concentration for two surfactants, SDS and Triton X-100, with constant aqueous and oil phase flow rates for each surfactant. To ascertain the optimum method of achieving the desired wettability/hydrophobicity, four methods of treating devices for increased hydrophobicity, 1) plasma bonding followed by 24 hours at 70°C, 2) plasma bonding followed by 45 seconds at 120°C, 3) plasma bonding followed by 24 hours at 70°C and Rain-X treatment, and 4) double-sided tape, were tested and the resulting hydrophobicity/wettability was visually observed. To ascertain pump effects, two pumps, Labsmith and Harvard apparatus, and two capillary lengths, 20 and 40 cm, were compared via droplet size analysis.

4.3 Results and Discussion

4.3.1 Surfactants

Droplets size and percent coalescence were measured in preliminary experiments and the results compiled as a function of SDS and Triton X-100 concentration (Figure 4.2) to assess monodispersity and stability. Experimental observations revealed that different SDS concentrations impacted both droplet stability and size. This was consistent in magnitude and trend with previous research [40, 41, 85]. Similar to the results of the SDS experiments, the preliminary Triton X-100 experimental results also revealed concentration affects droplet stability and size.

Both SDS (Figure 4.2a) and Triton X-100 (Figure 4.2c) showed a trend of decreasing droplet size with an increase in surfactant concentration. The trend of decreasing droplet size with increasing surfactant concentration was consistent with predictions from Equation 4.1. Figure 4.2 also illustrates the percent coalescence of droplets for each

surfactant concentration. The lowest percentage of coalesced droplets (highlighted yellow in Table 4.1 and highlighted blue in Figure 4.2b and d) occurred at concentrations greater than the critical micelle concentration (CMC marked with bold * in Table 4.1) for both SDS and Triton-X. Increased droplet polydispersity and coalescence were attributed to non-optimal surface tension.

The experimental results of SDS and Triton X-100 yielded too narrow of an operating region for these studies with only the 2.5 w/w% SDS resulting in droplets that did not coalesce within the first 1000 µm of the chamber. 1.25 w/w% SDS and 0.05 w/w% Triton X-100 did yield fairly stable droplets, as less than 10 percent of the droplets coalescenced within the first 1000 µm of the chamber. However, packing uniform droplets within the chamber was still a rare occurrence. Future experiments required both well packed, uniform droplets and multiple additives, the salts and dextrose needed to make isotonic solutions of various conductivity, that are known to alter the interfacial
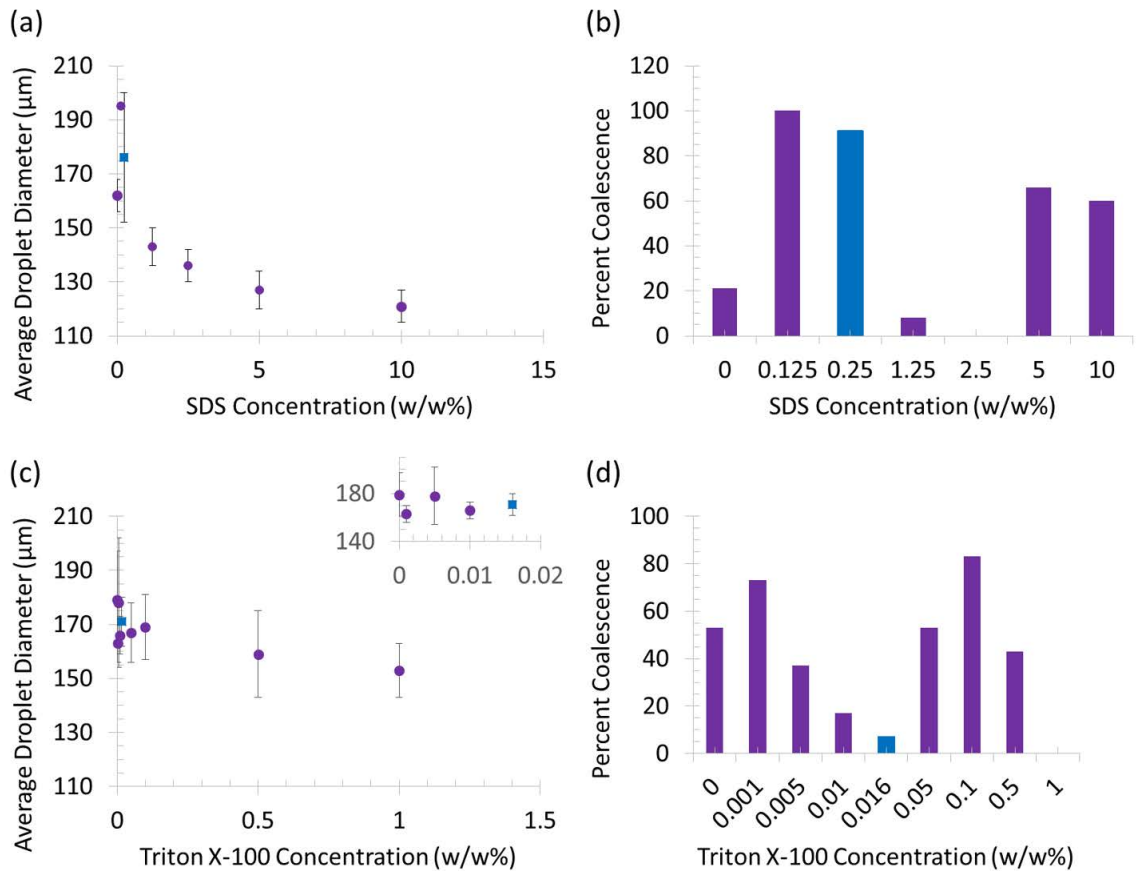
Figure 4-2. Data for 30<N<100 droplets. (a) Average droplet diameter and (b) percent coalescence as a function of SDS in the continuous phase at flow rates of 2.5 µl/min and 0.5 µl/min for the continuous and dispersed phase flow rates, respectively. (c) Average droplet diameter and (d) percent coalescence as a function of Triton X-100 in the continuous phase at flow rates of 3.0 µl/min and 1.5 µl/min for the continuous and dispersed phase flow rates, respectively. (Blue=CMC)

Table 4-1. Surfactant conditions explored with 31<N<100 droplets. SDS experiments had flow rates of 2.5 and 0.5 µl/min for the continuous and dispersed phases, respectively, while Triton-X experiments (shaded grey) had flow rates of 3.0 and 1.5 µl/min, respectively. The trends of decreasing droplet size with increasing surfactant concentration are consistent with surface tension expectations. The lowest percentage of droplets coalescing (highlighted yellow) is greater than the critical micelle concentration (CMC, marked with bold *) for both SDS and Triton-X.

Continuous Phase (Silicon Oil)	Dispersed Phase (water)	Average Droplet Size ± Standard Deviation (µm)	Percent droplets coalesced
Surfactant: Triton X-100 (w/w%)	Surfactant: SDS (w/w%)		
-	10.0	121±6	60
-	5.0	127±7	66
-	2.5	136±6	0
-	1.25	143±7	8
-	0.25*	176±24	91
-	0.125	195±3	100
-	-	162±6	21
-	-	179±18 **Δ flow	53
0.001	-	163±7	80
0.005	-	178±24	43
0.01	-	166±7	83
0.016*	-	171±9	53
0.05	-	167±11	7
0.1	-	169±12	17
0.5	-	159±16	37
1.0	-	153±10	73

tension [239-242] which may have resulted in unstable droplets if SDS or Triton X-100 was used. Since the application of this project was bio-related, biocompatibility was taken into account. Exposure to SDS and Triton X-100 can lead to cell death. This, along with growing knowledge of literature results, a change in material was identified to overcome the shortcomings of the SDS and Triton X-100.

A higher molecular weight surfactant would provide better stability because mass transport from and around the interface is slower. Therefore, Krytox FSH 157 (Dupont, MW = 7000-7500) was chosen as the surfactant instead of SDS (MW=288.38) or Triton X-100 (MW=647), and a fluorinated oil, FC-40 (3M) was chosen as the continuous phase. Krytox 157 FSH, a surfactant containing a PFPE (perfluorinated polyether) tail and a carboxylic acid head group [2, 47, 89] was chosen for this project due to benefits of its high molecular weight and low cost. Krytox is similar in size/structure to an available

biocompatible surfactant, (Ran Biotechnologies, Beverly, MA), but less than 1/100th the cost. This would allow for a smoother transition from using one surfactant to the other if a switch became necessary. Krytox showed promise as a stabilizer for a range of aqueous phases. At 0.38 w/w%, Krytox droplets of various aqueous phase composition resulted in the same size droplets, allowing direct comparison between dispersed phase compositions. The polydispersity at 0.38 w/w% was also within reported norms [53, 243] with coefficients of variance ranging from 2.7-10.3%. Thus a more thorough investigation of Krytox and the effect of additives on the Krytox system was studied and is presented in Chapter 6.

4.3.2 Hydrophobicity

Due to the significant influence of device wall wettability on droplet formation, four techniques were investigated to improve device hydrophobicity to aid the continuous oil phase. Technique 1 was air plasma bonding followed by 24 hours at 70°C. In the following experiments, observations of the aqueous phase attraction to device walls were made by recording the T-junction where the aqueous and oil phases met. Technique 2 involved air plasma bonding followed by 45 seconds in an oven at 120°C; this resulted in an increased attraction between the device walls and the aqueous phase. Thus, the shorter time at a higher temperature did not yield the desired hydrophobic effect. Technique 3 was air plasma bonding followed by 24 hours at 70°C followed by the Rain-X treatment. This resulted in the desired hydrophobicity. Technique 4 utilized double-sided tape between the glass slide and the PDMS and also yielded good hydrophobicity. However, the tape proved unreliable as it collected unwanted dust particles and did not display resiliency to long experiments or multiple uses as it became cloudy with time, interfering with image quality for data acquisition. Therefore, air plasma bonding followed by 24 hours at 70°C and then Rain-X treatment was chosen as the standard technique throughout the remaining experiments.

It was also observed that over time, exposure to the continuous oil phase with surfactant improved the hydrophobicity. This was most evident in the non- Rain-X treated devices suggesting that the surfactant was adsorbing to the microdevice surfaces. For this reason, before each experiment, the device was filled with the oil phase plus surfactant and allowed to sit for an hour to reach equilibrium within the continuous phase as well as with the device walls.

4.3.3 Pump Effects

High polydispersity was present in the droplets initially generated. To maximize monodispersity, 360-micron diameter PEEK tubing capillaries were doubled in length from 20 cm to 40 cm to attenuate flow fluctuations originating from the pump. Table 4.2 contains the droplet size standard deviation for a range of Krytox concentrations at the same flow rates of 1.0 µl/min and 0.5 µl/min for the continuous and dispersed phases,

Table 4-2. Comparison of droplet size standard deviation between short and long capillaries

Krytox Conc. (mM)	Short capillaries stdev (µm)	Long capillaries stdev (µm)	Stdev Difference (µm)	Stdev Percent Difference (%)
0.162	59	45	14	24
0.325	70	61	9	13
0.434	107	69	38	36
0.653	93	75	18	19
1.307	95	67	28	29

respectively. In each case, the longer capillary lengths yielded a desired decrease in polydispersity by decreasing the standard deviation from ~85 µm to ~60 µm.

However, the longer capillary did sufficiently reduce the polydispersity issue, by an average of ~24%. Therefore switching the pumping system from Labsmith syringe pumps to a Harvard Apparatus syringe pump was explored as a means to further reduce droplet polydispersity. The Harvard Apparatus syringe pump has a flow rate accuracy of ±0.25% and reproducibility of ±0.05% [244]. It also has a larger operating range (0.0001 µl/hr to 216 ml/min [244]) and capacity (0.5 µl to 140 ml [244]) compared to the Labsmith flow rate accuracy of ±1.0% and lower capacity (0.05-5600 µl/min, and 5-100 µL [245]). At the desired flow rates for this work, the very low end of the Labsmith's range of operation was being utilized, likely contributing to the unacceptable droplet
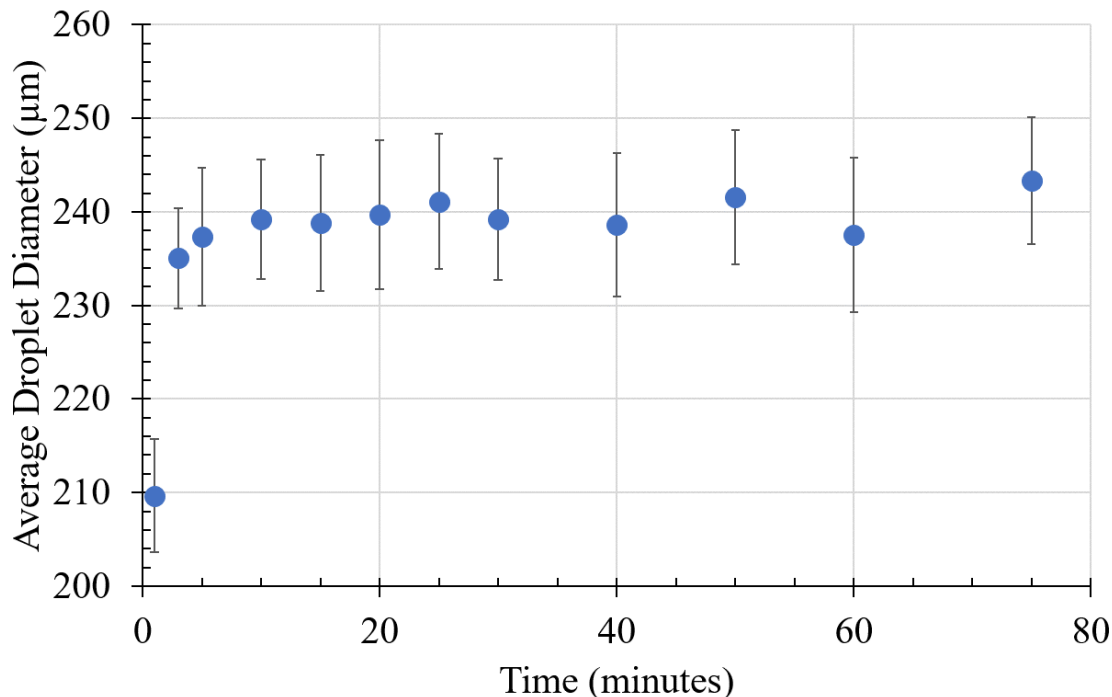
Figure 4-3. Average droplet size, with standard deviation, versus time. Within the first ten minutes, the system reached steady state.

polydispersity. The Harvard Apparatus syringe pump minimizes flow pulsation by utilizing a microprocessor-controlled, small step angle stepping motor to drive the lead screw and pusher block [244]. The droplet diameter standard deviation with the Harvard Apparatus (~6 µm) was an order of magnitude smaller than the Labsmith syringe pump (~60 µm).

Time-dependency experiments were then conducted with the Harvard Apparatus pump to determine when the system reached steady state. The results showed that after 10 minutes, droplet size stabilized to 240 ± 6 µm at 0.5 µl/min for both the continuous and dispersed phases (Figure 4.3). Therefore, 10 minutes was chosen as the standard time to achieve steady state before beginning to collect data.

4.4 Conclusions

As outlined in this chapter, experimental parameters and equipment optimizations were completed to achieve highly reproducible, monodispersed droplets over a broad operating range. First, the oil phase and surfactant were optimized for this T-junction system by utilizing droplet diameter and stability, keeping biocompatibility in mind. Experiments with SDS and Triton X-100 suggested that higher molecular weight surfactants needed to be explored because the operating windows for SDS and Triton X-100 were not sufficient to allow changes in interfacial tension while maintaining droplet stability. A fluorinated oil, FC-40, was chosen as the oil phase due to its biocompatibility and a fluorosurfactant, Krytox FSH 157, was chosen as the surfactant due to the high molecular weight, low cost, and similarity to a biocompatible surfactant. This resulted in the most promising system with reproducible droplets (standard deviation of 6 µm for droplet size) and improved packing within the chamber and thus was chosen for further experiments. Chapter 6 presents a further exploration of Krytox FSH 157.

Optimizations were also explored for the experimental setup. Longer microcapillaries were chosen because they attenuate pump-induced perturbations to increase flow stability before the fluid reached the T-junction. A Harvard Apparatus syringe pump was chosen because of its observed steady, reproducible flow. The capillary and pump improvements increased the monodispersity of the droplets generated; the standard deviation was decreased from ~85 µm to ~6 µm.

Improvements in the continuous oil phase, the surfactant, fluidics, and pump enable the broadest range of aqueous phase conductivities to be explored for droplet generation. In addition, the effect of additives needed for isotonic solutions was optimized in Chapter 6, which was critical for subsequent research in Chapter 7 exploring droplet stability in electric fields as well as particle and cell loading into the droplets for micro-environment characterization, and future work multiplexing experiments in Chapter 10.

5 Simulations via COMSOL Multiphysics

Work from this chapter on droplet generation was presented as a poster:

J.L. Collins and A.R. Minerick, "Comparison of simulations and experimental water-in-oil droplet formation in a microfluidic T-junction," 2nd Annual Chemical Engineering Research Symposia, Michigan Technological University, Jan 2014. [Author earned a 1st place Award]. Also presented at: Private Poster Viewing for Bill Colton, VP Exxon Mobil Corporation. Jan. 2014, 2014 Graduate Research Colloquium. Feb. 2014, 10th Annual Biotechnology Research Center (BRC) Student Research Forum. Mar. 2014, Alumni Reunion Graduate Research Poster Session. Aug. 2014

5.1 Introduction

Simulations can be used to design experiments, check experimental results versus theory, and to investigate unexplained phenomena encountered in experiments. For design of experiments, simulations can be completed for a range of operating conditions and parameters to help narrow down the set of experiments to hone in on the desired effect or phenomena. Throughout this dissertation, simulations on droplet generation, electric fields within droplets, and dielectrophoretic responses within droplets were run either to inform or to support the experimental results. Simulations were completed in COMSOL Multiphysics®. More complex simulations were run on one of the super-computing clusters (Portage and Superior) as discussed in Chapter 3, Section 3.5.

5.2 Droplet Generation

One of the main technologies used in this research was droplet microfluidics. T-junction dimensions affect droplet generation as discussed in Chapter 2 Section 2.1.3. [29, 40, 50, 55, 68, 69, 77] and a variety of models for the prediction of droplet break-up in a T-junction have been developed [68, 69, 77]. Previous published work demonstrated effective droplet diameter could be predicted through simulation before starting experiments [69, 70, 246-249]. Using one of the published models [68], the effect of the continuous and dispersed phase channel widths and flow rates were investigated (parameters in Table 5.1).

The results shown in Figure 5.1 demonstrate the same trends expected based on the predictive model [68]. For an increase in continuous phase flow rate, the droplet size decreased and for an increase in dispersed phase flow rate, the droplet size increased. The predicted droplet size and the experimental size differed by 9.8, most likely because the model only took geometry into account [68], while other factors including the presence of additives also affect droplet size as demonstrated in Chapters 4 and 6.

To help understand the mechanism behind droplet break-up at the T-junction, as well as to inform the experimental work completed, three-dimensional droplet generation simulations for a microfluidic T-junction were completed. These simulations were run using the computational fluid dynamics (CFD) and microfluidics modules in COMSOL

Table 5-1. Parameters for predicting droplet size

Parameter	Description	Value
wc	width of continuous channel	225 µm
wd	width of dispersed channel	150 µm
h	height	70 µm
ε	corner correction	50 µm
qc	continuous phase flow rate	1-5 µl/min
qd	dispersed phase flow rate	0.5-2.5 µl/min
qgutter	continuous phase flow rate around forming droplet	
Rfill	filling radius	
Rpinch	pinching radius	
α	fitting parameter	
Vfill	size of droplet at end of filling period	
V	final calculated droplet volume	
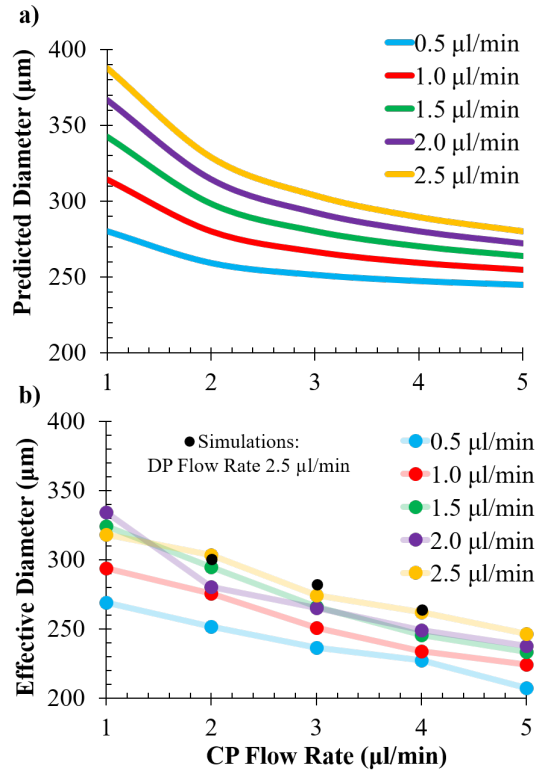
Figure 5-1. a) Predicted droplet diameter from a model and b) experimental effective diameter and COMSOL simulation results as a function of both continuous phase (CP) and dispersed phase (DP) flow rates for continuous and dispersed phase channel widths of 300 µm and 200 µm, respectively. Droplet size decreased with an increase in continuous phase flow rate and droplet size increased with an increase in dispersed phase flow rate. The predictive model and experimental results followed similar trends. Black dots in b) correspond to COMSOL simulation results for a single dispersed phase flow rate of 2.5 µl/min and continuous phase flow rates of 2, 3, and 4 µl/min. Experiments and COMSOL results were in close agreement with only 1.4% difference.

Table 5-2. Parameters/variables used in the droplet generation simulations

Parameter	Description	Value or Equation
φ	level set function	0.5
ρ	density (kg/m^3)	$\rho = \rho_1 + (\rho_2 - \rho_1)\varphi$
μ	viscosity (Pa·s)	$\mu = \mu_1 + (\mu_2 - \mu_1)\varphi$
u	velocity (m/s)	based on geometry and flow rate
t	time (s)	0.08 (s)
P	pressure (Pa)	from simulation
F$_{st}$	surface tension force (N/m^3)	5e-3
σ	surface tension coefficient	5e-3 (N/m)
γ	numerical stabilization parameter	0.05
ε	numerical stabilization parameter	6.25e-6
Ω	left most part of the channel	x < -0.2 (mm)
d$_{eff}$	effective droplet diameter (mm)	from simulation
ρ$_1$	continuous phase density	967 (kg/m^3)
ρ$_2$	dispersed phase density	1000 (kg/m^3)
μ$_1$	continuous phase viscosity	0.1 (Pa·s)
μ$_2$	dispersed phase viscosity	0.001 (Pa·s)
u$_1$	continuous phase volume flow	(varied 0.5-5.0) (µl/min)
u$_2$	dispersed phase volume flow	(varied 0.25-2.5) (µl/min)
C	continuous phase channel width	(varied 100-300) (µm)
D	dispersed phase channel width	(varied 50-200) (µm)
H	channel height	70 (µm)

Multiphysics®. The laminar two-phase flow and level set interface physics packages were used with prescribed geometry (dimensions of real devices) and volume flows (matched experiments), In addition, boundary conditions of the pressure, a no viscous stress condition at the outlet as well as a wetted wall condition for all boundaries were implemented. The four main equations utilized within the simulations were the momentum transport equation (Equation 5.1), the equation of continuity (Equation 5.2), the level set equation (Equation 5.3), and the effective droplet diameter (Equation 5.4).

$$\rho \frac{\partial \boldsymbol{u}}{\partial t} + \rho \boldsymbol{u} \cdot \nabla \boldsymbol{u} = -\nabla p + \mu \nabla^2 \boldsymbol{u} + \boldsymbol{F}_{st} \qquad 5.1$$

$$\nabla \cdot \boldsymbol{u} = 0 \qquad 5.2$$

$$\frac{\partial \phi}{\partial t} + \boldsymbol{u} \cdot \nabla \phi = \gamma \nabla \cdot \left(-\phi(1-\phi)\frac{\nabla \phi}{|\nabla \phi|} + \varepsilon \nabla \phi\right) \qquad 5.3$$

$$d_{eff} = 2 \cdot \sqrt[3]{\frac{3}{4\pi} \int_{\Omega} (\phi > 0.5) d\Omega} \qquad 5.4$$

Parameters not pulled from experimental conditions were based on a demo available within the COMSOL program. After designing, fabricating, and testing the T-junction microdevice, a comparison of the droplet formation within the device to simulation results was completed. Four frames from a recorded experiment were matched with four frames from a simulation animation. The simulation used the parameters presented in Table 5.2. Figure 5.2 depicts the agreement between an experiment and the corresponding simulation, with only 1.4% difference.

Consistent with previous research, the results presented herein demonstrated qualitative agreement between the COMSOL simulations and experimental droplet generation during steady-state operation. Relative quantitative results could also be gleaned from the simulations. The results from the predictive model, experiments, and COMSOL simulation comparisons provided insight into the selection of controllable experimental parameters, device geometry and flow rates, that targeted a specific droplet size between 100 to 200 µm. For all subsequent experiments, continuous and dispersed channel widths of 100 and 50 µm were utilized, respectively.
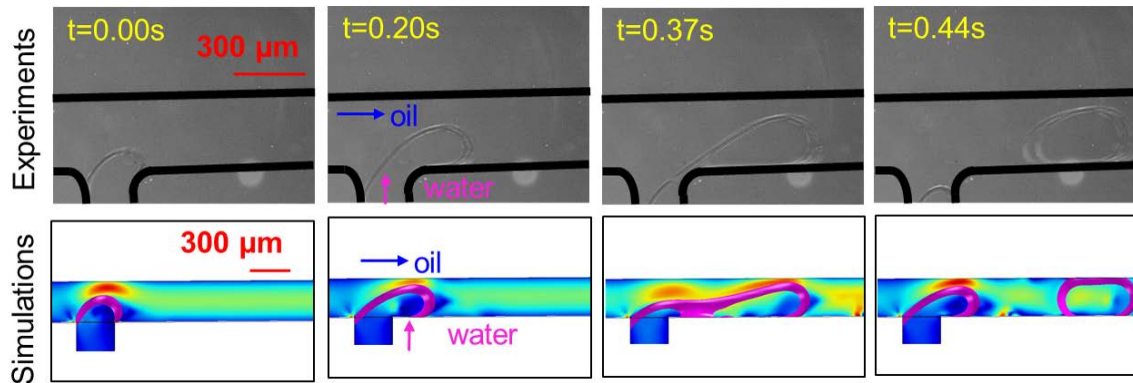
Figure 5-2. Comparison of droplet break-up in a T-junction in experiments (top row) and COMSOL simulations (bottom row) for continuous and dispersed phase widths of 200 µm and 300 µm as well as flow rates of 3.0 µl/min and 0.5 µl/min, respectively.

5.3 Electric Fields

This dissertation details the combination of droplet microfluidics with dielectrophoresis (DEP). In particular, insulator DEP, which uses insulator-shaped electric fields to manipulate polarizable particles or cells [34, 199]. Classical dielectrophoretic theory predicts particle behavior based on the particle's polarizability relative to the medium's polarizability [34, 199]. Therefore, **medium ion distributions surrounding particles/cells are of paramount importance to the cell's response in a DEP field**. Current flux lines are drawn through particles more polarizable than the medium [250] and charges realign inducing a particle dipole aligned with the field [251]. Field lines diverge around less polarizable particles creating ion depletion at the particle poles inducing a particle dipole aligned against the field [251]. When multiple particles are in

close proximity, their induced dipoles interact, and particle pearl chains form along field lines [131, 252-258]. Due to the dependence on a non-uniform electric field, both two and three-dimensional simulations of the electric fields within droplets were completed using the AC/DC module in COMSOL Multiphysics®.

Table 5-3. Parameters/variables used in the electric field simulations

Parameter	Description	Value or Equation
V	Potential	20 (V)
σ_d	Dispersed phase conductivity	(varied 0.028-1.0) (S/m)
σ_c	Continuous phase conductivity	1.0e-8 (S/m)
ε_d	Dispersed phase relative permittivity	78
ε_c	Continuous phase relative permittivity	2.7

Both alternating current (AC) and direct current (DC) electric fields are used for DEP [34, 199]. To reduce simulation complexity, a DC field was used. Parameters for the electric field simulations are listed in Table 5.3. The 2D simulations investigated two dependencies; a) the droplet packing scenario and b) the conductivity of the aqueous phase within the droplets. A 20 V DC electric field was applied across 100 µm diameter droplets packed within a chamber. The droplets were comprised of an aqueous phase with a conductivity ranging from **0.028-1.0 S/m** and with a relative permittivity of 78; the continuous phase was FC-40 with a conductivity of 1.0e-8 S/m and a relative permittivity of 2.7 [259, 260]. Five packing scenarios were investigated; square packing with no space between droplets, offset packing with zero µm, two µm, and three µm spacing between droplets, and non-uniform droplet size/packing.

The droplets' interfacial shaping of the electric field to yield spatially non-uniform electric field gradients was demonstrated in the simulations as shown in Figure 5.3. For the 1.0 S/m aqueous phase, shown in Figure 5.3, current traveled from droplet to droplet provided the oil gaps between droplets were less than 3 µm. Further, square packing yielded two high field density regions (red in the heat map in Figure 5.3) per droplet while the minimal void space offset packing yielded four smaller high field density regions per droplet. The offset packing scenarios showed similar electric field patterns from droplet to droplet, when the droplets are close enough for the electric field to penetrate from droplet to droplet (less than three microns). The non-uniform droplet
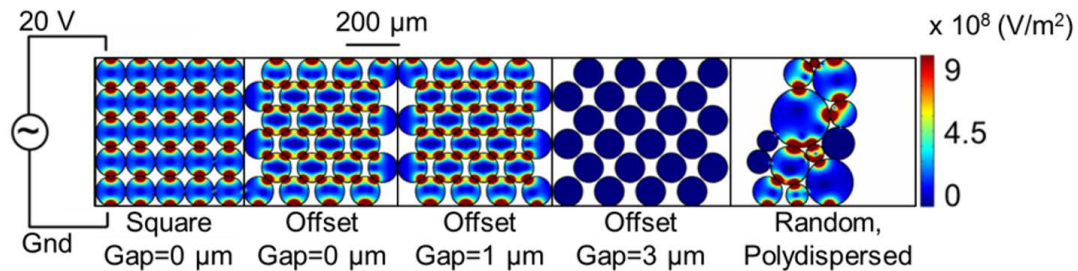
Figure 5-3. Electric field gradients (color map) in 1 S/m aqueous droplets packed 5 different ways (square, offset, offset with gaps, and random) in a 20 V DC field applied from top channel wall and grounded at the bottom channel wall. White space is insulative oil.

size/packing showed irregular electric field gradient patterns due to unpredictable contact points and droplet size. Each conductivity yielded these same results. These simulations demonstrated the importance of achieving monodisperse droplets and uniform packing of droplets in the chamber to get the same non-uniform electric field distribution within each droplet.

A three-dimensional simulation was used to further investigate the formation of non-uniform electric fields within droplets. A 20 V DC field was applied to a single 1.0 S/m droplet with two electrical contacts on either side of the droplet. The simulation showed the electric field gradient was greatest at the contacts (red in the heat map in Figure 5.4) and smallest in the middle (dark blue in the heat map in Figure 5.4).

Both the 2D and 3D simulations demonstrated the ability for the droplets to shape a non-uniform electric field within them, allowing dielectrophoretic characterizations of the particles/cells seeded within the droplets. The simulations also demonstrated how the packing arrangement could affect the shape of the electric field formed.
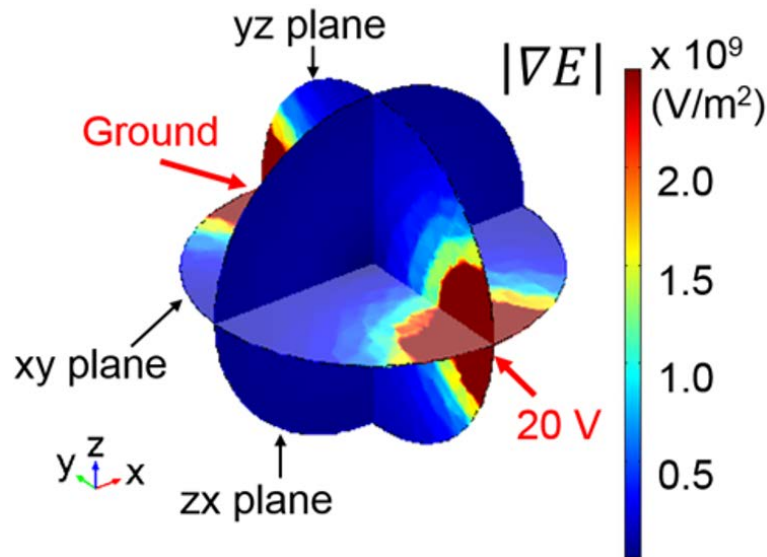
Figure 5-4. Electric field gradient (color map slices) within a 1 S/m aqueous 100 μm diameter droplet surrounded by 10-8 S/m oil. A 20 V DC potential is applied from one pole and grounded on the opposite pole. The electric field gradient is greatest at the poles (dark red on color map, where particles/cells move to during pDEP) and smallest in the middle (dark blue on color map, where particles/cells move to during nDEP). This illustrates the formation of a non-uniform electric field shaped by the droplet interface. For each plane, the view is perpendicular to that plane.

5.4 Dielectrophoretic Movement

Theoretical dielectrophoretic particle responses within droplets were investigated by using the particle tracing and AC/DC modules in COMSOL Multiphysics®. As

previously discussed, DEP manipulates polarizable particles or cells [34, 199]. Clausius and Mossotti developed a frequency (ω) dependent factor, K(ω), [261, 262] that dynamically reflects a perfectly spherical, homogeneous particle's polarizability in a conductive medium. It is a ratio of complex permittivities, ε, for the particle, p, and medium, m, where ω is frequency and σ is electrical conductivity [34, 199, 250, 262, 263]. The complex quantity K(ω) has an imaginary component out of phase with the applied electric field while the real component is in phase [264]. Equations 5.5 and 5.6 are the complex permittivity and real portion of the Clausius-Mossotti factors, respectively. The DEP force is dependent on the in-phase, or real component of the Clausius-Mossotti factor, which estimates the particle's induced dipole or effective polarizability in a dielectrophoretic field [265]. The dielectric force expression, which is time dependent due to K(ω)'s dependency on frequency, with particle volume expressed via radius, r, is shown in Equation 5.7.

$$\tilde{\varepsilon}_i = \varepsilon_i \varepsilon_0 - \frac{j\sigma}{\omega} \qquad 5.5$$

$$K(\omega) = \frac{\tilde{\varepsilon}_p - \tilde{\varepsilon}_m}{\tilde{\varepsilon}_p + 2\tilde{\varepsilon}_m} \qquad 5.6$$

$$\langle \bar{F}_{dep}(t) \rangle = 2\pi\varepsilon_m r^3 \text{Re}[K(\omega)]\nabla|\bar{E}_{rms}|^2 \qquad 5.7$$

Table 5-4. Parameters/variables used in the dielectrophoresis simulations

Parameter	Description	Value or Equation
V	Potential	(varied 5-20) (V)
σ_d	Dispersed phase conductivity	(varied 0.0001-1.0) (S/m)
σ_c	Continuous phase conductivity	1.0e-8 (S/m)
σ_p	PS conductivity	5e-7 (S/m)
ε_d	Dispersed phase relative permittivity	78
ε_c	Continuous phase relative permittivity	2.7
ε_p	PS relative permittivity	2.55
r	PS radius	3 (μm)

The resulting DEP force pushes particles toward regions of high field or low field depending on whether Re[K(ω)] is positive or negative. When the particle is more polarizable than the medium, Re[K(ω)] is positive and the resulting dipole moment causes a force toward high electric field regions, a phenomenon described as positive DEP (pDEP), red regions at the poles in Figure 5.4. When a particle is less polarizable than the medium, Re[K(ω)] is negative and negative DEP (nDEP) pushes the particle toward regions of low field density [34], blue regions in Figures 5.3-5.6. Effective polarizability is dependent on cell permittivity and conductivity through cellular components; cell membranes impact the ability of charges to penetrate the cell while intracellular proteins and cytosol molecules impact charges conducted through the cell [34, 128, 159, 199, 266, 267].
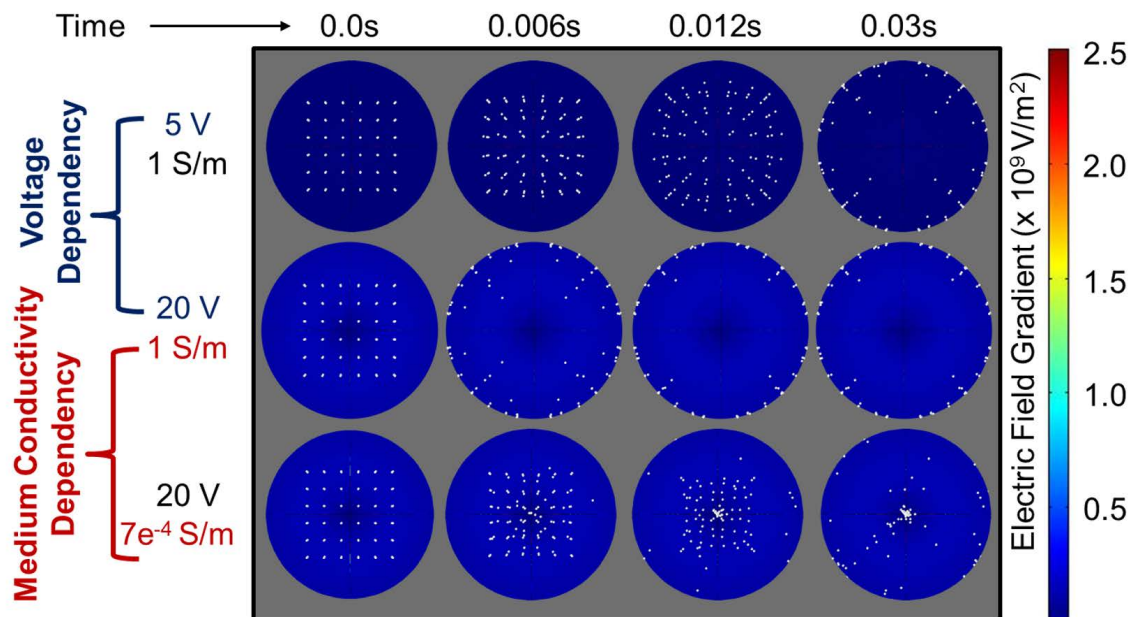
Figure 5-5. Voltage and medium conductivity comparisons in an aqueous 100 μm droplet. Time points from three cases are shown for the zx plane (gradient radiates from center) shown in Figure 5.4. Top: 5 V DC field across a 1 S/m droplet. Middle: 20 V DC field in a 1 S/m droplet. Bottom: 20 V DC in 0.0007 S/m droplet. Changing voltage (note gradient change too) does not change nDEP particle behavior but does increase behavior speed. Changing medium conductivity alters particle behavior from nDEP to pDEP.

For the sake of keeping simulations as simple as possible while still reflecting the experimental system, particle-particle interactions were not programmed into the simulation. A single 100 μm droplet was generated with 216 particles seeded within. Two dependencies were investigated; a) the applied voltage and b) the aqueous phase (droplet) medium conductivity. Simulations were completed using previous μM.D.-ERL research parameters for red blood cells. Parameters for the simulations are presented in Table 5.4 with the buffer solution conductivity ranging from 0.028-1.0 S/m and with a relative permittivity of 78 for the media conditions. Polystyrene beads (PS) were introduced as the particles then potentials were applied at various applied potentials to investigate both positive and negative dielectrophoretic responses at multiple conductivities.

The simulations in Figures 5.5 and 5.6 studied pDEP and nDEP PS particle motion due to solution/particle conductivity differences within a 100 μm droplet. Particles were initially positioned in a cubic grid circumscribed inside the droplet. Figure 5.5 demonstrates both the voltage and medium conductivity dependences of DEP responses as a function of time, shown in the zx plane (labeled in Figure 5.4). The zx plane was chosen for Figure 5.5 due to the high contrast between the particles and the color map of the electric field gradient. It was seen from the top and middle rows that an increase in voltage quickened the dielectric response of the particles. The middle and bottom rows demonstrate that

with a change in medium conductivity the particles shift from positive to negative DEP as evidenced by motion either to the poles versus motion to the center or "equator".
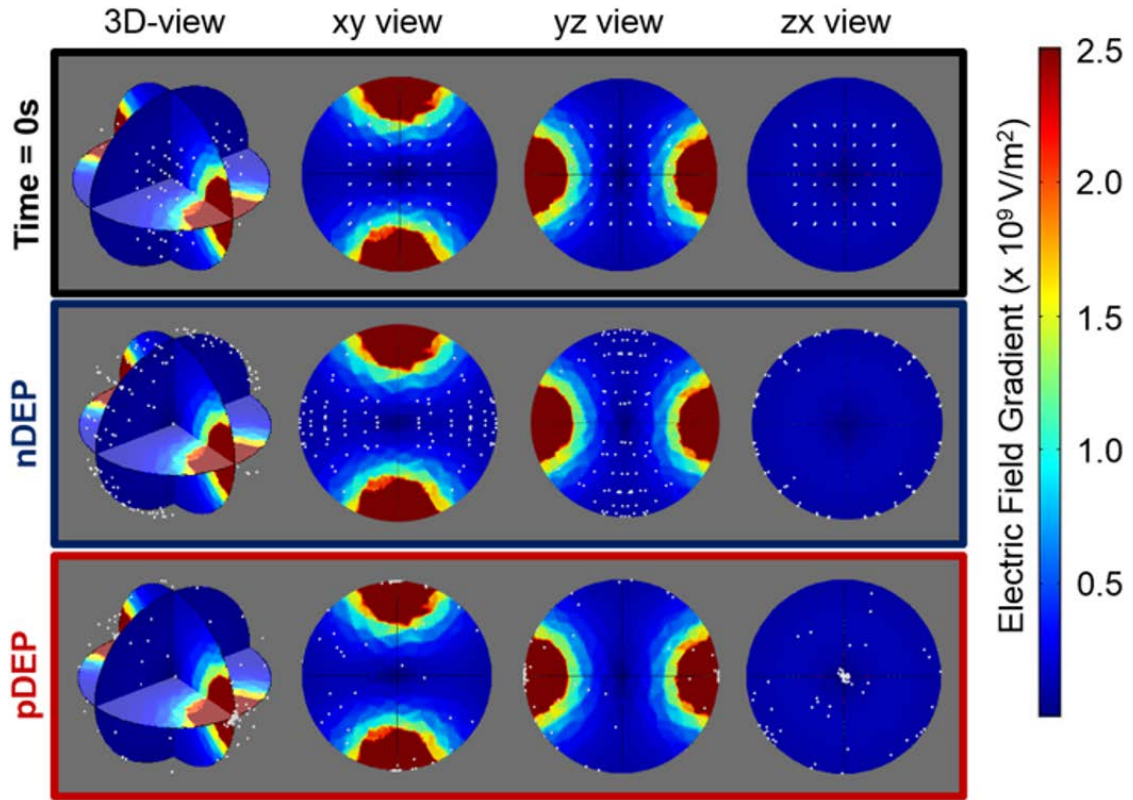
Figure 5-6. DEP particle tracing simulations in an aqueous 100 μm diameter droplet with 20V DC applied at the droplet poles to create a non-uniform field. Particles are white dots above the electric field gradient (color map); particles are driven up or down electric field gradient based upon their polarizability. Comparison of starting positions (top row, time=0.0s) to particle trajectory inside the droplet during nDEP (middle row, medium conductivity = 1 S/m) and pDEP (bottom row, 0.0001 S/m). When experiencing nDEP, particles travel to low field (dark blue) and for pDEP, particles move to high fields (dark red).

In Figure 5.6 at an applied electric field of 20 V DC and at an aqueous droplet conductivity of 1 S/m, simulations predicted nDEP at the low-frequency limit as observed via motion to the droplet "equator" (second row). Similarly, at low conductivities (0.0001 S/m), pDEP was predicted, and particle motion progressed to the high electric field poles (third row). As noted in Equations 5.1 and 5.3, DEP directionality and strength is also determined by applied frequency, such that simulations (data not shown) also predict nDEP at low AC frequencies (kHz), pDEP at middle range frequencies (1 MHz), and nDEP at high (6-10 MHz) frequencies. Conductivity results are shown in Figure 5.6 to reinforce how critically important controlling this variable is to map out DEP responses and thus back-calculate cell dielectric properties.

5.5 Conclusions

Simulations of droplet generation, non-uniform electric fields within droplets, and dielectrophoretic responses within droplets were completed. Experimental results followed the qualitative trends predicted by the simulations, but quantitative comparisons differed slightly, especially at the lowest flow rates. Droplet generation simulations were in close agreement to experimental results. Droplet size decreased with an increase in continuous phase flow rate, and droplet size increased with an increase in dispersed phase flow rate. The comparison of a predictive model, simulations, and experimental results informed a methodology for targeting specific droplet sizes, however, as discussed in Chapter 4, the composition of the two phases also affect the droplet size, and thus discrepancy in droplet size from a predicted value was anticipated and ultimately observed.

Two and three-dimensional simulations demonstrated how the droplet interfaces shaped a non-uniform electric field, which is a necessary condition for dielectrophoresis. Insulative oil surrounding aqueous droplets did allow the electric field to pass through from droplet to droplet, provided the droplets remained in close enough proximity (e.g. less than three microns apart). This result demonstrated that the droplet interface can shape a non-uniform electric field, generating the electric field gradients needed for dielectrophoresis.

Three-dimensional simulations demonstrated both positive and negative dielectrophoresis of simulated particles in agreement with theory. The droplet interface shaped a non-uniform electric field. The electric field gradient was greatest at the poles, or the points of contact between droplets where the electric field traverses from one droplet to the next. This is where particles migrated in the simulations when experiencing positive dielectrophoresis. The electric field gradient was smallest in the middle, around the edge of the droplet, the furthest distance from the high electric field gradient areas. This is where particles migrated when experiencing conditions for negative dielectrophoresis. Varying the voltage did not change the particle behavior but did change the speed of the behavior. Varying the conductivity within the droplet revealed a change in particle behavior consistent with that expected from theory and the literature. This suggests the ability to change particle behavior in different droplets in the same experiment by simply changing the conductivity of the media in the dispersed phase. The simulations outlined herein informed experimental conditions. Results showed qualitative agreement between experiments and simulations as well as quantitative deviations due to the limitations in chemistry and resulting interfacial physics possible within the COMSOL platform.

6 Effects of Additives on Droplet Size and Stability in a Microfluidic T-junction Device

Pieces of this chapter were presented as posters. This work will be submitted to *Biomicrofluidics* or similar.

J.L. Collins, and A.R. Minerick, "Effect of Surfactant on Droplet Size and Stability in a Microfluidic T-junction Device, a mini-study," ASME 4th Global Conference on Nanoengineering for Medicine and Biology, Minneapolis MN, April 2015.

J.L. Collins, and A.R. Minerick, "Effect of Surfactant on Droplet Size and Stability in a Microfluidic T-junction Device," External Advisory Board (EAB) Poster Session, Michigan Technological University, Oct. 2014. Also presented at: Biotechnology Research Center (BRC) Research Forum. Oct. 2014.

6.1 Introduction

Surfactant transport mechanisms, because of their efficiency and elegance are valuable in microelectronics, microfluidics, and biotechnology as they influence/dominate interface behaviors [84]. This work explores the complex interactions between surfactants as well as salts and dextrose in aqueous-droplet-in-oil microfluidic systems. A subclass of applications require isotonic, biocompatible aqueous solutions for the investigation of biological fluids, molecules, and cells. These complex surfactant interactions can be measured by changes in interfacial tension observable in droplet size behaviors. Since surfactants strongly influence droplet formation, stability, and biocompatibility, the effect of surfactants and other additives on droplet size and stability were explored as a simple, high reproducible tool to enable droplet microfluidic interrogation of particle and cells possible over a broad range of isotonic salt solutions.

Bodies of work have demonstrated that surfactants ease droplet formation and stability [62, 76, 78, 99, 100], and dominate emulsions where phase boundary area is large with respect to volume [84]. Decreasing interfacial tension, the interfacial free energy per unit area, decreases the interfacial energy and thus the work required to create an interface which manifests in stable droplet formation [84]. Due to the amphiphilic nature of surfactants in immiscible aqueous/oil solutions, surfactants align at the fluid interface with the hydrophobic portion of the molecule in the oil phase and the hydrophilic portion in the aqueous phase [85]. Surfactant molecules at each droplet interface act as shields (free energy minima) that help droplets resist coalescence [54, 86, 87]. Decreases in interfacial tension are dependent on the amount of molecules absorbed at the interface, which can be described by the Gibbs isotherm for dilute solutions (Equation 6.1; Γ is the surface concentration, c is the surfactant bulk concentration, γ is interfacial tension, R is the universal gas constant, and T is the temperature) [85]. At a specific concentration, surfactants begin to form micelles. This concentration is referred to as the critical micelle concentration (CMC), and above the CMC the interfacial tension is constant [88].

$$\Gamma = -\frac{c}{RT}\frac{d\gamma}{dc} \qquad 6.1$$

Surfactants play a key role in droplet biocompatibility [40, 47, 62, 87, 99, 100]. Because their addition can impact the adsorption of biomolecules at liquid-liquid and solid-liquid interfaces [47], surfactant biocompatibility has been shown to be important for polymerase chain reaction (PCR), cell culturing, and cell analysis applications [28, 29, 37, 268]. An electrical technique, electrowetting-on-dielectrics (EWOD), has sorted droplets based on contents [28], completed glucose assays [269], cell-based and enzyme assays [270], proteomic sample processing [271], and biomolecule investigations, such as proteins and DNA [272] for serum, plasma, urine, saliva , and tear samples [151]. These biological samples generally require the presence of electrolytes, which influence electrical properties of the solution. These electrical properties of droplets are foundational to EWOD responses, which has prompted the study of electrolytes within droplets [273]. In EWOD biofluid applications [151], biomolecule adsorption onto the bottom solid surface affects EWOD performance by altering the contact angle hysteresis and Young's equilibrium contact angle [272]. Previous work found that the use of a surfactant aided in controlling interfacial tension by hindering biomolecule absorption to maintain performance. While electrolyte-surfactant interactions were explored in EWOD, this air/droplet/solid surface system is different from the continuous oil, dispersed aqueous droplet system of interest in this manuscript.

Another area of microfluidics that extends to biological applications is electrokinetics, which encompasses linear electric field phenomena such as electrophoresis and nonlinear electric field phenomena such as dielectrophoresis (DEP) [130, 159, 190, 191]. Electrokinetic cell characterizations are closely dependent upon the supporting media conditions; precise control of electrolyte concentrations and thus conductivities are advantageous. Aqueous solution conductivities, while maintaining isotonic pressures for cells, are most easily controlled via a combination of buffer salts and sugars. When interrogating cells electrokinetically, isotonic media of different conductivities are essential to more precisely ascertain cell membrane permittivities and other cell characteristics [132, 194, 274]. Isotonicity is achieved by using non-ionic molecules such as dextrose to compensate for conductivity changes when altering salt concentrations. Isotonic, aqueous solutions with conductivities spanning 2-3 orders of magnitude have been used in electrokinetic research involving cells [222, 275, 276]. This work explores surfactant stabilization of such droplets over a broad range of media conditions.

Strategic tailoring of surfactants for specific applications can be achieved via molecule selection, head or tail group alterations, or via interactions with other molecules present in the solution. Research has shown a decrease in CMC with increasing salt concentration [239-241]. Sandoz et al. showed that addition of a surfactant increased droplet stability as desired, but an undesired side effect occurred; fluorescent resorufin derivatives added for enzymatic signal amplification leaked through the interface into the surrounding oil phase [242]. Further, interfacial transport was inhibited by adding sugar into the aqueous phase [242]. Addition of both salt and sugar to the aqueous phase, a condition needed for

isotonic media for many biological and electrokinetic applications, has not previously been explored. A preliminary exploration of this dependency is reported herein. A surfactant, Krytox FSH 157 was used to aid in stabilizing aqueous droplets containing the components needed for isotonic phosphate buffer saline/dextrose solutions (NaCl, K_2HPO_4, KH_2PO_4, and dextrose). Microfluidic T-junction generation of droplets was utilized to explore the effects of these components in combination with the surfactant on droplet formation and stability.

Measuring droplet sizes from a microfluidic T-junction indirectly measures the effect of interfacial tension, and hence surfactant efficacy [85]. This can be related to the droplet size by the Laplace pressure. Multiple equations for describing both static and dynamic interfacial tension via the Laplace pressure have been presented and are shown in Table 6.1 where d is the droplet diameter, r is the droplet radius, γ is the interfacial tension, and ΔP is the pressure difference between the two sides of the interface.

Table 6-1. Relationship between Laplace pressure, interfacial tension, and droplet size

Reference	Type of interfacial tension	Equation
[277]	static	$\Delta P = \dfrac{4 \cdot \gamma}{d}$
[243, 278, 279]	static r_a, radius in axial direction r_r, radius in radial direction	$\Delta P = \gamma \left(\dfrac{1}{r_a} + \dfrac{1}{r_r} \right)$
[77]	steady state, squeezing	$\Delta P = \dfrac{2 \cdot \gamma}{r}$
[76]	dynamic R_A, curvature of droplet head in width direction r_A, curvature of droplet head in depth direction R, curvature of droplet tail in width direction r, curvature of droplet tail in depth direction	$\Delta P = \gamma \left(\dfrac{1}{R_A} + \dfrac{1}{r_a} - \dfrac{1}{R} + \dfrac{1}{r} \right)$

Assuming the pressure difference to be constant, the Gibbs isotherm and the simplest form of the Laplace pressure relationship can be combined and rearranged into a relationship between surfactant concentration and droplet size, as shown in Equations 6.2-6.4 where b is the constant of integration.

$$\Gamma = -\frac{c\Delta P}{4RT}\frac{\partial d}{\partial c} \qquad 6.2$$

$$\frac{1}{c}\partial c = -\frac{\Delta P}{4\Gamma RT}\partial d \qquad 6.3$$

$$d = -\frac{4\Gamma RT}{\Delta P}\ln c - \frac{4\Gamma RT}{\Delta P}b \qquad 6.4$$

This equation was fit to diameter dependence from three types of additives. Generation, size, and stability of aqueous-in-oil droplets were measured for a range of aqueous phase compositions and surfactant concentrations in the oil phase. Control experiments for the salt and sugar concentrations present in each aqueous phase conductivity are also reported. Implications from the data are noted, including behaviors of isotonic conductivities, which are a complex combination of salt and dextrose interactions with the droplet interface. These observations of the interactions between salts, sugar, and surfactant add to the knowledge of additive effects on droplet interfacial tension, allowing for more precise tailoring of materials to desired experimental conditions within droplet microfluidic applications.

6.2 Materials and Methods

6.2.1 Materials

Devices were microfabricated using SU-8 features on a silicon wafer templating for PDMS castings, which were bonded to glass slides for fluidics. Devices were pretreated for hydrophobicity (as described in Chapter 4), then loaded with a continuous oil phase and a dispersed aqueous phase comprised of isotonic salts and dextrose. Droplets were imaged with video microscopy and analyzed for trends.

6.2.2 Device Fabrication

Microdevices were fabricated in Michigan Tech's Microfabrication Facility using customized soft lithography techniques [221, 222]. To make features on a master silicon wafer, SU-8 2025 (MicroChem, Westborough, MA) photoresist was masked and photopolymerized. Polydimethylsiloxane (Sylgard-184, Dow Corning, Midland, MI) was used to replicate fluidics from the SU-8 structures. PDMS castings were exposed to air plasma treatment (Harrick Plasma, Ithica, NY) to facilitate sealing to glass slides. The PDMS/glass slide devices were placed in an oven at 70°C for 24 hours to allow the PDMS to revert to its native hydrophobic state after the generation of silanol groups at the expense of methyl groups during oxygen plasma exposure [231].

6.2.3 Solution Preparation

The continuous oil phase was Fluorinert FC-40 (Sigma Aldrich, St. Louis, MO) with varying amounts (0-2 mM) of Krytox 157 FSH surfactant (Dupont, Morton Grove, IL). Krytox 157 FSH contains a PFPE (perfluorinated polyether) tail and a carboxylic acid head group [2, 47, 89] and was chosen for this project due to benefits of its high molecular weight and low cost. Three types of aqueous phases were investigated as the dispersed phase: salt only, dextrose only, and salt+dextrose. Each dispersed aqueous phase was made using epure water (Millipore, Billerica, MA) along with sodium chloride (NaCl, Sigma Aldrich), dibasic potassium phosphate (K_2HPO_4, Sigma Aldrich), monobasic potassium phosphate (KH_2PO_4, Sigma Aldrich), and dextrose (Sigma

Aldrich). Isotonic solutions of different conductivity were made of epure water containing a salt stock (equimolar amounts of NaCl, K_2HPO_4, and KH_2PO_4), and dextrose. To increase the conductivity, yet maintain constant tonicity, more salt stock and less dextrose were added. The five conductivities were 0.0000055 S/m (epure water), 0.05 S/m (0.960 mM salt, 290.4 mM dextrose), 0.1 S/m (2.616 mM salt, 273.8 mM dextrose), 0.5 S/m (13.892 mM salt, 161.1 mM dextrose), and 1.0 S/m (24.122 mM salt, 58.8 mM dextrose). For each molar concentration, control solutions contained salt-only (0.960-24.122 mM) or dextrose-only (58.8-290.4 mM) with the amounts corresponding to the amounts used for each conductivity solution.

6.2.4 Device Set-up: Equipment Uses and Settings

Device pretreatment: Two pretreatment steps were completed to aid in reproducible flows through devices. Rain-X®, a commercially available water repellent from glass, was used to treat PDMS devices before use. Rain-X® was flushed through the microdevice and left overnight at room temperature to evaporate. The device was then filled with the respective surfactant/oil solutions and allowed to sit for at least one hour before experiments to ensure proper wetting of the solid-liquid interface.

Experimental setup: A Harvard Apparatus syringe pump (PHD Ultra, Holliston, MA) was utilized to precisely control flow rates. The PHD Ultra pump has a flow rate accuracy of ±0.25% and reproducibility of ±0.05% [280]. Both the aqueous and oil solutions were infused into the microfluidic T-junction at a flow rate of 0.25 µL/min for
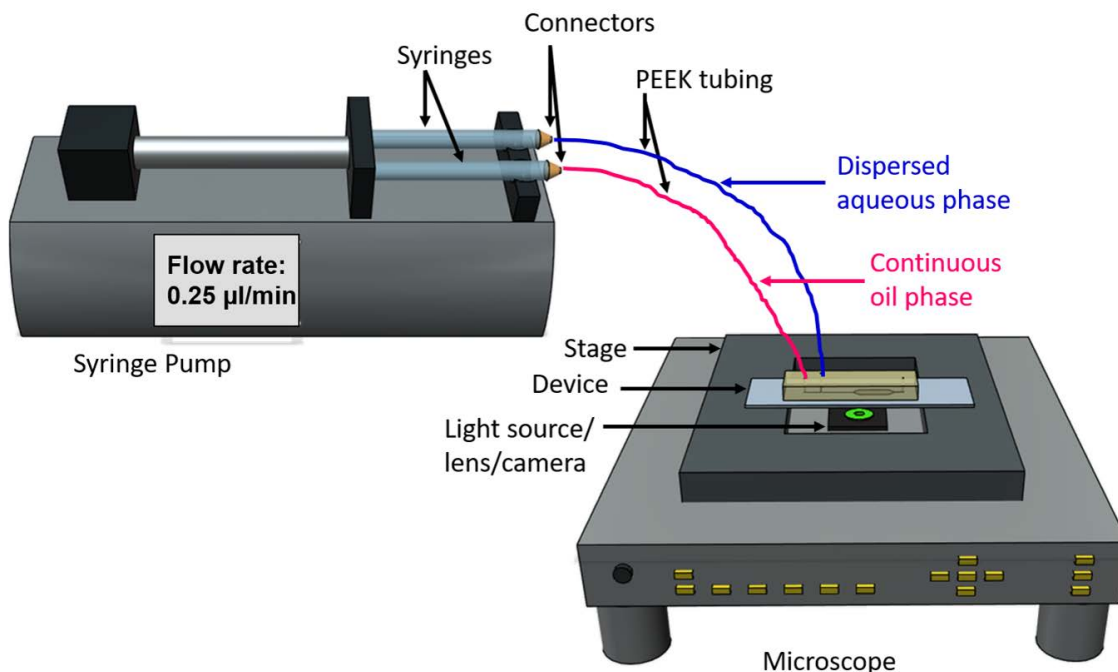
Figure 6-1. Diagram depicting the equipment setup. The microdevice was set on the microscope stage and PEEK tubing was used to connect the device to the syringe pump.

15 minutes to allow the system to reach steady state before beginning experiments. This 15-minute wait time was determined by measuring droplet size from 1 to 75 minutes; steady state was ascertained from droplet size consistency, as shown in Section 4.3.3 and Appendix A.6. A diagram of the equipment setup is shown in Figure 6.1, and the microfluidic device is shown in Figure 6.2a.

6.2.5 Imaging Software and Analysis Techniques

Experiments were recorded at 4x magnification and 30 frames per second via an SVM340 Synchronized Video Microscope using the UScope software (Labsmith, Livermore CA). Image data were analyzed using ImageJ [226].

Droplet Size Analysis: The effect of each additive, and the combination of additives, on droplet size, was analyzed using a temperature adjusted droplet size approach. For each experiment, 100 droplets were measured at the T-junction location shown in Figure 6.2a. The number of frames necessary to generate each droplet was counted by noting the break-up point as shown in Figure 6.2b-f. The number of frames was converted to the temperature adjusted droplet diameter as shown in Figure 6.3a. The number of frames was converted to time via the frame rate and the time was converted to the volume via the set volumetric flow rate. Volume was converted to an effective hydraulic diameter using the formula for sphere diameter. The diameter was then converted to a "temperature adjusted droplet size" by dividing by device temperature during the experiment.
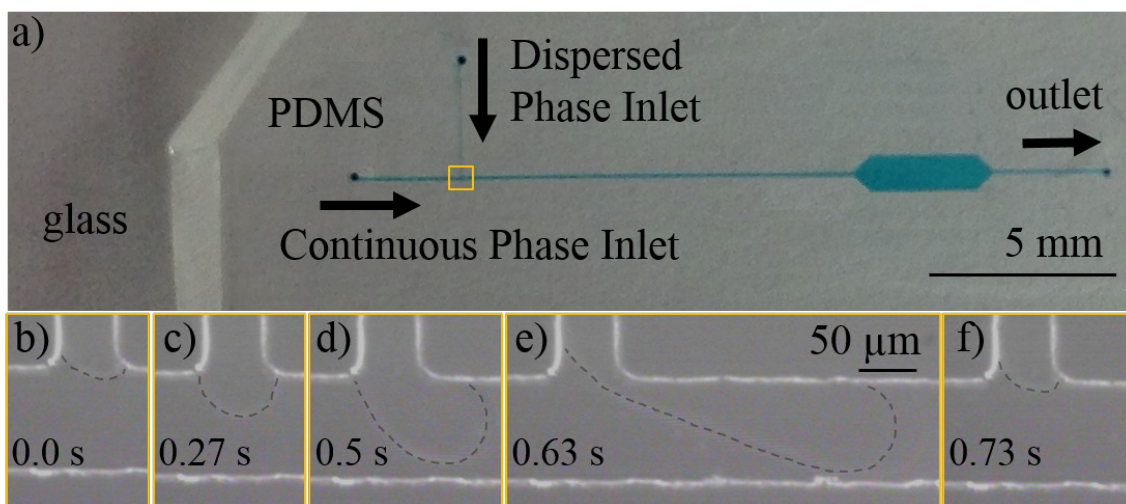
Figure 6-2. a) Fabricated microdevice (filled with food coloring to show fluidics). Continuous channel = 100 μm in width, dispersed channel = 50 μm in width, height = 100 μm, and chamber = 1 x 3 mm. b)-f) droplet break off within the T-junction (images from 72.45 mM salt-only in 0.66 mM Krytox at 0.25 μl/min), used for droplet size measurement, dotted lines drawn present for ease of distinguishing the liquid-liquid interface.

An increase in temperature increases the extent of solubilization [84], and thus the effect was removed to yield a more accurate representation of additive effects based on Gibbs isotherm and Laplace pressure. The temperature was measured via an infrared thermometer (Fischer Scientific, Waltham, MA) and ranged from 60°F to 77°F. Outliers, identified via the quartile method, were excluded from subsequent calculations to allow the monodispersity and reproducibility of one experiment as well as a set of experiments to be investigated. The temperature adjusted droplet sizes for 100 droplets in each experiment were averaged, and the standard deviation and coefficient of variance were calculated.

Droplet generation regime: Effects from additive combinations on the droplet generation regime were analyzed by visual determination. Five generation regimes [69, 77] were used for classification informed by previous research cataloging surfactant concentrations of interfacial equilibrium shifts where the different regimes occur [78, 79]. Recorded videos were assessed to ascertain which of the five flow regimes the flow exhibited:
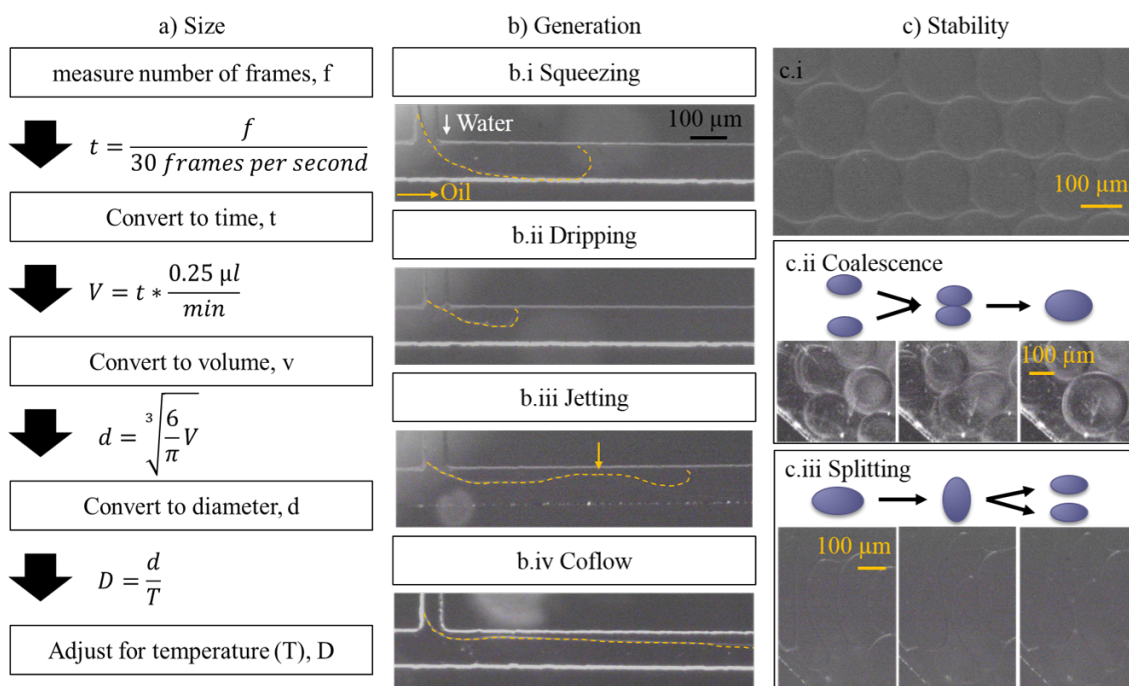
Figure 6-3. a) Algorithm for converting number of frames to temperature adjusted diameter. b) Examples of i) squeezing (2.616 mM salt in 1 mM Krytox in FC-40 at 0.25 µl/min), ii) dripping (0.05 S/m in 1 mM Krytox in FC-40 at 0.25 µl/min), iii) jetting (0.5 S/m in 0.66 mM Krytox in FC-40 at 0.25 µl/min), and iv) coflow (24.122 mM salt in 1 mM Krytox in FC-40 at 0.25 µl/min). c) Examples of i) stable droplets in the microfluidic chamber (13.899 mM salt-only droplets in 2.62 mM Krytox in FC-40, each at 1.0 µl/min), ii) droplets coalescing in the chamber entrance (161.108 mM dextrose-only droplets in 2.35 mM Krytox in FC-40, each at 1.0 µl/min), and iii) droplets splitting in the chamber entrance (0.05 S/m droplets in 1 mM Krytox in FC-40, each at 0.25 µl/min).

squeezing, dripping, thread formation, jetting, or co-flow. Thread formation was not observed in this system; examples of the four other regimes are shown in Figure 6.3b.

Droplet coalescence and splitting: Just as surfactants have been shown to alter the generation regime, they have also been shown to alter droplet stability [78]. Droplet stability was assessed as a function of additive concentrations by analyzing droplet behavior upon entrance into the microfluidic chamber shown in Figure 6.2 a) with a linear 35° pitch expansion from the 100 µm wide channel to the 1000 µm wide chamber. The tendency to coalesce (interfacial tension too high) and split (interfacial tension too low) within the first 1000 microns of the chamber was observed and tabulated from the recorded videos. Coalescence and splitting examples are visualized in Figure 6.3c.

6.3 Results and Discussion

Droplet characteristics were compiled to ascertain trends as a function of surfactant concentration in the continuous phase as well as compiled as a function of different composition and conductivities in the dispersed aqueous phases. Each dependency was determined by measuring droplet diameter, calculating the coefficient of variance, and cataloging generation and stability regimes. Physical mechanisms of additive interactions and their role in interfacial tension are inferred from the results.

Surfactant effects: The droplet size at generation, the observed generation regime, the stability entering the chamber, and the coefficient of variance were used to investigate the effect of surfactant in a microfluidic T-junction. Controls were completed with the Krytox surfactant as the only additive to the epure water/FC-40 system. The range of Krytox concentrations explored were below or near the CMC because leveling off of the expected natural log curve indicates homogeneous spreading of surfactant, which occurs at and above the CMC [79]. As available surfactant molecules increase, the interfacial tension between the two immiscible phases decreases and causes droplets to break off at smaller sizes. Temperature droplet diameter as a function of surfactant concentration for epure water can be seen individually in Figure A.1 and combined with additives in Figures 6.4a, 6.5a, and 6.6a, and the coefficients of variance for all experiments can be found in Table A.5 of Appendix A.

The droplet size increased with an increase in Krytox concentration, until 0.66 mM Krytox, at which point the droplet size decreased with an increase in Krytox concentration. For the epure water control, the generation regime of squeezing and the stability of complete coalescence were observed. Also, the coefficients of variance ranged from 4.1% to 15.4%, which was similar to the polydispersity of droplets generated in a T-junction generally reported between 2% to 10% [53, 243]. Trends observed with increases in surfactant concentration included that the size of the droplets at generation follow an overall natural log trend, which is consistent with Laplace pressure and Gibb's Isotherm, as discussed in Table 6.1 and Equations 6.1-6.4. For concentrations of 0.66 mM and greater, a natural log trend line R^2 value of 0.7515 was observed. The lower R^2 value was due to an unexplained divergence from the natural log trend at 1.75 mM

Krytox. The addition of Krytox FSH 157 into the epure water/FC-40 system altered the interfacial tension as expected, verifying the use of Laplace pressure and Gibb's Isotherm as an indirect measure of surface tension for the main experiments.

Salt effects: Control experiments were conducted with salt concentrations of 0, 0.96, 2.616, 13.892, and to 24.122 mM to investigate the effect of salt on droplet generation. The droplet size at generation, the observed generation regime, the stability entering the chamber, and the coefficient of variance were tracked for each concentration. Temperature adjusted droplet diameter was plotted as a function of Krytox concentration for each salt concentration, as shown in Figure 6.4. When compared to epure water, the presence of salt, at any concentration, decreased the droplet size. There was less of a decrease in droplet size at the highest surfactant concentration. At lower Krytox concentrations, there is a trend of decreasing droplet size with increasing salt concentration. At higher Krytox concentrations, the size of the droplets for all salt concentrations are not statistically different, as their standard deviations overlapped, as seen by the error bars in Figure 6.4. The addition of salt in the form of a phosphate buffer saline had an observable effect on the resulting droplets formed. For each salt concentration, the expected trend of decreasing droplet size with increasing surfactant concentration was observed, with natural log trend line R^2 values ranging from 0.7274 to 0.8767, as shown in Figure A.2.

The presence of salt decreased the temperature adjusted droplet size when compared to the epure water (0 mM salt) control experiments at the same surfactant concentrations, as

Figure 6-4. Compilation of curves for five salt concentrations. The error bars indicate that a surfactant concentration of 2 mM Krytox in FC-40 results in the lowest coefficient of variance. 1 mM and 2 mM Krytox in FC-40 also results in the point where all salt concentrations result in the same temperature adjusted droplet size.

Figure 6-5. a) Stability, b) generation regime, and c) combined stability and generation regime diagrams for the salt-only aqueous phases. There is decrease in interfacial tension in the presence of salt, shifting the generation regimes and stability.

shown in Figure 6.5. This trend indicates an interfacial tension decrease, which was consistent with the change in generation regimes observed. In the presence of salt, the regime remained squeezing at 0.66 mM Krytox, shifted from squeezing to dripping for 1 mM Krytox, and shifted from squeezing to dripping/jetting for 2 mM Krytox. As the salt concentration increased, the system transitioned from complete coalescence (0 mM Krytox) to either partial coalescence, a mixture of coalescence and splitting, partial splitting, or stable droplets. The most stable droplets in the salt-only controls occurred at a Krytox concentration of 1.75 mM. This result also suggests that the presence of salt decreases the interfacial tension. In the presence of salt, as the surfactant concentration increased the droplet generation regime shifted from squeezing at 0.33 and 0.66 mM Krytox, to dripping at 1 and 1.75 mM Krytox, and a mixture of dripping and jetting at 2 mM Krytox.

The coefficient of variance (CV) of the droplet generation size was also evaluated for salt affects the aqueous/oil/surfactant system. A full table of CV values is located in Appendix A. Figures 6.4-6.9 illustrate the average droplet size (averaged from multiple droplets (repeats) between multiple experiments (replicates)) with $\pm$ the standard deviation that resulted in each scenario. Data in Figure 6.4 revealed an overall trend of decreasing standard deviation with increasing surfactant concentration. This change in the monodispersity was tracked and compared to literature using the coefficient of variance. The presence of salt decreased the CV, as compared to the epure water control, for 68% of the experiments containing salt.

The relationships between salt presence and droplet size, and capillary number and flow regime corroborate that the interfacial tension was decreased in the presence of salt, likely due to charge stabilization of Krytox's carboxylic acid head groups. The decrease in CV in the presence of salt, and with increasing surfactant concentration also suggests that salt ions improve reproducibility by enabling charge stabilization of Krytox's carboxylic acid head group yielding consistent, stable packing of the surfactant molecules at the interface. When the Krytox molecules come in contact with the aqueous phase, a hydrogen ion dissociates, leaving a negatively charged particle, $KryCOO^-$. The salts dissolved in the aqueous phase result in Na^+, K^+, Cl^-, HPO_4^{2-}, and $H_2PO_4^-$. The Krytox molecules surround the droplet at the interface, creating a negatively charged layer, as shown in Figure 6.10a. The positively charged salt ions are attached to that layer, forming a thin Debye layer of positive counterions, as shown in Figure 6.10b.

Dextrose effects: Control experiments were conducted, investigating the effect of dextrose on droplet formation for dextrose concentrations of 0, 58.8, 161.1, 273.8, and 290.4 mM, corresponding to the amounts needed for 0.0000055, 1.0, 0.5, 0.1, and 0.05 S/m conductivity solutions, via droplet size at generation, the observed generation regime, the stability entering the chamber, and the coefficient of variance. Similar to the addition of salt, the addition of dextrose had an observable effect on the droplets formed at generation and stability in the chamber. At the lower surfactant concentrations of 0.33 and 0.66 mM Krytox, the presence of dextrose appeared to decrease the temperature adjusted droplet size. However, the resulting droplet sizes were not statistically different,
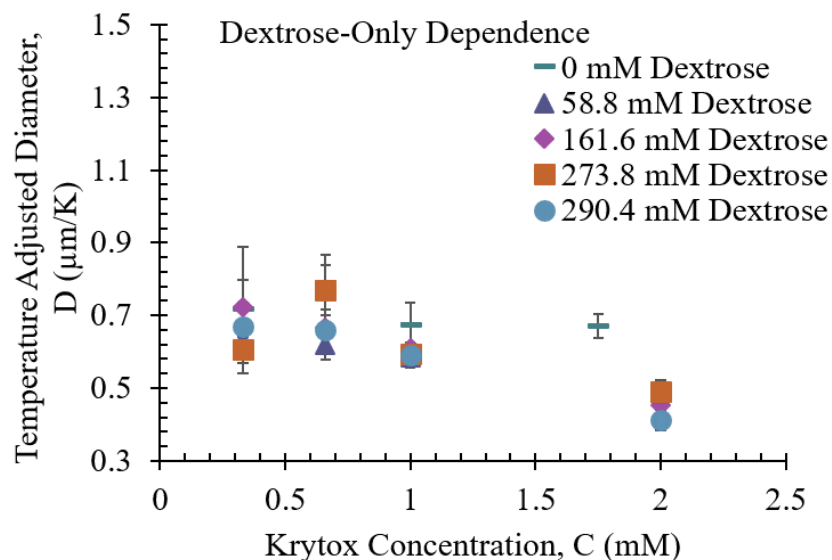
Figure 6-6. Compilation of curves for five dextrose concentrations. The error bars indicate that a surfactant concentration of 1 mM Krytox in FC-40 results in the lowest coefficient of variance. 1 mM Krytox in FC-40 also results in the point where all dextrose concentrations result in the same temperature adjusted droplet size.

except the 273.8 mM dextrose solution at 0.66 mM Krytox deviated for an unexplained reason. At the higher surfactant concentrations of 1 and 2 mM, the presence of dextrose appeared to increase the temperature adjusted droplet size when compared to the epure water control, as shown in Figure 6.6. No statistically significant differences between dextrose solutions were noted at 1.0 mM Krytox, but the droplets with dextrose were statistically larger than the epure water control at 2.0 mM. For each dextrose concentration, the expected trend of decreasing droplet size with increasing surfactant concentration was observed, with natural log trend line R^2 values ranging from 0.8312 to 0.9385, except for 273.845 mM dextrose which had an R^2 value of 0.2866, as shown in Figure A.3.

There was a change in generation regime observed in the presence of dextrose, as shown in Figure 6.7. At surfactant concentrations of 1.75 mM and lower, squeezing was observed. At higher surfactant concentrations, a mixture of dripping and jetting was observed, indicating an increase in interfacial tension. All dextrose-only concentrations (0 to 290.4 mM) yielded complete coalescence upon entering the chamber. This display of complete coalescence showed that the uncharged dextrose on its own was not able to stabilize the droplet interface in the same manner as the salt, but did interact through hydrogen bonding.

There was also an observable change in CV in the dextrose only controls. There was a decrease in CV with an increase in surfactant concentration for all but the 58.8 mM dextrose with 1 mM Krytox, 273.8 mM dextrose with 0.33 mM Krytox, and 290.4 mM
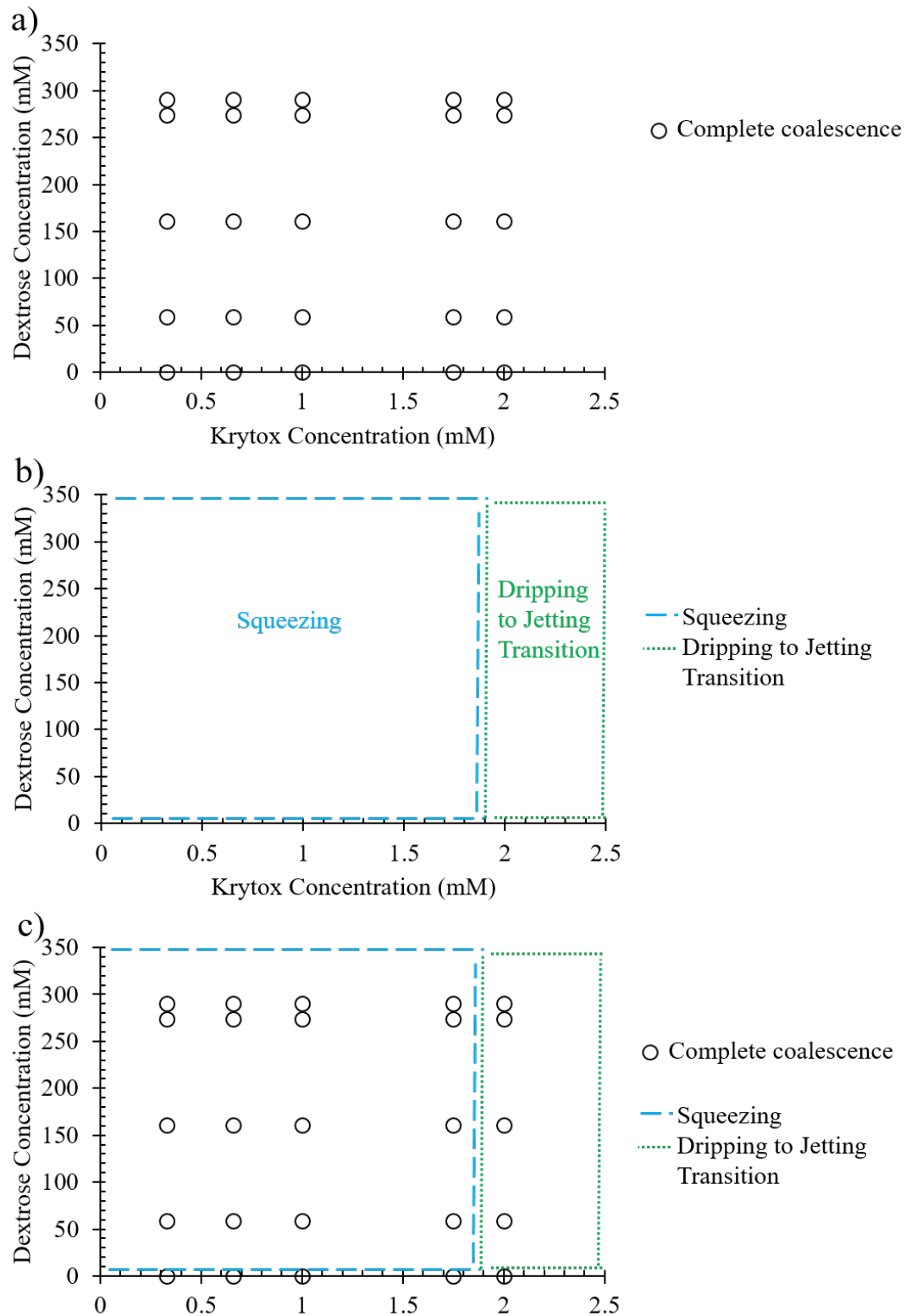
Figure 6-7. a) Stability, b) generation regime, and c) combined stability and generation regime diagrams for the dextrose-only aqueous phases. There is an effect on the generation regime at higher dextrose concentrations, but all dextrose concentrations yielded no impact on droplet stability.

dextrose with 1 mM Krytox. The dextrose-only experiments also showed a decrease in CV, compared to the epure water control, for 88% of the experiments.

The dextrose appeared to act as a buffer on the interfacial tension when compared to the epure water control (0 mM dextrose); identical shifts in surfactant concentration yielded smaller changes in droplet size at all concentrations of dextrose than the epure control. Since the droplet size was proportional to the interfacial tension between the two phases, this infers less of a shift in interfacial tension. Anionic surfactants have exhibited adsorption onto nonionic macromolecules [84], suggesting that surfactant molecules interact with the dextrose molecules, altering their transport at the droplet interface, as depicted in Figure 6.10c. Literature has also shown the presence of sugar derivatives (up to 25 w/v%) alter molecular transport through aqueous/oil interfaces [242].

Combined salt and dextrose effects: The effect of combinations of salt and dextrose, to make isotonic solutions of varied conductivity (5.5E-6, 0.05, 0.1, 0.5 and 1.0 S/m), were investigated by tracking droplet size at generation, the observed generation regime, the stability entering the chamber, and the coefficient of variance. The combination of salts and dextrose is necessary to maintain isotonic solutions at different conductivities. Isotonic solutions are essential for cellular and biological applications, while ion availability is a key control parameter for electronic manipulations. Figure 6.8 illustrates a combined effect of the presence of both salts and dextrose by comparing isotonic salts/dextrose solutions at different conductivities. It should be noted that the concentrations of the salt-only and the dextrose-only experiments are identical to the concentrations needed for the combined conductivity solutions. At the lowest 0.33 mM Krytox condition, droplets for each conductivity, or salt and dextrose combination, were
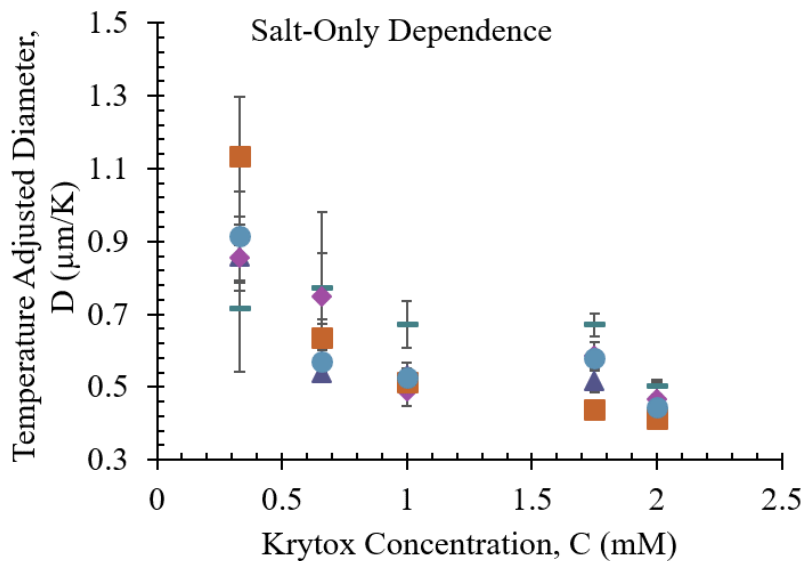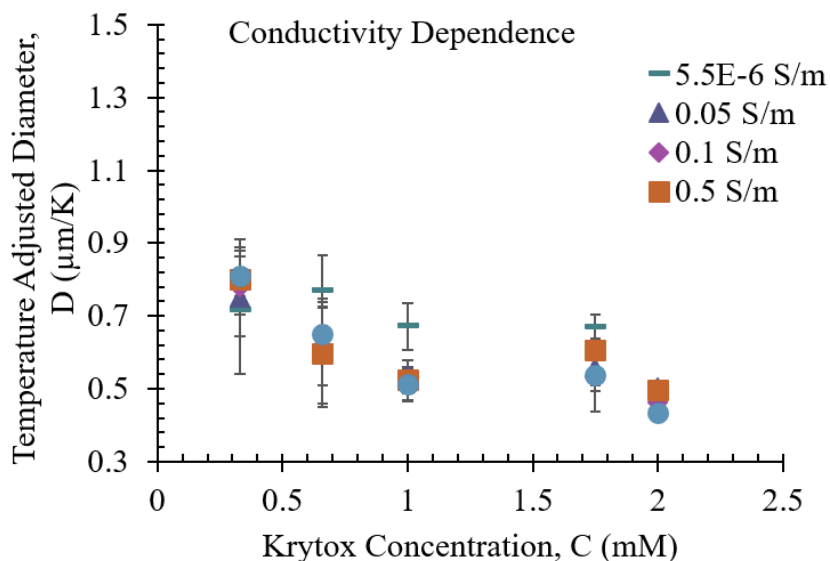

Figure 6-8. Compilation of curves for five conductivities. The error bars indicate that a surfactant concentration of 2 mM Krytox in FC-40 results in the lowest coefficient of variance. 0.66 mM Krytox in FC-40 results in the point where all conductivities result in the same temperature adjusted droplet size.
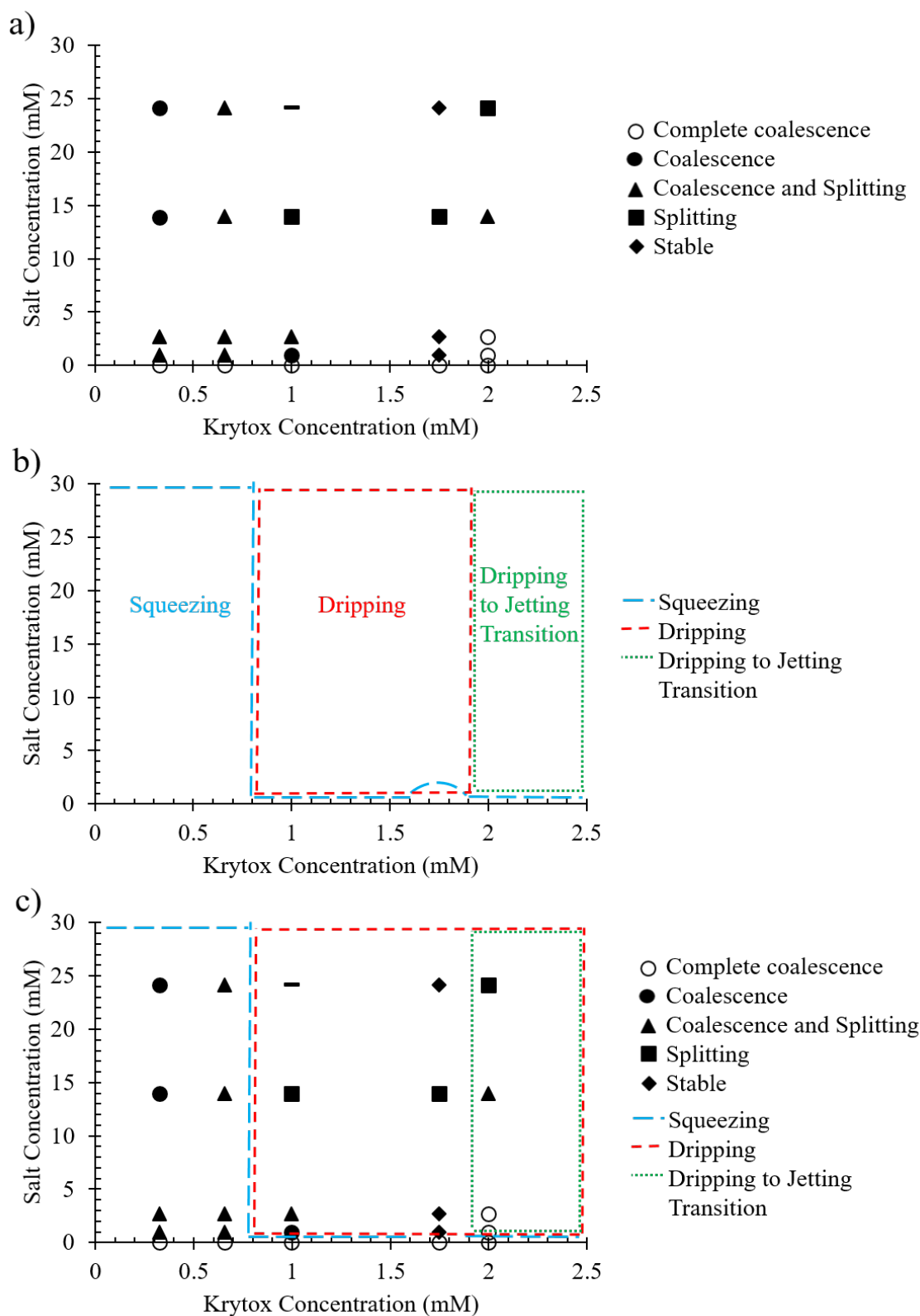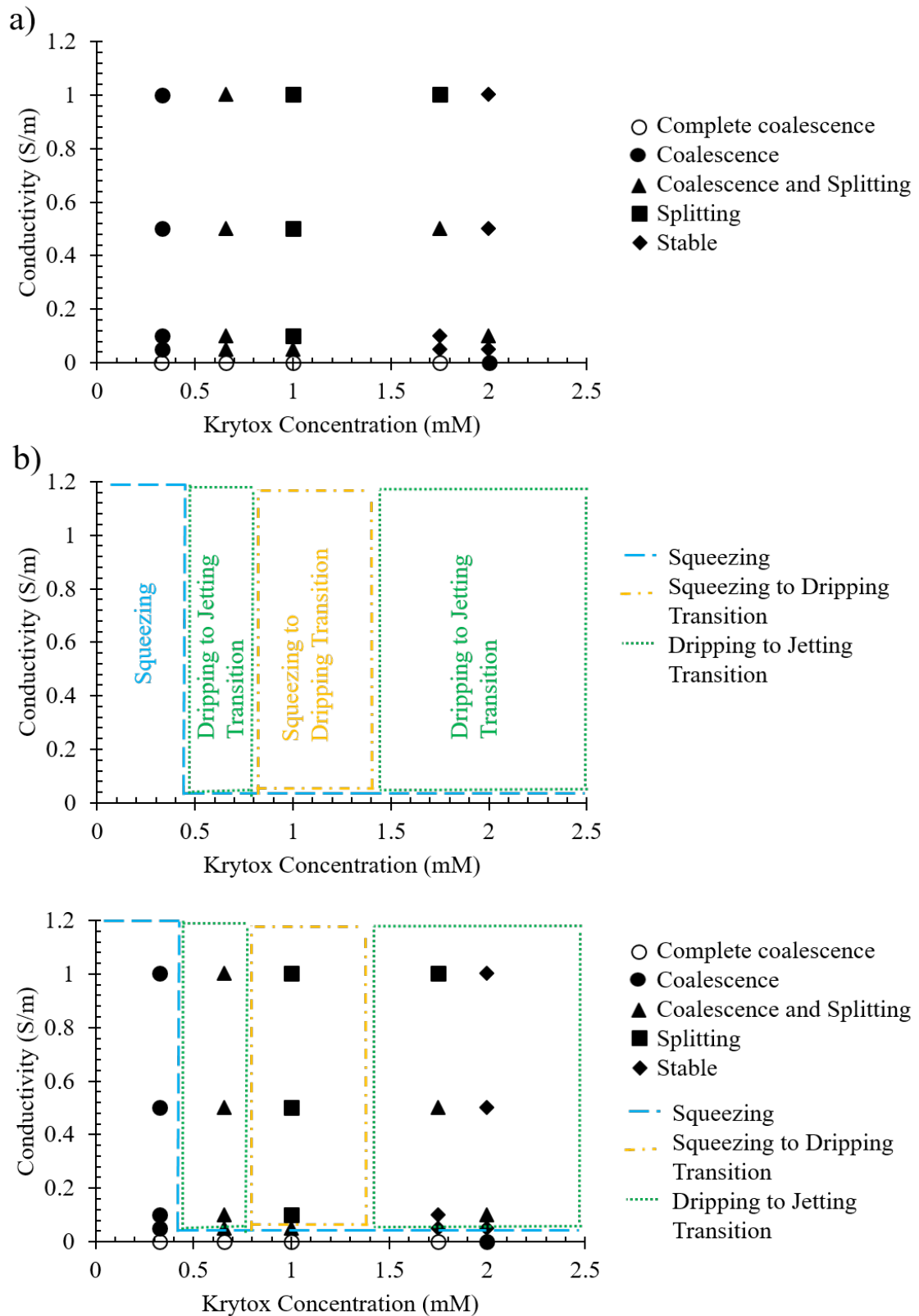
Figure 6-9. a) Stability, b) generation regime, and c) combined stability and generation regime diagrams for the conductivity aqueous phases. The combination of salt and dextrose in the isotonic PBS conductivity solutions affected both the generation regimes and stability in a combined interfacial tension reduction.

statistically larger than the epure-water control, except the 0.1 S/m whose standard deviation slight overlapped with the standard deviation of the epure water, as shown in Figure 6.8. For Krytox concentrations of 0.66, 1, and 2 mM, the presence of the salt and dextrose together showed a statistical decreased the temperature adjusted droplet size when compared to the control. 1.75 mM Krytox also showed a decrease in droplet size when compared to the epure water control, which was statistically different for all but the 1.0 S/m conductivity solution. Overall, the conductivity solutions followed the expected natural log trend of decreasing droplet size with increasing surfactant concentration, with R^2 values ranging from 0.6695 to 8876. Similar to the epure water control, the lower R^2 values are attributed to an unexplained deviation at 1.75 mM Krytox.

The combined presence of salt and dextrose to make isotonic solutions of various conductivity resulted in different generation regimes at different Krytox concentrations. At 0.33 mM, squeezing and was observed. As the Krytox concentration increased, the generation regime shifted to a mixture of dripping and jetting (0.66 mM Krytox), then a mixture of squeezing and dripping (1 mM Krytox), and finally back to a mixture of
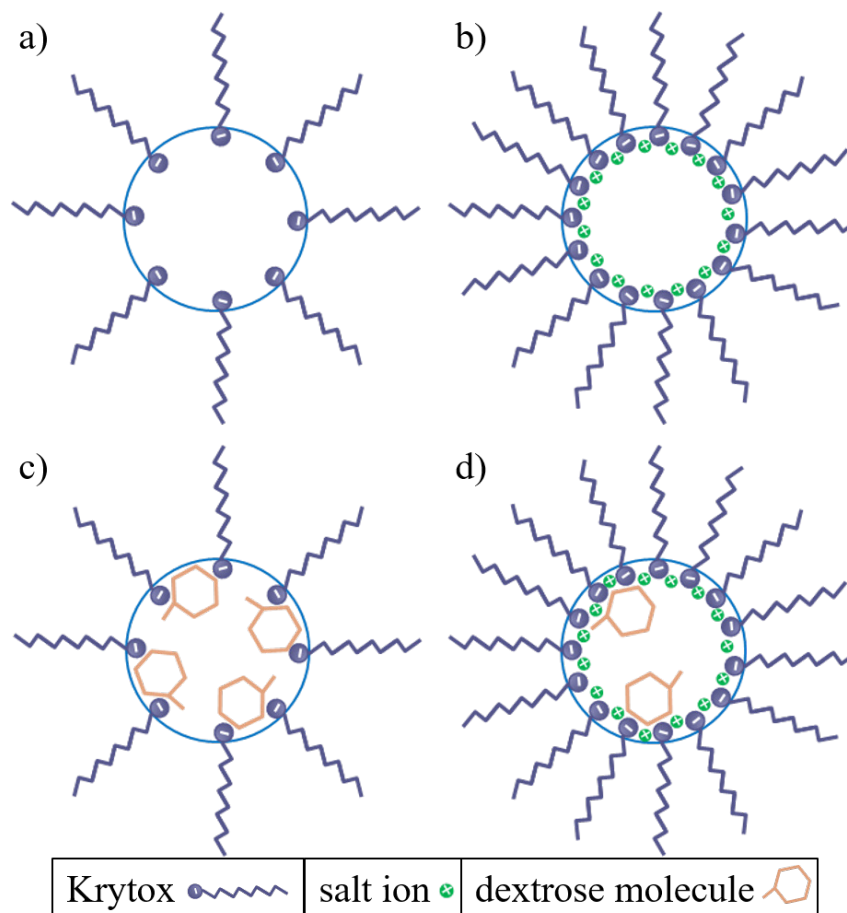
Figure 6-10. Cartooned molecular diagrams (not to scale) of possible mechanisms for a) surfactant only, b) surfactant and salt, c) surfactant and dextrose, and d) surfactant, salt, and dextrose.

dripping and jetting (1.75 and 2 mM Krytox). Partial coalescence was observed at 0.33 mM Krytox, and a mixture of coalescence and splitting at 0.66 mM Krytox. At 1 mM Krytox, a mixture of coalescence and splitting, was observed with the 0.05 S/m solution and partial splitting was observed for the 0.1, 0.5, and 1.0 S/m solutions. At 1.75 and 2 mM Krytox, a mixture of coalescence and splitting, partial splitting, and stable droplets were observed.

The coefficient of variance of droplet diameter decreased compared to the epure water control for 45% of the conductivity experiments. The overall trend of decreasing CV with increasing surfactant concentration held true for all conductivity solutions. Unexpectedly, CV was more favorable for salt-only and dextrose-only experiments than for the conductivity solutions further suggesting transport and molecular interactions are more variable in the more complex conductivity system. 72% of the CVs fell within the 2-10% range seen in literature. However, 88% of the CVs fell in the 2-10% range for Krytox concentrations of 1 mM and higher.

These behaviors suggest salt and dextrose interact with the Krytox to decrease the interfacial tension compared to epure water. When in contact with water, a hydrogen ion from the Krytox molecule dissociates into the water. The salts in the aqueous phase also dissociate into positive and negative ions. The dissociated ions from both the Krytox and the salt would form a layer of ions along the interface, stabilizing the interface against coalescence. When dextrose is dissolved in water, hydrogen bonds form between the hydroxyl groups on the dextrose molecules and the water molecules. The observable effect from the dextrose suggested that the dissolved molecules directly interacted with the surfactant and salt ions at the interface, as depicted in Figure 6.10d. ***The combination of salt and dextrose in the isotonic conductivity solutions affected the droplet size at generation, the generation regime, and the droplet stability entering the chamber in a combined interfacial tension reduction.***

6.4 Conclusions

To design a solution system for droplet microfluidics that was simultaneously biocompatible, isotonic, and variable conductivity, the effects of multiple additives in a droplet microfluidic system were investigated. Shifts in droplet generation regime, droplet stability, and droplet monodispersity were observed and quantified when additives, both individual and combined, were present in the aqueous phase. Surfactant concentration effects were consistent with the expected natural log trend, with R^2 values ranging from 0.6848 to 0.9988, which agreed with the combination of the Gibbs Isotherm and Laplace Pressure, which assumes a dilute system and constant pressure difference.

Controls were conducted with only epure water for the aqueous phase; droplets were not stable and complete coalescence was consistently observed. This indicated that Krytox alone was unable to effectively stabilize the interface to prevent coalescence in an epure water/FC-40 system. However, the simple addition of salt to the aqueous phase aided in stabilizing the interfacial surfactant distribution by reducing the interfacial tension,

resulting in zero experiments with complete coalescence; partial coalescence and splitting, along with some perfectly stable droplets, were observed. Availability of ions likely decreased the repulsion between Krytox's carboxylic head groups via a thin Debye layer of positive counterions. This ionic charge stabilization would have enabled closer packing of the surfactant molecules at the interface. Droplet behaviors upon entering the chamber also supported improved droplet stability as coalescence, splitting, and stable droplets were observed for different concentrations.

Separately, the addition of dextrose also reduced the interfacial tension and improved droplet stability at higher concentrations. However, complete droplet coalescence upon entering the chamber was observed for all of the dextrose-only experiments. At lower surfactant concentrations, the dextrose had the opposite effect of increasing the interfacial tension resulting in increased droplet size. The effect of the dextrose may be an indication that the surfactant molecules adsorb onto the dextrose. The combination of salt and dextrose to form an isotonic solution resulted in a combination of effects. This suggested interactions at the interface between the surfactant and the salt/dextrose additives played a key role in realized surface tension and stability. This work provided a map of droplet size, stability, and reproducibility along with regime tracking of coalescence and splitting to aid in engineering a stable bio-and electro-compatible droplet microfluidic platform.

The combination of salt and dextrose in the isotonic PBS conductivity solutions affected both the generation regimes and stability in a combined interfacial tension reduction. The fact that both the salt and dextrose affected the size and stability of the droplets is important for a wide range of biological applications. In biological and electrical applications, liquid-liquid, liquid-solid, and liquid-gaseous interfaces are common, and surfactants are ubiquitously employed to maintain the stability of droplets while in contact with other phases. This work provides a starting point to predetermining surfactants that can maintain stability and droplet size while altering aqueous phase composition can lead to more comparable and reproducible droplets for cellular and electrokinetic applications.

6.5 Supplementary Material

See Appendix A for supplementary material including complete tables of amounts of additives used along with their corresponding droplet size data, and a complete table of coefficients of variance for each combination.

7 Introduction to a New, Novel Dielectrophoretic Technique, Reverse Insulator Dielectrophoresis (riDEP)

This work will be submitted to *Biomicrofluidics* or similar.

7.1 Introduction

This work explored the development of a new dielectrophoretic technique for multiplexing/parallel experimentation of cells or particles that utilized droplets in microfluidic channels to shape non-uniform electric fields. Dielectrophoresis (DEP) employs alternating current (AC) or insulator-shaped direct current (DC) fields to manipulate polarizable particles or cells [34, 199]. Classical dielectrophoretic theory predicts particle behavior based on the particle's polarizability relative to the medium's polarizability [34, 199]. Therefore, **ion distributions within the medium surrounding particles/cells are of paramount importance to the particle/cell's response in a DEP field**. Particle polarizations transition with each half cycle of the AC field. When particles polarize more readily than the surrounding medium, current flux lines are drawn into and through particles [250]. Charges within the particle realign to induce a particle dipole aligned <u>with</u> the field [251]. In a similar half cycle with particles less polarizable than the medium, field lines will diverge around the less polarizable particles creating ion depletion at the particle poles inducing a dipole aligned <u>against</u> the applied field [251]. These induced dipoles reverse orientation as the sinusoidal AC waveform switches polarity in the next half cycle [281]. The dipoles cause the particle to experience a translational force yielding particle motion within the non-uniform electric field.

In a <u>uniform</u> field with a symmetric AC waveform, induced polarizations average out over time such that no net electrical forces act on the particles and no particle motion is observed [34]. When multiple particles are in close proximity, their induced dipoles interact, and particle pearl chains form along field lines [131, 252-258]. <u>Non-uniform</u> fields elicit a skewed charge dipole in polarizable particles. Due to the electric field gradients, current flux lines through and around particles are not uniformly spaced [34, 199] inducing dipoles that are not equal and opposite in each half cycle. A net polarization forms, based upon the particle's volume and effective polarizability, causing a dielectrophoretic force, F_{DEP}, either toward regions of high field density or low field density [34, 199]. Clausius and Mossotti developed a frequency (ω) dependent factor, K(ω), [261, 262] that dynamically reflects a perfectly spherical, homogeneous particle's polarizability in a conductive medium. Equation 7.1 shows the ratio of complex permittivities, ε, for the particle, p, and medium, m, of the form $\tilde{\varepsilon} = \varepsilon - i\sigma/\omega$, where ω is frequency and σ is electrical conductivity, that makes up the Clausius-Mossotti factor [34, 199, 250, 262, 263].

$$K(\omega) = \frac{\tilde{\varepsilon}_p - \tilde{\varepsilon}_m}{\tilde{\varepsilon}_p + 2\tilde{\varepsilon}_m} \qquad\qquad 7.1$$

The complex quantity K(ω) has an imaginary component out of phase with the applied electric field while the real component is in phase [264]. The imaginary component manifests as a particle torque in electrorotation measurements [139, 140, 282-286]. The DEP force is dependent on the in-phase, or real component of the Clausius-Mossotti factor, which estimates the particle's induced dipole or effective polarizability in non-uniform electric fields [265]. Equation 7.2 is the dielectrophoretic force expression, which is time-dependent due to K(ω)'s dependency on frequency, with particle volume expressed via radius, r:

$$\langle \bar{F}_{dep}(t) \rangle = 2\pi\varepsilon_m r^3 Re[K(\omega)]\nabla|\bar{E}_{rms}|^2 \qquad 7.2$$

F_{DEP} is also dependent upon the electric field gradient squared, $\nabla\bar{E}_{rms}^2$, which means significant forces can be exerted on particles at relatively low voltages [199]. This DEP force pushes particles toward regions of high electric field or low field depending on
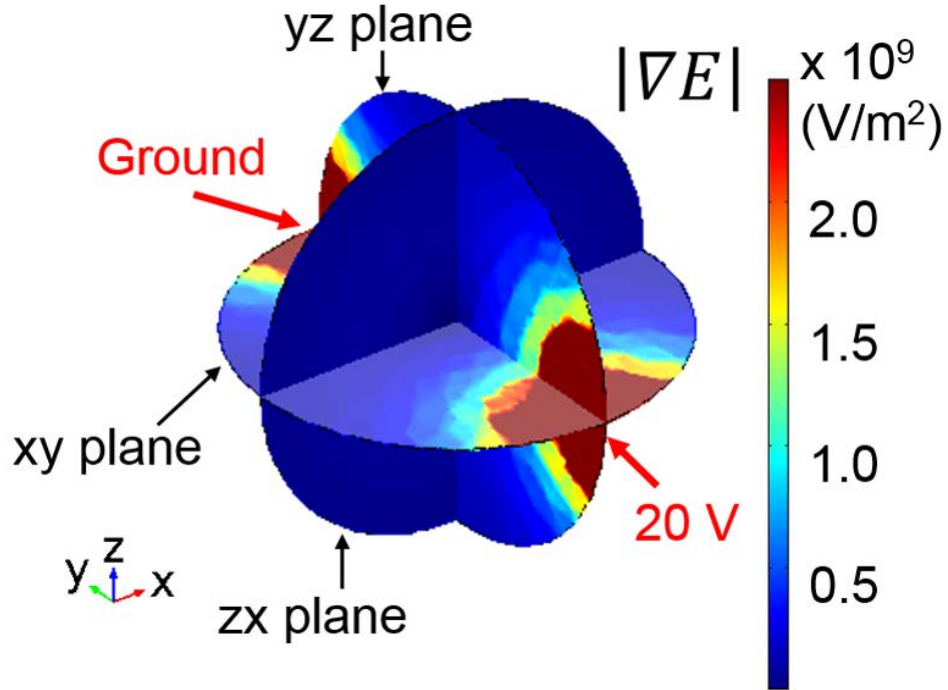
Figure 7-1. Electric field gradient (color map slices) within a 1 S/m aqueous 100 μm diameter droplet surrounded by 10-8 S/m oil. A 20 V DC potential is applied from one pole and grounded on the opposite pole. The electric field gradient is greatest at the poles (dark red on color map, where particles/cells move to during pDEP) and smallest in the middle (dark blue on color map, where particles/cells move to during nDEP). This illustrates the formation of a non-uniform electric field shaped by the droplet interface. For each plane, the view is perpendicular to that plane.

whether the real portion of the Clausius-Mossotti factor, $Re[K(\omega)]$, is positive or negative. When the particle is more polarizable than the medium, $Re[K(\omega)]$ is positive and the resulting dipole moment causes a force toward high electrical field regions, a phenomenon described as positive DEP (pDEP) and signified in red regions at the poles in Figure 7.1. When a particle is less polarizable than the medium, $Re[K(\omega)]$ is negative and negative DEP (nDEP) pushes the particle toward regions of low field density [34] as indicated by blue regions in Figure 7.1.

When translating homogeneous particle theory into the much more complex cellular dielectrophoretic theory, cell structure and composition directly correlate with the electrical properties influencing cell polarization. Effective polarizability is dependent on cell permittivity and conductivity through cellular components; cell membranes impact the ability of charges to penetrate the cell while intracellular proteins and cytosol molecules impact charges conducted through the cell [34, 128, 159, 199, 266, 267]. This work employs ideal spherical particles for demonstration and verification purposes, but is primarily focused on exploring the complex interactions of medium and cell polarizations within aqueous droplets.

This work introduces for the first time a new twist on insulator dielectrophoresis where the aqueous-in-oil droplets shape the electric field, replacing and advancing beyond static insulator geometries. A challenge when combining dielectrophoresis with droplet generation is that electric fields can impact the droplet interface itself. Electric fields have been used to control production, transport, deformation, fission, and fusion of droplets within microdevices [28, 29, 35, 37, 218]. Droplet deformation has been noted in uniform and non-uniform electric fields [218]. Electrocoalescence occurs when the electric field destabilizes the thin film between droplets and has been shown to depend on the materials present in the two phases [85] [11, 219, 220]. With increased conductivity, there is enhanced dielectrophoretic attraction between droplets and larger electric stress at the droplet interfaces [220]. Phase diagrams exist for droplet coalescence in a static fluid and AC fields as a function of frequency [6, 220]. Literature targeting droplet coalescence has illustrated that there is potential to achieve electric field effects within the droplets without destabilizing the droplet interface [6, 11, 219, 220].

Polystyrene bead and human red blood cell (RBC) dielectrophoretic responses were used to explore the novel riDEP technique described herein. Before adding complex particles/cells into a system, many researchers benchmark new dielectrophoretic devices using polystyrene beads [103-109]. Polystyrene beads are highly uniform, behave ideally in many systems, and can be synthesized in various sizes. This work focused on polystyrene beads ranging from 6.0 to 7.9 μm in size, with an average size of 6.78 μm, for comparison to RBCs (6-8 μm). RBC dielectrophoretic characterizations have been extensively studied in traditional spatially non-uniform microdevices. RBC membranes [112-120] are essentially non-conducting ($\sigma \leq 1$ μS/m) [121-125], vary from 50 nm to 90 nm thick depend,ing on exerted force [114], and are the reason RBCs are dielectrics – materials of low electrical conductivity [34, 123]. In contrast, RBC interiors are conductive ($\sigma = 0.53$ to 0.31 S/m) [125-127] and vary with cytosol composition such as

hemoglobin and cytoplasm molecules [125, 128, 129]. Biconcave RBCs range from 6 to 8 μm in transverse diameter with 0.5 μm (center) to 2 μm (edge) variations in thickness; shapes vary dynamically in response to solvent conditions, pH, tonicity, and temperature [127]. Blood cell molecule expression on the membrane varies by the person; classification is dominated by ABO-Rh type based on antigen polysaccharides expressed on the membrane surface and plasma antibodies (A+, B+, AB+, O+, A-, B- AB-, and O-) [112, 113]. Type designations dominate blood transfusions and blood product therapies for cancer and sickle cell disease.

Prior research in this research group, μM.D.-ERL has 1) experimentally quantified the DEP response of all ABO-Rh blood types (example in Figure 7.2), 2) definitively determined through selective antigen removal, the role of ABO antigens in dielectrophoretic polarizations, and 3) mapped out blood type membrane instabilities and rupturing for subsequent subcellular analysis. First efforts quantified RBC responses in a batch DEP device [36, 130, 131] where electric field non-uniformities were accomplished via electrode position. Then insulator DEP blood cell deflection at a microfluidic bifurcation was interrogated in a continuous DEP device where electric field non-uniformities were accomplished with a static insulator structure protruding into the flow channel [132]. ABO-Rh expression was shown to shift DEP spectral profiles including the cross-over frequencies (COF), which is the transitional point of zero cell motion between movement up the electric field gradient (pDEP) to movement down the electric field gradient (nDEP) or vice versa (see horizontal line in Figure 7.2). Results further revealed enzymatic removal of the ABO membrane antigens yielded a uniform DEP response consistent with a baseline RBC polarization [159]. Systematic experiments and automated intensity analysis revealed that ABO-Rh expression correlates to the cell DEP
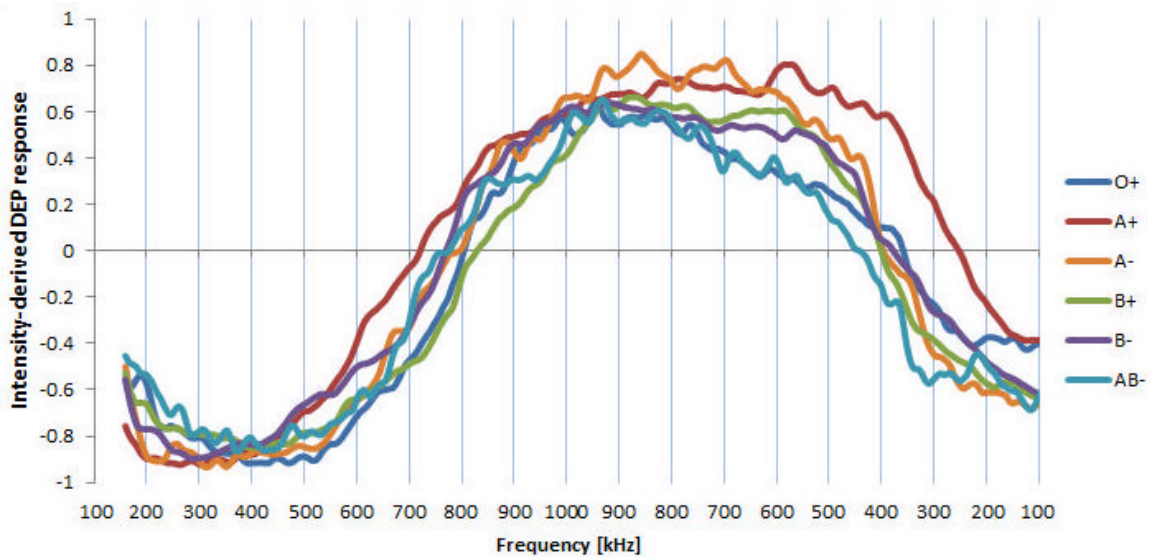
Figure 7-2. Dielectric spectra of O+, A+, A-, B+, B- and AB- red blood cells in 0.1 S/m subjected to a 2.5 Vpp AC signal swept from 0.1 to 1 MHz and back to 0.1 MHz. This demonstrates the subtleties of RBC DEP responses by ABO antigen expression. Data collection and graphic credit: Hector Moncada Hernandez

81

frequency spectra. Experiments were completed batch-wise (Figure 7.2) consuming five years of resources and person-hours. Studies outlined herein could enable multiplexed riDEP experiments yielding the same data in ~80 hrs. This work utilized the previous RBC typing database to compare and ascertain the reliability and reproducibility of reverse-insulator dielectrophoresis.

In summary, dielectrophoresis has not previously been demonstrated <u>within</u> droplets. This work builds upon dielectrophoresis demonstrated <u>around</u> an oil interface protruding into an aqueous channel [287], which adds credence to this work exploring aqueous/oil interfaces shaping electric fields. Current DEP techniques have been limited to a single media condition for each experiment. The novel riDEP technique outlined herein applied knowledge from the field of droplet microfluidics into the field of electrokinetics to create stable microenvironments for multiplexed dielectrophoretic characterizations. Multiple dependencies, including surfactant concentration in the oil phase, conductivity of the aqueous phase, voltage, and frequency, were investigated.

7.2 Materials and Methods

7.2.1 Chemical Reagents, Particles, and Cell Preparation

Aqueous-in-oil droplets, seeded with particles, were generated in a microfluidic T-junction using custom fabricated PDMS devices. The continuous oil phases were 0.33, 0.66, 1, 1.75, or 2 mM Krytox FSH 157 (Dupont, Wilmington, DE), a perfluoropolyether carboxylic acid, dispersed in FC-40 (3M, Maplewood, MN), a biocompatible fluorinated oil. The dispersed aqueous phases were solutions comprised of epure water, a salt stock (containing 1.1696 grams NaCl, 2.7223 grams KH_2PO_4, and 3.4961 grams K_2HPO_4), and dextrose (Sigma Aldrich, St. Louis, MO). Conductivities of 0.0000055 S/m (epure water), 0.05 S/m, 0.1 S/m, 0.5 S/m, and 1.0 S/m were used for this project. The isotonic solutions were phosphate buffer saline (PBS) solutions combined with dextrose. Concentrations and amounts combined for each isotonic solution are presented in Table 7.1 along with their respective conductivities.

A single continuous and dispersed phase combination was employed for the exploratory dielectrophoresis experiments. 1 mM Krytox in FC-40 was used as the continuous phase and 0.1 S/m PBS and dextrose seeded with particles or cells was used as the dispersed phase. One milliliter of the 0.1 S/m PBS and dextrose solution was combined with 10 microliters of either packed human red blood cells to yield ~1% concentration by volume. Human blood was collected from a healthy donor by a phlebotomist into EDTA Becton Dickinson vacutainers, following IRB approved protocols. The red blood cells were separated from the blood volume by centrifugation at 132 relative centrifugal force (rcf) for 10 minutes. All blood handling was completed in a biosafety level II facility using approved protocols and stored at 5ºC between experiments.

Table 7-1. Amounts of each component in each aqueous phase solution

Control Solution	Epure Water (ml)	Salt Stock (µl)	Dextrose (g)
Epure water	20.000	0.0	0.0000
0.960 mM	24.976	24.0	0.0000
2.616 mM	24.935	65.4	0.0000
13.892 mM	24.653	347.2	0.0000
24.122 mM	24.397	603.0	0.0000
Dextrose-only Solutions	Epure Water (ml)	Salt Stock (µl)	Dextrose (g)
58.837 mM	25.000	0.0	0.2650
161.108 mM	25.000	0.0	0.7256
273.845 mM	25.000	0.0	1.2334
290.404 mM	25.000	0.0	1.3080
Conductivity Solution	Epure Water (ml)	Salt Stock (µl)	Dextrose (g)
0.05 S/m	24.976	24.0	1.3080
0.1 S/m	24.935	65.4	1.2334
0.5 S/m	24.653	347.2	0.7256
1.0 S/m	24.397	603.0	0.2650

7.2.2 Microfluidic Device

The microfluidic device contained the following geometric parameters; a 50 µm wide dispersed phase channel joined a 100 µm wide continuous phase channel, both 70 µm tall and 3.5 mm in length arranged into a perpendicular T-junction. The continuous phase channel continued past the junction for 11 mm before opening, at a pitch of 35°, into a 1500 µm wide and 5000 µm long chamber. The device was fabricated to be 70 µm in height via soft-lithography with SU-8 photoresist (MicroChem, Westborough, MA). The SU-8 features were cast with PDMS and bonded to a glass microscope slide immediately after oxygen plasma treatment. 50 micron platinum wire (99% pure, Goodfellow, Coraopolis, PA) electrodes were positioned on either side of the 1500 µm wide microfluidic chamber. 360-micron holes were punched in all four corners in the microfluidic chamber. The 50 µm platinum wire was pulled through the holes to form two parallel electrodes. Uncured PDMS was placed at the top of each hole to make a watertight seal. The PDMS with the electrodes were cleaned with Scotch tape® and bonded to a glass slide as described in Section 3.1.2.

To connect the platinum electrodes to an external electric field source (AC generator, Agilent, Santa Clara, CA) silver conductive epoxy (MGChemicals, Surrey, B.C., Canada) was used to bond copper wires to the platinum wires as shown in Figure 3.2. The copper wires (22 GA Gauge AWG 2, local hardware store) were connected to alligator clips attached to the ground and potential; the copper wires provided a stronger connection than the fragile platinum wire alone. The silver conductive epoxy was a two-part mixture that was combined and well mixed in equal proportions. The epoxy was placed around

the copper wire on the seed layer. The microdevice was then placed in the oven at 70°C overnight to allow the epoxy to cure.

7.2.3 Experimental Set-up

Before beginning experiments, two pretreatment steps were completed to facilitate smooth dispersed and continuous phase flow through the microfluidic device. The first step was to ensure hydrophobic channels (detailed in Appendix A). Rain-X® (ITW Global Brands, Houston, TX), a commercially available glass water repellent, was flushed through the microdevice and kept at room temperature until the Rain-X® solution evaporated. A second step was completed ensured that the surfactant within the oil solutions was in equilibrium with the solid-liquid interface at the channel walls. This was accomplished by filling the device with the continuous oil phase and surfactant Krytox FSH 157 solution then allowing it to sit for ~one hour before experiments started.

Both the aqueous and oil solutions were withdrawn into 3 mL syringes (Becton Dickinson, Franklin Lakes, NJ). The syringes were connected to the microdevice via 360 micron polyether ether ketone (PEEK) tubing (Labsmith) and T-connectors. The microdevice was fixed onto the stage of a SVM340 synchronized video microscope (Labsmith, Livermore, CA) via tape to prevent movement during experiments. Once turned on, the brightness, contrast, and focus of the microscope were adjusted to the ideal settings for observing/recording the experiments at 4x or 10x magnification. The solutions were then infused through the PEEK tubing into the microdevice via a Harvard Apparatus syringe pump (Harvard Apparatus, Holliston, MA) 0.25 µl/min for 10 minutes to allow the system to reach steady state before beginning experiments. Due to device clogging issues, some experiments were completed by applying pressure to the dispersed phase syringe by hand.

For the dielectrophoretic experiments, droplets were either allowed to flow through the microchamber while the electric field was applied (continuous configuration) or flow was halted such that the droplets were stationary when the electric field was applied (batch). For continuous experiments, the syringe pump delivered a constant flow rate. For batch experiments, pressure was adjusted by hand to bring the droplets to a stop within the chamber. For the dielectrophoretic experiments, an AC generator was used to apply an electric field across the chamber. The applied potential was either a DC or AC and ranged from 1 to 10 volts. For AC experiments, the applied frequency ranged from 100 to 1000 kHz. The experimental setup can be seen in Figure 3.3.

7.2.4 Data Collection and Analysis

Experiments were observed and recorded using the UScope software (Labsmith). The collected data was then analyzed using ImageJ, a free image analysis program from the National Institute of Health [226]. Electric field stability was analyzed by observing and documenting droplet coalescence. For each conductivity and surfactant concentration, the voltage was slowly increased (at least 1 minute at each voltage) until droplet coalescence

was observed. For the dielectrophoresis experiments, a single voltage (DC) or voltage and frequency (AC) was applied and videos were recorded. Particles and cells were imaged within the droplets and tracked over time within the dielectrophoretic fields.

7.3 Results and Discussion

7.3.1 Droplet Stability within an Applied Electric Field

The voltage at which electrocoalescence began to be observed was recorded as a function of dispersed phase conductivity, continuous phase surfactant concentration, and frequency, as shown in Figure 7.3. For multiple conditions, no electrocoalescence was observed, and is indicated as a voltage of >10 in Figure 7.3. At the lowest two conductivities, 0.05 S/m and 0.1, there was a general trend of decreasing voltage needed for coalescence with an increase in surfactant concentration, with the highest surfactant concentration yielded stable droplets up to 7 Vpp for 0.05 S/m and 5 Vpp for 0.1 S/m.
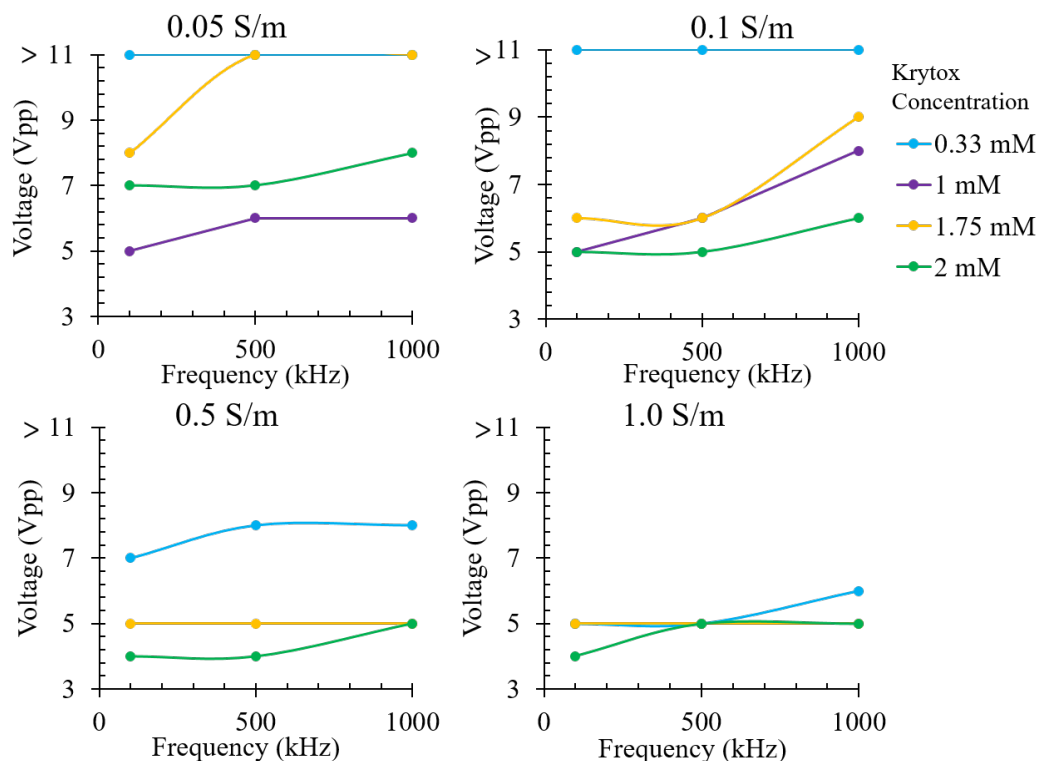
Figure 7-3. Voltage, as a function of frequency (x-axis) and surfactant concentration (different color data markers) in the continuous oil phase, that caused electrocoalescence for a) 1.0 S/m, b) 0.5 S/m, c) 0.1 S/m, and d) 0.05 S/m conductivity PBS and dextrose solutions as the dispersed aqueous phase. Data points at >11V indicate that for the full range of voltages (1-10 Vpp) no electrocoalescence was observed. The applied voltage needed for electrocoalescence decreased with increasing dispersed phase conductivity, increased frequency, and decreased surfactant concentration.

The 1 mM surfactant concentration did not fit this general trend due to the increased temperature (72→79ºF) and humidity (22→58%) during the experiments. The relative surfactant trend was consistent for the 0.5 S/m conductivity solution, however, electrocoalescence voltages are roughly half those at 0.1 S/m. At the highest conductivity of 1.0 S/m, electrocoalescence occurred predominantly at 5 Vpp with minor variations to 4 or 6 Vpp at the highest surfactant and lowest surfactant concentration, respectively.

In summary, the voltage that caused electrocoalescence increased with increasing frequency. Increased dispersed phase conductivity decreased the voltage needed for electrocoalescence. Both of these trends are consistent with literature [219, 220]. In addition, a third trend of decreased voltage required with increased continuous phase surfactant concentration was observed. These results are a foundational map of conditions feasible for dielectrophoretic characterizations within droplets since droplet stability is a necessary condition for any subsequent analysis.

7.3.2 Polystyrene beads

A completed electric circuit was verified as previously described, then the chamber was packed with 6 µm polystyrene bead-seeded aqueous droplets 100 to 300 µm in diameter. Note that this preliminary data was completed before stability experiment optimization, so the droplets are polydisperse and some coalesced resulting in less uniform DEP behavior, which is consistent with the 2D COMSOL simulation results discussed in Chapter 5, Section 5.3. As shown in Figure 7.4, pearl chain formation occurred indicating DEP forces acting upon the polystyrene beads within the droplets. This chaining as well as the translation to the center of the droplet indicates negative dielectrophoresis, which is consistent with theory predictions of polystyrene beads in low conductivity (0.055 µS/m)
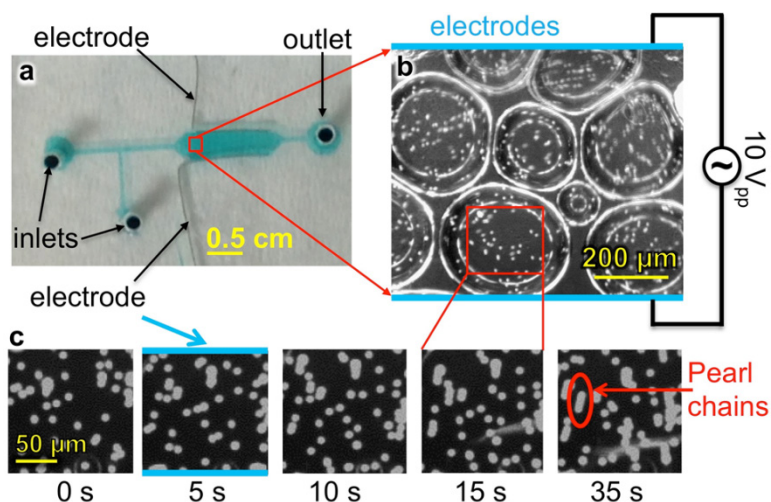
Figure 7-4. (a) Platinum wire electrodes (100 µm) were sealed between PDMS and glass slide, then used to apply a 10 Vpp, 100 kHz electric field across the chamber of 1 S/m aqueous droplets in 10-8 S/m silicon oil. (b) Image of 6 µm polystyrene particles in 200 µm droplets. (c) Images of particle pearl chain formation along electric field lines.

water. These all show the feasibility of riDEP as a new and powerful characterization technique.

7.3.3 Red Blood Cells

Human red blood cells were seeded into the 0.1 S/m PBS and dextrose solution and droplets were generated using the 1 mM Krytox in FC-40 solution since this surfactant range yielded the most stable droplets in the electrocoalescence screening experiments. The first set of experiments completed were conducted in a continuous flowing stream where the droplets migrated through the chamber. The aqueous and oil phases were steadily pumped at 0.25 µl/min to generate droplets packed within the chamber. A 4 Vpp and 100 kHz or 1 MHz frequency electric field was applied across the chamber as the
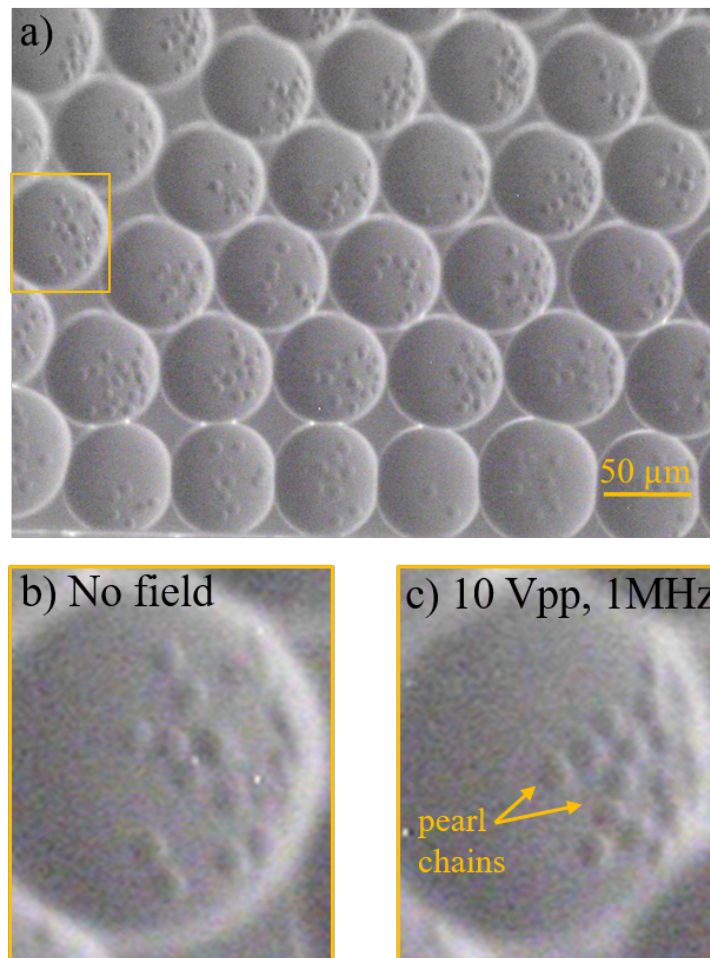
Figure 7-5. a) Red blood cells seeded into 0.1 S/m PBS and dextrose solution and packed within a microfluidic chamber. Successful droplet packing was observed. RBCs are shifted to the right from droplet generation due to the lower viscosity within the droplets. b) Before and c) after application of a 10 Vpp, 1 MHz electric field. Pearl chaining and movement toward high electric field gradient areas indicate a dielectrophoretic response.

droplets flowed through. The RBCs demonstrated a very weak DEP response which was visually observable in the form of pearl chain formation near the equator of the droplet. However qualitative analysis was challenging due to the motion of the droplets through the chamber. Thus, batch experiments were conducted.

Droplets were formed by using the syringe pump or by hand and the flow of droplets through the chamber was halted by applying pressure to the inlets/outlets by hand. Droplets were successfully generated, packed, and stopped within the chamber as shown by Figure 7.5a. The microscope was set to 10x magnification to more easily identify the RBCs within the droplets. As shown in Figure 7.5a, the cells within the droplet were affected by the droplet movement and are all shifted toward the right side of the droplets. Figure 7.5b contains stills from a video showing the RBCs before and 2 minutes after applying the electric field (10 Vpp and 1 MHz). The RBCs show a weak positive dielectrophoretic response, indicated by the pearl chaining and the slight movement towards high electric field gradient areas at the droplet poles closest to adjacent droplets.

These results, although preliminary in nature, demonstrate that utilizing the non-uniform electric fields within droplets can induce cell polarization. In short, these preliminary results provide evidence that riDEP is feasible.

7.4 Conclusions

Conceptually envisioned reverse insulator dielectrophoresis, riDEP, was investigated by 1) mapping out droplet stability in electric fields from 1-10 Vpp and 100-1000 kHz, 2) observing the response of 6 um PS particles in solutions with conductivities ranging from 0.055 µS/m to 1.0 S/m and 3) interrogating RBCs dispersed into droplets under similar solution and electrical conditions.

Droplet stability in an applied electric field was a function of dispersed phase conductivity, continuous phase surfactant concentration, frequency, and voltage. The results of this work start building a map of the operating windows possible for riDEP.

PS particle DEP responses were observed and demonstrated pearl chaining as well as the translation to the center of the droplet indicating negative dielectrophoresis, which is consistent with theory predictions of polystyrene beads in low conductivity (0.055 µS/m) water.

RBC interrogations demonstrated slow dielectrophoretic responses. This indicates that the electric field was shaped by the droplet interfaces, however the voltage drop within the droplets is likely weak. One plausible explanation is that the droplet to droplet interface functions as an electrical barrier that interferes with potential bridging between the droplets.

This challenge can be approached in the following manner: 1) interrogate additional particle types, polystyrene beads (of various sizes) and human red blood cells, based on

their known dielectrophoretic properties and predictability because both the electric properties and the size of the particles affect the DEP response, 2) test multiple media conductivities, from 0.05 to 1.0 S/m because the media conductivity has a large impact on dielectrophoretic response, 3) use a range of frequencies, from 100 to 1000 kHz because, based on the media conditions and particles, the frequency determines the direction of the dielectrophoretic response, 4) explore both AC and DC electrical fields because non-uniform fields are necessary to elicit DEP responses but AC frequencies are not essential, and 5) test both static and flow systems to investigate the possibility of both batch and continuous testing.

8 Electrical and Chemical Characterizations of Hafnium (IV) Oxide Films for Biological Lab-on-a-Chip Devices

Reverse insulator dielectrophoresis uses immiscible phases to shape a non-uniform electric field. Because there is a layer of oil between the electrodes and the aqueous sample phase, the samples are isolated/protected from the electrodes. For applications where droplet microfluidics is not advantageous, but preventing unwanted sample-electrode interaction is, an additional method of isolating/protecting samples from electrodes was also investigated. Hafnium oxide was used as a passivation layer to physically isolate the samples from the electrodes while allowing electric field penetration through the passivation into the sample. This investigation was a collaborative effort and has been published in Thin Solid Films. J. Collins was lead author. The contributing authors on this work included H. Moncada Hernandez, S. Habibi, C.E. Kendrick, Z. Wang, N. Bihari, P.L. Bergstrom, and A.R. Minerick.

Abstract: Many biological lab-on-a-chip applications require electrical and optical manipulation as well as detection of cells and biomolecules. This provides an intriguing challenge to design robust microdevices that resist adverse electrochemical side reactions yet achieve optical transparency. Physical isolation of biological samples from microelectrodes can prevent contamination, electrode fouling, and electrochemical byproducts; thus this manuscript explores hafnium oxide (HfO_2) films - originating from traditional transistor applications – for suitability in electrokinetic microfluidic devices for biological applications. HfO_2 films with deposition times of 6.5, 13, and 20 minutes were sputter deposited onto silicon and glass substrates. The structural, optical, and electrical properties of the HfO_2 films were investigated using atomic force microscopy (AFM), X-ray diffraction, energy dispersive X-ray spectroscopy, Fourier transform infrared spectroscopy, ellipsometry, and capacitance voltage. Electric potential simulations of the HfO_2 films and a biocompatibility study provided additional insights. Film grain size after corrosive Piranha treatment was observed via AFM. The crystalline structure investigated via X-ray diffraction revealed all films exhibited the (111) characteristic peak with thicker films exhibiting multiple peaks indicative of anisotropic structures. Energy dispersive X-ray spectroscopy via field emission scanning electron microscopy and Fourier transform infrared spectroscopy both corroborated the atomic ratio of the films as HfO_2. Ellipsometry data from Si yielded thicknesses of 58, 127, and 239 nm and confirmed refractive index and extinction coefficients within the normal range for HfO_2; glass data yielded unreliable thickness verifications due to film and substrate transparency. Capacitance-voltage results produced an average dielectric constant of 20.32, and the simulations showed that HfO_2 dielectric characteristics were sufficient to electrically passivate planar microelectrodes. HfO_2 biocompatibility was determined with human red blood cells by quantifying the hemolytic potential of the HfO_2 films. Overall results support hafnium oxide as a viable passivation material for biological lab-on-a-chip applications.

8.1 Introduction

8.1.1 Electrode Isolation in Lab-on-a-Chip Technology

Lab-on-a-chip (LOC) technologies and applications are continually expanding with an emphasis on electrical manipulations for chemical/biological detection. LOCs are prevalent in point-of-care clinical diagnostics due to the small sample and reagent volumes, cost effectiveness, rapid analyses, high sensitivity/selectivity, and potential for disposable devices [288]. For electric field utilization, electrode miniaturization improves sensitivity and device footprint [204]. However, electrode behaviors and subsequent solution characteristics are closely intertwined [289, 290]. Aqueous experimental samples in contact with electrodes can lead to electrode fouling [202, 291]. For example, platinum microelectrodes showed both morphological and chemical changes when exposed to biological buffer solutions in both AC and DC electric fields. These changes included oxidation and dissolution of platinum along with potassium deposition and chloride formation originating from buffer solutions [292]. Electrodes in contact with aqueous experimental samples can generate pH changes, target analyte interferences, and other byproducts. While electrode byproducts are sometimes harnessed for beneficial LOC functions: electrochemical impedance can detect foodborne pathogens [293], enzyme-catalyzed reactions can detect multiple metabolic biomarkers [294], and amperometric flow injection analysis can sense cholesterol [83], this is not uniformly desired.

Creative strategies to achieve electrode and target sample isolation include remote positioning of electrodes, membrane isolation, and passivation layers. In dielectrophoretic applications, insulating structures within channels replace embedded microelectrodes and effectively shape non-uniform electric fields (insulator dielectrophoresis) [132, 196, 202]. Membranes isolate electrode wells from LOC channels preventing unwanted electrode/solution effects, such as electrolysis bubbles [295]. A key approach is to apply dielectric thin film coatings over planar electrode surfaces as passivation layers to reduce ion production, Faradaic reactions, and electrode surface fouling [51, 289, 292, 296]. In electrowetting on dielectric (EWOD) devices, a dielectric layer is deposited on top of the electrodes to energize droplet motion across surfaces without causing solution interferences [273]. Some LOC applications desire complete electrical passivation from the fluidics [297]. In cell culturing, sensing windows monitored spreading kinetics via impedance while the remaining electrode region was passivated to isolate cells and reduce the risk of contamination from and reaction with electrode surfaces [297]. Thus, passivation layers over electrodes are a viable and growing method to selectively isolate electrodes from samples and preventing unwanted electrochemical byproducts.

8.1.2 Choosing a Passivation Layer

In electronics, high dielectric constant passivation in capacitors, resistors, and transistors improves performance during miniaturization. This knowledge can be translated into LOC applications bridging electronics and fluidics. The most common high dielectric constant shielding material is silicon dioxide (SiO_2). At thicknesses less than 1.5 nm, SiO_2 has physical and electrical limitations that manifest in a leakage current [298, 299]. While leakage current is desired in some LOC applications, aqueous electrolyte solutions required for many biological applications can cause alkali ion contamination in the SiO_2 leading to undesirable device instability [300]. Common SiO_2 replacements include HfO_2, Si_3N_4, La_2O_3, Al_2O_3, ZrO_2, TiO_2, HfSiO, CeO_2, and $LaAlO_3$ [299-301]. Dielectric constants for these materials range from 3.9 for SiO_2 to 80 for TiO_2; the material explored here, HfO_2, is 20-25 [302].

In LOC devices, passivation materials must withstand mechanical/chemical stresses and not interfere with electric field characteristics or detection schemas at fluidic interfaces [303]. Passivation layer characteristics frequently assessed are dielectric strength and biocompatibility, along with mechanical, chemical, thermal, and charge stability [304], and are tailored to the application. LOC passivation materials have included Teflon, Parylene C, polydimethylsiloxane, polyimide, silicon dioxide, silicon nitride, SU-8, dry-film, and others [273, 303-306].

Biological LOCs require films with optical transparency and biocompatibility. Optical transparency within LOCs enables optical detection techniques such as absorbance, reflectance, fluorescence, and chemiluminescence, among others [307]. Common biocompatible passivation materials include cover glass, photoresist, epoxy, polyimide, SiO_2, and Si_3N_4 [297]. However, these materials display undesirable refractive properties, limited optical transparency, and/or non-ideal electrical passivation characteristics. HfO_2 stability in aqueous solutions and biomolecule functionalization was demonstrated [300]. Thus, this work investigated hafnium (IV) oxide as a biocompatible passivation layer for biological LOCs due to its relatively high dielectric constant [302] and optically transparency [308].

8.1.3 Hafnium Oxide (HfO_2)

Advantageous properties of hafnium oxide (HfO_2) include its chemical stability, high dielectric constant (20-25), wide band gap (5.8 eV), conduction band offset (1.4 eV), optical transparency from 300 to 10,000 nm in the electromagnetic spectrum, and refractive index (~2) based on deposition conditions [302, 308-310]. These properties prompted HfO_2 use in gate oxide in metal–oxide–semiconductor field-effect transistors (MOSFET) [298, 299, 308-315] whereby SiO_2 is unsuitable due to scaling limitations [299]. Other common HfO_2 uses include optical coatings [299, 309, 310, 313],

optoelectronics [299, 308, 310], and ceramics [308, 310]. This substantial foundation of electrical and optical knowledge is advantageous to build upon for LOC applications.

Hafnium oxide's utilization for biological applications is increasing, especially within nanopore and nanowire structures. HfO_2 increased the sensitivity of silicon-based multi-nanowires for DNA and protein detection due to its chemical stability, pH sensitivity, high dielectric constant, hydrophilicity, and isoelectric point of 7 [300, 316-319]. HfO_2 demonstrated stability within an aqueous electrolyte environment and was successfully functionalized with biotin biomolecule probes when used as a gate dielectric for charge based biosensors [300]. Hafnium oxide pH responses (51.0-55.8 mV/pH) [320] were comparable to other Si nanowire, Al_2O_3/SiO_2 pH sensors (54.9-60.2 mV/pH) [321] when investigated for ion sensitive field effect transistors (ISFET) and MOSFETs. Table 8.1 summarizes biological applications that utilized HfO_2 along with deposition methods, characterization methods, and substrates. In this paper, fabrication and multi-dimensional characterizations of HfO_2 films needed for LOC technologies are presented with a particular emphasis on concurrent optical and electrokinetic cell characterizations.

Table 8-1: Hafnium oxide in biological applications

Ref.	Deposition Method	HfO_2 (nm)	Substrate	Application	Characterization Methods
[300]	ALD	~2.8, 45	Si (100) Prime grade 1-10 Ωcm	Charged based biosensors	SE, AFM, CV, XPS
[320]	ALD	13	Si-NW on Si-O-I p-type doped	Small nucleic acid oligomer detection	SE, AFM, SEM, CV, FLIC
[316, 317]	ALD	2-7	Si/SiO$_2$/SiN$_x$	DNA transport through nanopores and Protein analysis	AFM, CV, EDS, TEM
[318]	ALD	10	Si-NW on Si-O-I	Cardiac troponin 1 detection (biosensor)	TEM
[319]	ALD	16	Graphene/TiO$_2$ and Si, p-type, highly doped	Nanopores for biosensing	FFT, Contact angle, IV, Leakage current, TEM

8.1.4 Deposition and Characterization of Hafnium Oxide (HfO₂)

Optical and electrical properties of HfO_2 are affected by crystallography, microstructure, integral stoichiometry, binding states, morphology, contamination, and defect density

[309], making HfO$_2$ deposition important. For very thin films, industry typically uses atomic layer deposition (ALD) [298]. Other deposition methods include organic vapor deposition [322], metal-organic vapor deposition [298], electron-beam evaporation, reactive vacuum evaporation [313], and a variety of sputtering techniques [299, 301, 308-310, 314]. Herein, RF sputtering was used for all HfO$_2$ film depositions.

Table 8-2: Non-sputter deposition techniques and HfO$_2$ characterization

Ref.	Deposition Method	HfO$_2$ (nm)	Substrate	Deposition Parameters	Characterization Methods
[319]	ALD	16	Graphene/TiO$_2$ and Si, p-type, highly doped	Annealing temperature (none, 500-700 °C)	FFT, Contact angle, IV, Leakage current, TEM
[298]	ALD MO-CVD	<7	Si and Si covered with SiO$_2$	Study of possibilities and limitations of near UV-visible range SE	*SE,* AR-XPS, RBS
[322]	MO-CVD	4	Si, p-type	Estimation of dielectric density	*SE,* XRR
[313]	Reactive vacuum evap.	~75-170	Si, single-crystal	Deposition temperature (40-280 °C)	*SE, AFM, XRD*

Deposition parameters affecting HfO$_2$ film properties include temperature, pressure, voltage, plasma composition, and annealing [299, 301, 313]. Tables 8.2 and 8.3 contain the deposition methods, characterization methods, and substrates used to determine HfO$_2$ characteristics/quality for non-sputter (Table 8.2) and sputter deposition techniques (Table 8.3). Characterization methods include spectroscopic ellipsometry (SE), scanning electron microscopy (SEM), and Fourier transform infrared spectroscopy (FTIR) for thickness; atomic force microscopy (AFM), X-ray diffraction (XRD), energy dispersive X-ray spectroscopy (EDS), X-ray photoelectron spectroscopy (XPS), and X-ray reflectometry (XRR), for structural properties; SE, FTIR, and ultraviolet-visible spectroscopy (UV-VIS) for optical properties; and SE, capacitance-voltage (CV), and current-voltage (IV) for electrical properties, among others including grazing incidence X-ray diffraction (GIXRD), angle-resolved X-ray photoelectron spectroscopy (AR-XPS), Rutherford backscattering spectroscopy (RBS), Doppler broadening spectroscopy (DBS), transmission electron microscopy (TEM), fast Fourier transform (FFT), and fluorescence interference contrast (FLIC).

To expand knowledge of HfO$_2$ performance for biological LOC technologies, this work explored HfO$_2$ deposition and characterization for isolating electrodes from aqueous,

Table 8-3: Sputter deposition parameters and HfO$_2$ characterization

Ref.	HfO$_2$ (nm)	Deposition	Substrate	O$_2$ and Ar Flow	RF (W)	T (°C)	BP (Pa) DP (Pa)	DT (min)	CM
[a, b]	78, 156, 240	RF	SSP DSP Glass	4 SCCM O$_2$ 18 SCCM Ar	700	Room	2.7x10^{-4} to 4.0x10^{-4} 0.93-1.02	6.5, 13, 20	*AFM, XRD,* EDS-FESEM, *FTIR, SE, CV*
[312] [b]	67.6, 86.3, 104, 128.9	RF magnetron	Si (001) 2-5 Ω/cm Quartz	20 SCCM Ar	50, 60, 70, 80	Room	>2.0 x 10^{-4} 0.35	120	*AFM, XRD, FTIR,* UV-Vis, *SE*
[299] [c]	33.19 to 35.38	RF magnetron	Si (100) p-type 4-7 Ω/cm	-	-	-	1.5 x 10^{-3} 2.2	7	*AFM, FTIR,* IV, *SE, CV*
[301] [d]	7.8 to 71.6	RF magnetron	Si (100) p-type 1-10 Ωcm	5, 10, 15 ml/min O$_2$	100, 300, 500	-	- 0.4, 0.8, 1.2	2, 5, 10	*AFM, XRD,* IV, RBS, *CV*
[308] [b]	40	RF magnetron	Si (100)	12 SCCM O$_2$ 28 SCCM Ar	100	Room to 700	1.3 x 10^{-3} -	-	GIXRD, XRR, *SE*
[309] [b]	-	Magnetron	Si (100) n-type	30 SCCM total O$_2$/(O$_2$+Ar) ratio (0.07, 0.26, 0.59)	25, 45, 100	-	2.0 x 10^{-3} 0.7, 1.0, 4.0	-	*XRD,* DBS, *SE*
[310] [b]	~95 to 155	RF magnetron (reactive)	Si (100)	0, 0.1, 0.2, 0.3, 0.4 O$_2$/(Ar+O$_2$)	100	300	1.3 x 10^{-3} -	45	*XRD,* SEM, *SE*
[311] [b,e]	7.3	DC magnetron	Si (100) p-type 7-17 Ωcm	12 SCCM O$_2$ 30 SCCM Ar	30	200	<2.7 x 10^{-3} 5.9 x 10^{-2}	5	*XRD, FTIR,* XPS, *SE*
[314] [b,f]	-	Reactive w/ pulsed DC power	Si	10 SCCM O$_2$ 28.3 SCCM Ar	42	-	2 x 10^{-3} 1	60	DBS, XRR, *SE*

[a] This paper   T=Temperature, BP=Base Pressure, DP=Deposition Temperature, DT=Deposition Time, CM=Characterization Methods
[b] Papers that reported the target used: all ≥99.9% hafnium oxide or hafnium metal target   [c] Annealing temp. 350, 550, 750 °C
[d] Annealing temp. 300, 600, 900 °C   [e] Study of SiO$_x$ formation at HfO$_2$/Si interface   [f] 40 kHz pulse, 70% duty factor, study of atomic O$_2$ treatment

biological samples. Three HfO_2 thicknesses were sputter deposited on both opaque silicon and transparent glass substrates. HfO_2 characterizations included AFM, XRD, energy dispersive X-ray spectroscopy field emission scanning electron microscopy (EDS-FESEM), and FTIR characterizations for structural properties; SE for thickness and optical properties; and SE, CV, and simulations for electrical properties. In addition, this study explored HfO_2 biocompatibility with cells. These results have implications in biological LOC devices that use optical measurement methods concurrent with electrode isolation.

8.2 Materials & Methods

8.2.1 Hafnium Oxide Deposition

Hafnium oxide thin films were deposited on four types of substrates: 500 µm thick (100) oriented single side polished (SSP) and 500 µm thick double side polished (DSP) 10 Ω-cm resistivity silicon wafers, 75x25x1±0.1 mm soda lime glass microscope slides, and 500 µm thick Borofloat 33 borosilicate glass wafers (UniversityWafer.com). The latter two were optically transparent and utilized for many LOC devices [4]. HfO_2 RF sputter deposition (Perkin-Elmer 2400-8J, Waltham, MA) progressed at room temperature with an RF power of 700 W, a 99.95% pure hafnium target (Kurt J. Lesker, Jefferson Hills, PA), and base and operating pressures of $2.7x10^{-4}$ to $4.0x10^{-4}$ Pa and 0.93-1.02 Pa, respectively. Film stoichiometry was maintained using 4 SCCM O_2 and 18 SCCM Ar and was characterized in Section 3.3. Films were treated as HfO_x until film stoichiometry was confirmed. Depositions ran for 6.5, 13, and 20 minutes with an average deposition rate of 12 nm/min, as determined by ellipsometry calibration of HfO_2 deposited on silicon. For each deposition time, Si and glass substrates were sputtered together to enable direct comparisons.

Surface cleaning processes used in LOC fabrication were compared in Section 3.1 by cleaving HfO_2 coated substrates into three pieces: as-deposited control, oxygen plasma treatment, and Piranha treatment. The oxygen plasma treatment was performed via RIE at $3.2x10^4$ Pa for 40 seconds (Jupiter II, March Instruments, Concord, CA). The Piranha treatment was performed by soaking substrates in Piranha solution, a strong corrosive oxidizing agent prepared by mixing 12N H_2SO_4 and 30% H_2O_2 (1:1 v/v) (Sigma Aldrich, St. Louis, MO), for 5 minutes, rinsing with deionized water, and drying with nitrogen gas.

8.2.2 Hafnium Oxide Characterization

8.2.2.1 Atomic Force Microscopy

Structural properties and morphology of the HfO_2 films were examined on both DSP silicon and soda lime glass substrates, with pre- and post-oxygen plasma and Piranha

treatments. A Veeco Dim 3000 atomic force microscope (Plainview, NY) in tapping mode at 1 Hz was utilized to scan areas of 5x5 μm^2 with a resolution of 103 pixels per micron. Nanoscope V530 software collected data and measured surface roughness. Grain size analysis was conducted with Image-J software (NIH, https://imagej.nih.gov/ij/). The minimum and maximum pixel area threshold sizes were systematically adjusted on the B&W images to identify both grains and grain agglomerates from the background, 100 to 1000 pixels squared and 100 to infinity pixels squared, respectively. Data was compiled and compared across treatments, substrates, and film thicknesses. The size of the grains, along with roughness and surface morphology revealed film growth conditions and the impact of oxygen plasma and Piranha treatments.

8.2.2.2 X-Ray Diffraction

Because the film crystal structure and size can affect the film's optical and electric properties, the bulk morphology of the deposited HfO_2 was further explored with XRD for different deposition times on SSP silicon and soda lime glass substrates. XRD was used in a glancing angle mode to obtain crystalline structure as a function of film thickness. A 2θ scan was performed from 18-67.98°, using a 2000 W Cu target X-ray tube on a Scintag XDS-2000 θ/θ powder diffractometer (CA, USA). The X-ray tube utilized Cu Kα1 radiation (wavelength: 1.540562 Å) and a tungsten filament. The step scan mode was used with a scan rate of 0.003 deg/min. The Scherrer equation was employed to relate crystallite size in the deposited films to the broadening of a peak in the diffraction pattern. The mean size of the crystallites (τ) was calculated using $\tau = K\lambda/\beta cos\theta$, with K as a dimensionless shape factor, λ as the X-ray wavelength, β as half the maximum intensity in radians, and θ as the Bragg angle. The dimensionless shape factor utilized was 0.9, because values range from 0.86 to 0.94 depending on crystallite's circular to cubic shape, respectively [323]. The Cu tube on the system yielded an X-ray wavelength of 0.154056 nm, which is the characteristic wavelength for K-alpha radiation [324].

8.2.2.3 Energy Dispersive X-Ray Spectroscopy and Fourier Transform Infrared Spectroscopy

Film thickness, morphology, and composition were measured via field emission scanning electron microscopy (FE-SEM, Hitachi S-4700, Tarrytown, NY) at 20 keV and 200k magnification. A sputtered carbon coating on the HfO_2 films prevented charging to obtain higher quality images. Morphology comparisons were made between AFM and SEM. To gain insights to compliment morphology and crystalline structure, the film composition was analyzed via SEM-EDS and FTIR. Films on DSP silicon and soda lime glass were analyzed with deposition times of 13 and 20 minutes, respectively. In addition, the 20-minute deposition on DSP silicon was scanned, and a thickness comparison was made between the SEM and ellipsometry results. To achieve a cross-sectional analysis and thus discern thickness, the HfO_2 coated silicon wafer was cleaved and mounted on a holder

perpendicular to the electron beam. EDS composition was compared to FTIR by scanning the DSP silicon film (Genesis II, Mattson Instruments, Madison, WI) from 400-4000 cm^{-1}. Silicon background peaks were removed. SEM-EDS and FTIR both corroborated stoichiometric HfO2.

8.2.2.4 Spectroscopic Ellipsometry

Thickness and optical characterizations were completed via spectroscopic ellipsometry for all deposition times and substrates. Each film was scanned across 400 to 1000 nm wavelengths at angles of 65°, 70°, and 75° to measure the ellipsometric parameters psi (ψ) and delta (Δ) (JA Woollam V-VASE, Lincoln, NE). Material models were fitted to the collected data, and a regression analysis was used to find the mean square error (MSE). Minimizing the MSE was the criteria used to select optimal material models. The films were modeled as Lorentz-Tauc Oscillators, which considered the bandgap [325] and included a 10 nm SiO2 layer. The model required surface roughness which was obtained via AFM, presented in Section 3.1. The WVASE32 software used ψ and Δ models to predict film thickness, refractive index, and extinction coefficient, from which the optical properties of the deposited films were assessed.

8.2.2.5 Capacitance-Voltage

Capacitance-voltage measurements were used to extract the film dielectric constant. Experiments were conducted using a series of 1000-2000 µm circles that had an Al/HfO2 (6.5-minute deposition)/Al configuration, as shown in Figure 9.5. A HfO2 film was sputtered on an Al (100 nm) coated SiO2/Si wafer, with a portion protected with a glass slide to allow for probing to the underlying Al film, followed by a 100 nm Al film deposited through a shadow mask. The shadow mask had 1000, 1500, and 2000 µm diameter circles. Due to the step change, the thickness of the Al and HfO2 films were measured with a 3D profilometer (Filmetrics Profilm3D, San Diego, CA). CV measurements were collected using an HP 4284A Precision LCR Meter (Agilent, Santa Clara, CA) by connecting to the underlying and top Al films. Capacitance values were converted to the dielectric constant using $C = A(\kappa/d)$, with C as the measured capacitance, A as the area of the capacitor (e.g., each respective circle), κ as the dielectric constant of the insulator, and d as the separation of the two Al films.

8.2.2.6 Simulations

Along with the determination of the dielectric constant of the HfO2 films, COMSOL Multiphysics (Burlington, MA, USA) simulation software was used to model HfO2 electrical isolation of the electrodes from the fluidic layer. Electric potential distributions in a 2D geometry were obtained by solving Laplace's equation using the Lagrange element method. The 2D model geometry, shown in Figure 9.6a, consisted of a 200 x 40 µm substrate, two 20 x 0.15 µm Au electrodes (excitation and ground), the HfO2 passivation with targeted thicknesses (0.078, 0.156, and 0.240 µm) over the substrate and

electrodes, in contact with a 200 x 70 μm chamber filled with 0.1 S/m phosphate buffer saline (PBS) fluidic layer. Material properties utilized are shown in Table 8.4. Boundary conditions were *Electric Potential* (5 V) from the Au excitation electrode, *Ground* at the Au ground electrode, and *Electrical Insulation* at all outer boundaries. To evaluate the electric potential distribution, the simulated was run between 10 Hz and 10 MHz with a mesh consisting of elements ranging from 0.004 to 2 μm.

Table 8-4. Material properties and parameters employed for electric potential simulations.

Material	Relative ε	σ [S/m]
Borosilicate glass	4.5	1×10^{-15}
Silicon	11.7	0
Hafnium Oxide	20.32*	1×10^{-16}
Water	80	0.1

*Value obtained from CV measurements, section 8.3.5

8.2.2.7 Biocompatibility

In addition to physical, optical, and electrical properties, the deposited film biocompatibility was investigated. Healthy red blood cells (RBCs) were contacted with HfO$_2$ films, and the extent of hemolysis was determined by measuring the absorbance of free hemoglobin according to standards by Xiong et al. [326, 327]. Whole blood was drawn from a healthy, anonymous consenting donor via IRB approved protocols into ethylenediaminetetraacetic acid (EDTA) Becton Dickinson vacutainers (MTU IRB M0540[318164-11]). Blood was centrifuged at 132 relative centrifugal force (rcf) for 10 minutes to separate into platelet-rich plasma, white blood cells, and packed RBCs. Packed RBCs were re-suspended and diluted in sterile, isotonic 0.9 w/v% NaCl to a 1:100 ratio for the hemolysis assay. A 4" borosilicate glass wafer coated with HfO$_2$ was diced into 20 x 20 mm pieces and separately submerged into 50 mL tubes containing the 1:100 RBC suspension, then incubated at 37° C for 1, 3, and 5 hours. A negative control of the 1:100 RBC suspension was conducted without HfO$_2$. A positive control (100% lysis expected) was conducted with the 1:100 RBC suspension incubated with 1 w/v% Triton X-100 and without HfO$_2$. All conditions were concurrently conducted in triplicate. After incubation, RBC suspensions were centrifuged at 1075 rcf for 10 minutes and the supernatant collected. Free hemoglobin absorbance readings were obtained via UV/Vis spectrophotometry (Genesis 10 UV Scanning, Thermo Fisher Scientific, Waltham, MA) at 380, 415, and 450 nm, corresponding to the hemoglobin peaks [326]. A 0.9 w/v% NaCl blank control was measured to calculate the corrected absorbance of free hemoglobin (*Ab$_{free\ hemoglobin}$*) (Equation 8.1) and percent hemolysis was obtained relative to the 100% hemolysis positive control to compare across exposure conditions (Equation 8.2). Materials were deemed biocompatible if hemolysis was negligible [326].

$$Ab_{free\ hemoglobin} = 2 \times A_{415} - (A_{380} + A_{450}) \qquad (8.1)$$

$$\% \ hemolysis = \frac{Ab_{free\ hemoglobin}\ of\ test\ sample}{Ab_{free\ hemoblobin}\ of\ positive\ control} \times 100\% \qquad (8.2)$$

8.3 Results & Discussion

Diverse characterization techniques were utilized to investigate the effectiveness of hafnium oxide properties as a passivation layer for biological LOC devices. Morphology/crystallinity was measured and compared via AFM and XRD. Composition was measured and compared via SEM-EDS and FTIR. FTIR results were also used to determine potential optical interferences from HfO_2. Measurements, except FTIR, were compared between crystalline silicon and amorphous glass substrates. Film thickness was measured via ellipsometry and SEM. Ellipsometry also provided optical properties including refractive index and extinction coefficient. Dielectric constant measurements were completed via CV. COMSOL simulations utilized these properties to explore the electrical passivation capabilities of the HfO_2 films. In addition to the physical, optical, and electrical properties, HfO_2 film biocompatibility was studied via hemolysis.

8.3.1 Atomic Force Microscopy

Surface morphology of the deposited HfO_2 was studied via AFM. Topographical images for three HfO_2 film thicknesses are shown in Figure 8.1, organized by columns to
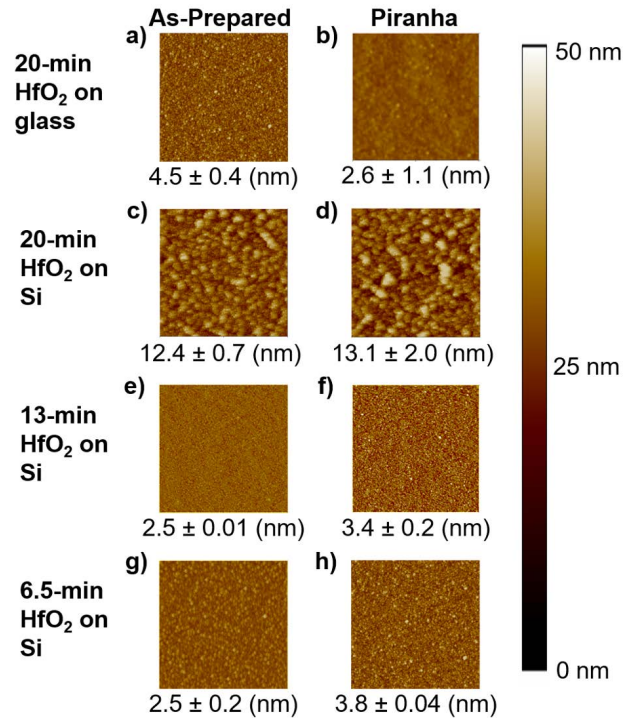
Figure 8-1. AFM images of three different HfO_2 thicknesses deposited on soda lime glass (a-b) and DSP silicon (c-h) substrates before and after a 5-minute Piranha treatment. The substrate utilized effected grain size with the thickest, 20-minute deposition films on glass showing comparable grain size to that of the thinner films on silicon. Piranha treatment changed surface roughness of the 20-minute deposition on glass, but not of the 20-minute deposition on silicon.

compare as-prepared films to piranha-treated films with rows organized to allow comparisons between DSP silicon and soda lime glass substrates as well as film thickness. Oxygen plasma and piranha treatments were employed to ascertain the impact of an oxidizing agent on film surface morphology. The oxygen plasma treatment showed no discernible change and thus is not shown. Piranha treatment smoothed the glass/HfO$_2$ surfaces as shown in Figure 8.1a and b, but no significant changes were observed for Si/HfO$_2$ surfaces with different thicknesses.

For the 20 minute HfO$_2$ depositions, roughness (RMS) on the silicon substrate was 12.4±0.7 nm as compared to 4.5±0.4 nm on the glass. Comparable literature values for RMS roughness increased from 5 to 12 nm for 13-minute depositions on silicon films with increasing substrate temperatures from 25°C to 120°C [328]. Generally, as the grain size increased, the roughness increased. Figure 8.1c, e, and g illustrate that as the HfO$_2$ thickness increased on silicon, agglomeration at the grain boundaries occurred. Such grain agglomeration could be due to temperature effects during HfO$_2$ deposition [329-331] because, with longer deposition times, the substrate heated up due to free energy losses in the system. Interestingly, the grain size of the thinnest, 6.5 and 13-minute, HfO$_2$ films on the molecularly ordered silicon resembled that of the thickest, 20-minute, HfO$_2$ on the molecularly disordered glass. The secondary grain size analysis using Image-J confirmed that the HfO$_2$ molecules organized into smaller grains on glass than on silicon, and demonstrated that there were fewer grain boundaries in the HfO$_2$ film on the silicon.

8.3.2 X-Ray Diffraction

X-ray diffraction was used to expand the grain analysis investigating the crystalline structure of the HfO$_2$ films. Figure 8.2 shows the effect of HfO$_2$ deposition time, and thus thickness, on the XRD pattern for SSP silicon and soda lime glass substrates. All HfO$_2$ films exhibited the characteristic peak for the (111) plane at 28.47°. For the 6.5-minute deposition of HfO$_2$ on silicon, there was a broad peak from 32.22 to 38.91° which suggested a (200) orientation. Narrow peaks at 47.22, 54.56, 55.4, 56.33, and 65.87° were attributed to stray atoms from the energized tungsten filament, which were attracted to the water-cooled copper target and emit tungsten radiation [332].

As the film thickness increased on silicon, more planes were observed. Both the 13 and 20-minute depositions showed peaks (34.21° and 35.7°) corresponding to the (200) plane, and the 20-minute deposition showed an additional peak (50.8°) corresponding to the (220) plane. There was preferred growth along the (111) plane, as demonstrated by the dominance of the (111) peak at 28.47°. The presence of additional peaks for longer depositions showed HfO$_2$ growth along different planes. The thickest layer of HfO$_2$ on glass had a similar result as the thinnest layer of HfO$_2$ on silicon and was consistent with literature [333, 334]. Based on the Scherrer equation, crystallites from the 6.5, 13, and 20-minute HfO2 depositions on silicon were calculated to be 2.9, 2.6, and 4.1 nm while the 20-minute HfO2 deposition on glass was 3.8 nm.
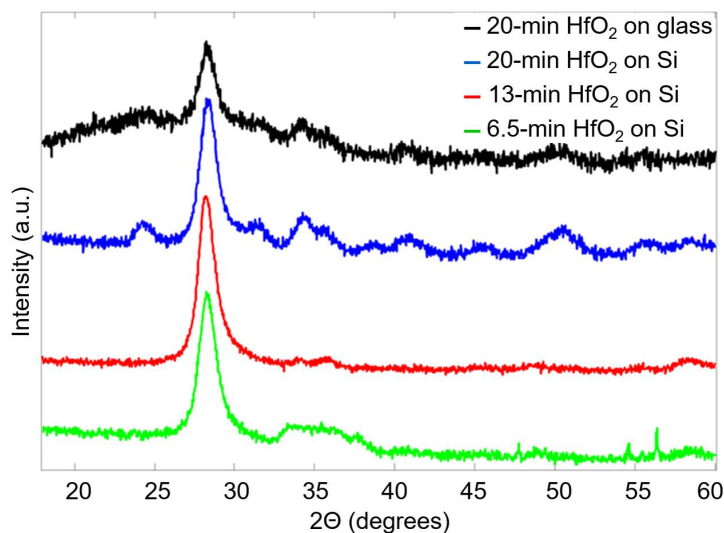
Figure 8-2: XRD pattern for 6.5, 13, and 20-minute depositions on SSP silicon and a 20-minute deposition on soda lime glass. All spectra exhibit the characteristics peak of (111) plane at 28.47°; however, as the thickness of the HfO_2 film increases more peaks appear in the XRD spectra suggesting crystallite growth in multiple planes demonstrating the tendency for HfO_2 to grow along different planes.

HfO_2 roughness and crystallite size differed between glass and silicon. The XRD results for the 20-minute deposition on glass and the 6.5-minute deposition on silicon yielded the same orientation of (111) with roughness and crystallite size 78% and 81% greater on glass than on silicon, respectively. For the same film thickness (20-minute depositions), the roughness was 64% smaller, and the crystallite size was 11% smaller for the glass than the silicon. These results suggested the structured silicon, when compared to the amorphous glass, supported larger HfO_2 crystallite formation. As the film thickness increased, not only did the grain size increase, as demonstrated by the AFM results, but there was also a trend of increasing crystalline domain size.

8.3.3 Energy Dispersive X-ray Spectroscopy and Fourier Transform Infrared Spectroscopy

Once grain size was determined, energy dispersive X-ray spectroscopy was done at both 20 kV and 5 kV to determine the composition of two HfO_2 films: 13 minutes on DSP silicon and 20 minutes on soda lime glass. Figure 8.3a shows the EDS spectra using a 20 kV acceleration voltage that penetrated the HfO_2 film resulting in a small substrate signal; oxygen and hafnium dominated the spectra. For the silicon substrate, oxygen, hafnium, and carbon peaks were apparent; carbon originated from the carbon coating sputtered to enable imaging. For glass, the same oxygen, hafnium, and carbon peaks were observed along with nickel, sodium, calcium, and silicon peaks attributed to the soda-lime glass slide composition [335]. An accelerating voltage of 5 kV was employed to minimize contributions from the substrate; the atomic percent for oxygen and hafnium
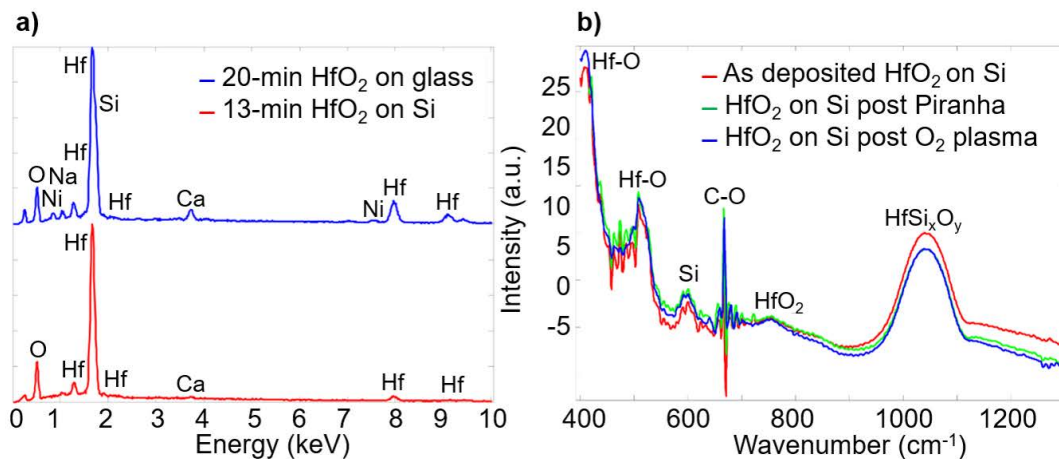
Figure 8-3: a) EDS analysis at 20kV of the 13-minute HfO₂ film on DSP silicon and the 20-minute HfO₂ film on soda lime glass confirming stoichiometric deposition for HfO₂. b) Transmission mode FTIR analysis of the HfO₂ deposited on a 20 Ωcm DSP silicon wafer as prepared and after oxygen plasma and Piranha treatments. FTIR corroborates that the deposited films are stoichiometric HfO₂.

were 66.92% and 33.08%, respectively, confirming that the films were 99% stoichiometric HfO₂ for a penetration depth of ~250 nm. The cross-sectional analysis of the 20-minute deposition showed an HfO₂ layer 180-230 nm thick, on top of a thin layer of SiO₂, as shown in Figure 8.4c.

Films were also scanned using FTIR to investigate composition. No peaks were observed at wavenumbers greater than 1300 cm^{-1}; therefore the data was truncated to 400-1300 cm^{-1} as shown in Figure 8.3b. The sharp peak at 670 cm^{-1} was a C-O chemical bond resulting from measuring in ambient air. The peak at 610 cm^{-1} was due to silicon phonon absorption [336, 337]. The peak at 1050 cm^{-1} was attributed to the Si-HfO₂ interface where a HfSi$_x$O$_y$ composite was formed [311, 337]. Peaks at 748 cm^{-1}, 512 cm^{-1}, and 412 cm^{-1} were related to the HfO₂ film. The first peak was HfO₂, while the latter two were Hf-O chemical bonds [311, 336, 337]. This agreed with the EDS results demonstrating that the deposited films were stoichiometric HfO₂. The peak locations not only indicated composition, but they also inferred that there is optical interference at those wavelengths. This information can inform experimental designs in optical lab-on-a-chip systems to exclude wavelengths with HfO₂ interference.

8.3.4 Spectroscopic Ellipsometry

Spectroscopic ellipsometry measurements included inference of each deposited HfO₂ film thickness from silicon and glass model fits as well as refractive index and extinction coefficient as shown in Figure 8.4 and Table 8.5. Figure 8.4 illustrates a representative experimental data set with an angle 70° and the fitted model for psi (ψ) and delta (Δ) as a function of wavelength for three HfO₂ thicknesses. Glass substrate transparency did not allow standard reflection measurements, instead lower accuracy transmission

measurements were performed. MSE values indicated that glass yielded unreliable data, caused by refractive index similarities between HfO_2 and glass. SE was not the optimal tool for characterizing HfO_2 on glass, and thus glass ellipsometry results are not presented herein. HfO_2 was deposited on glass and silicon in the same chamber run, so thicknesses measured on silicon were inferred for the respective films on glass.

Table 8-5: Ellipsometry results for different HfO_2 deposition times

Deposition time (min)	6.5	13	20
Targeted thickness (nm)	78	156	240
Thickness (nm)	58	127	239
Mean Square Error	0.5411	52	7.727
Refractive Index	2.03±0.02	1.99±0.03	1.82±0.01
Extinction Coefficient	0.002±0.002	0.004±0.004	0.006±0.009

The MSE values for the 6.5 and 20-minute depositions on silicon indicated good model fits [338]. The Cauchy dispersion relationship, which assumed isotropic material, was used as the primary model and the thinnest film followed the trend of previously published data [308]. Model deviations and higher MSE values were obtained for the 13 and 20-minute depositions, suggesting that the increasing thickness increased the anisotropy of the films. This agreed with the XRD results presented in Section 3.2, which also showed HfO_2 anisotropy. A more complex model may be able to account for anisotropy in the thicker deposited HfO_2 films [338, 339] and increase accuracy.
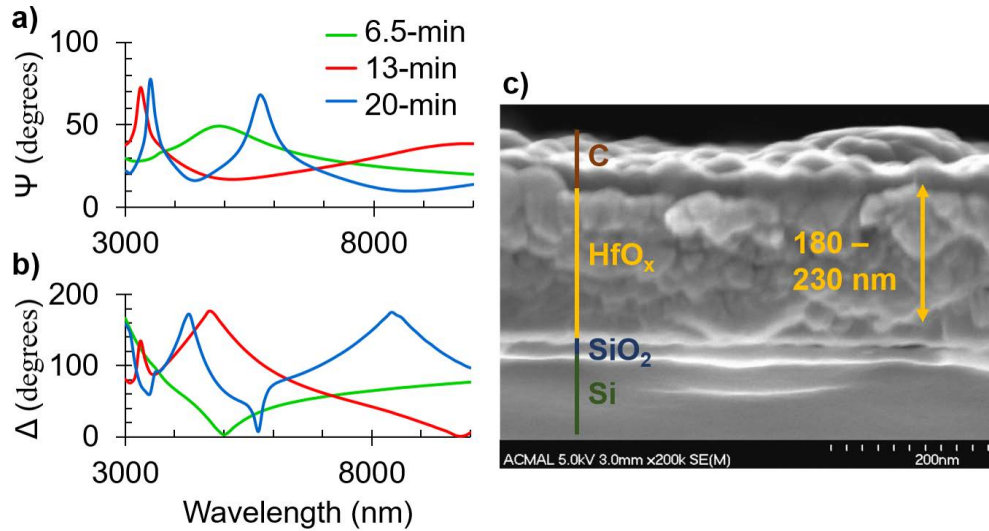
Figure 8-4: Ellipsometry a) psi and b) delta waves for an angle of 70° for HfO_2 measured on silicon for all three deposition times: 6.5, 13, and 20-minutes yielding 58, 127, and 239 nm thicknesses with MSEs of 0.5411, 52, and 7.727, respectively. Measurements were conducted for all three deposition times on silicon and glass and were used to determine thickness, refractive index, and extinction coefficient. (b) Cross-sectional SEM image showing the silicon substrate, SiO_2 interfacial layer, HfO_2 film, and the carbon over layer used for data collection for a 20-minute deposition of HfO_2. Results show a HfO_2 film of 180-230 nm based on the location.

Both the 13 and 20-minute depositions contained a characteristic ψ absorption peak around 3400 nm. The 20-minute deposition contained an addition ψ peak around 5700 nm, which indicated another resonance mode due to the thicker film thickness. The thickness inferred from the ellipsometry model was highly consistent with instrument calibration for the 20-minute deposition. The cross-sectional SEM image in Figure 8.4c illustrates spatial variations in film thickness from 180-230 nm for HfO_2 and 20 nm for SiO_2; this thickness was fairly consistent with the ellipsometry results of 239 nm.

As shown in Table 8.5, SE modeled refractive index (n) for wavelengths from 400 nm to 1000 nm and varied around 2, consistent with literature [308, 313]. Refractive index profiles for each film thickness were not identical as a function of wavelength due to the increasing anisotropy with thickness. Lastly, the extinction coefficient was close to zero, which was expected for a transparent material and was consistent with previously reported data [340].

8.3.5 Capacitance-Voltage

Capacitive measurements were collected at 100 kHz for applied potentials from -5V to 5V. However, due to the thickness, the HfO_2 films could not be fully depleted, and therefore no modulation was observed. Figure 8.5a-d depicts fabrication for the utilized $Al/HfO_2/Al$ configuration. The thicknesses of the Al and HfO_2 films were 100 nm for the Al and 72 nm for the 6.5-minute HfO_2 deposition– fairly consistent with the 78 nm thickness interpolated from the deposition calibration. The dielectric constant was calculated from the measured capacitance, per the equation $C = A(\kappa/d)$, as a function of HfO_2 area as shown in Figure 8.5e. For the 1000-2000 μm diameter circles, the dielectric
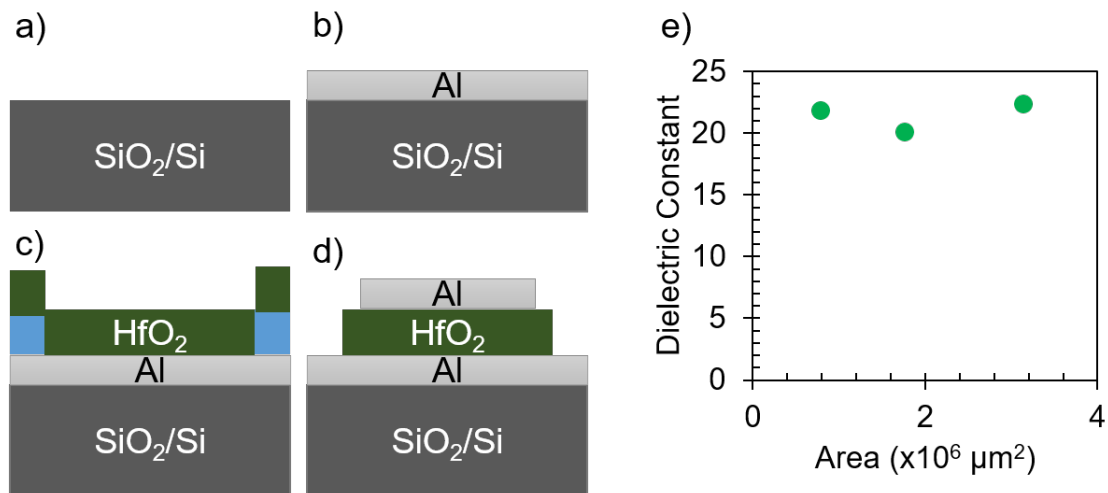
Figure 8-5: a-d) Microfabrication of 1000-2000 μm diameter, sandwiched (100/72/100 nm) $Al/HfO_2/Al$ pattern used for CV measurements. e) Dielectric constant as a function of area for a 6.5-minute HfO_2 deposition. The average dielectric constant of 20.32±1.55 is consistent with literature values for HfO_2.

constant ranged from 17.97 to 23.64, with an average of 20.32±1.55, consistent with 20-25 reported in the literature [302].

8.3.6 Simulations

Once HfO_2 material properties were determined, AC electrostatics simulations were used to investigate the electrical passivation of different thicknesses of HfO_2 over frequencies from 10 to 10000 kHz. Simulations were performed for both silicon and borosilicate glass substrates, but these substrates did not significantly affect dielectric performance (the difference between silicon and glass ranged from 1.172×10^{-5} to 1.179×10^{-3} V) or electric potential profiles. Figure 8.6a shows the 2D geometry modeled over borosilicate comprised of a 20 µm fluidic span between two 20 µm electrodes, all uniformly
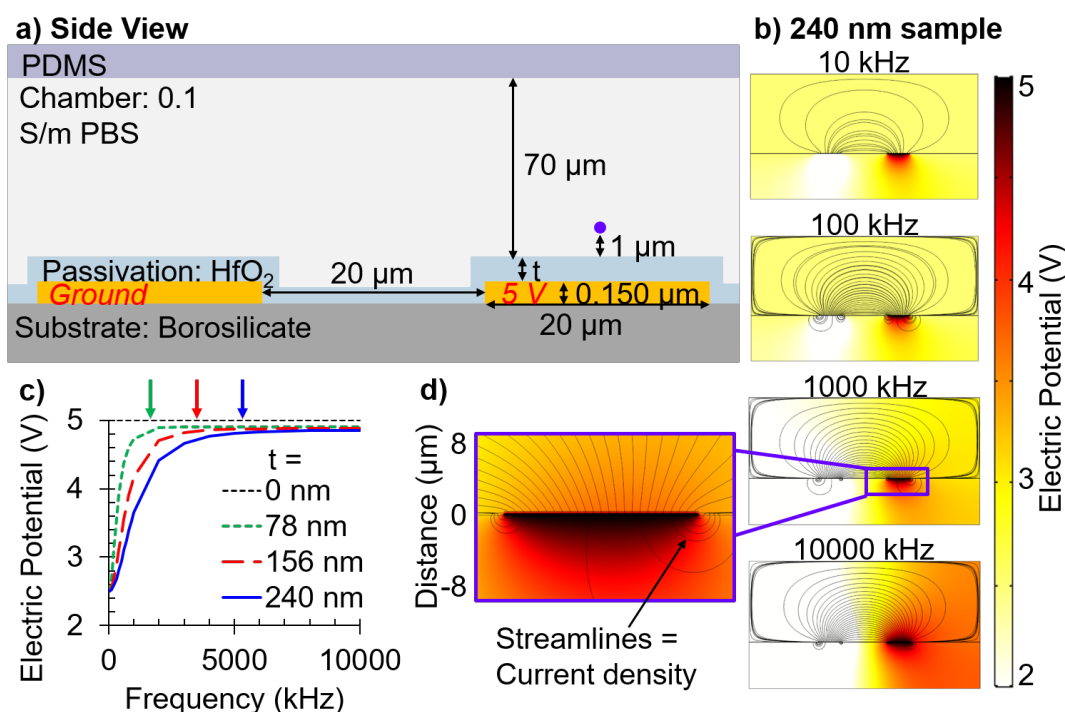
Figure 8-6: a) 2D geometry used for COMSOL simulations with 200 x 40 µm substrate, two 20 x 0.15 µm Au electrodes (excitation and ground), HfO_2 thickness (t = 78, 156, and 240 nm) over the substrate and electrodes, in contact with a 200 x 70 µm 0.1 S/m PBS fluidic layer. b) Electric potential distribution (surface plot) and current density (streamlines) for the 240 nm thick HfO_2 passivation layer at frequencies of 10, 100, 1000, and 10000 kHz. c) Magnitude of the electric potential that penetrated through the passivation layer into the chamber at a height of 1 µm above the working electrode (purple dot in a) as a function of frequency and film thickness. Arrows correspond to the frequency threshold whereby the maximum potential of ~4.85 V was reached. d) Close up of working electrode at a frequency of 1000 kHz. Results demonstrate that HfO_2 allowed electric field penetration into the fluidic layer while preventing direct physical contact between electrodes and fluidic layer.

passivated with 78, 156, or 240 nm of HfO$_2$. Figure 8.6b shows color maps of the chamber's electric potential distributions for 240 nm of HfO$_2$ as a function of frequency, while Figure 8.6c illustrates dependence on both frequency and film thickness at a location 1 μm above the working electrode. For all thicknesses, a potential of 5 V was applied at the working electrode and 0 V at the ground electrode to then observe heat maps of the current between the working and ground electrodes through the fluidic chamber. Simulations illustrated that HfO$_2$ allowed electric field penetration into the fluidic layer while preventing direct physical contact of the fluidic layer with the electrodes, thus preventing unwanted side reactions and electrode fouling. Potential leakage within the substrate resulted from the dielectric nature of borosilicate whereby no charge flowed, as indicated by the lack of current density streamlines.

For all cases, the electric field penetrated the passivation layer yet varied with HfO$_2$ thickness and frequency. At frequencies below 10 kHz, HfO$_2$ suppressed half of the applied electric potential regardless of thickness. A similar but opposite behavior was observed at frequencies greater than 10 MHz, at which a potential of 4.85 V was reached regardless of the thickness. This confirmed that the capacitive coupling through the HfO$_2$ film was higher at higher frequencies. The frequency at which the HfO$_2$ film became nearly electrically transparent, with a potential of 4.85 V in the fluidic layer, was dependent on thickness. The arrows in Figure 8.6c demonstrate this threshold for each film thickness. Simulations provide a foundation of electrical passivation characteristics of the HfO$_2$ for different thicknesses and different AC frequencies; this simulation framework may be useful for design and parameter optimizations for specific operating conditions or applications, such as constant current for field gradients.

8.3.7 Biocompatibility

HfO$_2$ film hemocompatibility was evaluated by exposing red blood cells in an isotonic 0.9 w/v% NaCl solution to a 20 x 20 mm borosilicate glass substrate coated with HfO$_2$ for up to 5 hours and measuring the amount of free hemoglobin in the supernatant after centrifugation. Figure 8.7 shows the percent hemolysis results for RBCs after 1, 3, and 5 hours of incubation at 37° C with HfO$_2$, along with the negative (no substrate or HfO$_2$) and positive (1% w/v Triton X-100 surfactant) controls completed in triplicate. Hemolysis varied between 0.75% and 1.45% when exposed to the HfO$_2$ without an apparent trend with exposure time. The negative control not exposed to HfO$_2$ showed 0.06% hemolysis, while the positive control showed 100% hemolysis. These results illustrated that HfO$_2$ was compatible with RBCs and is suitable as a passivation layer on lab-on-a-chip devices using blood as a primary sample.
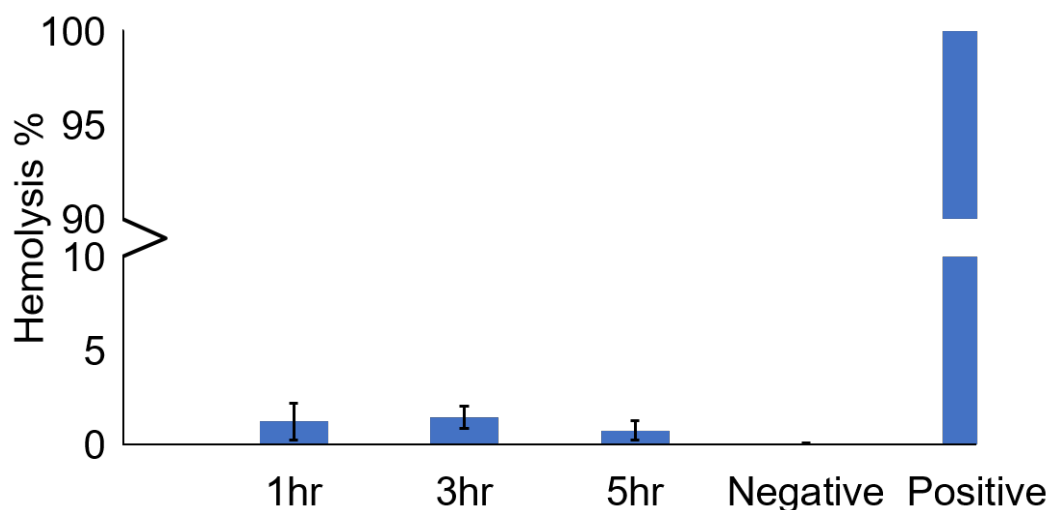
Figure 8-7: RBC hemolysis after 1, 3, and 5 hours of exposure to borosilicate glass coated with HfO_2, as well as, negative (no HfO_2), and positive (1 w/v% Triton X-100) controls. This demonstrated that HfO_2 is a suitable material for passivating electrodes within biological LOC devices that use cells.

8.4 Conclusions

Sputter-deposited hafnium oxide films of three different deposition times, 6.5, 13, and 20-minutes, were fabricated and characterized for use as a passivation layer in a biological electrokinetic microdevice system requiring sufficient optical transparency, electrode isolation, and biocompatibility.   EDS and FTIR both confirmed that the composition of the films were stoichiometric HfO_2. Film structural properties were explored via AFM, XRD, EDS, and FTIR. AFM results show surface roughness depended upon the substrate, with 64% smaller grain sizes and 11% smaller crystallite size on amorphous glass than silicon for the same 20-minute deposition. Surface roughness increased with deposition time from 5 nm to 12 nm on silicon. XRD results agreed with AFM results, showing an increase in crystallite size from 0.844 to 1.193 nm, with increasing deposition time. The XRD results for the 20-minute deposition on glass and the 6.5-minute deposition on silicon yielded the same orientation of (111) with roughness and crystallite size 78% and 81% greater on glass than on silicon, respectively. These results suggested that, based on the substrate used, the thickness of the HfO_2 film can be tailored to achieve desired grain structure.

Ellipsometry thicknesses of 58, 127, and 239 nm were determined for the 6.5, 13, and 20-minute depositions on silicon, respectively. The models included a SiO_2 interfacial layer and resulted in mean square errors of 0.54, 52, and 7.727 for the 6.5, 13, and 20-minute depositions, respectively. The multiple orientations seen by the XRD show that the films were anisotropic, explaining why the ellipsometry data deviated from the Cauchy

dispersion model fit. SEM thickness measurements revealed HfO_2 thicknesses ranging from 180-230 nm for the 20-minute deposition due to crystallite packing on top of a thin layer of SiO_2. The bulk ellipsometry measurements and the SEM measurements were deemed acceptably consistent.

Refractive index and extinction coefficient of the HfO_2 films were also determined from the ellipsometry data. For all three thicknesses, the refractive index was near the expected value of 2 from the literature [308, 313] and the extinction coefficient was near the expected value of zero [340]. These optical measurements confirm that HfO_2 was optically transparent. The FTIR results suggested wavelengths to be avoided, due to interference, if designing a set of fluorescence-based experiments on LOCs.

CV measurements were used to calculate dielectric constant as a function of film area for the 6.5-minute deposition. The resulting average dielectric constant was 20.32, which is close to the expected value of 25 [302]. The dielectric constant of HfO_2 is suitable for use as a passivation layer because the layer allows current to pass through into an adjacent fluidic layer while being thick enough to physically isolate the electrodes from the fluidic layer to prevent corrosive degradation.

COMSOL electrostatic simulations were utilized to further explore electric field behaviors through and around the HfO_2 films. Results demonstrated HfO_2 films of 78, 156, and 240 physically passivated the electrodes and enabled the electric field to penetrate into a fluidic layer above the film. Thicker HfO_2 films attenuated the electric potential penetration into the fluid, which was more pronounced at lower frequencies. Conveniently, electrical signal frequency enables straightforward modulation of the potential drop across the dielectric HfO_2 film.

For biological LOC applications, biocompatibility was tested via standard hemolytic potential protocols with human RBCs. When exposed to HfO_2 for up to 5 hours, less than 1.5% RBC lysis occurred, demonstrating that HfO_2 can be used with minimal reservation in LOC devices interrogating cells.

Implications of this work include increased HfO_2 structural, optical, and electrical film property knowledge as a function of film thickness. These attributes, along with the biocompatibility characteristic are highly useful for LOC applications involving electrokinetic separations and characterizations combined with optical detection of biological samples.

9 Microdevice Replication and Design Using a Water-Based Acrylic Polymer Emulsion

Microfabrication of high-aspect-ratio SU-8 features can be a difficult process. Small changes in the processing conditions can result in wafers that only last two or three castings. This chapter describes a solution that was investigated to avoid excess microfabrication costs and time. Puffy Paint, a commercially available children's paint, was used to make molds of PDMS devices made from SU-8 features. The work was then expanded to include designing new devices by hand drawing them, and eventually 3D-printing them, with Puffy Paint. Through this chapter, the Puffy Paint is referred to as a water-based acrylic polymer emulsion or WBAPE. This investigation was a collaborative effort and has been submitted to the ACS Journal of Education. J. Collins was lead author. The contributing authors on this work included A.M. Nelson and A.R. Minerick. Destiny Robinson, Rob Minerick, and Jerry Norkel assisted with adapting the 3D printer.

Abstract: Microfabrication of poly(dimethylsiloxane) (PDMS) microdevices via photolithography can be an expensive and time-consuming process. Processing materials and conditions can lead to high aspect ratio features peeling off the silicon master wafer after being replicated only a few times. Water-based acrylic polymer emulsion (WBAPE) was investigated as an easy to use and low-cost material for replicating PDMS features, reducing the need to use a silicon master wafer. Devices with features of various aspect ratios, ranging from 50-1500 microns in width and 70 microns in height, were designed and fabricated. The devices (master wafer, PDMS castings, WBAPE replicas, and PDMS replicas from the WBAPE) were compared by measuring the feature's dimensions with a stylus profilometer. PDMS replicas created via WBAPE maintained the desired feature shape and were 19 ±13 percent smaller than the silicon master wafer. WBAPE can also be used to alter existing features on a silicon wafer, to prototype microdevice designs before investing in costly wafer photolithography via drawing by hand or 3D printing, or to teach process steps for designing and fabricating a microdevice.
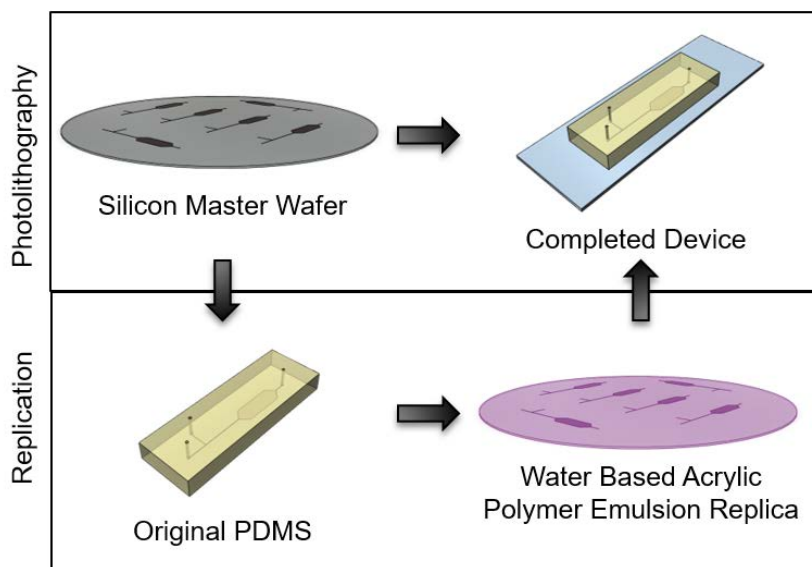
9.1 Introduction

Microfabrication can be a usage/time-intensive and costly process. Presented herein is a method of duplicating already fabricated fluidic designs, as well as prototyping microscale fluidic devices quickly and with less cost. One of the most common techniques for microdevice fabrication is using photolithography to make a silicon master wafer for poly(dimethylsiloxane) (PDMS) castings. PDMS is commonly used in the fabrication of microfluidic devices. Advantageous properties of PDMS include ease of use, mechanical/chemical stability, biocompatibility, optical properties, and low-cost [82, 83].

The process starts by designing the microfluidic features. Then a dark field/light field mask is made with those features. Making a mask can take anywhere from a day if developing the mask in-house to up to two weeks if ordered from suppliers and can cost up to $200 or more depending on the size, type, and feature resolution of the mask. The features are then translated from the mask to a silicon wafer using photolithography. Photolithography can be completed in a single day and costs around $100, depending on the microfabrication facility and photoresist used. After the silicon master wafer is developed and completed, the fluidic layer is created by casting, degassing, and baking PDMS on top of the master silicon wafer. Once cured, the PDMS is peeled off, and plasma bonded to a glass microscope slide.

The process of fabricating a silicon master wafer takes time (~2 weeks) and money (~$300) but does not guarantee a long-lasting wafer. A silicon master wafer may only last two or three castings before the features peel off, due to poor processing conditions or creating feature sizes that push the limits of the photolithography process and materials. High aspect ratio features are especially hard to fabricate due to Fresnel diffraction at the edge of the dark field areas of the mask and reflections off the silicon wafer itself causing stray light beneath the dark field areas [224]. SU-8, a negative photoresist commonly used for a wide range of feature sizes, is highly susceptible to this stray light [224].

 During the fabrication process, the feature sizes can change due to processing conditions. Edge beading may occur during spin coating, resulting in non-uniform feature sizes across a silicon wafer [341]. UV-exposure during photolithography, which depends on the time of the exposure, the intensity of the UV lamp, and the type and thickness of photoresist, significantly affects microchannel width [224]. PDMS casting can also alter the desired feature sizes. Fabrication of high aspect ratio features can be difficult with PDMS [342] and whether or not the PDMS is fully cured or not can lead to either an increase or decrease in feature size, respectively [343].

Due to the time and cost involved with fabricating a silicon master wafer via photolithography, a method for preserving the life of the wafer was investigated. This work was based on previous work presented by the MRSEC education group at the University of Wisconsin Madison [344]. WBAPE (Tulip, Walmart), a water-based acrylic polymer emulsion, was investigated to extend the life of a wafer and reduce

fabrication time and cost. This was done by making molds of existing PDMS features, adding to features on existing silicon wafer, or designing new devices by hand or 3D printing.

9.2 Materials and Methods

Original Master and Poly(dimethylsiloxane) *Fabrication:* A 4-inch silicon master wafer with 70 micron SU-8 2075 (MicroChem, Westborough, MA) features was fabricated using previously developed soft lithography techniques [221, 222]. The features were designed in AutoCAD (Autodesk, San Rafael, CA) and translated onto a mask[345]. The wafer was cleaned via sonication in acetone followed by isopropyl alcohol then deionized water, each for 5 minutes. The silicon wafer was then placed on a hot plate at 150 °C for 30 minutes to remove any volatiles. Negative photoresist, SU-8 2075, was spin coated at 500 rpm with an acceleration of 10 rpm/s for 55 seconds followed by 3000 rpm with an acceleration of 150 rpm/s for 47 seconds. The pre-bake was completed at 65 °C for 10 minutes followed by 95 °C for 25 minutes. Crosslinking of the SU-8 was achieved by masking with UV exposure at a dose of 196.5 mJ/cm^2 followed by a post bake at 65 °C
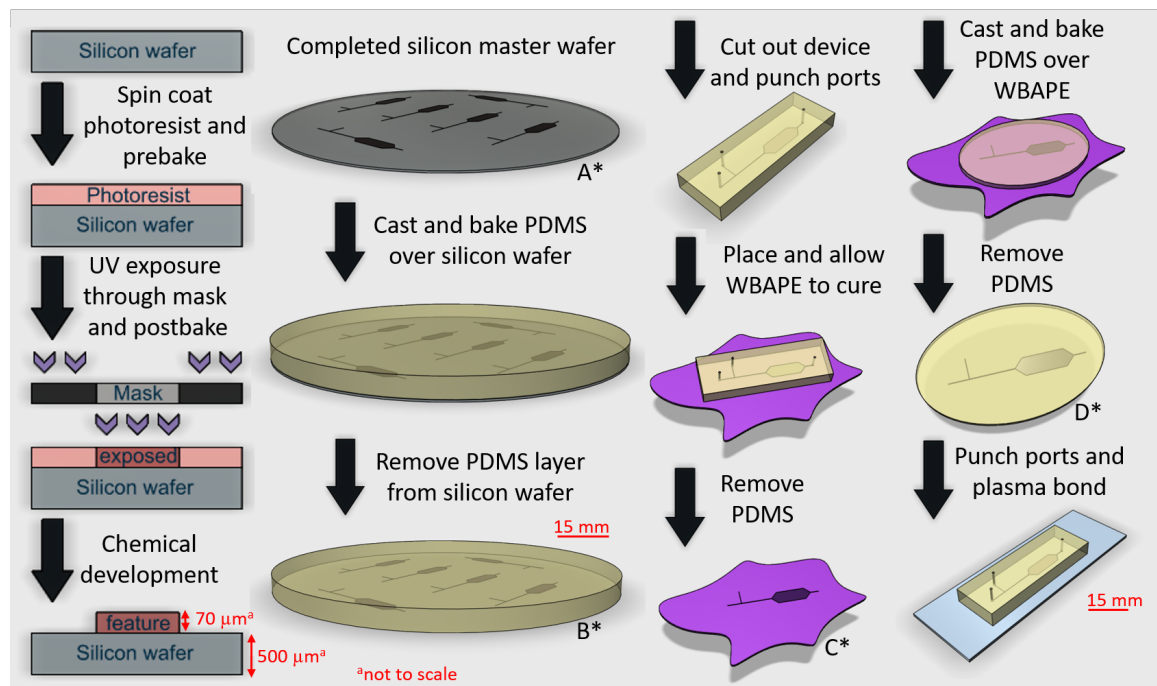
Figure 9-1. Flow diagram of the fabrication and replication process. The process began with a blank wafer, which underwent photolithography to create a master wafer (A) with SU-8 photoresist features. PDMS was then cast and baked over the features before being peeled off to fabricate the original PDMS (B). The original PDMS was then placed in WBAPE. The WBAPE was allowed to cure then the original PDMS was removed, leaving the WBAPE mold (C). PDMS was then cast and baked over the WBAPE before being peeled off to fabricate the replica PDMS (D). *The four fabrication steps A, B, C, and D are referenced in Figures 9.2-9.4.

112

for 5 minutes and 95 °C for 25 minutes. Features were developed in the SU-8 developer (MicroChem, Westborough, MA), resulting in the completed silicon master wafer.

A PDMS casting was made by mixing a 10:1 ratio of base to curing agent (Sylgard 184, Dow Corning, Auburn MI). The casting was placed in a vacuum to remove bubbles created by mixing. After bubbles were removed, the PDMS was poured over the silicon master wafer, and cured in an oven at 70°F for 4 hours. The cured PDMS layer was carefully peeled off the silicon master wafer, and each device layout was separated by cutting with a scalpel.

Water Based Acrylic Polymer Emulsion Replica and Replica Poly(dimethylsiloxane): After being removed from the oven and peeled off the wafer, WBAPE molds of the original PDMS were immediately made. Two-inch inner diameter, hexagonal plastic weigh boats (Sigma Aldrich, St. Louis, MO) were cleaned with deionized water and air dried. Each original PDMS was cleaned via scotch tape (3M) and a WBAPE replica mold was created by pressing the feature side of the PDMS into a shallow pool of WBAPE. Air bubbles in the WBAPE were carefully removed by strategically applying pressure to the top of the original PDMS.

The WBAPE was cured at atmospheric conditions and checked regularly for air bubbles; if any were present, pressure was applied to the top of the features to remove any bubbles. After the WBAPE cured, ranging from a day to a week, the original PDMS was carefully removed. The WBAPE was then allowed to further cure for 24 hours at atmospheric conditions. The cured WBAPE was used as a mold for replicate PDMS features. A new batch of 10:1 PDMS was then cast over the WBAPE replica following similar conditions/procedures as the original PDMS. After being removed from the oven, the replica PDMS was allowed to cool for about 12 hours. Once all replicates of the PDMS replicas were cured, the replica PDMS was carefully removed from the PDMS. The process flow of fabricating a silicon wafer via soft lithography (A in Figures 9.1-9.4), creating the PDMS casting (B in Figures 9.1-9.4), making the WBAPE mold (C in Figures 9.1-9.4), and creating the PDMS replica (D in Figures 9.1-9.4) is shown in Figure 9.1.

Alternate Water Based Acrylic Polymer Emulsion Uses: WBAPE was also investigated for applications including prototyping preliminary device designs, manipulating current designs by adding ports, and selecting single devices for replication on large wafers. To prototype, designs were drawn on the bottom of a weigh boat using a three mL syringe (Becton Dickinson, Franklin Lakes, NJ) filled with WBAPE and fitted with a precision tip (Nordson, Westlake, OH). Feature sizes were controlled by the size of the precision tip (0.1 to 1.54 mm inner diameter) and the amount of pressure applied to the syringe. Ports were added by carefully drawing them onto the silicon master wafer using a precision tip, and single devices were isolated from the rest of the silicon master wafer by building a wall of WBAPE around the single device.

Characterization Methods: Original features made via the silicon wafer and replicate features made via WBAPE were imaged, measured, and compared using an SVM340 synchronized video microscope (Labsmith, Livermore, CA) at 4x magnification. Three different sized sections of a microfluidic T-junction device were measured. The three sections included a small channel (I), large channel (II), and a chamber (III), which were designed to be 50, 100, and 1500 microns, respectively, as depicted in Figure 9.2. The SU-8 was fabricated to target a feature height of 70 microns.

Feature heights and widths were measured using a Dektak 6M Stylus Profilometer (Vecco, Plainview, NY). The measurements were completed using the stylus to scan across each feature perpendicularity at a force of 5 mg and a resolution of 0.513 μm/sample. The applied force was kept low since all materials being measured, PDMS and WBAPE, were soft materials and could easily be scratched or catch and break the scanning tip. Each step was measured in the locations shown in Figure 9.2. The results of the scans were loaded into a MATLAB program designed to output the height and width of each feature measured. Depending on the inversion of the curve, the average of the minima/maxima determined the height of each feature. To determine the width of the feature sizes, a derivative of each profilometer curve was taken, and the two resulting peaks were subtracted. The derivative curve was visually checked to confirm that the correct peaks were chosen, and not an artifact within the data. The average and standard deviation for the height and width of the small channel (I), the large channel (II), and chamber (III) for each step of the process (A-D) were calculated to determine how each processing step affected feature sizes.

9.3 Hazards

Original Master and Poly(dimethylsiloxane) *Fabrication:* The photolithography process includes chemical and equipment hazards. Processing was completed in a clean room requiring personal protective equipment (PPE): a bouffant cap, safety glasses with side shields, a face mask, a lab coat, gloves, and two sets of shoe coverings. Acetone and IPA were used to clean the silicon wafer, required secondary gloves, and handling in a chemical hood. These are both highly flammable chemicals that can cause serious eye irritation and drowsiness or dizziness if inhaled. In addition, acetone may cause organ damage through prolonged or repeated exposure. SU-8 was spun onto the silicon wafers. SU-8 and SU-8 developer both pose flammability and health hazards with GHS ratings of 3 for flammability, 4 for acute toxicity, 2 for skin and eye irritation, and 1 for skin sensitivity for the SU-8 and with a GHS rating of 2 for flammability and NFPA rating of 1 for health for the SU-8 developer. In addition, SU-8 developer is slightly toxic and was handled in a chemical hood. UV light, which can cause severe eye damage, was utilized in the photolithographic process. UV light protective eyewear was required during the UV exposure step. Safety training on all chemicals and equipment present was required before entering the clean room facility.

Water Based Acrylic Polymer Emulsion Replica and Poly(dimethylsiloxane): WBAPE is non-flammable, non-reactive; the and is classified as non-toxic in the commercially

available product. There are no PPE requirements associated with the handling of the WBAPE, however, safety glasses with side shields and gloves are recommended and were utilized. PDMS casting were made using a base and curing agent, both of which are non-hazardous. Safety glasses with side shields are required with PDMS handling and gloves are recommended. Following the standard operating procedures for the equipment, air bubbles were removed from the PDMS via vacuum, and the PDMS was cured in an oven at 70°C. PDMS castings were cut with a scalpel using care to cut away from hands/body.

9.4 Results and Discussion

To explore whether WBAPE could be utilized to reproduce microscale features, microfabricated features on a silicon wafer were cast with PDMS. Once cured, the PDMS was pressed into WBAPE. WBAPE successfully formed a secondary mold.
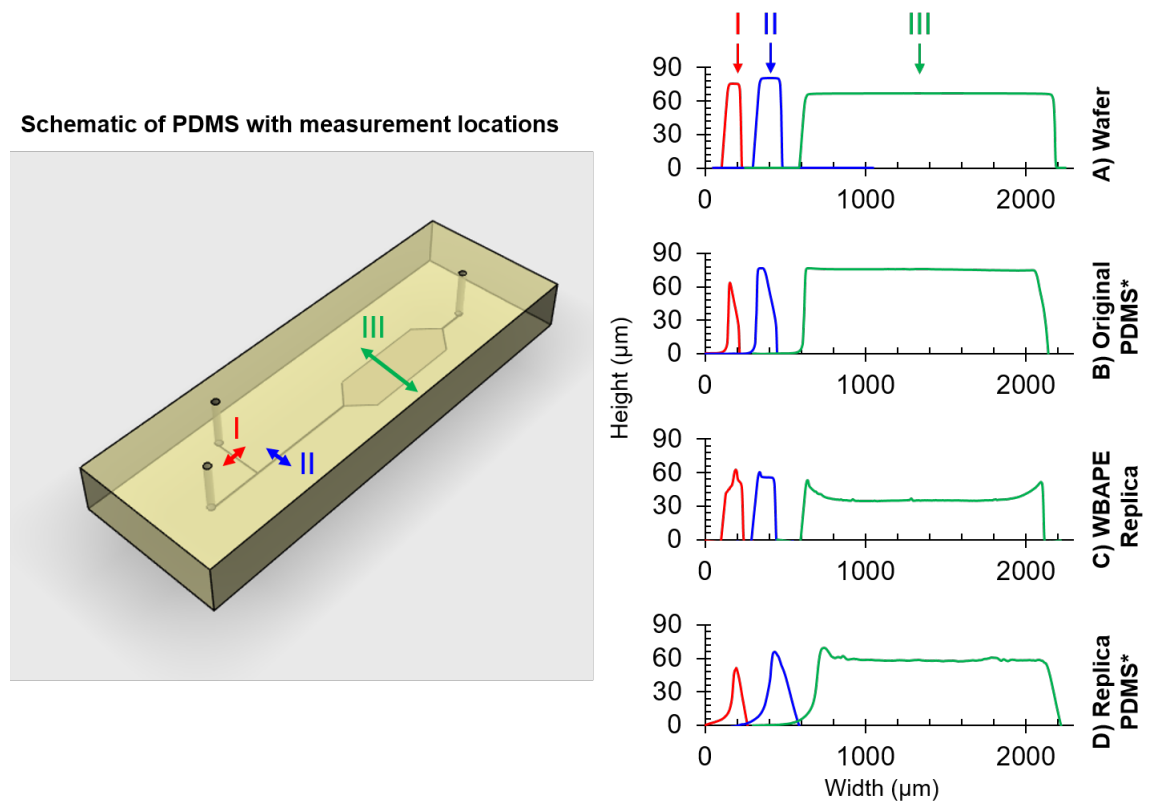
Figure 9-2. Schematic showing three measurement locations using a profilometer. Mask design dimensions were small channel: I = 50 μm, large channel: II = 100 μm, and chamber: III = 1500 μm. Measurements were completed on the A) wafer, B) original PDMS, C) WBAPE replica, and D) replica PDMS (see Figure 9.1). Wafer and WBAPE replica features were "hills" whereas PDMS features were "valleys' and were inverted for direct comparison. Overall, feature shape and size were retained by the replication process.

115

Figures 9.2- 9.4 show qualitative and quantitative comparisons between each of the four fabrication steps; the wafer, original PDMS, WBAPE, and replica PDMS (A, B, C, and D in Figure 1, respectively). Comparisons were made between three features of a microfluidic T-junction designed to have a small channel width of 50 microns and a large channel width of 100 microns (I and II in Figure 9.2) and a wide 1500 micron chamber (III in Figure 9.2). Qualitative images in Figure 9.3 demonstrate channel integrity of the small and large channels at the T-junction. Channel shape and wall roughness are optically comparable with only minor shape distortion in the smaller channel for the final replicate PDMS. Channel dimensions were measured with optical microscopy tools as shown in Figure 9.3, but subsequent analysis relied predominantly on stylus profilometer results.

Height and width measurements were obtained with a stylus profilometer for each of the four fabrication steps; the silicon master wafer, the original PDMS casting, the WBAPE, and the replica PDMS casting. Representative raw data from the profilometer are shown in Figure 9.2, and compiled results of the height and width comparisons are shown in Figure 9.4 as well as in Tables 9.1-9.2.

Table 9-1. Height and width measurements for each replication step. Corresponds to Figure 9.4a.

	Original Master	Original PDMS	WBAPE	Replica PDMS
Number of measurements	1	5	5	5
H_I (µm)	75.6	64.9 ± 1.3	63.4 ± 6.6	48.0 ± 2.9
H_{II} (µm)	80.9	78.2 ± 0.9	61.0 ± 5.6	65.0 ± 2.4
H_{III} (µm)	67.0	77.0 ± 0.8	41.6 ± 5.2	62.8 ± 8.1
W_I (µm)	119.2	64.0 ± 11.0	87.2 ± 36.7	89.0 ± 16.2
W_{II} (µm)	166.7	129.2 ± 8.0	122.1 ± 18.0	123.1 ± 18.2
W_{III} (µm)	1587.2	1512.8 ± 0.5	1496.4 ± 3.0	1550.0 ± 9.8

Height differences between measurement locations I, II, and III on the silicon wafer (step 1) were due to the photolithography process and are typical with thicker photoresist spins [224, 341]. On average the height of the SU-8 features were about 1% larger than the planned 70 µm. The average widths of the small channel, large channel, and chamber were about 138%, 11%, and 6% larger than the desired feature size.

The original PDMS casting (step 2) was on average 13% smaller than the wafer with comparable variations by between locations I, II, and III. This universal shrinkage suggests that the PDMS may not have been fully cured [343], as it was in the oven for approximately 4 hours before being removed and put in contact with the WBAPE. The average height was 1% larger than the SU-8 and 5% larger than the designed 70 µm, showing that the shrinkage mainly occurred in the width of the features. When compared to the SU-8 features and the design dimension the small channel, the chamber width was the most consistent at 5% larger than the SU-8 and 1% larger than the design dimensions.
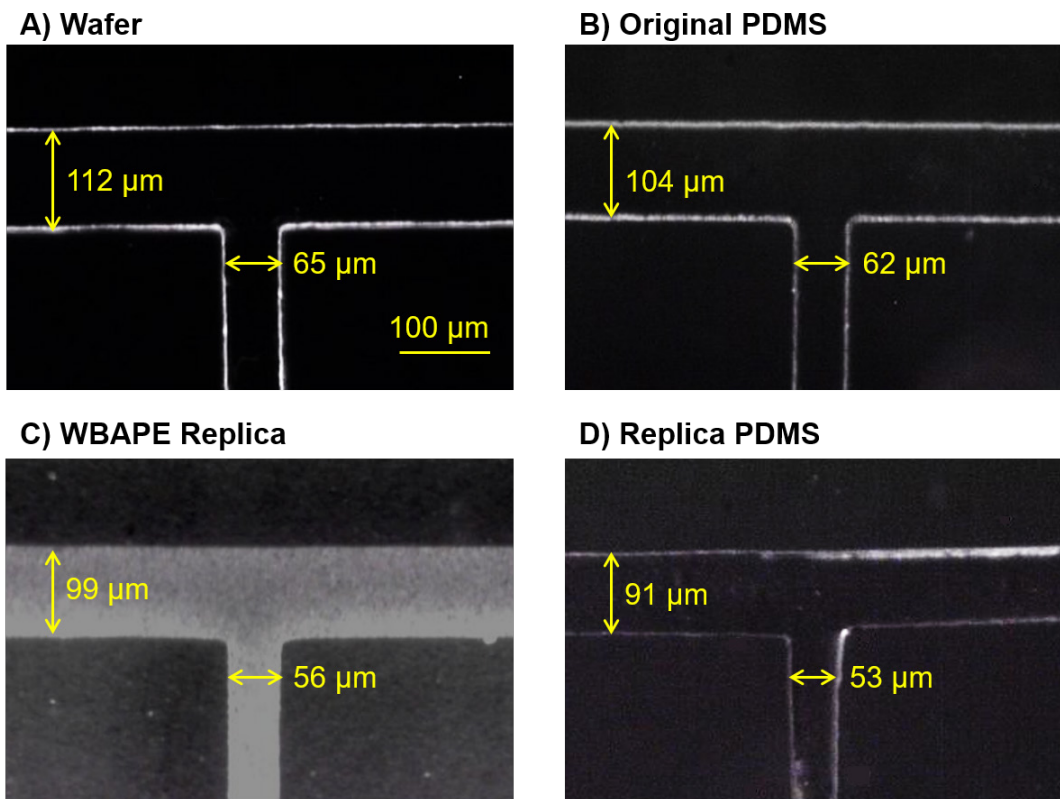
Figure 9-3. Comparison of the small and large channels (I and II in Figure 9.2) for the four fabrication steps (A, B, C, and D in Figure 9.1) under 4x magnification: A) silicon wafer with SU-8 features made via photolithography, B) original PDMS casting, C) WBAPE replica, and D) replica PDMS casting. Channel shape and size were fairly well maintained throughout the replication processes.

The small and large channels had more variation, demonstrating that larger features, with the smaller aspect ratios, were more reproducible.

All WBAPE (step 3) feature heights and widths were smaller than the original PDMS, except for the width of the small channel. The heights were 21% smaller than the designed height. While drying the interfacial tension between the WBAPE and the original PDMS created a meniscus, which was most prominent in the chamber as seen in Figure 9.2c. The widths of the small and large channels were 74% and 22% larger than the designed dimensions, respectively, and the width of the chamber was less than 1% smaller than the designed dimensions.

The replica PDMS (step 4) displayed heights that were ~7% larger than the WBAPE. This is consistent with literature, which has shown PDMS features to increase ~10% for fully cured PDMS [343]. The replica PDMS was able to cure for at least an additional 12 hours after being removed from the oven. The average height of the replica PDMS was about 41% smaller than the designed height and the widths of the small channel, large channel, and chamber were 78%, 23%, and 3% larger than the designed dimensions.

Table 9-2. Comparison of relative size (percentage). Corresponds to Figure 9.4b.

	Wafer /Wafer	Original PDMS /Wafer	WBAPE /Wafer	Replica PDMS /Wafer
H_I	100	86	84	63
H_{II}	100	97	75	80
H_{III}	100	115	62	94
W_I	100	54	73	75
W_{II}	100	78	73	74
W_{III}	100	95	94	98
Average Ratio	100 ± 0	87 ± 21	77 ± 11	81 ± 13
Average Height Ratio	100 ± 0	99 ± 15	74 ± 11	79 ± 15
Average Width Ratio	100 ± 0	76 ± 21	80 ± 12	82 ± 14

Each step of the replication process resulted in a size change, as seen in Tables 9.1 and 9.2. After measuring each device at multiple points, on average, the replica PDMS features were 81 ± 13% of the wafer features sizes, 96 ± 23% of the original PDMS feature sizes, and 109 ± 38% of the designed dimensions. It is important to note that the variation in size was dependent on feature size with greater accuracy for the largest features with the smallest aspect ratios than for the smallest features with the largest aspect ratios. The standard deviation for WBAPE tended to be larger than the other fabrication steps and was more pronounces in the feature widths. PDMS had the least variation for the largest features. Both channel widths (I and II in Figure 9.2) decreased during the original PDMS casting, the small channel (I) increased during the last two fabrication steps, and the large channel (II) remained fairly constant.

The standard deviation of the width of the small and large channels for five castings of the same SU-8 features, measured via profilometer, were 11 and 8 microns, respectively. In the context of 50 and 100-micron features, the reproducibility of the original PDMS castings was within 22% and 8%, respectively. The chamber had a standard deviation of 0.5 microns, showing that the larger features were more reproducible. The standard deviation of the small and large channels from five castings of the same WBAPE replica, via bright field microscopy, were 2 and 6 microns, respectively, demonstrating much better reproducibility of the PDMS replicas. These results demonstrated that the WBAPE replicas are sufficiently reliable to cast PDMS features. Further, WBAPE was able to withstand more than five castings without discernable integrity effects on the mold.

The reproducibility of these results suggests WBAPE can be used to replicate features on a silicon wafer with microscale SU-8 features. This method is both beneficial in duplicating multiple devices in a short amount of time, as well as preserving a master silicon wafer. High aspect ratio photolithographic features are known to be vulnerable to slight shifts in temperature and humidity, causing weaker adherence of the SU-8 features to the wafer and manifesting as feature flaking after a few PDMS castings [224]. If WBAPE is employed to replicate the master mold, then predominantly used for PDMS casting, wear and tear on the silicon wafer would be decreased. From the observations
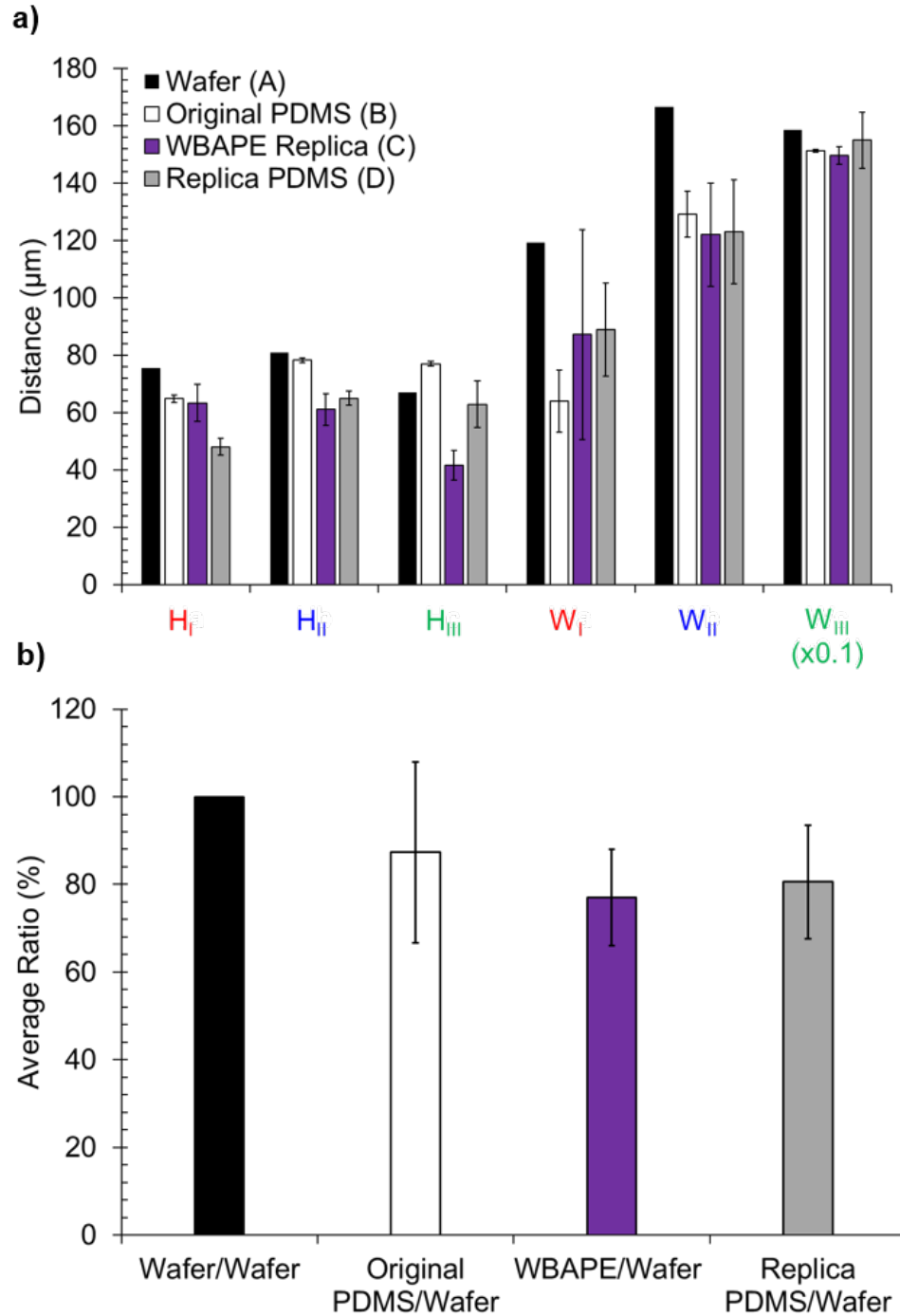
Figure 9-4. a) Profilometer results of each measurement location for each fabrication step (see Figure 9.1): A = master silicon wafer, B = original PDMS, C = WBAPE replica, and D = replica PDMS. The chamber width (Wc) was the least changed by each step of the process and WBAPE tended to have greater variation as compared to PDMS. b) Average relative magnitude between each step and the silicon wafer. Overall there was a decrease in size throughout the replication process.

that the PDMS replica was smaller than the original wafer, designs can be proportionally adjusted to account for size decreases. It is important to note that depending on the feature size the profile shape of the features may differ, as seen in Figure 9.2.

WBAPE can also be employed to add features to an existing wafer, increase the height of a chamber, add features ports, or build a barrier around a single device, such that less PDMS is required per casting. The ability to duplicate and manipulate devices using WBAPE increases the versatility and usability of microfabricated wafers for microfluidics.

The entire design process, from initial design to fabricated device, can also be accomplished directly with WBAPE. Figure 9.5 depicts a comparison between traditional photolithographic methods and WBAPE. Both start by creating a design in a CAD software application and laser printing on paper. A glass coverslip overlaid over the printed design can function as a surface upon which three-dimensional features can be
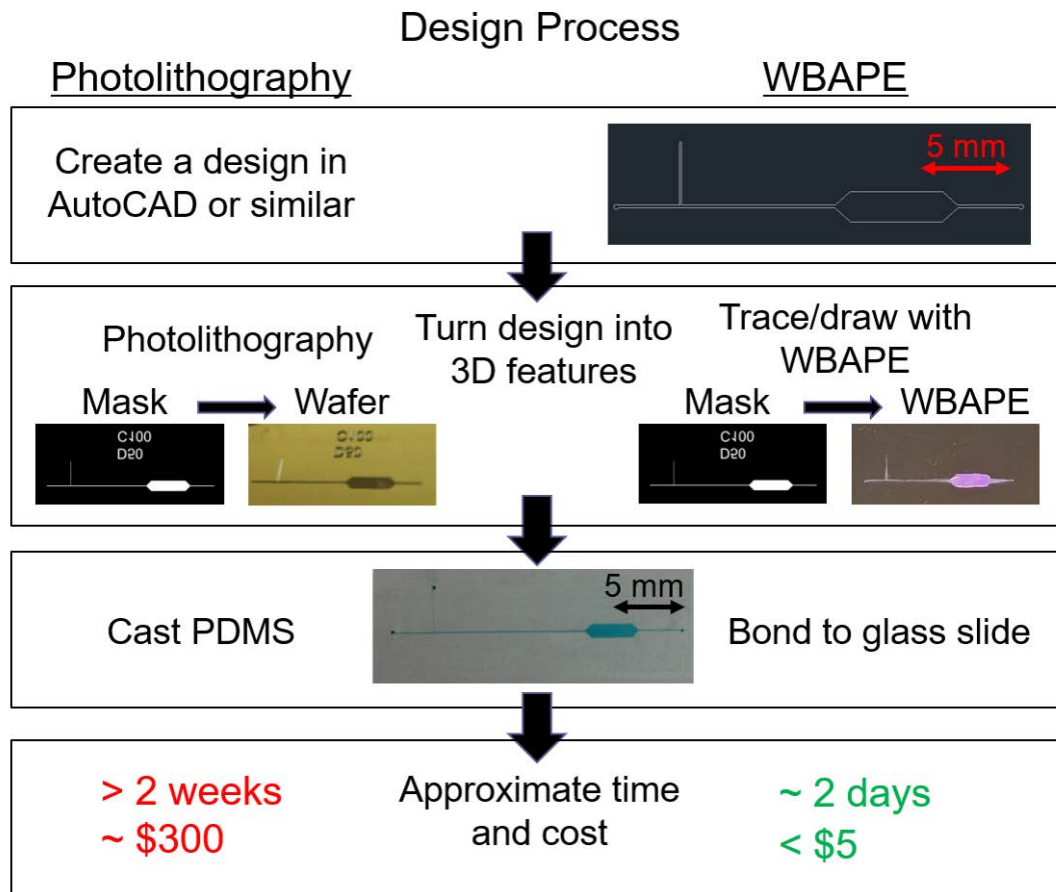
Figure 9-5. Design process comparison between traditional photolithography and WBAPE. Both begin by creating a design in CAD software and then translating into three-dimensional features. PDMS castings are made of the features, removed and bonded to glass slides. The photolithography process is highly reproducible and accurate, but takes more time and resources than the WBAPE process.

achieved by tracing the designs with WBAPE. WBAPE features can also be printed directly from CAD drawings using a paste extruder attachment on a 3D printer for more accurate features. Features drawn by hand or by the 3D printer have a rounded profile due to WBAPE surface tension with air. Photolithographically created SU-8 features have flat wall profiles while WBAPE yields curved wall profiles. WBAPE, while less accurate and more crude, can generate three-dimensional features in less than two days for under $5, making WBAPE a good material to test concepts and initial designs before investing in a silicon wafer. This can also be a fun and informative way to teach the design process without needed money, time, or training for microfabrication.

9.5 Conclusions

This work demonstrated that a low-cost, readily available water-based acrylic polymer emulsion can be used to make replications of PDMS castings and to make new designs. Replica PDMS features were made from a WBAPE mold of a PDMS casting from a microfabricated silicon wafer. Qualitative and quantitative comparisons revealed that overall feature shape was retained during each step of the replication process. Channel shape and wall roughness were optically comparable with only minor shape distortion in the smaller channel for the final replicate PDMS. The WBPAE profile showed a meniscus, created by the interfacial tension between the WBAPE and the PDMS while the WBAPE dried.

Given that high aspect ratio photolithographic features experience weaker adherence of the SU-8 features to the wafer, WBAPE has been demonstrated to be an acceptable augment to increase casting yields and reduce the frequency with which new silicon wafers must be microfabricated. The chamber had less variation than the small and large channels, demonstrating a dependence on size. Larger features, with smaller aspect ratios, were more producible. There was an overall decrease in feature size throughout the replication process, resulting in replicate PDMS devices that were 19 ± 13 percent smaller than the silicon master wafer. The size measurements at each step in the replication process indicate that designs could be implemented to reflect the expected change in feature size allowing for the replica PDMS to result in the desired feature sizes. PDMS casting reproducibility of the WBAPE molds and the ability to withstand multiple castings without discernable integrity effects demonstrated that they are sufficiently reliable to cast PDMS features.

In addition to replicating PDMS features from traditional microfabrication, WBAPE was investigated for testing new device designs. The photolithography process is highly reproducible and accurate but takes more time and resources than the WBAPE process. WBAPE can be used to trace features printed via a laser printer or to 3D print features from a CAD file, allowing testing of new designs before investing in fabrication. Between device replication, device alteration, and device design, WBAPE is a fun way to teach the process of microfluidic design and fabrication before re/investing in the fabrication of a silicon master wafer.

10 Future Work

The work in this dissertation revealed differing droplet stability windows as a function of droplet composition and applied electric field. A novel combination of droplet microfluidics and insulator dielectrophoresis, reverse insulator dielectrophoresis, was demonstrated. This new technique reduces the time, sample volume, reagent volume, and number of experiments necessary to complete a DEP response curve on a given particle or cell for a single media condition. The next logical step is to consolidate experiments further by simultaneous testing multiple media conditions. Figure 10.1 demonstrates how this project could reduce the number of necessary experiments by up to 93%. A systematic study to quantify stability and reliability of co-flowing droplets of different composition is outlined for future work.
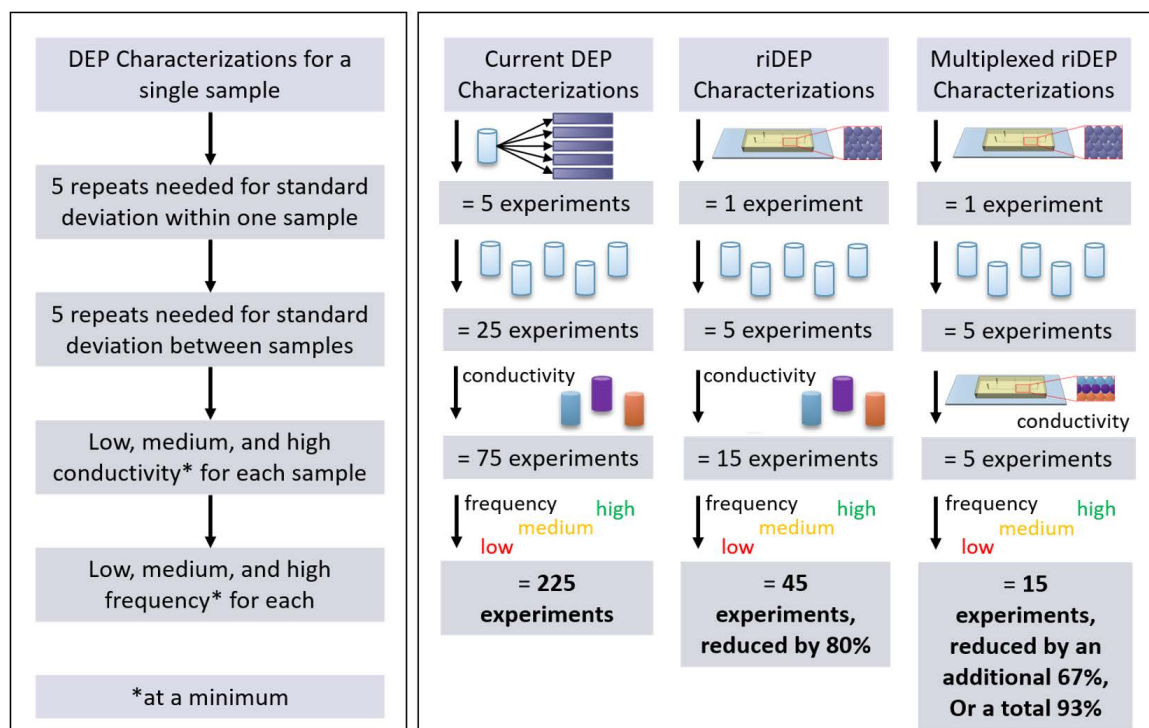
Figure 10-1. The potential impact of the new technique, riDEP, on reducing the amount of time needed to complete experiments by up to 93% when multiplexed.

10.1 Purpose and Motivation

One of the key limitations to current DEP devices is the amount of time it takes to generate DEP frequency spectra curves. This project aims to eliminate this by implementing parallel experimentation. Utilizing droplet microfluidics for parallelization of experimental repeats, each within a droplet with all of the droplets packed within one device, has been discussed and demonstrated. The new electrokinetic technique presented in this dissertation, riDEP, uses droplet interfaces to shape a non-uniform electric field

within the droplets for DEP characterization on particles or cells seeded within the droplets. Because DEP responses are highly dependent on media conditions, simultaneous experimentation could eliminate large amounts of time in the lab. The proposed system was engineered to allow for parallelization and multiplexation simultaneously. Two technologies are combined in this design; (a) droplet microfluidics, which provides isolated microenvironments for multiplexing the number of experiments and (b) a microfluidic tree structure, which allows simultaneous testing of different media conditions.

10.2 Background on Other Methods

As previously discussed in Sections 2.1.1 and 2.1.2, droplet microfluidics provides a platform for multiplexation by generating isolated microenvironments. However, it is limited in the number of phases/conditions that can be tested at once. Gradients have been used to alter concentrations of media/reactants. The challenge is knowing the exact concentration within each droplet, as well as keeping track of which droplet has each concentration once they enter a large microfluidic chamber. Microwell arrays have also been used for parallel experimentation, but there are limitations in altering sample volume and carrying out reaction steps [346], unlike droplets that can be transported, sorted, and mixed in a designated fashion.

10.3 Multiplexing in Microdevices via Microfluidic Tree Structures

Microfluidic tree structures provide means of multiplexing experiments by joining streams together from the 'branch' channels into a larger 'trunk' channel. This is feasible to accomplish with negligible mixing between streamlines since flow is solidly in the laminar flow regime. Applications of microfluidic tree structures include the formation of gradients, modeling branches of lungs, fission/fusion of droplets, and more [5, 347-354]. Multiplexing droplets with multiple dispersed phase composition requires careful control of multiple microfluidic streams. N.L. Jeon demonstrated the first use of a microfluidic tree structure in 2000 for gradient generation [347]. In 2004, D.R. Link demonstrated a microfluidic tree structure for droplet splitting [355]. It has since been adapted to applications from multicolor nanoparticles to modeling branches in a lung [5, 349-354]. In research presented by Riche et al., the use of multiple T-junctions was utilized, however, due to the chip design multiple fluidics layers were necessary and different pressures occurred in each junction resulting in different sized droplets from each [356]. Higher throughput of droplet generation for both single and double emulsions has been achieved by using the pressure at each split in the tree structure to break larger droplets into smaller ones [5], as seen in Figure 2.2a [5]. Large droplets can be broken up into smaller droplets without altering the total dispersed phase volume and concentration [349]. Collection of droplets within a large microfluidic chamber post tree structure splitting was also achieved in an ordered fashion [5] which is critical for this work. *The proposed design contains an array of T-junctions, each with its own media condition,*

which join into a microfluidic tree structure to create a gradient from droplet to droplet across the microfluidic chamber.

10.4 Experimental Plan

Multiple devices have been designed to approach multiplexation incrementally. The goal is to concurrently generate droplets with varying aqueous phase compositions, and stably pack the droplets into a slowly flowing electrokinetic chamber for real-time, medium dependent dielectrophoretic characterizations. Design optimizations will be conducted using hydrodynamic flow simulations in COMSOL (see foundations in Chapter 5), along with 3D printed Puffy Paint devices (refer to demonstrations in Chapter 9), before finalizing masks for microfabrication. Once the design is completed, device operation will be tested to quantify the accuracy of droplet ordering into linear lines (as shown in Figure 10.2); this can be done by adding different dyes to the dispersed phase of each T-
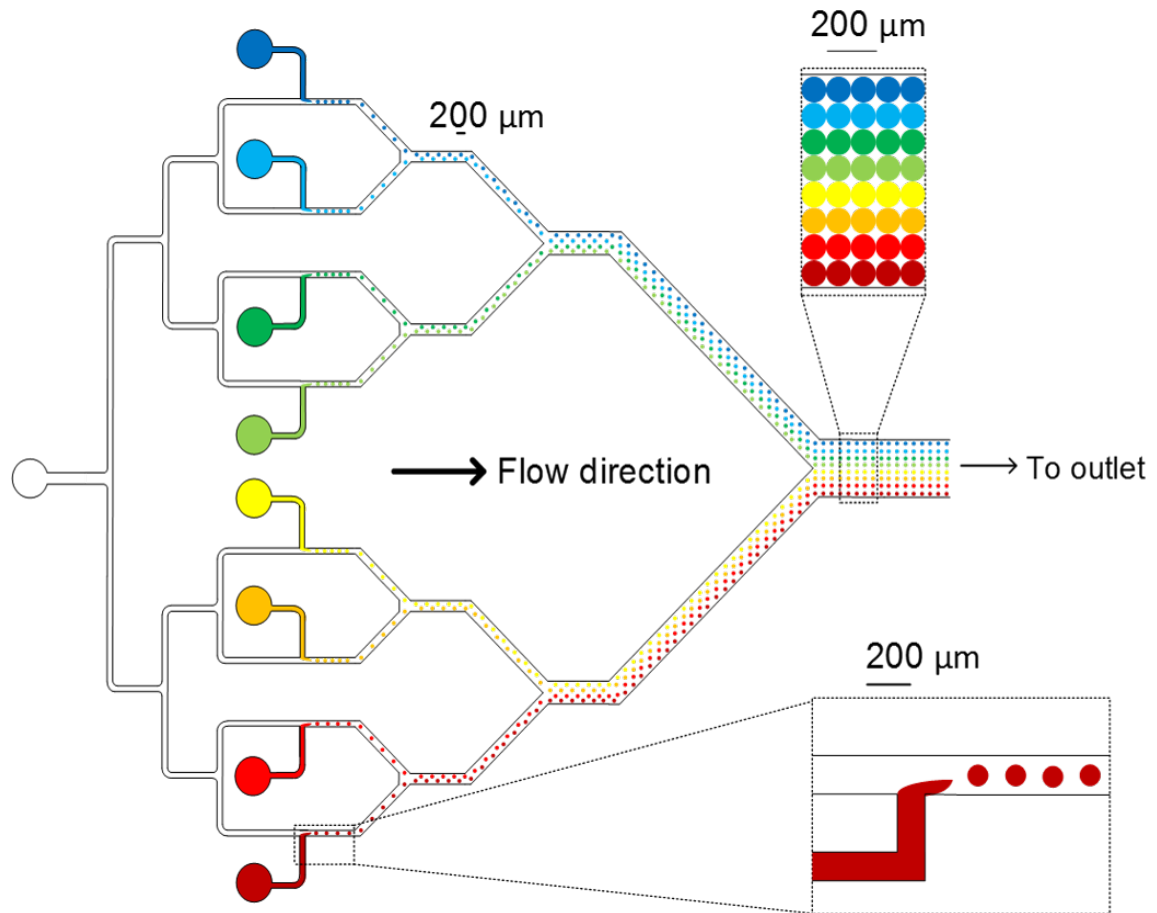
Figure 10-2. Conceptual drawing of a microfluidic tree structure used to generate droplets of varying concentrations, pH, or cell composition. Top inset illustrates that via laminar flow, the droplet alignment into a chamber region retains relative position alignment based on composition. Electric fields applied across the chamber enable r-iDEP responses within the different composition droplets.

junction. The approach to study this will be to begin with two coflowing junctions of the same composition to test the hydrodynamics, followed by two coflowing junctions with conductivities of 0.1 and 1 S/m. DEP experiments will be conducted by sweeping the frequency from high to low at a fixed voltage to reveal the differences in the two conductivities (RBCs in the 0.1 S/m droplets should reveal a switch from negative to positive DEP with an increase in frequency, whereas RBCs in the 1.0 S/m droplets should only demonstrate negative DEP). From there devices with four T-junctions will be fabricated, and both uniform droplets and droplets with conductivities of 0.05, 0.1, 0.5, and 1.0 S/m will be tested. COMSOL simulations will be conducted to simulate how the electric field gradient will vary within adjacent, different conductivity droplets; it is expected that potential drops will be greater across the lower conductivity droplets and thus impact the gradients achievable in the inner rows. Conductivity order will be systematically explored to ascertain droplet row configurations that will preserve gradients truest to the results of a single media present in adjacent droplets. Outcomes from this task will include insights into interfacial stability between two different conductivity droplets (this has not been extensively studied in the literature) as well as droplet conductivity arrangement for maximum DEP performance and stability. Once this system is fully explored, it will be expanded to up to ten coflowing droplets.

10.5 Implications

Knowledge from all prior objectives and tasks culminate in this final research task. This will be the true test of the versatility and power of the envisioned, novel r-iDEP technique. First particles, and then a single RBC blood type seeded into varying composition droplets will be dielectrophoretically interrogated simultaneously. The frequency sweeping technology patented by Minerick, Collins, Leonard, and Adams [357] will be used to investigate a full range of frequencies within a single experiment. Flow will be controlled to allow sufficient time for the particles or cells to sufficiently polarize and demonstrate DEP motion during the droplet's residence time in the chamber. Image analysis algorithms will be used to quantify DEP responses as a function of droplet position (and thus composition) and as a function of time. Multiplexing power will be tested via this approach. Outcomes of this task will include being able to fully characterize with DEP eight different blood types (in separate experiments) for at least four medium conductivities in roughly 80 hours of experiments and analysis compared to the (mathematically) 2 years of steady experiments/analysis. Quality of data will be determined by comparing with prior published RBC DEP data and results of the T-junction devices. In summary, these proposed investigations will increase multiplexing control within droplet microfluidics and allow that field to transform dielectrophoretic research.

11 Conclusions

This dissertation combined principles of droplet microfluidics and insulator dielectrophoresis to create a microdevice for parallel characterization of particles/cells via droplet microfluidics. Dielectrophoresis is a fast, noninvasive, and nondestructive technique with instrumentation simplicity, favorable scaling effects, and label-free operation. Although there are many advantages to using DEP there are disadvantages, including the number of required experiments and unwanted sample-electrode interactions. Insulator DEP reduces the sample-electrode interactions by remotely placing the electrodes and using insulating structures to shape the non-uniform electric field. This dissertation investigated the use of droplet microfluidics to form aqueous-in-oil droplets to act as individual, isolated microenvironments whose interfaces shaped non-uniform electric fields (needed for DEP) within each droplet. This work was the first to explore a novel technique envisioned by the author and advisor termed reverse insulator dielectrophoresis. There were three main objectives: 1) experimentally generate monodisperse droplets and pack them into a microfluidic chamber, 2) experimentally explore reverse insulator dielectrophoresis within droplets, and 3) ascertain feasibility via simulations of reverse insulator dielectrophoresis within droplets. There were also two secondary objectives: 1) characterize hafnium oxide as a material to physically isolate samples from electrodes as an alternative to riDEP and 2) investigate Puffy Paint as a microfabrication tool to prolong the lifetime of silicon master wafers.

11.1 Implications of stabilizing a droplet microfluidic system via surfactants/additives

The first main objective, to experimentally generate monodisperse droplets 100-200 μm in diameter and pack them into a microfluidic chamber, was split into two main aims. The first engineering-based aim, was to design and fabricate a microdevice with a T-junction for droplet generation and a chamber for droplet packing. This work used T-junctions due to their prior robust performance in the field, adaptability to a wide range of velocities and pressures, and utility in containing chemical reactions and cell encapsulations. Simulations, fabrication limitations, and preliminary experiments all informed device designs. The final device contained the following geometric parameters; a 50 μm wide dispersed phase channel joined a 100 μm wide continuous phase channel, both 3.5 mm in length, to form a T-junction. The continuous phase channel continued past the junction for 11 mm before opening, at a pitch of 35°, to a 1500 μm wide and 5000 μm long chamber. The device was fabricated to be 70 μm in height via soft-lithography with SU-8 photoresist. The SU-8 features were cast with PDMS and bonded to a glass microscope slide after oxygen plasma treatment.

The second, science-based aim, was to study the effect of chemical additives on the two-fluid system. Three surfactants, two oil phases, and thirteen aqueous phases were investigated. First, the oil phase and surfactant were optimized for the T-junction geometry by utilizing droplet diameter and stability. Experiments with SDS and Triton

X-100 suggested that a higher molecular weight surfactant would perform better, and thus Krytox FSH 157, a fluorosurfactant, was chosen. It demonstrated a large operating window that allowed changes in interfacial tension while maintaining droplet stability, along with lower cost and structural similarity to a commercially available biocompatible surfactant. A fluorinated oil, FC-40, was chosen as the oil phase due to its biocompatibility.

The effect of aqueous phase composition on droplet generation and packing was investigated. The droplet size at generation, the observed generation regime, the stability entering the chamber, and the coefficient of variance were tracked for each aqueous phase composition. Aqueous phase compositions explored included epure water, salt-only solutions containing 0.960, 2.616, 13.892, and 24.122 mM salt stock in epure water, dextrose only solutions containing 58.837, 161.108, 273.845, and 290.404 mM dextrose in epure water, and isotonic PBS and dextrose solutions of 0.05, 0.1, 0.5, and 1.0 A/m conductivities. All aqueous phase compositions demonstrated the expected natural log trend of decreasing droplet size with increasing surfactant concentration. The epure water control experiments showed that Krytox alone was unable to effectively stabilize the interface to prevent coalescence in an epure water/FC-40 system. However, the addition of salt into the aqueous phase resulted in a reduction in droplet size, and thus interfacial tension, which stabilized the droplets and increased droplet monodispersity. Availability of ions likely decreased the repulsion between Krytox's carboxylic head groups via a thin Debye layer of positive counterions. This ionic charge stabilization enabled closer packing of the surfactant molecules at the interface yielding stable droplets.

The addition of dextrose also had an observable effect on the droplet interfacial equilibrium. At low surfactant concentrations, droplet size increased indicating an increase in interfacial tension. At high surfactant concentrations, the presence of dextrose decreased the droplet size, and thus the interfacial tension to improve droplet stability. All Krytox and dextrose combinations of concentrations were not able to fully prevent droplet coalescence. This effect with the dextrose may be an indication that the surfactant molecules adsorb onto the large molecular weight dextrose molecules. The combination of salt and dextrose, to form isotonic solutions, resulted in a combination of droplet stability effects. ***The combination of salt and dextrose in the isotonic conductivity solutions affected the droplet size at generation, the generation regime, and the droplet stability entering the chamber in a combined interfacial tension reduction.*** This suggested interactions at the interface between the surfactant and the salt/dextrose additives played a key role in realized surface tension and stability. This work provided a map of droplet size, stability, and reproducibility along with regime tracking of coalescence and splitting, demonstrating the ability to strategically engineer surfactant concentration to eliminate droplet coalescence within a droplet microfluidic device. Further, this body of work has provided a starting point to aid in engineering a stable bio- and electro-compatible droplet microfluidic platform.

11.2 Implications of Introduction to a new, novel dielectrophoretic technique, Reverse Insulator Dielectrophoresis

The second objective of this project, achieving reverse insulator dielectrophoresis within droplets, was broken down into three main aims, one engineering based and two science-based. The first, engineering-based aim of objective two was to design and implement parallel electrodes within the microdevice. The previously explored T-junction and chamber device was adapted to include two 50 μm platinum wire electrodes. The platinum wires were successfully placed on either side of the chamber to create an electric field traverse to the droplet flow direction (when flow was included).

The second, science-based aim of the second main objective was to study the effect of the electric field on droplet stability. It is important that the droplets stay intact for the parallel DEP experiments within droplets. Experiments showed that droplet stability, as a function of voltage and frequency, changed with aqueous phase conductivity. For both an increase in surfactant concentration in the oil phase and conductivity of the aqueous phase, droplets coalescenced at lower applied potentials. In addition at higher frequencies, droplets were able to resist coalescence even as higher potentials were applied. This work successfully demonstrated stable droplets for frequencies from 100 kHz to 1 MHz and for applied potentials as high as 10 Vpp. This work provided a stability map for strategically choosing voltage and frequency to avoid electrocoalescence of droplets.

The third, science-based aim of the second main objective was to seed particles/cells into the droplets in order to conduct riDEP characterizations. Three-dimensional simulations in the third objective demonstrated both positive and negative dielectrophoresis in agreement with theory. Polystyrene beads and human red blood cells were successfully seeded into droplets and packed within the chamber. The electric field did bend to create non-uniform electric fields within the droplets, resulting in observed dielectrophoretic responses. The responses were slower than expected at the electrical and material conditions employed suggesting a decrease in voltage when the electric field traversed from droplet to droplet. However, riDEP was successfully demonstrated and steps for further improvement have been identified. These observations further support the premise that successful multiplexation of dielectrophoretic particle/cell characterization is achievable. This could greatly decrease the amount of time spent on experimentally generating DEP spectral curves for the determination of particle/cell properties.

11.3 Simulations to explore the feasibility of a new, novel dielectrophoretic technique, Reverse Insulator Dielectrophoresis

For objective three, two and three-dimensional simulations demonstrated the potential for aqueous droplets, surrounded by insulative oil, to shape non-uniform electric fields and

thus generate the electric field gradients necessary for dielectrophoresis. The simulations revealed that the insulative oil surrounding aqueous droplets does allow the electric field to pass through from droplet to droplet, as long as the droplets are closer than three microns apart.

Three-dimensional simulations demonstrated both positive and negative dielectrophoresis in agreement with theory. The electric field gradient was greatest at the poles, or the points of contact between droplets where the electric field traverses from one droplet to the next and the electric field gradient was smallest in the middle, around the edge of the droplet, the furthest distance from the high electric field gradient areas. The dielectrophoretic response within three-dimensional droplets at different voltages and aqueous phase conductivities reinforced how critically important controlling these variables is to map out DEP responses and thus back-calculate cell dielectric properties

11.4 Implications of Hafnium Oxide as a Material to Physically Isolate Samples from Electrodes

Reverse insulator dielectrophoresis uses immiscible phases to shape a non-uniform electric field. Because there is a layer of oil between the electrodes and the aqueous sample phase, the samples are isolated/protected from the electrodes. In this secondary objective, hafnium oxide was to investigated as a material to physically isolate samples from electrodes; this approach served as an additional method beyond droplets for isolating/protecting samples from electrode surface reactions. Hafnium oxide was used as a passivation layer to physically isolate the samples from the electrodes while allowing electric field penetration through the passivation into the sample. Seven characterization tools were used to investigate the potential of hafnium oxide film to function as a passivation layer. Results showed that hafnium oxide is both biocompatible and able to physically isolate samples while allowing the electric field to pass through. Implications of this work include increased HfO_2 structural, optical, and electrical film property knowledge as a function of film thickness. These attributes, along with the biocompatibility characteristic are highly useful for LOC applications involving electrokinetic separations and characterizations combined with optical detection of biological samples.

11.5 Implications of Puffy Paint as a Fabrication Tool

The high aspect ratios used in this work to create the necessary microfluidic channels proved challenging to microfabricate with limited shelf-life of the resulting silicon wafer masters. This secondary objective involved investigating Puffy Paint, a water-based acrylic polymer emulsion, as a microfabrication tool to augment PDMS castings. WBAPE proved to be an acceptable augment to increase casting yields and reduce the frequency with which new silicon wafers must be microfabricated by creating molds of previously fabricated PDMS features. Variations in size were dependent on feature size with greater accuracy for the largest features with the smallest aspect ratios than for the

smallest features with the largest aspect ratios. The size measurements at each step in the replication process indicated that designs could be implemented to reflect the expected change in feature size allowing for the replica PDMS to result in the desired feature sizes. PDMS casting reproducibility of the WBAPE molds and the ability to withstand multiple castings without discernable integrity effects demonstrated that they are sufficiently reliable to cast PDMS features. WBAPE was also investigated for testing new device designs. The photolithography process is highly reproducible and accurate but takes more time and resources than the WBAPE process. WBAPE can be used to trace features printed via a laser printer or to 3D print features from a CAD file, allowing testing of new designs before investing in fabrication. This work provided a fun, low-cost way to replicate, alter, and design devices and to teach the process of microfluidic design and fabrication before re/investing in the fabrication of a silicon master wafer.

11.6 Implications of Multiplexing riDEP with a microfluidic tree structure

A microfluidic tree structure has the potential, when coupled with the riDEP approach, to enable further multiplexing of cellular DEP characterizations. The microfluidic tree enables multiple different solutions to be pumped into T-junctions and generate droplets in parallel before being fluidically joined into a single chamber. Implications of this multiplexing will be less time, cost, and sample volume needed to complete the same number of experiments, as well as being able to uniformly control global parameters such as temperature. RBC DEP is highly dependent upon media conditions, and the ability to simultaneously conduct up to10 media conditions would fundamentally change this field as an enabling technology. Combined with the body of work completed thus far, involving biocompatible surfactant, ionic species, and nonionic species concentration effects on droplet interfacial stability, this future vision will also advance the field of droplet microfluidics and dielectrophoretic research.

11.7 Broader Implications

This dissertation discussed a combination of three microfluidic techniques; droplet microfluidics, dielectrophoresis, and microfluidic tree structures, for the goal of reducing the number of experiments required for dielectrophoretic characterizations. This exciting new riDEP approach could enable highly reliable multi-dimensional (such as medium conductivity and cell concentration) analysis at it has the potential to reduce the number of experiments necessary by up to 93%. Thus riDEP could provide cellular level reliability of diagnostics for an entire population of cells with fewer resources and time than existing technologies.

12 Reference List

[1] M. Zagnoni, J. Anderson, J.M. Cooper, Hysteresis in Multiphase Microfluidics at a T-Junction, Langmuir, 26 (2010) 9416-9422.

[2] E. Fradet, C. McDougall, P. Abbyad, R. Dangla, D. McGloin, C.N. Baroud, Combining rails and anchors with laser forcing for selective manipulation within 2D droplet arrays, Lab on a Chip, 11 (2011) 4228-4234.

[3] M. Nasabi, K. Khoshmanesh, F.J. Tovar-Lopez, K. Kalantar-Zadeh, A. Mitchell, Dielectrophoresis with 3D microelectrodes fabricated by surface tension assisted lithography, Electrophoresis, 34 (2013) 3150-3154.

[4] S.K. Srivastava, A. Gencoglu, A.R. Minerick, DC insulator dielectrophoretic applications in microdevice technology: a review, Analytical and Bioanalytical Chemistry, 399 (2011) 301-321.

[5] A. Abate, D. Weitz, Faster multiple emulsification with drop splitting, Lab on a chip, 11 (2011) 1911-1915.

[6] M. Chabert, K. Dorfman, J.-L. Viovy, Droplet fusion by alternating current (AC) field electrocoalescence in microchannels, Electrophoresis, 26 (2005) 3706-3715.

[7] K. Khoshmanesh, S. Nahavandi, S. Baratchi, A. Mitchell, K. Kalantar-zadeh, Dielectrophoretic platforms for bio-microfluidic systems, Biosensors & bioelectronics, 26 (2011) 1800-1814.

[8] P. Abbyad, R. Dangla, A. Alexandrou, C.N. Baroud, Rails and anchors: guiding and trapping droplet microreactors in two dimensions, Lab on a Chip, 11 (2011) 813-821.

[9] C. Iliescu, G.L. Xu, V. Samper, F.E.H. Tay, Fabrication of a dielectrophoretic chip with 3D silicon electrodes, Journal of Micromechanics and Microengineering, 15 (2005) 494-500.

[10] H.Y. Geng, J. Feng, L.M. Stabryla, S.K. Cho, Dielectrowetting manipulation for digital microfluidics: creating, transporting, splitting, and merging of droplets, Lab on a Chip, 17 (2017) 1060-1068.

[11] C. Priest, S. Herminghaus, R. Seemann, Controlled electrocoalescence in microfluidics: Targeting a single lamella, Applied physics letters, 89 (2006).

[12] C.H.J. Schmitz, A.C. Rowat, S. Koster, D.A. Weitz, Dropspots: a picoliter array in a microfluidic device, Lab on a Chip, 9 (2009) 44-49.

[13] E. Um, M.E. Rogers, H.A. Stone, Combinatorial generation of droplets by controlled assembly and coalescence, Lab on a Chip, 13 (2013) 4674-4680.

[14] A.J. deMello, Control and detection of chemical reactions in microfluidic systems, Nature, 442 (2006) 394-402.

[15] G.J.M. Bruin, Recent developments in electrokinetically driven analysis on microfabricated devices, Electrophoresis, 21 (2000) 3931-3951.

[16] L. Oconnor, MEMS - MICROELECTROMECHANICAL SYSTEMS, Mechanical Engineering, 114 (1992) 40-47.

[17] G.M. Whitesides, The origins and the future of microfluidics, Nature, 442 (2006) 368-373.

[18] D.R. Walt, Miniature analytical methods for medical diagnostics, Science, 308 (2005) 217-219.

[19] G.M. Whitesides, The origins and the future of microfluidics, Nature, 442 (2006) 368-373.

[20] K.-H. Han, R.D. McConnell, C.J. Easley, J.M. Bienvenue, J.P. Ferrance, J.P. Landers, A.B. Frazier, An active microfluidic system packaging technology, Sensors and Actuators B-Chemical, 122 (2007) 337-346.

[21] M.A. Burns, Analytic chemistry: Everyone's a (future) chemist, Science, 296 (2002) 1818-1819.

[22] E.D. Pratt, C. Huang, B.G. Hawkins, J.P. Gleghorn, B.J. Kirby, Rare cell capture in microfluidic devices, Chemical Engineering Science, 66 (2011) 1508-1522.

[23] H. Shafiee, J.L. Caldwell, R.V. Davalos, A Microfluidic System for Biological Particle Enrichment Using Contactless Dielectrophoresis, Jala, 15 (2010) 224-232.

[24] A. Salmanzadeh, L. Romero, H. Shafiee, R.C. Gallo-Villanueva, M.A. Stremler, S.D. Cramer, R.V. Davalos, Isolation of prostate tumor initiating cells (TICs) through their dielectrophoretic signature, Lab on a Chip, 12 (2012) 182-189.

[25] J. Zhu, X. Xuan, Curvature-induced dielectrophoresis for continuous separation of particles by charge in spiral microchannels, Biomicrofluidics, 5 (2011) 24111.

[26] B.H. Lapizco-Encinas, M. Rito-Palomares, Dielectrophoresis for the manipulation of nanobioparticles, Electrophoresis, 28 (2007) 4521-4538.

[27] R. Seemann, M. Brinkmann, T. Pfohl, S. Herminghaus, Droplet based microfluidics, Reports on Progress in Physics, 75 (2012).

[28] S.J. Zeng, X. Liu, H. Xie, B.C. Lin, Basic Technologies for Droplet Microfluidics, in: B.C. Lin (Ed.) Microfluidics: Technologies and Applications, Place Published, 2011, pp. 69-90.

[29] S.Y. Teh, R. Lin, L.H. Hung, A.P. Lee, Droplet microfluidics, Lab on a Chip, 8 (2008) 198-220.

[30] C.F. Ivory, Several new electrofocusing techniques, Electrophoresis, 28 (2007) 15-25.

[31] N. Piacentini, G. Mernier, R. Tornay, P. Renaud, Separation of platelets from other blood cells in continuous-flow by dielectrophoresis field-flow-fractionation, Biomicrofluidics, 5 (2011).

[32] F. Camacho-Alanis, L. Gan, A. Ros, Transitioning streaming to trapping in DC insulator-based dielectrophoresis for biomolecules, Sensors and Actuators B-Chemical, 173 (2012) 668-675.

[33] N.M. Jesus-Perez, B.H. Lapizco-Encinas, Dielectrophoretic monitoring of microorganisms in environmental applications, Electrophoresis, 32 (2011) 2331-2357.

[34] R. Pethig, Review Article-Dielectrophoresis: Status of the theory, technology, and applications, Biomicrofluidics, 4 (2010).

[35] P. Singh, N. Aubry, Transport and deformation of droplets in a microdevice using dielectrophoresis, Electrophoresis, 28 (2007) 644-657.

[36] A.R. Minerick, The rapidly growing field of micro and nanotechnology to measure living cells, AIChE Journal, 54 (2008) 2230-2237.

[37] E. Livak-Dahl, I. Sinn, M. Burns, Microfluidic Chemical Analysis Systems, in: J.M. Prausnitz (Ed.) Annual Review of Chemical and Biomolecular Engineering, Vol 2, Place Published, 2011, pp. 325-353.

[38] S.L. Anna, N. Bontoux, H.A. Stone, Formation of dispersions using "flow focusing" in microchannels, Applied Physics Letters, 82 (2003) 364-366.

[39] S.L. Anna, H.C. Mayer, Microscale tipstreaming in a microfluidic flow focusing device, Physics of Fluids, 18 (2006).

[40] W. Lee, L.M. Walker, S.L. Anna, Role of geometry and fluid properties in droplet and thread formation processes in planar flow focusing, Physics of Fluids, 21 (2009).

[41] W. Lee, L.M. Walker, S.L. Anna, Competition Between Viscoelasticity and Surfactant Dynamics in Flow Focusing Microfluidics, Macromolecular Materials and Engineering, 296 (2011) 203-213.

[42] V. Taly, D. Pekin, A. El Abed, P. Laurent-Puig, Detecting biomarkers with microdroplet technology, Trends in Molecular Medicine, 18 (2012) 405-416.

[43] A.R. Abate, C.H. Chen, J.J. Agresti, D.A. Weitz, Beating Poisson encapsulation statistics using close-packed ordering, Lab on a Chip, 9 (2009) 2628-2631.

[44] E.Y. Basova, F. Foret, Droplet microfluidics in (bio)chemical analysis, Analyst, 140 (2015) 22-38.

[45] M. Chabert, J.L. Viovy, Microfluidic high-throughput encapsulation and hydrodynamic self-sorting of single cells, Proceedings of the National Academy of Sciences of the United States of America, 105 (2008) 3191-3196.

[46] F. Courtois, L.F. Olguin, G. Whyte, D. Bratton, W.T.S. Huck, C. Abell, F. Hollfelder, An integrated device for monitoring time-dependent in vitro expression from single genes in picolitre droplets, Chembiochem, 9 (2008) 439-446.

[47] C. Holtze, A.C. Rowat, J.J. Agresti, J.B. Hutchison, F.E. Angile, C.H.J. Schmitz, S. Koster, H. Duan, K.J. Humphry, R.A. Scanga, J.S. Johnson, D. Pisignano, D.A. Weitz, Biocompatible surfactants for water-in-fluorocarbon emulsions, Lab on a Chip, 8 (2008) 1632-1639.

[48] E. Um, S.G. Lee, J.K. Park, Random breakup of microdroplets for single-cell encapsulation, Applied Physics Letters, 97 (2010).

[49] H.B. Yin, D. Marshall, Microfluidics for single cell analysis, Current Opinion in Biotechnology, 23 (2012) 110-119.

[50] O.E. Shklyaev, A.Q. Shen, Microfluidics enhanced control of the microstructure and flow of complex fluids, Mechanics Research Communications, 36 (2009) 121-124.

[51] L.R. Shang, Y. Cheng, J. Wang, H.B. Ding, F. Rong, Y.J. Zhao, Z.Z. Gu, Double emulsions from a capillary array injection microfluidic device, Lab on a Chip, 14 (2014) 3489-3493.

[52] M.J. Fuerstman, P. Garstecki, G.M. Whitesides, Coding/decoding and reversibility of droplet trains in microfluidic networks, Science, 315 (2007) 828-832.

[53] W. Zeng, I. Jacobi, S.J. Li, H.A. Stone, Variation in polydispersity in pump- and pressure-driven micro-droplet generators, Journal of Micromechanics and Microengineering, 25 (2015).

[54] P.A. Zhu, L.Q. Wang, Passive and active droplet generation with microfluidics: a review, Lab on a Chip, 17 (2017) 34-75.

[55] M. Joanicot, A. Ajdari, Applied physics - Droplet control for microfluidics, Science, 309 (2005) 887-888.

[56] J. Dai, H.S. Kim, A.R. Guzman, W.B. Shim, A. Han, A large-scale on-chip droplet incubation chamber enables equal microbial culture time, Rsc Advances, 6 (2016) 20516-20519.

[57] A. Golberg, M.L. Yarmush, T. Konry, Picoliter droplet microfluidic immunosorbent platform for point-of-care diagnostics of tetanus, Microchimica Acta, 180 (2013) 855-860.

[58] S.A. Leung, R.F. Winkle, R.C.R. Wootton, A.J. deMello, A method for rapid reaction optimisation in continuous-flow microfluidic reactors using online Raman spectroscopic detection, Analyst, 130 (2005) 46-51.

[59] B. Kirby, Micro- and Nanoscale Fluid Mechanics: Transport in Microfluidic Devices, Place Published, 2010.

[60] B.M. Jose, T. Cubaud, Droplet arrangement and coalescence in diverging/converging microchannels, Microfluidics and Nanofluidics, 12 (2012) 687-696.

[61] X.M. Chen, A. Brukson, C.L. Ren, A simple droplet merger design for controlled reaction volumes, Microfluidics and Nanofluidics, 21 (2017).

[62] R.K. Shah, H.C. Shum, A.C. Rowat, D. Lee, J.J. Agresti, A.S. Utada, L.Y. Chu, J.W. Kim, A. Fernandez-Nieves, C.J. Martinez, D.A. Weitz, Designer emulsions using microfluidics, Materials Today, 11 (2008) 18-27.

[63] S. Haeberle, R. Zengerle, J. Ducree, Centrifugal generation and manipulation of droplet emulsions, Microfluidics and Nanofluidics, 3 (2007) 65-75.

[64] C.N. Baroud, J.P. Delville, F. Gallaire, R. Wunenburger, Thermocapillary valve for droplet production and sorting, Physical Review E, 75 (2007).

[65] S.J. Zeng, B.W. Li, X.O. Su, J.H. Qin, B.C. Lin, Microvalve-actuated precise control of individual droplets in microfluidic devices, Lab on a Chip, 9 (2009) 1340-1343.

[66] T.T. Fu, Y.G. Ma, D. Funfschilling, C.Y. Zhu, H.Z. Li, Squeezing-to-dripping transition for bubble formation in a microfluidic T-junction, Chemical Engineering Science, 65 (2010) 3739-3748.

[67] J.S. Edgar, C.P. Pabbati, R.M. Lorenz, M.Y. He, G.S. Fiorini, D.T. Chiu, Capillary electrophoresis separation in the presence of an immiscible boundary for droplet analysis, Analytical Chemistry, 78 (2006) 6948-6954.

[68] V. van Steijn, C.R. Kleijn, M.T. Kreutzer, Predictive model for the size of bubbles and droplets created in microfluidic T-junctions, Lab on a Chip, 10 (2010) 2513-2518.

[69] H. Yang, Q. Zhou, L.S. Fan, Three-dimensional numerical study on droplet formation and cell encapsulation process in a micro T-junction, Chemical Engineering Science, 87 (2013) 100-110.

[70] S. Yeom, S.Y. Lee, Size prediction of drops formed by dripping at a micro T-junction in liquid-liquid mixing, Experimental Thermal and Fluid Science, 35 (2011) 387-394.

[71] M.L.J. Steegmans, A. Warmerdam, K. Schroen, R.M. Boom, Dynamic Interfacial Tension Measurements with Microfluidic Y-Junctions, Langmuir, 25 (2009) 9751-9758.

[72] N.N. Deng, Z.J. Meng, R. Xie, X.J. Ju, C.L. Mou, W. Wang, L.Y. Chu, Simple and cheap microfluidic devices for the preparation of monodisperse emulsions, Lab on a Chip, 11 (2011) 3963-3969.

[73] W. Li, E.W.K. Young, M. Seo, Z. Nie, P. Garstecki, C.A. Simmons, E. Kumacheva, Simultaneous generation of droplets with different dimensions in parallel integrated microfluidic droplet generators, Soft Matter, 4 (2008) 258-262.

[74] C.C. Roberts, R.R. Rao, M. Loewenberg, C.F. Brooks, P. Galambos, A.M. Grillet, M.B. Nemer, Comparison of monodisperse droplet generation in flow-focusing devices with hydrophilic and hydrophobic surfaces, Lab on a Chip, 12 (2012) 1540-1547.

[75] S.P.C. Sim, T.G. Kang, L. Yobas, C. Holtze, D.A. Weitz, The shape of a step structure as a design aspect to control droplet generation in microfluidics, Journal of Micromechanics and Microengineering, 20 (2010).

[76] X.Y. Wang, A. Riaud, K. Wang, G.S. Luo, Pressure drop-based determination of dynamic interfacial tension of droplet generation process in T-junction microchannel, Microfluidics and Nanofluidics, 18 (2015) 503-512.

[77] M. Azarmanesh, M. Farhadi, The effect of weak-inertia on droplet formation phenomena in T-junction microchannel, Meccanica, 51 (2016) 819-834.

[78] S.L. Anna, Droplets and Bubbles in Microfluidic Devices, in: S.H. Davis, P. Moin (Eds.) Annual Review of Fluid Mechanics, Vol 48, Place Published, 2016, pp. 285-309.

[79] S. van Loo, S. Stoukatch, M. Kraft, T. Gilet, Droplet formation by squeezing in a microfluidic cross-junction, Microfluidics and Nanofluidics, 20 (2016).

[80] A. Gupta, R. Kumar, Effect of geometry on droplet formation in the squeezing regime in a microfluidic T-junction, Microfluidics and Nanofluidics, 8 (2010) 799-812.

[81] W.A.C. Bauer, M. Fischlechner, C. Abell, W.T.S. Huck, Hydrophilic PDMS microchannels for high-throughput formation of oil-in-water microdroplets and water-in-oil-in-water double emulsions, Lab on a Chip, 10 (2010) 1814-1819.

[82] M.J. Schoning, M. Jacobs, A. Muck, D.T. Knobbe, J. Wang, M. Chatrathi, S. Spillmann, Amperometric PDMS/glass capillary electrophoresis-based biosensor microchip for catechol and dopamine detection, Sensors and Actuators B-Chemical, 108 (2005) 688-694.

[83] A. Wisitsoraat, P. Sritongkham, C. Karuwan, D. Phokharatkul, T. Maturos, A. Tuantranont, Fast cholesterol detection using flow injection microfluidic device with functionalized carbon nanotubes based electrochemical sensor, Biosensors & Bioelectronics, 26 (2010) 1514-1520.

[84] M.J. Rosen, J.T. Kunjappu, Characteristic Features of Surfactants, Surfactants and Interfacial Phenomena, John Wiley & Sons, Inc., Place Published, 2012, pp. 1-38.

[85] J.C. Baret, Surfactants in droplet-based microfluidics, Lab on a Chip, 12 (2012) 422-433.

[86] J.C. Baret, F. Kleinschmidt, A. El Harrak, A.D. Griffiths, Kinetic Aspects of Emulsion Stabilization by Surfactants: A Microfluidic Analysis, Langmuir, 25 (2009) 6088-6093.

[87] C.J. DeJournette, J. Kim, H. Medlen, X.P. Li, L.J. Vincent, C.J. Easley, Creating Biocompatible Oil-Water Interfaces without Synthesis: Direct Interactions between Primary Amines and Carboxylated Perfluorocarbon Surfactants, Analytical Chemistry, 85 (2013) 10556-10564.

[88] S.F. Burlatsky, V.V. Atrazhev, D.V. Dmitriev, V.I. Sultanov, E.N. Timokhina, E.A. Ugolkova, S. Tulyani, A. Vincitore, Surface tension model for surfactant solutions at the critical micelle concentration, J. Colloid Interface Sci., 393 (2013) 151-160.

[89] B. Ahn, K. Lee, H. Lee, R. Panchapakesan, L.F. Xu, J. Xu, K.W. Oh, Guiding, distribution, and storage of trains of shape-dependent droplets, Lab on a Chip, 11 (2011) 3915-3918.

[90] J. Park, A. Kerner, M.A. Burns, X.X.N. Lin, Microdroplet-Enabled Highly Parallel Co-Cultivation of Microbial Communities, Plos One, 6 (2011).

[91] J.C. Baret, Y. Beck, I. Billas-Massobrio, D. Moras, A.D. Griffiths, Quantitative Cell-Based Reporter Gene Assays Using Droplet-Based Microfluidics, Chemistry & Biology, 17 (2010) 528-536.

[92] J. Clausell-Tormos, D. Lieber, J.C. Baret, A. El-Harrak, O.J. Miller, L. Frenz, J. Blouwolff, K.J. Humphry, S. Koster, H. Duan, C. Holtze, D.A. Weitz, A.D. Griffiths,

C.A. Merten, Droplet-based microfluidic platforms for the encapsulation and screening of mammalian cells and multicellular organisms, Chemistry & Biology, 15 (2008) 427-437.

[93] H. Boukellal, S. Selimovic, Y.W. Jia, G. Cristobal, S. Fraden, Simple, robust storage of drops and fluids in a microfluidic device, Lab on a Chip, 9 (2009) 331-338.

[94] C.N. Baroud, M.R. de Saint Vincent, J.P. Delville, An optical toolbox for total control of droplet microfluidics, Lab on a Chip, 7 (2007) 1029-1033.

[95] E. Verneuil, M.L. Cordero, F. Gallaire, C.N. Baroud, Laser-Induced Force on a Microfluidic Drop: Origin and Magnitude, Langmuir, 25 (2009) 5127-5134.

[96] L.L. Shui, A. van den Berg, J.C.T. Eijkel, Interfacial tension controlled W/O and O/W 2-phase flows in microchannel, Lab on a Chip, 9 (2009) 795-801.

[97] J.H. Xu, S.W. Li, J. Tan, Y.J. Wang, G.S. Luo, Preparation of highly monodisperse droplet in a T-junction microfluidic device, Aiche Journal, 52 (2006) 3005-3010.

[98] P.B. Umbanhowar, V. Prasad, D.A. Weitz, Monodisperse emulsion generation via drop break off in a coflowing stream, Langmuir, 16 (2000) 347-351.

[99] X.Z. Niu, A.J. deMello, Building droplet-based microfluidic systems for biological analysis, Biochemical Society Transactions, 40 (2012) 615-623.

[100] S. Xu, Z. Nie, M. Seo, P. Lewis, E. Kumacheva, H. Stone, P. Garstecki, D. Weibel, I. Gitlin, G. Whitesides, Generation of monodisperse particles by using microfluidics: control over size, shape, and composition, Angewandte Chemie (International ed.), 44 (2005) 724-728.

[101] Z. Zhu, O. Frey, F. Franke, N. Haandbaek, A. Hierlemann, Real-time monitoring of immobilized single yeast cells through multifrequency electrical impedance spectroscopy, Analytical and Bioanalytical Chemistry, 406 (2014) 7015-7025.

[102] N. Pamme, C. Wilhelm, Continuous sorting of magnetic cells via on-chip free-flow magnetophoresis, Lab on a chip, 6 (2006) 974-980.

[103] T.N. Adams, C.J. Yang, J. Gress, N. Wimmer, A.R. Minerick, A Tunable Microfluidic Device for Drug Delivery, in: B. Bofeng (Ed.) Microfluidics, InTech, Place Published, 2012.

[104] H.Y. Jiang, Y.K. Ren, Y. Tao, Microwire formation based on dielectrophoresis of electroless gold plated polystyrene microspheres, Chinese Physics B, 20 (2011).

[105] H. Kim, H.-S. Moon, B. Kwak, H.-I. Jung, Microfluidic device to separate micro-beads with various fluorescence intensities, Sensors and actuators. B, Chemical, 160 (2011) 1536-1543.

[106] S. Ozuna-Chacón, B.H. Lapizco-Encinas, M. Rito-Palomares, S.O. Martínez-Chapa, C. Reyes-Betanzo, Performance characterization of an insulator-based dielectrophoretic microdevice, ELECTROPHORESIS, 29 (2008) 3115-3122.

[107] S.K. Srivastava, J.I. Baylon-Cardiel, B.H. Lapizco-Encinas, A.R. Minerick, A continuous DC-insulator dielectrophoretic sorter of microparticles, Journal of Chromatography A, 1218 (2011) 1780-1789.

[108] C.M. White, L.A. Holland, P. Famouri, Application of capillary electrophoresis to predict crossover frequency of polystyrene particles in dielectrophoresis, Electrophoresis, 31 (2010) 2664-2671.

[109] S.I. Han, H.S. Kim, A. Han, In-droplet cell concentration using dielectrophoresis, Biosensors & Bioelectronics, 97 (2017) 41-45.

[110] D.M.S. C.W. Bishop, The Blood Cell: A Comprehensive Treatise, Academic Press, New York, 1964.

[111] T.J.G. G.A. Jamieson, Red Cell Membrane: Structure and Function, J.B. Lippincott Company, Philadelphia, 1969.

[112] C.W. Bishop, D.M. Surgenor, The Blood Cell: A Comprehensive Treatise, Academic Press, Place Published, 1964.

[113] G.A. Jamieson, T.J. Greenwalt, Red Cell Membrane: Structure and Function, J.B. Lippincott Company, Place Published, 1969.

[114] V. Heinrich, K. Ritchie, N. Mohandas, E. Evans, Elastic thickness compressibilty of the red cell membrane, Biophysical Journal, 81 (2001) 1452-1463.

[115] N. Mohandas, P.G. Gallagher, Red cell membrane: past, present, and future, Blood, 112 (2008) 3939-3948.

[116] N. Mohandas, E. Evans, Mechanical-Properties Of The Red-Cell Membrane In Relation To Molecular-Structure And Genetic-Defects, Annual Review of Biophysics and Biomolecular Structure, 23 (1994) 787-818.

[117] N. Mohandas, J.A. Chasis, S.B. Shohet, The Influence Of Membrane Skeleton On Red-Cell Deformability, Membrane Material Properties, And Shape, Seminars in Hematology, 20 (1983) 225-242.

[118] B.M. Cooke, N. Mohandas, R.L. Coppel, Malaria and the red blood cell membrane, Seminars in Hematology, 41 (2004) 173-188.

[119] T. Bulai, D. Bratosin, A. Pons, J. Montreuil, J.P. Zanetta, Diversity of the human erythrocyte membrane, sialic acids in relation with blood groups, Febs Letters, 534 (2003) 185-189.

[120] D. Bratosin, C. Motas, Effect Of Procaine And Donor Age On Human Erythrocyte-Membrane - Lectins Binding Study, Revue Roumaine De Biochimie, 26 (1989) 345-353.

[121] C. Ballario, A. Bonincontro, C. Cametti, A. Rosi, L. Sportelli, Conductivity of normal and pathological human-erythrocytes (homozygous beta-thalassemia) at radio frequencies, Zeitschrift Fur Naturforschung C-A Journal of Biosciences, 39 (1984) 160-166.

[122] B. Rappaz, A. Barbul, Y. Emery, R. Korenstein, C. Depeursinge, P.J. Magistretti, P. Marquet, Comparative study of human erythrocytes by digital holographic microscopy, confocal microscopy, and impedance volume analyzer, Cytometry Part A, 73A (2008) 895-903.

[123] H. Fricke, The Electric Capacity Of Suspensions With Special Reference To Blood, J. Gen. Physiol., 9 (1925) 137-152.

[124] J.Z. Bao, C.C. Davis, R.E. Schmukler, Frequency domain impedance measurements of erythrocytes. Constant phase angle impedance characteristics and a phase transition, 61 (1992) 1427-1434.

[125] J. Gimsa, T. Muller, T. Schnelle, G. Fuhr, Dielectric Spectroscopy of Single Human Erythrocytes at Physiological Ionic Strength: Dispersin of the Cytoplasm, Biophysical Journal, 71 (1996) 495-506.

[126] H. Pauly, H.P. Schwan, Dielectric Properties and Ion Mobility in Erythrocytes, Biophysical Journal, 6 (1966) 621-639.

[127] P. Gascoyne, C. Mahidol, M. Ruchirawat, J. Satayavivad, P. Watcharasit, F.F. Becker, Microsample preparation by dielectrophoresis: isolation of malaria, Lab on a Chip, 2 (2002) 70-75.

[128] O. Martinsen, S. Grimnes, H. Schwann, Interface Phenomena and Dielectric Properties of Biological Tissue, Encyclopedia of Surface and Colloidal Science, Marcel Dekker, Place Published, 2002.

[129] W. Arnold, A. Gessner, U. Zimmermann, Dielectric measurements on electro-manipulation media, Biochim Biophys Acta, 1157 (1993) 32-44.

[130] S.K. Srivastava, P.R. Daggolu, S.C. Burgess, A.R. Minerick, Dielectrophoretic characterization of erythrocytes: Positive ABO blood types, Electrophoresis, 29 (2008) 5033-5046.

[131] A.R. Minerick, R.H. Zhou, P. Takhistov, H.C. Chang, Manipulation and characterization of red blood cells with alternating current fields in microdevices, Electrophoresis, 24 (2003) 3703-3717.

[132] S.K. Srivastava, A. Artemiou, A.R. Minerick, Direct current insulator-based dielectrophoretic characterization of erythrocytes: ABO-Rh human blood typing, Electrophoresis, 32 (2011) 2530-2540.

[133] B.G. Hawkins, C. Huang, S. Arasanipalai, B.J. Kirby, Automated Dielectrophoretic Characterization of Mycobacterium smegmatis, Analytical Chemistry, 83 (2011) 3507-3515.

[134] R. Pethig, A. Menachery, S. Pells, P. De Sousa, Dielectrophoresis: A Review of Applications for Stem Cell Research, Journal of Biomedicine and Biotechnology, (2010).

[135] G.H. Markx, M.S. Talary, R. Pethig, Separation of viable and non-viable yeast using dielectrophoresis, Journal of Biotechnology, 32 (1994) 29-37.

[136] P.R.C. Gascoyne, Dielectrophoretic-Field Flow Fractionation Analysis of Dielectric, Density, and Deformability Characteristics of Cells and Particles, Analytical Chemistry, 81 (2009) 8878-8885.

[137] H. Shafiee, M.B. Sano, E.A. Henslee, J.L. Caldwell, R.V. Davalos, Selective isolation of live/dead cells using contactless dielectrophoresis (cDEP), Lab on a Chip, 10 (2010) 438-445.

[138] F.F. Becker, X.B. Wang, Y. Huang, R. Pethig, J. Vykoukal, P.R. Gascoyne, Separation of human breast cancer cells from blood by differential dielectric affinity, Proceedings of the National Academy of Sciences of the United States of America, 92 (1995) 860-864.

[139] R. Holzel, Non-invasive determination of bacterial single cell properties by electrorotation, Biochimica et Biophysica Acta, 1450 (1999) 53-60.

[140] N.G. Green, A. Ramos, H. Morgan, Ac electrokinetics: a survey of sub-micrometre particle dynamics, J. Phys. D-Appl. Phys., 33 (2000) 632-641.

[141] H. Moncada-Hernandez, J.L. Baylon-Cardiel, V.H. Perez-Gonzalez, B.H. Lapizco-Encinas, Insulator-based dielectrophoresis of microorganisms: Theoretical and experimental results, Electrophoresis, 32 (2011) 2502-2511.

[142] B. Cetin, D.Q. Li, Lab-on-a-chip device for continuous particle and cell separation based on electrical properties via alternating current dielectrophoresis, Electrophoresis, 31 (2010) 3035-3043.

[143] H.P. Schwan, Electrical properties of blood and its constitutents: Alternating current spectroscopy, Annals of Hematology, 46 (1983) 185-197.

[144] F.F. Becker, X.B. Wang, Y. Huang, R. Pethig, J. Vykoukal, P.R.C. Gascoyne, The removal of human leukaemia cells from blood using interdigitated microelectrodes, Journal of Physics D: Applied Physics, 27 (1994) 2659.

[145] H. Huang, J.M. Yang, P.J. Hopkins, S. Kassegne, M. Tirado, A.H. Forster, H. Reese, Separation of Simulants of Biological Warfare Agents from Blood by a Miniaturized Dielectrophoresis Device, Biomedical Microdevices, 5 (2003) 217-225.

[146] Y. Polevaya, I. Ermolina, M. Schlesinger, B.-Z. Ginzburg, Y. Feldman, Time domain dielectric spectroscopy study of human cells: II. Normal and malignant white blood cells, Biochimica et Biophysica Acta (BBA) - Biomembranes, 1419 (1999) 257-271.

[147] C. Wang, X. Wang, Z. Jiang, Dielectrophoretic Driving Of Blood Cells In A Microchannel, Biotechnology & Biotechnological Equipment, 25 (2011) 2405-2411.

[148] D.M. Vykoukal, P.R.C. Gascoyne, J. Vykoukal, Dielectric characterization of complete mononuclear and polymorphonuclear blood cell subpopulations for label-free discrimination, Integrative Biology, 1 (2009) 477-484.

[149] J. Vienken, U. Zimmermann, A. Alonso, D. Chapman, Orientation of sickle red blood cells in an alternating electric field, Naturwissenschaften, 71 (1984) 158-160.

[150] M. Stephens, M.S. Talary, R. Pethig, A.K. Burnett, K.I. Mills, The dielectrophoresis enrichment of CD34(+) cells from peripheral blood stem cell harvests, Bone Marrow Transplantation, 18 (1996) 777-782.

[151] V. Srinivasan, V.K. Pamula, R.B. Fair, An integrated digital microfluidic lab-on-a-chip for clinical diagnostics on human physiological fluids, Lab on a Chip, 4 (2004) 310-315.

[152] K. Maswiwat, D. Wachner, J. Gimsa, Effects of cell orientation and electric field frequency on the transmembrane potential induced in ellipsoidal cells, Bioelectrochemistry, 74 (2008) 130-141.

[153] P.V. Jones, S.J.R. Staton, M.A. Hayes, Blood cell capture in a sawtooth dielectrophoretic microchannel, Analytical and Bioanalytical Chemistry, 401 (2011) 2103-2111.

[154] Z. Gagnon, J. Gordon, S. Sengupta, H.C. Chang, Bovine red blood cell starvation age discrimination through a glutaraldehyde-amplified dielectrophoretic approach with buffer selection and membrane cross-linking, Electrophoresis, 29 (2008) 2272-2279.

[155] F. Dignat-George, J. Sampol, G. Lip, A.D. Blann, Circulating endothelial cells: Realities and promises in vascular disorders, Pathophysiology of Haemostasis and Thrombosis, 33 (2003) 495-499.

[156] I.F. Cheng, C. Cheng-Che, C. Hsien-Chang, High-throughput electrokinetic bioparticle focusing based on a travelling-wave dielectrophoretic field, Microfluidics and Nanofluidics, 10 (2011).

[157] D.R. Arifin, L.Y. Yeo, J.R. Friend, Microfluidic blood plasma separation via bulk electrohydrodynamic flows, Biomicrofluidics, (2007).

[158] A. Alazzam, I. Stiharu, R. Bhat, A.N. Meguerditchian, Interdigitated comb-like electrodes for continuous separation of malignant cells from blood using dielectrophoresis, Electrophoresis, 32 (2011) 1327-1336.

[159] K.M. Leonard, A.R. Minerick, Explorations of ABO-Rh antigen expressions on erythrocyte dielectrophoresis: Changes in cross-over frequency, Electrophoresis, 32 (2011) 2512-2522.

[160] M.D. Vahey, J. Voldman, High-Throughput Cell and Particle Characterization Using Isodielectric Separation, Analytical Chemistry, 81 (2009) 2446-2455.

[161] G.V. Gass, L.V. Chernomordik, L.B. Margolis, Local Deformation of Human Red-Blood-Cells in High-Frequency Electric-fields, Biochimica Et Biophysica Acta, 1093 (1991) 162-167.

[162] S.I. Han, S.M. Lee, Y.D. Joo, K.H. Han, Lateral dielectrophoretic microseparators to measure the size distribution of blood cells, Lab on a Chip, 11 (2011) 3864-3872.

[163] H. Zhou, L.R. White, R.D. Tilton, Lateral separation of colloids or cells by dielectrophoresis augmented by AC electroosmosis, J. Colloid Interface Sci., 285 (2005) 179-191.

[164] Y. Xu, Q. Cao, X. Zeng, Y.J. Wu, W.P. Zhang, Research of Cell Concentration and Separation on the Dielectrophoretic Chip with Arrayed Opposite Electrodes, Chemical Journal of Chinese Universities-Chinese, 30 (2009) 876-881.

[165] I.C. Tsoneva, D.V. Zhelev, D.S. Dimitrov, Red blood cell dielectrophoresis in axisymmetric fields, Cell Biophys, 8 (1986).

[166] N.V. Tolan, L.I. Genes, W. Subasinghe, M. Raththagala, D.M. Spence, Personalized Metabolic Assessment of Erythrocytes Using Microfluidic Delivery to an Array of Luminescent Wells, Analytical Chemistry, 81 (2009) 3102-3108.

[167] M.K.a.F. Thom, Deformability and Stability of Erythrocytes in High-Frequency Electric Fields Down to Subzero Temperatures Biophysical Journal, 73 (1997) 2653-2666.

[168] T. Sun, S. Gawad, C. Bernabini, N.G. Green, H. Morgan, Broadband single cell impedance spectroscopy using maximum length sequences: theoretical analysis and practical considerations, Measurement Science & Technology, 18 (2007) 2859-2868.

[169] M.B. Sano, E.A. Henslee, E. Schmelz, R.V. Davalos, Contactless dielectrophoretic spectroscopy: Examination of the dielectric properties of cells found in blood, Electrophoresis, 32 (2011) 3164-3171.

[170] R. Georgieva, B. Neu, V.M. Shilov, E. Knippel, A. Budde, R. Latza, E. Donath, H. Kiesewetter, H. Baumler, Low Frequency Electrorotation of Fixed Red Blood Cells, 74 (1998) 2114-2120.

[171] B.P. Lynch, A.M. Hilton, G.J. Simpson, Nanoscale dielectrophoretic spectroscopy of individual immobilized mammalian blood cells, Biophysical Journal, 91 (2006) 2678-2686.

[172] J. Sudsiri, D. Wachner, J. Donath, J. Gimsa, Can molecular properties of human red blood cells be accessed by electrorotation, (2003).

[173] J.-Y. Jung, H.-Y. Kwak, Separation of Microparticles and Biological Cells Inside an Evaporating Droplet Using Dielectrophoresis, Anal. Chem., 79 (2007) 5087-5092.

[174] D.V.Z. Iana Ch. Tsoneva, and Dimiter S. Dmitrov, Red Blood Cell Dielectrophoresis in Axisymmetric Fields, Inside, 22 (2003) 2-14.

[175] Y. Hubner, K.F. Hoettges, G.E.N. Kass, S.L. Ogin, M.P. Hughes, Parallel measurements of drug actions on erythrocytes by dielectrophoresis, using a three-dimensional electrode design, Nanobiotechnology, IEE Proceedings -, 152 (2005) 150-154.

[176] J. Gimsa, T. Schnelle, G. Zechel, R. Glaser, Dielectric spectroscopy of human erythrocytes: investigations under the influence of nystatin, 66 (1994) 1244-1253.

[177] I.F. Cheng, V.E. Froude, Z. Yingxi, C. Hsueh-Chia, C. Hsien-Chang, A continuous high-throughput bioparticle sorter based on 3D traveling-wave dielectrophoresis, Lab on a Chip, 9 (2009).

[178] J. Auerswald, H.F. Knapp, Quantitative assessment of dielectrophoresis as a micro fluidic retention and separation technique for beads and human blood erythrocytes, Microelectronic Engineering, 67-68 (2003) 879-886.

[179] J. Yang, Y. Huang, X.B. Wang, F.F. Becker, P.R.C. Gascoyne, Differential analysis of human leukocytes by dielectrophoretic field-flow-fractionation, Biophysical Journal, 78 (2000) 2680-2689.

[180] J. Yang, Y. Huang, X.-B. Wang, F.F. Becker, P.R.C. Gascoyne, Dielectric Properties of Human Leukocyte Subpopulations Determined by Electrorotation as a Cell Separation Criterion, Biophysical Journal, 76 (1999) 3307-3314.

[181] W.N. White, A. Raj, M.D. Nguyen, S.J. Bertolone, P. Sethu, Clinical application of microfluidic leukocyte enrichment protocol in mild phenotype sickle cell disease (SCD), Biomedical Microdevices, 11 (2009) 477-483.

[182] A. Revzin, K. Sekine, A. Sin, R.G. Thompkins, M. Toner, Development of a microfabricated cytometry platform for characterization and sorting of individual leukocytes, Lab on a Chip, 5 (2005) 30-37.

[183] X.-B.W.a.J. Yang, Cell sesparation by dielectrophoretic field-flow-fractionation, Analytical Chemistry, 72 (2000).

[184] D. Holmes, H. Morgan, Cell sorting and separation using dielectrophoresis, in: H. Morgan (Ed.) Electrostatics 2003, Place Published, 2004, pp. 107-112.

[185] R. Pethig, V. Bressier, C. Carswell-Crumpton, Y. Chen, L. Foster-Haje, M.E. Garcia-Ojeda, R.S. Lee, G.M. Lock, M.S. Talary, K.M. Tate, Dielectrophoretic studies of the activation of human T lymphocytes using a newly developed cell profiling system, Electrophoresis, 23 (2002) 2057-2063.

[186] V.I. Furdui, D.J. Harrison, Immunomagnetic T cell capture from blood for PCR analysis using microfluidic systems, Lab on a Chip, 4 (2004) 614-618.

[187] C.M. Das, F. Becker, S. Vernon, J. Noshari, C. Joyce, P.R.C. Gascoyne, Dielectrophoretic segregation of different human cell types on microscope slides, Analytical Chemistry, 77 (2005) 2708-2719.

[188] Y. Huang, S. Joo, M. Duhon, M. Heller, B. Wallace, X. Xu, Dielectrophoretic cell separation and gene expression profiling on microelectronic chip arrays, Analytical Chemistry, 74 (2002) 3362-3371.

[189] K.L. Chan, H. Morgan, E. Morgan, I.T. Cameron, M.R. Thomas, Measurements of the dielectric properties of peripheral blood mononuclear cells and trophoblast cells using AC electrokinetic techniques, Biochimica et Biophysica Acta, 1500 (2000) 313-322.

[190] T.N.G. Adams, K. Leonard, A.R. Minerick, Frequency Sweep Rate Dependence on the Dielectrophoretic Response of Polystyrene Beads and Red Blood Cells, Biomicrofluidics, 7 (2013).

[191] K.M. Leonard, E. Rutan, S. Reeves, M. Walton, A. Pate, S. Thompson, A.R. Minerick, Dielectrophoretic Characterization of Red Blood Cells, AIChE Annual Proceedings, AIChE, 2008.

[192] M. Przybylska, M. Faber, A. Zaborowski, J. Swietoslawski, M. Bryszewska, J. SwietosÅ‚awski, Morphological changes of human erythrocytes induced by cholesterol sulphate, Clinical biochemistry, 31 (1998) 73-79.

[193] E. Du, M. Diez-Silva, G.J. Kato, M. Dao, S. Suresh, Kinetics of sickle cell biorheology and implications for painful vasoocclusive crisis, Proceedings of the National Academy of Sciences of the United States of America, 112 (2015) 1422-1427.

[194] T.N.G. Adams, P.A. Turner, A.V. Janorkar, F. Zhao, A.R. Minerick, Characterizing the dielectric properties of human mesenchymal stem cells and the effects of charged elastin-like polypeptide copolymer treatment, Biomicrofluidics, 8 (2014).

[195] R. Pethig, Dielectrophoresis: A Review of Applications for Stem Cell Research, Journal of Biomedicine and Biotechnology, (2010).

[196] B. Cetin, D.Q. Li, Dielectrophoresis in microfluidics technology, Electrophoresis, 32 (2011) 2410-2427.

[197] J. Regtmeier, R. Eichhorn, M. Viefhues, L. Bogunovic, D. Anselmetti, Electrodeless dielectrophoresis for bioanalysis: Theory, devices and applications, Electrophoresis, 32 (2011) 2253-2273.

[198] M.B. Sano, A. Salmanzadeh, R.V. Davalos, Multilayer contactless dielectrophoresis: Theoretical considerations, Electrophoresis, 33 (2012) 1938-1946.

[199] H.A. Pohl, Dielectrophoresis, Cambridge University Press, Place Published, 1978.

[200] I. Ermolina, H. Morgan, The electrokinetic properties of latex particles: comparison of electrophoresis and dielectrophoresis, J. Colloid Interface Sci., 285 (2005) 419-428.

[201] T.N.G. Adams, K.M. Leonard, A.R. Minerick, Frequency sweep rate dependence on the dielectrophoretic response of polystyrene beads and red blood cells, Biomicrofluidics, 7 (2013).

[202] S. Ozuna-Chacon, B.H. Lapizco-Encinas, M. Rito-Palomares, S.O. Martinez-Chapa, C. Reyes-Betanzo, Performance characterization of an insulator-based dielectrophoretic microdevice, Electrophoresis, 29 (2008) 3115-3122.

[203] R.C. Gallo-Villanueva, V.H. Perez-Gonzalez, R.V. Davalos, B.H. Lapizco-Encinas, Separation of mixtures of particles in a multipart microdevice employing insulator-based dielectrophoresis, Electrophoresis, 32 (2011) 2456-2465.

146

[204] R. Martinez-Duarte, Microfabrication technologies in dielectrophoresis applications-A review, Electrophoresis, 33 (2012) 3110-3132.

[205] H.O. Fatoyinbo, D. Kamchis, R. Whattingham, S.L. Ogin, M.P. Hughes, A high-throughput 3-D composite dielectrophoretic separator, Ieee Transactions on Biomedical Engineering, 52 (2005) 1347-1349.

[206] B.Y. Park, M.J. Madou, 3-D electrode designs for flow-through dielectrophoretic systems, Electrophoresis, 26 (2005) 3745-3757.

[207] Z.Z. Abidin, L. Downes, G.H. Markx, Novel electrode structures for large scale dielectrophoretic separations based on textile technology, Journal of Biotechnology, 130 (2007) 183-187.

[208] S.C. Kilchenmann, E. Rollo, E. Bianchi, C. Guiducci, Metal-coated silicon micropillars for freestanding 3D-electrode arrays in microchannels, Sensors and Actuators B-Chemical, 185 (2013) 713-719.

[209] R. Martinez-Duarte, F. Camacho-Alanis, P. Renaud, A. Ros, Dielectrophoresis of lambda-DNA using 3D carbon electrodes, Electrophoresis, 34 (2013) 1113-1122.

[210] R. Martinez-Duarte, P. Renaud, M.J. Madou, A novel approach to dielectrophoresis using carbon electrodes, Electrophoresis, 32 (2011) 2385-2392.

[211] G. Mernier, R. Martinez-Duarte, R. Lehal, F. Radtke, P. Renaud, Very High Throughput Electrical Cell Lysis and Extraction of Intracellular Compounds Using 3D Carbon Electrodes in Lab-on-a-Chip Devices, Micromachines, 3 (2012) 574-581.

[212] J. Voldman, M.L. Gray, M. Toner, M.A. Schmidt, A microfabrication-based dynamic array cytometer, Analytical chemistry, 74 (2002) 3984-3990.

[213] E.B. Cummings, Streaming dielectrophoresis for continuous-flow microfluidic devices, Ieee Engineering in Medicine and Biology Magazine, 22 (2003) 75-84.

[214] J.L. Baylon-Cardiel, B.H. Lapizco-Encinas, C. Reyes-Betanzo, A.V. Chavez-Santoscoy, S.O. Martinez-Chapa, Prediction of trapping zones in an insulator-based dielectrophoretic device, Lab on a Chip, 9 (2009) 2896-2901.

[215] F. Camacho-Alanis, L. Gan, A. Ros, Transitioning streaming to trapping in DC insulator-based dielectrophoresis for biomolecules, Sensors and Actuators B: Chemical, 173 (2012) 668-675.

[216] N. Lewpiriyawong, C. Yang, Y.C. Lam, Electrokinetically driven concentration of particles and cells by dielectrophoresis with DC-offset AC electric field, Microfluidics and Nanofluidics, 12 (2012) 723-733.

[217] J.J. Zhu, S. Sridharan, G.Q. Hu, X.C. Xuan, Joule heating effects on electrokinetic focusing and trapping of particles in constriction microchannels, Journal of Micromechanics and Microengineering, 22 (2012).

[218] C.K. Hua, D.W. Lee, I.S. Kang, Analyses on a charged electrolyte droplet in a dielectric liquid under non-uniform electric fields, Colloids and Surfaces a-Physicochemical and Engineering Aspects, 372 (2010) 86-97.

[219] Y.K. Jia, Y. Ren, L.K. Hou, W.Y. Liu, T.Y. Jiang, X.K. Deng, Y. Tao, H.Y. Jiang, Electrically controlled rapid release of actives encapsulated in double-emulsion droplets, Lab on a Chip, 18 (2018) 1121-1129.

[220] Y.K. Jia, Y.K. Ren, W.Y. Liu, L.K. Hou, Y. Tao, Q.M. Hu, H.Y. Jiang, Electrocoalescence of paired droplets encapsulated in double-emulsion drops, Lab on a Chip, 16 (2016) 4313-4318.

[221] R. An, K. Massa, D. Wipf, A. Minerick, Solution pH change in non-uniform alternating current electric fields at frequencies above the electrode charging frequency, Biomicrofluidics, 8 (2014) 064126-064126.

[222] H. Moncada Hernandez, E. Nagler, A. Minerick, Theoretical and experimental examination of particle-particle interaction effects on induced dipole moments and dielectrophoretic responses of multiple particle chains, Electrophoresis, 35 (2014) 1803-1813.

[223] SU-8 2000 Permanent Epoxy Negative PhotoresistPROCESSING GUIDELINES FOR:SU-8 2025, SU-8 2035, SU-8 2050 and SU-8 2075, in: M. Chem (Ed.).

[224] M.B. Chan-Park, J. Zhang, Y.H. Yan, C.Y. Yue, Fabrication of large SU-8 mold with high aspect ratio microchannels by UV exposure dose reduction, Sensors and Actuators B-Chemical, 101 (2004) 175-182.

[225] H.Y. Lee, C. Barber, A.R. Minerick, Improving electrokinetic microdevice stability by controlling electrolysis bubbles, Electrophoresis, 35 (2014) 1782-1789.

[226] A.R. Minerick, NSF REU Site: Chemistry / Chemical Engineering: The Bonds Between Us - A Three Year Retrospective, American Society of Engineering Education Southeast Region Proceedings, (2008).

[227] T. Trantidou, Y. Elani, E. Parsons, O. Ces, Hydrophilic surface modification of PDMS for droplet microfluidics using a simple, quick, and robust method via PVA deposition, Microsystems &Amp; Nanoengineering, 3 (2017) 16091.

[228] J.D. Wehking, M. Gabany, L. Chew, R. Kumar, Effects of viscosity, interfacial tension, and flow geometry on droplet formation in a microfluidic T-junction, Microfluidics and Nanofluidics, 16 (2014) 441-453.

[229] Y. Pang, H. Kim, Z.M. Liu, H.A. Stone, A soft microchannel decreases polydispersity of droplet generation, Lab on a Chip, 14 (2014) 4029-4034.

[230] C.S. Thompson, A.R. Abate, Adhesive-based bonding technique for PDMS microfluidic devices, Lab on a Chip, 13 (2013) 632-635.

[231] S. Bhattacharya, A. Datta, J.M. Berg, S. Gangopadhyay, Studies on surface wettability of poly(dimethyl) siloxane (PDMS) and glass under oxygen-plasma treatment and correlation with bond strength, Journal of Microelectromechanical Systems, 14 (2005) 590-597.

[232] J.C. McDonald, D.C. Duffy, J.R. Anderson, D.T. Chiu, H.K. Wu, O.J.A. Schueller, G.M. Whitesides, Fabrication of microfluidic systems in poly(dimethylsiloxane), Electrophoresis, 21 (2000) 27-40.

[233] J.N. Lee, C. Park, G.M. Whitesides, Solvent compatibility of poly(dimethylsiloxane)-based microfluidic devices, Analytical Chemistry, 75 (2003) 6544-6554.

[234] A.R. Abate, A.T. Krummel, D. Lee, M. Marquez, C. Holtze, D.A. Weitz, Photoreactive coating for high-contrast spatial patterning of microfluidic device wettability, Lab on a Chip, 8 (2008) 2157-2160.

[235] Z. Li, S.Y. Mak, A. Sauret, H.C. Shum, Syringe-pump-induced fluctuation in all-aqueous microfluidic system implications for flow rate accuracy, Lab on a Chip, 14 (2014) 744-749.

[236] W. Zeng, I. Jacobi, D.J. Beck, S. Li, H.A. Stone, Characterization of syringe-pump-driven induced pressure fluctuations in elastic microchannels, Lab on a Chip, 15 (2015) 1110-1115.

[237] W. Zeng, S.J. Li, H. Fu, Modeling of the pressure fluctuations induced by the process of droplet formation in a T-junction microdroplet generator, Sensors and Actuators a-Physical, 272 (2018) 11-17.

[238] A. Kalantarifard, E.A. Haghighi, C. Elbuken, Damping hydrodynamic fluctuations in microfluidic systems, Chemical Engineering Science, 178 (2018) 238-247.

[239] N. Kumar, R. Tyagi, Synthesis of anionic carboxylate dimeric surfactants and their interactions with electrolytes, Journal of Taibah University for Science, 9 (2015) 69-74.

[240] S. Miyagishi, K. Okada, T. Asakawa, Salt effect on critical micelle concentrations of nonionic surfactants, N-acyl-N-methylglucamides (MEGA-n), J. Colloid Interface Sci., 238 (2001) 91-95.

[241] P. Palladino, R. Ragone, Ionic Strength Effects on the Critical Mice liar Concentration of Ionic and Nonionic Surfactants: The Binding Model, Langmuir, 27 (2011) 14065-14070.

[242] P.A. Sandoz, A.J. Chung, W.M. Weaver, D. Di Carlo, Sugar Additives Improve Signal Fidelity for Implementing Two-Phase Resorufin-Based Enzyme Immunoassays, Langmuir, 30 (2014) 6637-6643.

[243] H.B. Zhou, Y. Yao, Q. Chen, G. Li, S.H. Yao, A facile microfluidic strategy for measuring interfacial tension, Applied Physics Letters, 103 (2013).

[244] Standard Infuse/Withdraw PHD ULTRA™ Syringe Pumps, Harvard Apparatus.

[245] Labsmith SPS01 Syringe Pump Brouchure.

[246] S. Bashir, J.M. Rees, W.B. Zimmerman, Simulations of microfluidic droplet formation using the two-phase level set method, Chemical Engineering Science, 66 (2011) 4733-4741.

[247] X.B. Li, F.C. Li, J.C. Yang, H. Kinoshita, M. Oishi, M. Oshima, Study on the mechanism of droplet formation in T-junction microchannel, Chemical Engineering Science, 69 (2012) 340-351.

[248] H.H. Liu, Y.H. Zhang, Droplet formation in a T-shaped microfluidic junction, Journal of Applied Physics, 106 (2009).

[249] Y. Yan, D. Guo, S.Z. Wen, Numerical simulation of junction point pressure during droplet formation in a microfluidic T-junction, Chemical Engineering Science, 84 (2012) 591-601.

[250] T.B. Jones, Electromechanics of Particles, Cambridge University Press, Place Published, 1995.

[251] J.C. Maxwell, A Treatise on Electricity and Magnetism, 3rd ed., Clarendon Press, Place Published, 1891.

[252] U. Zimmermann, J. Vienken, Electric field-induced cell-to-cell fusion, Journal of Membrane Biology, 67 (1982) 165-182.

[253] R. Kretschmer, W. Fritzsche, Pearl chain formation of nanoparticles in microelectrode gaps by dielectrophoresis, Langmuir, 20 (2004) 11797-11801.

[254] Y. Ai, S. Qian, DC dielectrophoretic particle-particle interactions and their relative motions, J. Colloid Interface Sci., 346 (2010) 448-454.

[255] N. Aubry, P. Singh, Control of electrostatic particle-particle interactions in dielectrophoresis, Europhysics Letters, 74 (2006) 623-629.

[256] V. Giner, M. Sancho, R.S. Lee, G. Martinez, R. Pethig, Transverse dipolar chaining in binary suspensions induced by rf fields, J. Phys. D-Appl. Phys., 32 (1999) 1182-1186.

[257] J. Kadaksham, P. Singh, N. Aubry, Manipulation of particles using dielectrophoresis, Mechanics Research Communications, 33 (2006) 108-122.

[258] M. Sancho, G. Martinez, S. Munoz, J.L. Sebastian, R. Pethig, Interaction between cells in dielectrophoresis and electrorotation experiments, Biomicrofluidics, 4 (2010).

[259] S. Park, Y. Zhang, T.H. Wang, S. Yang, Continuous dielectrophoretic bacterial separation and concentration from physiological media of high conductivity, Lab on a Chip, 11 (2011) 2893-2900.

[260] H.B. Zhang, M.J. Edirisinghe, S.N. Jayasinghe, Flow behaviour of dielectric liquids in an electric field, Journal of Fluid Mechanics, 558 (2006) 103-111.

[261] P.R.C. Gascoyne, J. Vykoukal, Particle separation by dielectrophoresis, Electrophoresis, 23 (2002).

[262] A. Ramos, H. Morgan, N.G. Green, A. Castellanos, Ac electrokinetics: a review of forces in microelectrode structures, Journal of Physics D: Applied Physics, 31 (1998) 2338.

[263] B.G. Hawkins, A.E. Smith, Y.A. Syed, B.J. Kirby, Continuous-flow particle separation by 3D insulative dielectrophoresis using coherently shaped, dc-biased, ac electric fields, Analytical Chemistry, 79 (2007) 7291-7300.

[264] X.B. Wang, M.P. Hughes, Y. Huang, F.F. Becker, P.R.C. Gascoyne, Non-uniform spatial distributions of both the magnitude and phase of AC electric fields determine dielectrophoretic forces, Biochimica et Biophysica Acta (BBA) - General Subjects, 1243 (1995) 185-194.

[265] J. Gimsa, Particle characterization by AC-electrokinetic phenomena: 1. A short introduction to dielectrophoresis (DP) and electrorotation (ER), Colloids and Surfaces A: Physicochemical and Engineering Aspects, 149 (1999) 451-459.

[266] P. Gascoyne, R. Pethig, J. Satayavivad, F.F. Becker, M. Ruchirawat, Dielectrophoretic detection of changes in erythrocyte membranes following malarial infection, Biochimica et Biophysica Acta (BBA) - Biomembranes, 1323 (1997) 240-252.

[267] J. Teissie, C. Ramos, Correlation between electric field pulse induced long-lived permeabilization and fusogenicity in cell membranes, Biophysical Journal, 74 (1998) 1889-1898.

[268] Z. Zhu, G. Jenkins, W.H. Zhang, M.X. Zhang, Z.C. Guan, C.Y.J. Yang, Single-molecule emulsion PCR in microfluidic droplets, Analytical and Bioanalytical Chemistry, 403 (2012) 2127-2143.

[269] R. Fair, A. Khlystov, T. Tailor, V. Ivanov, R. Evans, Chemical and biological applications of digital-microfluidic devices, IEEE Design & Test of Computers, 24 (2007) 10-24.

[270] H. Yang, V. Luk, M. Abeigawad, I. Barbulovic Nad, A. Wheeler, M. Abelgawad, A world-to-chip interface for digital microfluidics, Analytical chemistry, 81 (2009) 1061-1067.

[271] V. Luk, L. Fiddes, E. Kumacheva, A. Wheeler, Digital microfluidic hydrogel microreactors for proteomics, Proteomics, 12 (2012) 1310-1318.

[272] F. Mugele, J.C. Baret, Electrowetting: From basics to applications, Journal of physics. Condensed matter, 17 (2005) R705-R774.

[273] Y.B. Sawane, S.M. Wadhai, A.V. Limaye, A.G. Banpurkar, Electrolyte concentration effects on DC voltage electrowetting, Sensors and Actuators a-Physical, 240 (2016) 126-130.

[274] H. Moncada-Hernandez, E. Nagler, A.R. Minerick, Theoretical and experimental examination of particle-particle interaction effects on induced dipole moments and dielectrophoretic responses of multiple particle chains, Electrophoresis, 35 (2014) 1803-1813.

[275] R. An, D. Wipf, A. Minerick, Spatially variant red blood cell crenation in alternating current non-uniform fields, Biomicrofluidics, 8 (2014) 021803-021803.

[276] S. Srivastava, A. Artemiou, A. Minerick, Direct current insulator-based dielectrophoretic characterization of erythrocytes: ABO-Rh human blood typing, Electrophoresis, 32 (2011) 2530-2540.

[277] Transport phenomena, R. B. Bird, W. E. Stewart, and E. N. Lightfoot, John Wiley and Sons, Inc., New York (1960). , AIChE Journal, 7 (1961) 5J-6J.

[278] P. Garstecki, M.J. Fuerstman, H.A. Stone, G.M. Whitesides, Formation of droplets and bubbles in a microfluidic T-junction - scaling and mechanism of break-up, Lab on a Chip, 6 (2006) 437-446.

[279] S. Kole, P. Bikkina, A parametric study on the application of microfluidics for emulsion characterization, Journal of Petroleum Science and Engineering, 158 (2017) 152-159.

[280] A.R. Minerick, Advice for New Faculty: Structuring a Summer REU Project and Mentoring the Participant to a Publication, American Society of Engineering Education Proceedings, (2008).

[281] K.W. Wagner, Arch. Elektrotech (Berlin), 2 (1914) 371-387.

[282] R. Georgieva, B. New, V.M. Shilov, E. Knippel, A. Budde, R. Latza, E. Donath, H. Kiesewetter, H. Baumler, Low Frequency Electrorotation of Fixed Red Blood Cells, Biophysical Journal, 74 (1998) 2114-2120.

[283] A.D. Goater, R. Pethig, Electrorotation and dielectrophoresis, Parasitology, 117 (1998) S177-S189.

[284] U. Lei, Y.J. Lo, Review of the theory of generalised dielectrophoresis, IET Nanobiotechnol., 5 (2011) 86-106.

[285] K.L. Chan, P.R.C. Gascoyne, F.F. Becker, R. Pethig, Electrorotation of liposomes: verification of dielectric multi-shell model for cells, Biochimica et Biophysica Acta (BBA) - Lipids and Lipid Metabolism, 1349 (1997) 182-196.

[286] M.P. Hughes, AC electrokinetics: applications for nanotechnology, Nanotechnology, 11 (2000) 124.

[287] P.K. Thwar, J.J. Linderman, M.A. Burns, Electrodeless direct current dielectrophoresis using reconfigurable field-shaping oil barriers, Electrophoresis, 28 (2007) 4572-4581.

[288] C.H. Ahn, J.W. Choi, G. Beaucage, J.H. Nevin, J.B. Lee, Disposable Smart lab on a chip for point-of-care clinical diagnostics, Proceedings of the IEEE, 92 (2004) 154-173.

[289] S. Habibi, H. Moncada-Hernandez, H. Lee, A. Minerick, Exploring the Role and Impact of Faradaic Reactions on Hemolysis in Non-Uniform AC Electric Fields, Unpublished Manuscript, (2018).

[290] R. An, K. Massa, D.O. Wipf, A.R. Minerick, Solution pH change in non-uniform alternating current electric fields at frequencies above the electrode charging frequency, Biomicrofluidics, 8 (2014).

[291] H. Lee, C. Barber, A. Minerick, Platinum electrode modification: Unique surface carbonization approach to improve performance and sensitivity, Electrophoresis, 36 (2015) 1666-1673.

[292] A. Gencoglu, A. Minerick, Chemical and morphological changes on platinum microelectrode surfaces in AC and DC fields with biological buffer solutions, Lab on a Chip, 9 (2009) 1866-1873.

[293] Q. Chen, D. Wang, G.Z. Cai, Y.H. Xiong, Y.T. Li, M.H. Wang, H.L. Huo, J.H. Lin, Fast and sensitive detection of foodborne pathogen using electrochemical impedance analysis, urease catalysis and microfluidics, Biosensors & Bioelectronics, 86 (2016) 770-776.

[294] C. Zhao, M.M. Thuo, X.Y. Liu, A microfluidic paper-based electrochemical biosensor array for multiplexed detection of metabolic biomarkers, Science and Technology of Advanced Materials, 14 (2013).

[295] H. Lee, C. Barber, A. Minerick, Improving electrokinetic microdevice stability by controlling electrolysis bubbles, Electrophoresis, 35 (2014) 1782-1789.

[296] Z. Wang, C. Ivory, A.R. Minerick, Surface isoelectric focusing (sIEF) with carrier ampholyte pH gradient, Electrophoresis, (2017).

[297] S. Narayanan, M. Nikkhah, J.S. Strobl, M. Agah, Analysis of the passivation layer by testing and modeling a cell impedance micro-sensor, Sensors and Actuators a-Physical, 159 (2010) 241-247.

[298] O. Buiu, Y. Lu, I.Z. Mitrovic, S. Hall, P. Chalker, R.J. Potter, Spectroellipsometric assessment of HfO2 thin films, Thin Solid Films, 515 (2006) 623-626.

[299] A.G. Khairnar, A.M. Mahajan, Effect of post-deposition annealing temperature on RF-sputtered HfO2 thin film for advanced CMOS technology, Solid State Sciences, 15 (2013) 24-28.

[300] Y.W. Chen, M.Z. Liu, T. Kaneko, P.C. McIntyre, Atomic Layer Deposited Hafnium Oxide Gate Dielectrics for Charge-Based Biosensors, Electrochemical and Solid State Letters, 13 (2010) G29-G32.

[301] M. Szymanska, S. Gieraltowska, L. Wachnicki, M. Grobelny, K. Makowska, R. Mroczynski, Effect of reactive magnetron sputtering parameters on structural and electrical properties of hafnium oxide thin films, Applied Surface Science, 301 (2014) 28-33.

[302] Z.C.Y.a.P.K.C. A. P. Huang, Hafnium-based High-k Gate Dielectrics, Advances in Solid State Circuit Technologies,, in: P.K. Chu (Ed.), InTech, Place Published, 2010.

[303] Y. Temiz, A. Ferretti, Y. Leblebici, C. Guiducci, A comparative study on fabrication techniques for on-chip microelectrodes, Lab on a Chip, 12 (2012) 4920-4928.

[304] H. Liu, S. Dharmatilleke, D. Maurya, Dielectric materials for electrowetting-on-dielectric actuation, Microsystem Technologies, 16 (2010) 449-460.

[305] J. Lee, H. Moon, J. Fowler, T. Schoellhammer, C.J. Kim, Electrowetting and electrowetting-on-dielectric for microscale liquid handling, Sensors and actuators. A, Physical, 95 (2002) 259-268.

[306] F. Fassbender, G. Schmitt, M.J. Schoning, H. Luth, G. Buss, J.W. Schultze, Optimization of passivation layers for corrosion protection of silicon-based microelectrode arrays, Sensors and Actuators B-Chemical, 68 (2000) 128-133.

[307] B. Kuswandi, Nuriman, J. Huskens, W. Verboom, Optical sensing systems for microfluidic devices: A review, Analytica Chimica Acta, 601 (2007) 141-155.

[308] M. Vargas, N.R. Murphy, C.V. Ramana, Tailoring the index of refraction of nanocrystalline hafnium oxide thin films, Applied Physics Letters, 104 (2014).

[309] Z.W. Ma, L.X. Liu, Y.Z. Xie, Y.R. Su, H.T. Zhao, B.Y. Wang, X.Z. Cao, X.B. Qin, J. Li, Y.H. Yang, E.Q. Xie, Spectroscopic ellipsometry and positron annihilation investigation of sputtered HfO2 films, Thin Solid Films, 519 (2011) 6349-6353.

[310] C.V. Ramana, M. Vargas, G.A. Lopez, M. Noor-A-Alam, M.J. Hernandez, E.J. Rubio, Effect of oxygen/argon gas ratio on the structure and optical properties of sputter-deposited nanocrystalline HfO2 thin films, Ceramics International, 41 (2015) 6187-6193.

[311] G. Aygun, I. Yildiz, Interfacial and structural properties of sputtered HfO2 layers, Journal of Applied Physics, 106 (2009).

[312] B. Deng, G. He, J.G. Lv, X.F. Chen, J.W. Zhang, M. Zhang, Z.Q. Sun, Modulation of the structural and optical properties of sputtering-derived HfO2 films by deposition power, Optical Materials, 37 (2014) 245-250.

[313] D. Franta, I. Ohlidal, D. Necas, F. Vizda, O. Caha, M. Hason, P. Pokorny, Optical characterization of HfO2 thin films, Thin Solid Films, 519 (2011) 6085-6091.

[314] Z.W. Ma, Y.Z. Xie, L.X. Liu, Y.R. Su, H.T. Zhao, B.Y. Wang, X.B. Qin, P. Zhang, J. Li, E.Q. Xie, The effect of atomic oxygen treatment on the oxygen deficiencies of Hafnium oxide films, Optoelectronics and Advanced Materials-Rapid Communications, 4 (2010) 1493-1496.

[315] G. He, J. Gao, H.S. Chen, J.B. Cui, Z.Q. Sun, X.S. Chen, Modulating the Interface Quality and Electrical Properties of HfTiO/InGaAs Gate Stack by Atomic-Layer-Deposition-Derived Al2O3 Passivation Layer, Acs Applied Materials & Interfaces, 6 (2014) 22013-22025.

[316] J. Larkin, R. Henley, D. Bell, T. Cohen Karni, J. Rosenstein, M. Wanunu, Slow DNA transport through nanopores in hafnium oxide membranes, ACS nano, 7 (2013) 10121-10128.

[317] J. Larkin, R. Henley, M. Muthukumar, J. Rosenstein, M. Wanunu, High-bandwidth protein analysis using solid-state nanopores, Biophysical Journal, 106 (2014) 696-704.

[318] S.H. Shen, I.S. Wang, H. Cheng, C.T. Lin, An enhancement of high-k/oxide stacked dielectric structure for silicon-based multi-nanowire biosensor in cardiac troponin I detection, Sensors and Actuators B-Chemical, 218 (2015) 303-309.

[319] J. Shim, J. Rivera, R. Bashir, Electron beam induced local crystallization of HfO2 nanopores for biosensing applications, Nanoscale, 5 (2013) 10887-10893.

[320] B. Dorvel, B. Reddy, J. Go, C. Guevara, E. Salm, C. Duarte Guevara, M. Alam, R. Bashir, Silicon nanowires with high-k hafnium oxide dielectrics for sensitive detection of small nucleic acid oligomers, ACS nano, 6 (2012) 6150-6164.

[321] J. Oh, H.-J. Jang, W.-J. Cho, M.S. Islam, Highly sensitive electrolyte-insulator-semiconductor pH sensors enabled by silicon nanowires with Al2O3/SiO2 sensing membrane, Sensors and actuators. B, Chemical, 171 (2012) 238-243.

[322] W. Davey, O. Buiu, M. Werner, I.Z. Mitrovic, S. Hall, P. Chalker, Estimate of dielectric density using spectroscopic ellipsometry, Microelectronic Engineering, 86 (2009) 1905-1907.

[323] J. Wang, U. Author, R.A. Fava, L.L. Marton, 6.2 Crystallite Size and Lamellar Thickness by X-Ray Methods Crystal Structure and Morphology, Place Published, 1980.

[324] B.D.a.W. Cullity, J.W., Elements of X-ray Diffraction, American Journal of Physics, 25 (1957) 394-395.

[325] G. He, L.D. Zhang, G.H. Li, M. Liu, L.Q. Zhu, S.S. Pan, Spectroscopic ellipsometry characterization of nitrogen-incorporated HfO2 gate dielectrics grown by radio-frequency reactive sputtering, Applied Physics Letters, 86 (2005) 3.

[326] G.M. Xiong, S.J. Yuan, J.K. Wang, A.T. Do, N.S. Tan, K.S. Yeo, C. Choong, Imparting electroactivity to polycaprolactone fibers with heparin-doped polypyrrole: Modulation of hemocompatibility and inflammatory responses, Acta Biomaterialia, 23 (2015) 240-249.

[327] Q. Shi, Q.F. Fan, W. Ye, J.W. Hou, S.C. Wong, X.D. Xu, J.H. Yin, Binary release of ascorbic acid and lecithin from core-shell nanofibers on blood-contacting surface for reducing long-term hemolysis of erythrocyte, Colloids and Surfaces B-Biointerfaces, 125 (2015) 28-33.

[328] M. Ramzan, A.M. Rana, E. Ahmed, M.F. Wasiq, A.S. Bhatti, M. Hafeez, A. Ali, M.Y. Nadeem, Optical characterization of hafnium oxide thin films for heat mirrors, Materials Science in Semiconductor Processing, 32 (2015) 22-30.

[329] D.M. Hausmann, R.G. Gordon, Surface morphology and crystallinity control in the atomic layer deposition (ALD) of hafnium and zirconium oxide thin films, Journal of Crystal Growth, 249 (2003) 251-261.

[330] D.M. Hausmann, E. Kim, J. Becker, R.G. Gordon, Atomic layer deposition of hafnium and zirconium oxides using metal amide precursors, Chemistry of Materials, 14 (2002) 4350-4358.

[331] D. Triyoso, R. Liu, D. Roan, M. Ramon, N.V. Edwards, R. Gregory, D. Werho, J. Kulik, G. Tam, E. Irwin, X.D. Wang, L.B. La, C. Hobbs, R. Garcia, J. Baker, B.E. White, P. Tobin, Impact of deposition and annealing temperature on material and electrical characteristics of ALD HfO2, Journal of the Electrochemical Society, 151 (2004) F220-F227.

[332] H. O'Connor, A. van Riessen, G. Burton, D. Cookson, R. Garrett, Characterisation of Standard Reference Materials Using Synchrotron Radiation Diffraction Data, Advances in X-ray Analysis. This volume, (1999).

[333] C.W. Lin, Y.T. Chiang, Tetragonal hafnium oxide film prepared by low-temperature oxidation, Japanese Journal of Applied Physics, 53 (2014).

[334] L. Pereira, P. Barquinha, E. Fortunato, R. Martins, Influence of the oxygen/argon ratio on the properties of sputtered hafnium oxide, Materials Science and Engineering B-Solid State Materials for Advanced Technology, 118 (2005) 210-213.

[335] B.R. Laboratories, Slide Composition Sheet, 2017.

[336] S. Pandey, P. Kothari, S.K. Sharma, S. Verma, K.J. Rangra, Impact of post deposition annealing in O-2 ambient on structural properties of nanocrystalline hafnium oxide thin film, Journal of Materials Science-Materials in Electronics, 27 (2016) 7055-7061.

[337] M. Toledano-Luque, E.S. Andres, A. del Prado, I. Martil, M.L. Lucia, G. Gonzalez-Diaz, F.L. Martinez, W. Bohne, J. Rohrich, E. Strub, High-pressure reactively sputtered HfO2: Composition, morphology, and optical properties, Journal of Applied Physics, 102 (2007).

[338] G.E. Jellison, Spectroscopic ellipsometry data analysis: measured versus calculated quantities, Thin Solid Films, 313 (1998) 33-39.

[339] Q.H. Phan, Y.L. Lo, Characterization of optical/physical properties of anisotropic thin films with rough surfaces by Stokes-Mueller ellipsometry, Optical Materials Express, 6 (2016) 1774-1789.

[340] A. Hakeem, M. Ramzan, E. Ahmed, A.M. Rana, N.R. Khalid, N.A. Niaz, A. Shakoor, S. Ali, U. Asghar, M.Y. Nadeem, Effects of vacuum annealing on surface and

optical constants of hafnium oxide thin films, Materials Science in Semiconductor Processing, 30 (2015) 98-103.

[341] H. Lee, K. Lee, B. Ahn, J. Xu, L.F. Xu, K. Woh, A new fabrication process for uniform SU-8 thick photoresist structures by simultaneously removing edge bead and air bubbles, Journal of Micromechanics and Microengineering, 21 (2011).

[342] X.D. Ye, H.Z. Liu, Y.C. Ding, H.S. Li, B.H. Lu, Research on the cast molding process for high quality PDMS molds, Microelectronic Engineering, 86 (2009) 310-313.

[343] S. Natarajan, D.A. Chang-Yen, B.K. Gale, Large-area, high-aspect-ratio SU-8 molds for the fabrication of PDMS microfluidic devices, Journal of Micromechanics and Microengineering, 18 (2008).

[344] M.E. Group, PDMS ISOPROPANOL MICROFLUIDICS.

[345] CAD/Art Services :: outputcity, photomasks, photomask services, phototools, photolithography.

[346] A.C. Hatch, J.S. Fisher, S.L. Pentoney, D.L. Yang, A.P. Lee, Tunable 3D droplet self-assembly for ultra-high-density digital micro-reactor arrays, Lab on a Chip, 11 (2011) 2509-2517.

[347] N.L. Jeon, S.K.W. Dertinger, D.T. Chiu, I.S. Choi, A.D. Stroock, Generation of solution and surface gradients using microfluidic systems, Langmuir, 16 (2000) 8311-8316.

[348] D.R. Link, Geometrically mediated breakup of drops in microfluidic devices, Physical review letters, 92 (2004) 054503.

[349] C. Ody, C. Baroud, E. de Langre, Transport of wetting liquid plugs in bifurcating microfluidic channels, J. Colloid Interface Sci., 308 (2007) 231-238.

[350] W. Saadi, S.-J. Wang, F. Lin, N. Jeon, A parallel-gradient microfluidic chamber for quantitative analysis of breast cancer cell chemotaxis, Biomedical Microdevices, 8 (2006) 109-118.

[351] Y. Song, M. Baudoin, P. Manneville, C. Baroud, The air-liquid flow in a microfluidic airway tree, Medical engineering & physics, 33 (2011) 849-856.

[352] Y. Song, P. Manneville, C. Baroud, Local interactions and the global organization of a two-phase flow in a branching tree, Physical review letters, 105 (2010) 134501.

[353] H.A. Stone, A.D. Stroock, A. Ajdari, Engineering flows in small devices: Microfluidics toward a lab-on-a-chip, Annual Review of Fluid Mechanics, 36 (2004) 381-411.

[354] C.-G. Yang, Z.-R. Xu, A. Lee, J.-H. Wang, A microfluidic concentration-gradient droplet array generator for the production of multi-color nanoparticles, Lab on a chip, 13 (2013) 2815-2820.

[355] D.R. Link, S.L. Anna, D.A. Weitz, H.A. Stone, Geometrically mediated breakup of drops in microfluidic devices, Physical Review Letters, 92 (2004).

[356] C.T. Riche, E.J. Roberts, M. Gupta, R.L. Brutchey, N. Malmstadt, Flow invariant droplet formation for stable parallel microreactors, Nature Communications, 7 (2016).

[357] A.R. Minerick, J.L. Collins, K.M. Leonard, T.N.G. Adams, Methods and systems for identifying a particle using dielectrophoresis, Michigan Technological University, United States, 2018.

A   Effects of Additives on Droplet Size and Stability in a Microfluidic T-junction Device

A.1   Surfactant Effects

Epure water was used as a baseline control, exploring how the presence of a surfactant (Krytox 157 FSH, from here on referred to as Krytox) affected droplet size and stability when being generated in a microfluidic T-junction and collected in a chamber. Research has shown that the presence of surfactant decreases interfacial tension with increasing concentration [84]. Table A.1 presents each set of continuous and dispersed phases used for the control experiments. Figure A.1 demonstrates the expected natural log trend of the effect of surfactant concentration on droplet size.

Table A-1. Aqueous dispersed phase and continuous oil phase compositions used for the epure water control experiments.

Dispersed Phase	Continuous Phase
epure water	0.33 mM Krytox in FC-40
epure water	0.66 mM Krytox in FC-40
epure water	1.00 mM Krytox in FC-40
epure water	1.75 mM Krytox in FC-40
epure water	2.00 mM Krytox in FC-40
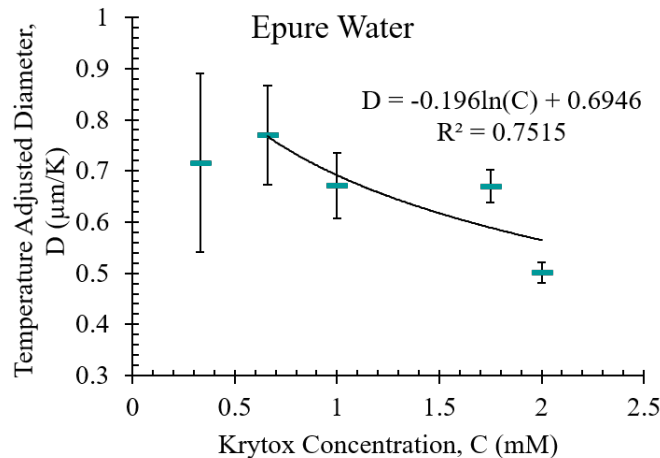
Figure A-1. Epure water control for confirming surfactant effect on droplet size. The droplet size, as a function of surfactant concentration, follows the expected natural log trend.

A.2   Salt Effects

Salts are an important part of making isotonic solutions of different conductivity, and their presence has been shown to decrease the critical micelle concentration (CMC) with increasing salt concentration [239-241]. Before exploring isotonic solutions (containing both salts and dextrose), the presence of salts alone was investigated and the behavior

compared to literature. Table A.2 presents each set dispersed phase used for the salt-only experiments. Continuous phases were FC-40 with a range of Krytox concentrations (0.33 to 2 mM). Figure A.2 presents the results of each salt concentration. The trend of decreasing droplet size with increasing surfactant concentration, as seen with epure water and as expected from literature, held for each salt concentration. When compared to epure water, the presence of salt decreased the droplet size in every case, which is consistent with literature findings that state that the presence of salt decreases the interfacial tension.

Table A-2. Aqueous dispersed phase compositions used for the salt-only control experiments.

Salt -only Solution	Epure Water (ml)	Salt Stock (µl)
0 mM	25.000	0.0
0.960 mM	24.976	24.0
2.616 mM	24.935	65.4
13.892 mM	24.653	347.2
24.122 mM	24.397	603.0
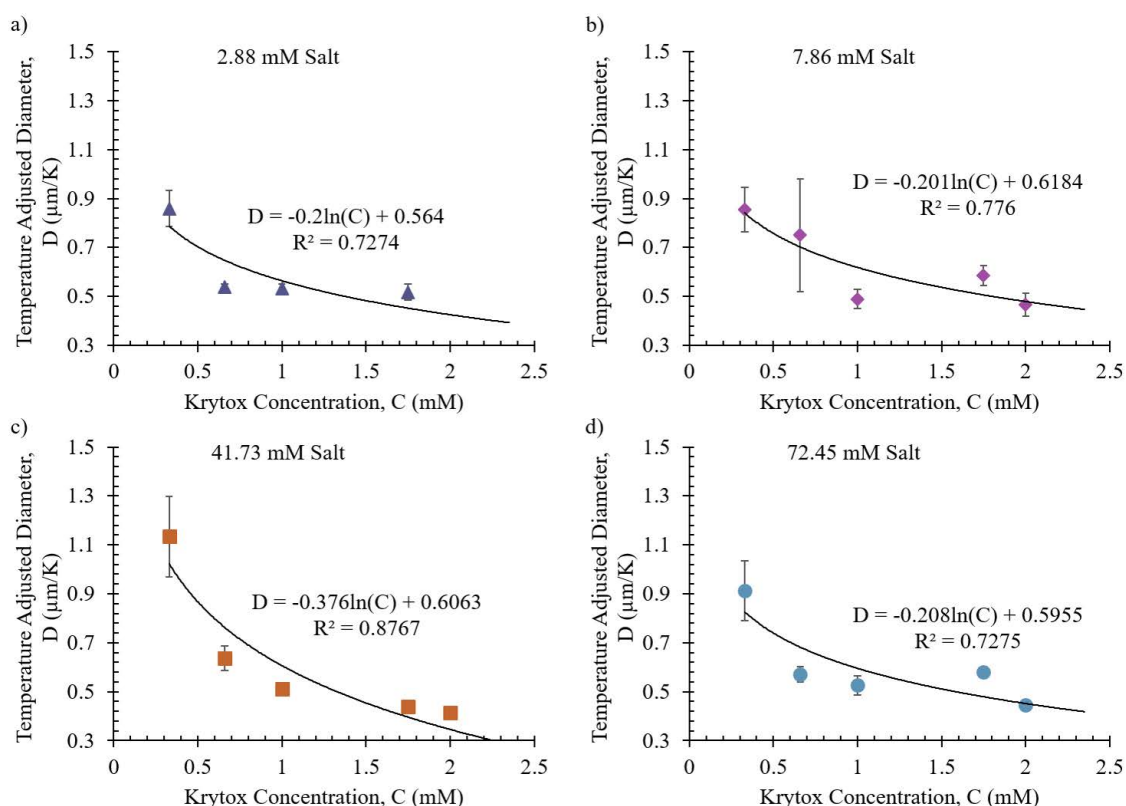
Figure A-2. Temperature adjusted droplet size versus surfactant concentration for a) 0.960 mM salt, b) 2.616 mM salt, c) 13.892 mM salt, and d) 24.122 mM salt. Increasing surfactant concentration yielded a natural log trend line consistent with literature for each salt-only solution.

A.3　　　Dextrose Effects

Dextrose-only solutions were also investigated. It has been seen that the presence of sugar does affect the interface and thus must be included when exploring isotonic solutions [242]. Table A.3 presents each dispersed phase used for the dextrose-only experiments. Continuous phases were FC-40 with a range of Krytox concentrations (0.33 to 2 mM). Figure A.3 presents the results of each dextrose concentration. The natural log trend on decreasing droplet size with increasing surfactant concentration was consistent for all dextrose concentrations. Unlike the salt, whose presence always decreased the droplet size, only the lowest surfactant concentration, 0.33 mM, resulted in a decrease in droplet size for each dextrose concentration. The highest three surfactant concentrations, 1-2 mM, all dextrose concentrations increased in droplet size, indicating an increase in interfacial tension. At 0.66 mM Krytox, the second highest dextrose concentration caused an increase in droplet size, while all others decreased the average droplet size.
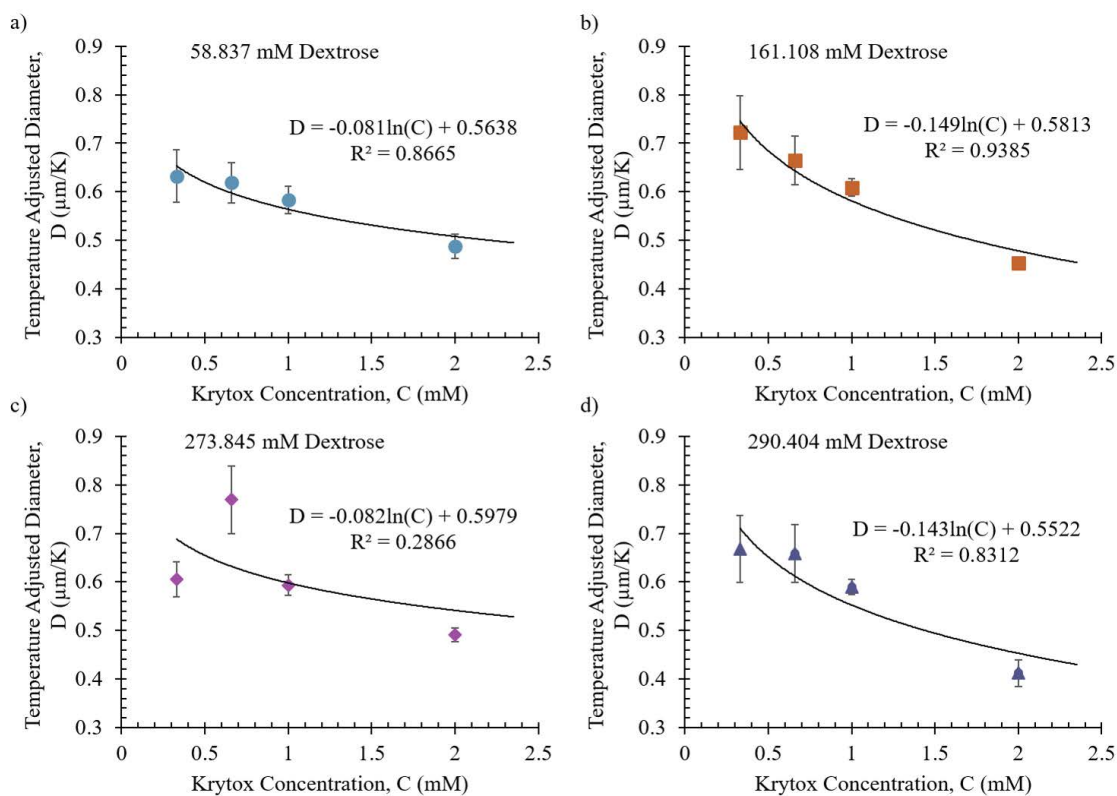
Figure A-3. Temperature adjusted droplet size versus surfactant concentration for a) 58.837 mM dextrose, b) 161.108 mM dextrose, c) 273.845 mM dextrose, and d) 290.404 mM dextrose. The increase of surfactant concentration yields a natural log trendline consistent with literature for each slat-only aqueous phase.

Table A-3. Aqueous dispersed phase compositions used for the dextrose-only control experiments.

Dextrose -only Solution	Epure Water (ml)	Dextrose (g)
0 mM	25.000	0.0000
58.837 mM	25.000	0.2650
161.108 mM	25.000	0.7256
273.845 mM	25.000	1.2334
290.404 mM	25.000	1.3080

A.4 Combined Salt/Dextrose Effects (Conductivity)

Since both salt and dextrose affect droplet breakup and stability in droplet microfluidics, their combination to form isotonic solutions of varied conductivity were explored. Table A.4 presents each dispersed phase used for the conductivity experiments. Continuous phases were FC-40 with a range of Krytox concentrations (0.33 to 2 mM). Figure A.4 present the results of each conductivity. When compared to epure water, all but the lowest surfactant concentration, 0.33 mM, when combined with solutions of different
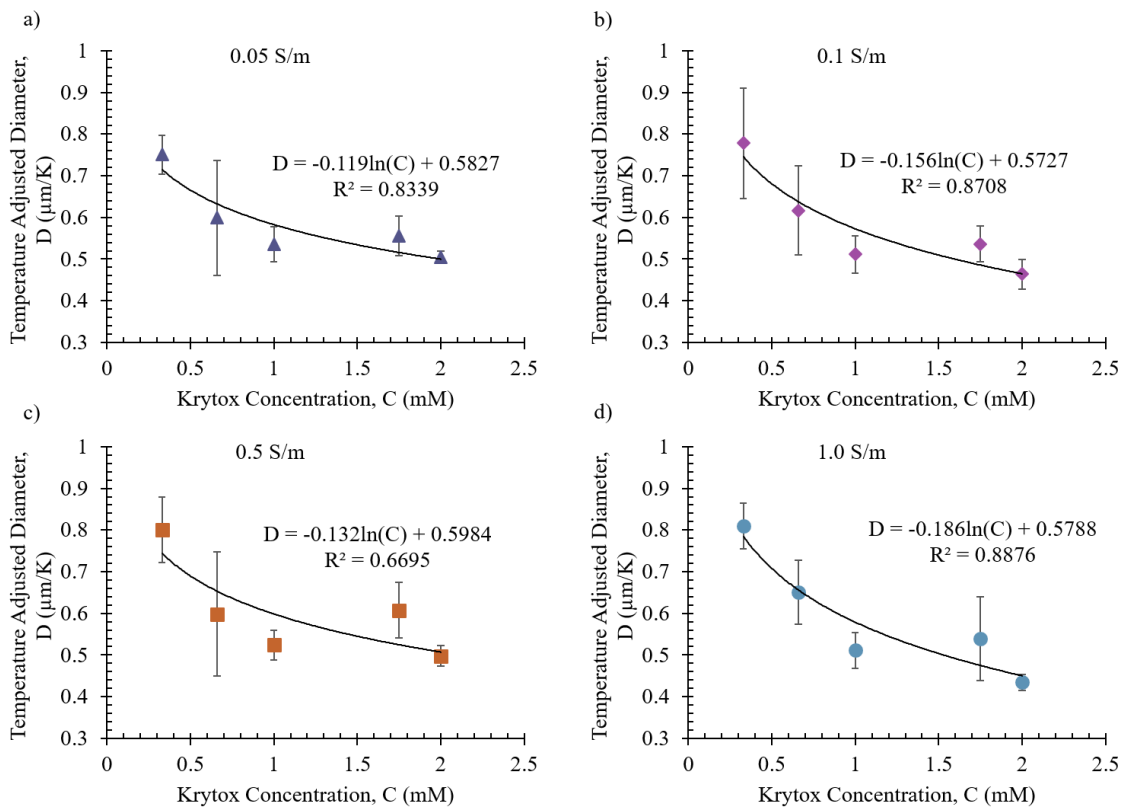
Figure A-4. Temperature adjusted droplet size versus surfactant concentration for a) 0.05 S/m, b) 0.1 S/m, c) 0.5 S/m, and d) 1.0 S/m. The increase of surfactant concentration yields a natural log trend line consistent with literature for each slat-only aqueous phase.

conductivities, decreased the average droplet size. The average droplet size was increased for the lowest concentration.

Table A-4. Aqueous dispersed phase compositions used for the conductivity experiments.

Conductivity Solution	Epure Water (ml)	Salt Stock (µl)	Dextrose (g)
0.0000055 S/m	25.000	0.0	0.0000
0.05 S/m	24.976	24.0	1.3080
0.1 S/m	24.935	65.4	1.2334
0.5 S/m	24.653	347.2	0.7256
1.0 S/m	24.397	603.0	0.2650

A.5   Coefficient of Variance

The coefficient of variance was found for each combination of additives. The results are shown in Table A.5. All bolded values fall in the typical range seen in literature of 2-10% [53, 243]. All values in green are below 5%. Overall, CV decreased with increased surfactant concentration.

Table A-5. Coefficient of Variance (in Percent) of droplet diameter for each combination of phases.

Krytox (mM)		*0.33*	*0.66*	*1*	*1.75*	*2*
Epure Water		15.4	12.9	10.3	**5.2**	**4.1**
Salt-Only (mM)	0.960	**8.7**	**2.2**	**3.5**	6.4	-
	2.616	10.5	30.7	**8.3**	**6.9**	10.1
	13.892	14.5	**8.0**	**4.5**	**2.0**	**4.3**
	24.122	13.4	**5.5**	**7.5**	**3.4**	**4.3**
Dextrose-Only (mM)	58.8	**8.6**	**6.7**	**4.8**	-	**5.1**
	161.6	10.5	**7.6**	**3.0**	-	**2.9**
	273.8	**5.9**	**9.1**	**3.6**	-	**2.8**
	290.4	10.3	**9.0**	**2.7**	-	6.6
Conductivity (S/m)	0.05	**6.3**	23.1	**7.9**	**8.6**	**2.8**
	0.1	17.0	17.3	**8.8**	**8.0**	7.8
	0.5	**9.8**	24.9	**6.9**	11.0	**4.9**
	1.0	**6.7**	11.8	**8.4**	18.6	**4.5**

A.6   Steady State Determination

An experiment was conducted to determine when the pump reached steady state. Droplets were measured starting at 1 minute up to 75 minutes. The results, in Figure A.5, show that after 10 minutes the droplet size stabilized, meaning the pump had reached steady state.
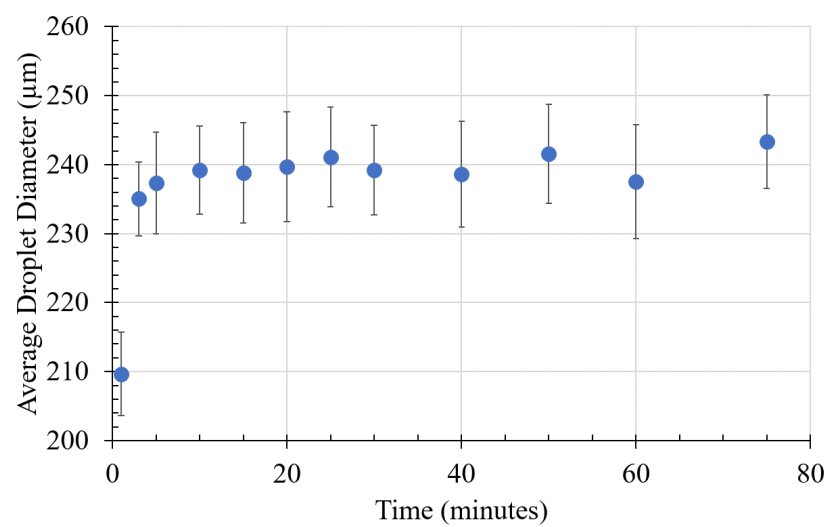
Figure A-5. Average droplet size, with standard deviation, versus time. Within the first ten minutes, the system reached steady state.

B   Simulations on Portage and Superior

Superior and Portage, high-performance computing infrastructure at Michigan Technological University, were used in obtaining results presented in this dissertation. (Note: the number of processors is equal to the CPU time divided by the wall time)

B.1   Simulations on Superior

Wall time	CPU time	Memory (GB)
0:01:48	0:14:58	6.00
3:07:42	40:21:27	6.05
0:02:27	0:20:57	6.71
0:57:05	4:38:13	6.71
0:00:14	0:00:10	3.67
0:00:01	0:00:01	3.00
0:00:01	0:00:01	3.00
0:00:01	0:00:01	3.00
0:00:02	0:00:01	3.00
0:00:01	0:00:01	3.00
0:00:02	0:00:01	3.07
0:00:02	0:00:01	3.07
0:00:02	0:00:01	3.00
0:00:02	0:00:01	3.07
0:00:01	0:00:01	3.00
0:00:01	0:00:01	3.00
0:00:02	0:00:01	3.72
0:00:01	0:00:01	3.00
0:00:01	0:00:01	3.00
0:00:01	0:00:01	0
0:00:02	0:00:01	3.00
0:00:01	0:00:01	3.00
0:00:00	0:00:01	0
0:00:01	0:00:01	3.00
0:00:01	0:00:01	3.00
0:00:02	0:00:01	1.92
0:00:01	0:00:01	1.94
0:00:04	0:00:01	1.87
0:00:01	0:00:01	1.87
0:00:01	0:00:01	0
0:00:01	0:00:01	1.87

Wall time	CPU time	Memory (GB)
0:00:02	0:00:01	1.95
0:00:22	0:00:55	2.41
0:00:52	0:03:38	3.21
98:36:11	606:46:31	5.37
0:10:27	0:38:50	24.65
2:05:25	16:04:47	29.82
13:53:25	104:47:30	50.89
1:26:58	11:27:43	24.30
1:40:22	14:42:03	30.70
1:56:55	15:46:18	25.08
1:55:53	15:32:56	32.81
3:02:28	23:31:07	31.50
3:04:27	21:53:22	36.01
0:00:24	0:00:52	2.39
0:00:29	0:00:54	2.39
0:00:20	0:00:52	2.40
0:09:24	0:34:16	19.14
0:00:59	0:08:16	2.71

B.2   Simulations on Portage

Wall time	CPU time	Memory (GB)	Wall time	CPU time	Memory (GB)
0:05:34:51	03:07:33:15	10.87	0:13:24:47	07:09:11:16	15.36
0:03:37:55	02:03:23:00	11.42	0:06:08:26	03:07:50:58	14.66
0:00:00:20	00:00:00:56	6.10	0:05:31:15	02:23:47:47	16.46
0:04:08:27	02:10:48:51	11.14	0:04:59:28	02:16:08:46	14.31
0:05:55:22	03:14:36:22	11.66	0:04:23:22	02:08:33:37	15.31
0:03:27:56	02:02:32:15	11.35	0:10:42:42	05:20:02:20	16.86
0:03:06:44	01:21:18:56	11.49	3:07:44:46	42:01:22:47	15.44
0:02:58:45	01:18:08:04	11.26	2:21:03:22	36:05:31:34	14.77
0:04:25:58	02:15:00:53	11.05	0:00:00:59	00:00:07:36	10.40
0:03:05:52	01:21:06:16	11.48	3:08:05:43	38:06:16:19	16.79
0:02:57:47	01:19:09:52	11.98	0:18:28:18	06:00:47:52	16.73
0:02:38:57	01:14:26:49	11.63	0:08:41:23	04:16:58:57	15.84
0:00:00:09	00:00:00:11	3.67	0:09:02:16	04:21:18:37	15.35
0:03:57:27	02:09:41:57	11.39	0:00:00:12	00:00:00:11	3.67
0:03:19:53	01:23:13:24	11.33	0:00:00:06	00:00:00:11	3.67
0:02:33:04	01:12:55:29	11.38	0:00:00:21	00:00:01:01	6.03
0:02:46:55	01:16:32:10	11.44	0:00:00:36	00:00:04:09	6.93
0:00:00:23	00:00:00:46	6.15	0:00:38:43	00:10:09:38	6.05
0:00:00:18	00:00:00:50	6.15	0:00:00:18	00:00:01:02	6.02
0:00:00:17	00:00:00:45	6.14	0:00:00:18	00:00:01:07	6.02
0:00:00:17	00:00:00:52	6.15	0:00:00:19	00:00:01:02	6.02
0:00:00:18	00:00:00:49	6.14	0:00:00:20	00:00:01:03	6.03
0:00:00:18	00:00:00:51	6.14	0:00:00:17	00:00:01:01	6.03
0:00:00:18	00:00:00:48	6.15	0:00:38:02	00:09:59:32	6.02
0:00:00:18	00:00:00:49	6.14	0:00:32:26	00:07:58:57	6.09
0:00:00:18	00:00:00:48	6.15	0:00:29:56	00:07:21:38	6.04
0:00:00:18	00:00:00:49	6.15	0:00:19:52	00:05:09:33	11.83
0:00:00:06	00:00:00:11	3.67	0:00:18:16	00:04:44:32	6.02
0:00:00:17	00:00:00:44	6.15	0:00:20:38	00:05:22:00	6.03
0:00:00:18	00:00:00:50	6.15	0:00:19:33	00:05:04:31	6.02
0:00:00:21	00:00:00:54	6.15	0:00:30:22	00:07:27:53	5.96
0:00:00:21	00:00:00:56	6.16	0:00:19:49	00:05:08:05	6.02
0:00:08:34	00:01:31:09	22.88	0:00:19:45	00:05:08:00	5.96
0:02:47:39	01:12:34:27	17.10	0:00:26:06	00:06:24:34	6.02
0:16:29:51	00:16:28:42	5.09	0:00:00:23	00:00:00:49	6.02
0:01:40:17	00:21:42:52	15.23	0:00:00:19	00:00:00:46	6.03

Wall time	CPU time	Memory (GB)	Wall time	CPU time	Memory (GB)
0:00:00:24	00:00:00:59	6.03	0:00:56:49	00:10:09:24	6.19
0:00:00:16	00:00:00:58	6.03	0:00:21:20	00:02:12:22	9.56
0:00:38:44	00:10:09:23	6.09	0:00:21:04	00:02:14:42	9.57
0:00:00:23	00:00:01:47	6.12	0:00:00:14	00:00:00:43	6.08
2:16:30:28	42:17:57:11	6.25	0:06:27:00	03:06:38:18	6.09
0:00:11:14	00:02:52:41	6.09	0:00:00:14	00:00:00:41	6.08
0:00:00:17	00:00:00:57	6.03	0:00:00:14	00:00:00:44	6.08
0:00:11:16	00:02:53:25	6.09	0:00:00:14	00:00:00:43	6.08
0:01:28:56	00:22:07:11	6.09	0:00:00:21	00:00:00:38	6.08
0:02:17:07	01:12:13:06	6.09	0:00:00:13	00:00:00:39	6.08
0:00:56:06	00:14:47:12	6.09	0:00:00:18	00:00:01:11	6.03
0:00:04:29	00:01:06:06	6.09	0:00:00:20	00:00:01:33	6.09
0:00:07:13	00:01:49:45	6.29	0:00:00:15	00:00:00:43	6.04
0:02:15:23	01:09:39:11	6.09	0:00:00:16	00:00:01:04	6.03
0:01:07:48	00:16:43:26	6.13	0:00:00:20	00:00:01:34	6.09
0:00:01:04	00:00:10:21	6.11	0:00:00:21	00:00:01:34	6.09
0:01:01:01	00:16:01:23	6.10	0:00:00:20	00:00:01:39	6.09
0:05:33:40	03:13:26:58	6.03	0:00:00:21	00:00:01:35	6.09
0:00:32:22	00:04:05:54	6.14	0:00:00:20	00:00:01:37	6.09
0:01:27:48	00:19:08:11	6.18	0:21:00:37	10:16:09:30	6.23
0:08:36:09	05:05:51:29	11.85	0:02:10:48	01:07:04:09	9.07
0:05:08:34	03:03:53:17	6.14	1:01:34:09	11:06:56:31	13.22
0:00:38:29	00:09:59:47	6.15	1:10:20:35	15:01:00:38	12.94
0:01:01:46	00:14:48:20	6.14	0:00:07:27	00:01:54:03	6.21
0:00:00:22	00:00:01:52	6.09	0:00:00:56	00:00:10:32	6.13
0:00:00:55	00:00:09:13	6.31	0:06:02:49	03:14:29:40	10.89
0:00:01:51	00:00:07:54	6.22	0:01:17:16	00:20:22:49	6.07
0:00:01:56	00:00:07:49	6.22	0:08:57:54	05:07:46:26	10.88
0:00:26:47	00:01:46:44	6.25	0:02:38:47	01:14:17:06	10.87
0:00:01:07	00:00:02:27	6.13	0:00:00:35	00:00:04:21	6.19
0:00:00:40	00:00:02:07	6.09	0:03:05:25	01:19:38:58	10.33
0:00:00:58	00:00:03:20	6.03	1:04:00:00	16:22:29:42	10.45
0:00:00:16	00:00:00:42	6.08	0:23:07:54	14:00:42:00	10.52
0:01:00:46	00:10:14:49	6.19	0:00:00:21	00:00:01:03	6.03
0:00:20:58	00:02:15:37	9.57	3:20:00:12	56:13:26:18	10.56
0:00:20:33	00:02:11:45	9.57			
0:00:22:57	00:02:25:42	9.56			
0:00:21:39	00:02:27:19	9.57			

C   Copyright Documentation: Permission for Material Reproduced in Chapter 2

C.1   Permission for Figure 2.1 a and b

	1400 Townsend Drive HOUGHTON, MI 49931 United States Attn: Adrienne Minerick
Billing Type	Invoice
Billing address	Adrienne Minerick Chemical Sciences and Engineering Office 202H 1400 Townsend Drive HOUGHTON, MI 49931 United States Attn: Adrienne Minerick
Total	0.00 USD

ORDER MORE   CLOSE WINDOW

170

C.2 Permission for Figure 2.1 c

Order Completed

Thank you for your order.

This Agreement between Adrienne Minerick ("You") and Royal Society of Chemistry ("Royal Society of Chemistry") consists of your license details and the terms and conditions provided by Royal Society of Chemistry and Copyright Clearance Center.

Your confirmation email will contain your order number for future reference.

printable details

License Number	4377220213635
License date	Jun 27, 2018
Licensed Content Publisher	Royal Society of Chemistry
Licensed Content Publication	Lab on a Chip
Licensed Content Title	Rails and anchors: guiding and trapping droplet microreactors in two dimensions
Licensed Content Author	Paul Abbyad,Rémi Dangla,Antigoni Alexandrou,Charles N. Baroud
Licensed Content Date	Nov 9, 2010
Licensed Content Volume	11
Licensed Content Issue	5
Type of Use	Thesis/Dissertation
Requestor type	academic/educational
Portion	figures/tables/images
Number of figures/tables/images	1
Distribution quantity	10
Format	print and electronic
Will you be translating?	no
Order reference number	
Title of the thesis/dissertation	Reverse Insulator Dielectrophoresis: Utilizing Droplet Microenvironments for Discerning Molecular Expressions on Cell Surfaces
Expected completion date	Jul 2018
Estimated size	175
Requestor Location	Adrienne Minerick Chemical Sciences and Engineering Building 203

1400 Townsend Drive
HOUGHTON, MI 49931
United States
Attn: Adrienne Minerick

Billing Type   Invoice

Billing address   Adrienne Minerick
                      Chemical Sciences and Engineering
                      Office 202H
                      1400 Townsend Drive
                      HOUGHTON, MI 49931
                      United States
                      Attn: Adrienne Minerick

Total   0.00 USD

ORDER MORE   CLOSE WINDOW

172

C.3   Permission for Figure 2.1 d

ROYAL SOCIETY OF CHEMISTRY LICENSE
TERMS AND CONDITIONS

Jul 03, 2018

This Agreement between Adrienne Minerick ("You") and Royal Society of Chemistry ("Royal Society of Chemistry") consists of your license details and the terms and conditions provided by Royal Society of Chemistry and Copyright Clearance Center.

License Number	4377830264079
License date	Jun 28, 2018
Licensed Content Publisher	Royal Society of Chemistry
Licensed Content Publication	Lab on a Chip
Licensed Content Title	Dropspots: a picoliter array in a microfluidic device
Licensed Content Author	Christian H. J. Schmitz,Amy C. Rowat,Sarah Köster,David A. Weitz
Licensed Content Date	Oct 28, 2008
Licensed Content Volume	9
Licensed Content Issue	1
Type of Use	Thesis/Dissertation
Requestor type	academic/educational
Portion	figures/tables/images
Number of figures/tables/images	2
Format	print and electronic
Distribution quantity	10
Will you be translating?	no
Order reference number	
Title of the thesis/dissertation	Reverse Insulator Dielectrophoresis: Utilizing Droplet Microenvironments for Discerning Molecular Expressions on Cell Surfaces
Expected completion date	Jul 2018
Estimated size	175
Requestor Location	Adrienne Minerick Chemical Sciences and Engineering Building 203 1400 Townsend Drive HOUGHTON, MI 49931 United States Attn: Adrienne Minerick
Billing Type	Invoice
Billing Address	Adrienne Minerick Chemical Sciences and Engineering Office 202H 1400 Townsend Drive HOUGHTON, MI 49931 United States Attn: Adrienne Minerick
Total	0.00 USD

Terms and Conditions

This License Agreement is between {Requestor Name} ("You") and The Royal Society of Chemistry ("RSC") provided by the Copyright Clearance Center ("CCC"). The license consists of your order details, the terms and conditions provided by the Royal Society of Chemistry, and the payment terms and conditions.

RSC / TERMS AND CONDITIONS

INTRODUCTION

The publisher for this copyrighted material is The Royal Society of Chemistry. By clicking "accept" in connection with completing this licensing transaction, you agree that the following terms and conditions apply to this transaction (along with the Billing and Payment terms and conditions established by CCC, at the time that you opened your RightsLink account and that are available at any time at .

LICENSE GRANTED

The RSC hereby grants you a non-exclusive license to use the aforementioned material anywhere in the world subject to the terms and conditions indicated herein. Reproduction of the material is confined to the purpose and/or media for which permission is hereby given.

RESERVATION OF RIGHTS

The RSC reserves all rights not specifically granted in the combination of (i) the license details provided by your and accepted in the course of this licensing transaction; (ii) these terms and conditions; and (iii) CCC's Billing and Payment terms and conditions.

REVOCATION

The RSC reserves the right to revoke this license for any reason, including, but not limited to, advertising and promotional uses of RSC content, third party usage, and incorrect source figure attribution.

THIRD-PARTY MATERIAL DISCLAIMER

If part of the material to be used (for example, a figure) has appeared in the RSC publication with credit to another source, permission must also be sought from that source. If the other source is another RSC publication these details should be included in your RightsLink request. If the other source is a third party, permission must be obtained from the third party. The RSC disclaims any responsibility for the reproduction you make of items owned by a third party.

PAYMENT OF FEE

If the permission fee for the requested material is waived in this instance, please be advised that any future requests for the reproduction of RSC materials may attract a fee.

ACKNOWLEDGEMENT

The reproduction of the licensed material must be accompanied by the following acknowledgement:

Reproduced ("Adapted" or "in part") from {Reference Citation} (or Ref XX) with permission of The Royal Society of Chemistry.

If the licensed material is being reproduced from New Journal of Chemistry (NJC), Photochemical & Photobiological Sciences (PPS) or Physical Chemistry Chemical Physics (PCCP) you must include one of the following acknowledgements:

For figures originally published in NJC:

Reproduced ("Adapted" or "in part") from {Reference Citation} (or Ref XX) with permission of The Royal Society of Chemistry (RSC) on behalf of the European Society for Photobiology, the European Photochemistry Association and the RSC.

For figures originally published in PPS:

Reproduced ("Adapted" or "in part") from {Reference Citation} (or Ref XX) with permission of The Royal Society of Chemistry (RSC) on behalf of the Centre National de la Recherche Scientifique (CNRS) and the RSC.

For figures originally published in PCCP:

Reproduced ("Adapted" or "in part") from {Reference Citation} (or Ref XX) with permission of the PCCP Owner Societies.

174

HYPERTEXT LINKS

With any material which is being reproduced in electronic form, you must include a hypertext link to the original RSC article on the RSC's website. The recommended form for the hyperlink is http://dx.doi.org/10.1039/DOI suffix, for example in the link http://dx.doi.org/10.1039/b110420a the DOI suffix is 'b110420a'. To find the relevant DOI suffix for the RSC article in question, go to the Journals section of the website and locate the article in the list of papers for the volume and issue of your specific journal. You will find the DOI suffix quoted there.

LICENSE CONTINGENT ON PAYMENT

While you may exercise the rights licensed immediately upon issuance of the license at the end of the licensing process for the transaction, provided that you have disclosed complete and accurate details of your proposed use, no license is finally effective unless and until full payment is received from you (by CCC) as provided in CCC's Billing and Payment terms and conditions. If full payment is not received on a timely basis, then any license preliminarily granted shall be deemed automatically revoked and shall be void as if never granted. Further, in the event that you breach any of these terms and conditions or any of CCC's Billing and Payment terms and conditions, the license is automatically revoked and shall be void as if never granted. Use of materials as described in a revoked license, as well as any use of the materials beyond the scope of an unrevoked license, may constitute copyright infringement and the RSC reserves the right to take any and all action to protect its copyright in the materials.

WARRANTIES

The RSC makes no representations or warranties with respect to the licensed material.

INDEMNITY

You hereby indemnify and agree to hold harmless the RSC and the CCC, and their respective officers, directors, trustees, employees and agents, from and against any and all claims arising out of your use of the licensed material other than as specifically authorized pursuant to this licence.

NO TRANSFER OF LICENSE

This license is personal to you or your publisher and may not be sublicensed, assigned, or transferred by you to any other person without the RSC's written permission.

NO AMENDMENT EXCEPT IN WRITING

This license may not be amended except in a writing signed by both parties (or, in the case of "Other Conditions, v1.2", by CCC on the RSC's behalf).

OBJECTION TO CONTRARY TERMS

You hereby acknowledge and agree that these terms and conditions, together with CCC's Billing and Payment terms and conditions (which are incorporated herein), comprise the entire agreement between you and the RSC (and CCC) concerning this licensing transaction, to the exclusion of all other terms and conditions, written or verbal, express or implied (including any terms contained in any purchase order, acknowledgment, check endorsement or other writing prepared by you). In the event of any conflict between your obligations established by these terms and conditions and those established by CCC's Billing and Payment terms and conditions, these terms and conditions shall control.

JURISDICTION

This license transaction shall be governed by and construed in accordance with the laws of the District of Columbia. You hereby agree to submit to the jurisdiction of the courts located in the District of Columbia for purposes of resolving any disputes that may arise in connection with this licensing transaction.

LIMITED LICENSE

The following terms and conditions apply to specific license types:

Translation

This permission is granted for non-exclusive world English rights only unless your license was granted for translation rights. If you licensed translation rights you may only translate

175

this content into the languages you requested. A professional translator must perform all translations and reproduce the content word for word preserving the integrity of the article.

Intranet

If the licensed material is being posted on an Intranet, the Intranet is to be password-protected and made available only to bona fide students or employees only. All content posted to the Intranet must maintain the copyright information line on the bottom of each image. You must also fully reference the material and include a hypertext link as specified above.

Copies of Whole Articles

All copies of whole articles must maintain, if available, the copyright information line on the bottom of each page.

Other Conditions

v1.2

Gratis licenses (referencing $0 in the Total field) are free. Please retain this printable license for your reference. No payment is required.

If you would like to pay for this license now, please remit this license along with your payment made payable to "COPYRIGHT CLEARANCE CENTER" otherwise you will be invoiced within 48 hours of the license date. Payment should be in the form of a check or money order referencing your account number and this invoice number {Invoice Number}. Once you receive your invoice for this order, you may pay your invoice by credit card. Please follow instructions provided at that time.

Make Payment To:

Copyright Clearance Center

29118 Network Place

Chicago, IL 60673-1291

For suggestions or comments regarding this order, contact Rightslink Customer Support: customercare@copyright.com or +1-855-239-3415 (toll free in the US) or +1-978-646-2777.

Questions? customercare@copyright.com or +1-855-239-3415 (toll free in the US) or +1-978-646-2777.

C.4 Permission for Figure 2.2 a

**ROYAL SOCIETY OF CHEMISTRY LICENSE
TERMS AND CONDITIONS**

Jul 02, 2018

This Agreement between Adrienne Minerick ("You") and Royal Society of Chemistry ("Royal Society of Chemistry") consists of your license details and the terms and conditions provided by Royal Society of Chemistry and Copyright Clearance Center.

License Number	4377211112056
License date	Jun 27, 2018
Licensed Content Publisher	Royal Society of Chemistry
Licensed Content Publication	Lab on a Chip
Licensed Content Title	Faster multiple emulsification with drop splitting
Licensed Content Author	Adam R. Abate, David A. Weitz
Licensed Content Date	Apr 19, 2011
Licensed Content Volume	11
Licensed Content Issue	11
Type of Use	Thesis/Dissertation
Requestor type	academic/educational
Portion	figures/tables/images
Number of figures/tables/images	1
Format	print and electronic
Distribution quantity	10
Will you be translating?	no
Order reference number	
Title of the thesis/dissertation	Reverse Insulator Dielectrophoresis: Utilizing Droplet Microenvironments for Discerning Molecular Expressions on Cell Surfaces
Expected completion date	Jul 2018
Estimated size	175
Requestor Location	Adrienne Minerick Chemical Sciences and Engineering Building 203 1400 Townsend Drive HOUGHTON, MI 49931 United States Attn: Adrienne Minerick
Billing Type	Invoice
Billing Address	Adrienne Minerick Chemical Sciences and Engineering Office 202H 1400 Townsend Drive HOUGHTON, MI 49931 United States Attn: Adrienne Minerick
Total	0.00 USD

This License Agreement is between {Requestor Name} ("You") and The Royal Society of Chemistry ("RSC") provided by the Copyright Clearance Center ("CCC"). The license consists of your order details, the terms and conditions provided by the Royal Society of Chemistry, and the payment terms and conditions.

RSC / TERMS AND CONDITIONS

INTRODUCTION

The publisher for this copyrighted material is The Royal Society of Chemistry. By clicking "accept" in connection with completing this licensing transaction, you agree that the following terms and conditions apply to this transaction (along with the Billing and Payment terms and conditions established by CCC, at the time that you opened your RightsLink account and that are available at any time at .

LICENSE GRANTED

The RSC hereby grants you a non-exclusive license to use the aforementioned material anywhere in the world subject to the terms and conditions indicated herein. Reproduction of the material is confined to the purpose and/or media for which permission is hereby given.

RESERVATION OF RIGHTS

The RSC reserves all rights not specifically granted in the combination of (i) the license details provided by your and accepted in the course of this licensing transaction; (ii) these terms and conditions; and (iii) CCC's Billing and Payment terms and conditions.

REVOCATION

The RSC reserves the right to revoke this license for any reason, including, but not limited to, advertising and promotional uses of RSC content, third party usage, and incorrect source figure attribution.

THIRD-PARTY MATERIAL DISCLAIMER

If part of the material to be used (for example, a figure) has appeared in the RSC publication with credit to another source, permission must also be sought from that source. If the other source is another RSC publication these details should be included in your RightsLink request. If the other source is a third party, permission must be obtained from the third party. The RSC disclaims any responsibility for the reproduction you make of items owned by a third party.

PAYMENT OF FEE

If the permission fee for the requested material is waived in this instance, please be advised that any future requests for the reproduction of RSC materials may attract a fee.

ACKNOWLEDGEMENT

The reproduction of the licensed material must be accompanied by the following acknowledgement:

Reproduced ("Adapted" or "in part") from {Reference Citation} (or Ref XX) with permission of The Royal Society of Chemistry.

If the licensed material is being reproduced from New Journal of Chemistry (NJC), Photochemical & Photobiological Sciences (PPS) or Physical Chemistry Chemical Physics (PCCP) you must include one of the following acknowledgements:

For figures originally published in NJC:

Reproduced ("Adapted" or "in part") from {Reference Citation} (or Ref XX) with permission of The Royal Society of Chemistry (RSC) on behalf of the European Society for Photobiology, the European Photochemistry Association and the RSC.

For figures originally published in PPS:

Reproduced ("Adapted" or "in part") from {Reference Citation} (or Ref XX) with permission of The Royal Society of Chemistry (RSC) on behalf of the Centre National de la Recherche Scientifique (CNRS) and the RSC.

For figures originally published in PCCP:

Reproduced ("Adapted" or "in part") from {Reference Citation} (or Ref XX) with permission of the PCCP Owner Societies.

HYPERTEXT LINKS

With any material which is being reproduced in electronic form, you must include a hypertext link to the original RSC article on the RSC's website. The recommended form for the hyperlink is http://dx.doi.org/10.1039/DOI suffix, for example in the link http://dx.doi.org/10.1039/b110420a the DOI suffix is 'b110420a'. To find the relevant DOI suffix for the RSC article in question, go to the Journals section of the website and locate the article in the list of papers for the volume and issue of your specific journal. You will find the DOI suffix quoted there.

LICENSE CONTINGENT ON PAYMENT

While you may exercise the rights licensed immediately upon issuance of the license at the end of the licensing process for the transaction, provided that you have disclosed complete and accurate details of your proposed use, no license is finally effective unless and until full payment is received from you (by CCC) as provided in CCC's Billing and Payment terms and conditions. If full payment is not received on a timely basis, then any license preliminarily granted shall be deemed automatically revoked and shall be void as if never granted. Further, in the event that you breach any of these terms and conditions or any of CCC's Billing and Payment terms and conditions, the license is automatically revoked and shall be void as if never granted. Use of materials as described in a revoked license, as well as any use of the materials beyond the scope of an unrevoked license, may constitute copyright infringement and the RSC reserves the right to take any and all action to protect its copyright in the materials.

WARRANTIES

The RSC makes no representations or warranties with respect to the licensed material.

INDEMNITY

You hereby indemnify and agree to hold harmless the RSC and the CCC, and their respective officers, directors, trustees, employees and agents, from and against any and all claims arising out of your use of the licensed material other than as specifically authorized pursuant to this licence.

NO TRANSFER OF LICENSE

This license is personal to you or your publisher and may not be sublicensed, assigned, or transferred by you to any other person without the RSC's written permission.

NO AMENDMENT EXCEPT IN WRITING

This license may not be amended except in a writing signed by both parties (or, in the case of "Other Conditions, v1.2", by CCC on the RSC's behalf).

OBJECTION TO CONTRARY TERMS

You hereby acknowledge and agree that these terms and conditions, together with CCC's Billing and Payment terms and conditions (which are incorporated herein), comprise the entire agreement between you and the RSC (and CCC) concerning this licensing transaction, to the exclusion of all other terms and conditions, written or verbal, express or implied (including any terms contained in any purchase order, acknowledgment, check endorsement or other writing prepared by you). In the event of any conflict between your obligations established by these terms and conditions and those established by CCC's Billing and Payment terms and conditions, these terms and conditions shall control.

JURISDICTION

This license transaction shall be governed by and construed in accordance with the laws of the District of Columbia. You hereby agree to submit to the jurisdiction of the courts located in the District of Columbia for purposes of resolving any disputes that may arise in connection with this licensing transaction.

LIMITED LICENSE

The following terms and conditions apply to specific license types:

Translation

This permission is granted for non-exclusive world English rights only unless your license was granted for translation rights. If you licensed translation rights you may only translate

179

this content into the languages you requested. A professional translator must perform all
translations and reproduce the content word for word preserving the integrity of the article.
Intranet
If the licensed material is being posted on an Intranet, the Intranet is to be password-
protected and made available only to bona fide students or employees only. All content
posted to the Intranet must maintain the copyright information line on the bottom of each
image. You must also fully reference the material and include a hypertext link as specified
above.
Copies of Whole Articles
All copies of whole articles must maintain, if available, the copyright information line on the
bottom of each page.
Other Conditions
v1.2
Gratis licenses (referencing $0 in the Total field) are free. Please retain this printable license
for your reference. No payment is required.
If you would like to pay for this license now, please remit this license along with
yourpayment made payable to "COPYRIGHT CLEARANCE CENTER" otherwise you will
be invoiced within 48 hours of the license date. Payment should be in the form of a check or
money order referencing your account number and this invoice number {Invoice Number}.
Once you receive your invoice for this order, you may pay your invoice by credit card.
Please follow instructions provided at that time.
Make Payment To:
Copyright Clearance Center
29118 Network Place
Chicago, IL 60673-1291
For suggestions or comments regarding this order, contact Rightslink Customer Support:
customercare@copyright.com or +1-855-239-3415 (toll free in the US) or +1-978-646-2777.

**Questions? customercare@copyright.com or +1-855-239-3415 (toll free in the US) or
+1-978-646-2777.**

C.5 Permission for Figure 2.2 b

AIP PUBLISHING LICENSE
TERMS AND CONDITIONS

Jul 03, 2018

This Agreement between Adrienne Minerick ("You") and AIP Publishing ("AIP Publishing") consists of your license details and the terms and conditions provided by AIP Publishing and Copyright Clearance Center.

License Number	4377220732941
License date	Jun 27, 2018
Licensed Content Publisher	AIP Publishing
Licensed Content Publication	Applied Physics Letters
Licensed Content Title	Controlled electrocoalescence in microfluidics: Targeting a single lamella
Licensed Content Author	Craig Priest, Stephan Herminghaus, Ralf Seemann
Licensed Content Date	Sep 25, 2006
Licensed Content Volume	89
Licensed Content Issue	13
Type of Use	Thesis/Dissertation
Requestor type	Student
Format	Print and electronic
Portion	Figure/Table
Number of figures/tables	1
Title of your thesis / dissertation	Reverse Insulator Dielectrophoresis: Utilizing Droplet Microenvironments for Discerning Molecular Expressions on Cell Surfaces
Expected completion date	Jul 2018
Estimated size (number of pages)	175
Requestor Location	Adrienne Minerick Chemical Sciences and Engineering Building 203 1400 Townsend Drive HOUGHTON, MI 49931 United States Attn: Adrienne Minerick
Billing Type	Invoice
Billing Address	Adrienne Minerick Chemical Sciences and Engineering Office 202H 1400 Townsend Drive HOUGHTON, MI 49931 United States Attn: Adrienne Minerick
Total	0.00 USD

Terms and Conditions

AIP Publishing -- Terms and Conditions: Permissions Uses

AIP Publishing hereby grants to you the non-exclusive right and license to use and/or distribute the Material according to the use specified in your order, on a one-time basis, for the specified term, with a maximum distribution equal to the number that you have ordered. Any links or other content accompanying the Material are not the subject of this license.

1. You agree to include the following copyright and permission notice with the reproduction of the Material:"Reprinted from [FULL CITATION], with the permission of AIP Publishing." For an article, the credit line and permission notice must be printed on the first page of the article or book chapter. For photographs, covers, or tables, the notice may appear with the Material, in a footnote, or in the reference list.
2. If you have licensed reuse of a figure, photograph, cover, or table, it is your responsibility to ensure that the material is original to AIP Publishing and does not contain the copyright of another entity, and that the copyright notice of the figure, photograph, cover, or table does not indicate that it was reprinted by AIP Publishing, with permission, from another source. Under no circumstances does AIP Publishing purport or intend to grant permission to reuse material to which it does not hold appropriate rights.
   You may not alter or modify the Material in any manner. You may translate the Material into another language only if you have licensed translation rights. You may not use the Material for promotional purposes.
3. The foregoing license shall not take effect unless and until AIP Publishing or its agent, Copyright Clearance Center, receives the Payment in accordance with Copyright Clearance Center Billing and Payment Terms and Conditions, which are incorporated herein by reference.
4. AIP Publishing or Copyright Clearance Center may, within two business days of granting this license, revoke the license for any reason whatsoever, with a full refund payable to you. Should you violate the terms of this license at any time, AIP Publishing, or Copyright Clearance Center may revoke the license with no refund to you. Notice of such revocation will be made using the contact information provided by you. Failure to receive such notice will not nullify the revocation.
5. AIP Publishing makes no representations or warranties with respect to the Material. You agree to indemnify and hold harmless AIP Publishing, and their officers, directors, employees or agents from and against any and all claims arising out of your use of the Material other than as specifically authorized herein.
6. The permission granted herein is personal to you and is not transferable or assignable without the prior written permission of AIP Publishing. This license may not be amended except in a writing signed by the party to be charged.
7. If purchase orders, acknowledgments or check endorsements are issued on any forms containing terms and conditions which are inconsistent with these provisions, such inconsistent terms and conditions shall be of no force and effect. This document, including the CCC Billing and Payment Terms and Conditions, shall be the entire agreement between the parties relating to the subject matter hereof.

This Agreement shall be governed by and construed in accordance with the laws of the State of New York. Both parties hereby submit to the jurisdiction of the courts of New York County for purposes of resolving any disputes that may arise hereunder.

V1.2

Questions? customercare@copyright.com or +1-855-239-3415 (toll free in the US) or +1-978-646-2777.

182

C.6   Permission for Figure 2.2 c

Order Completed

Thank you for your order.

This Agreement between Adrienne Minerick ("You") and Royal Society of Chemistry ("Royal Society of Chemistry") consists of your license details and the terms and conditions provided by Royal Society of Chemistry and Copyright Clearance Center.

Your confirmation email will contain your order number for future reference.

printable details

License Number	4377830434662
License date	Jun 28, 2018
Licensed Content Publisher	Royal Society of Chemistry
Licensed Content Publication	Lab on a Chip
Licensed Content Title	Combinatorial generation of droplets by controlled assembly and coalescence
Licensed Content Author	Eujin Um, Matthew E. Rogers, Howard A. Stone
Licensed Content Date	Sep 26, 2013
Licensed Content Volume	13
Licensed Content Issue	23
Type of Use	Thesis/Dissertation
Requestor type	academic/educational
Portion	figures/tables/images
Number of figures/tables/images	1
Distribution quantity	10
Format	print and electronic
Will you be translating?	no
Order reference number	
Title of the thesis/dissertation	Reverse Insulator Dielectrophoresis: Utilizing Droplet Microenvironments for Discerning Molecular Expressions on Cell Surfaces
Expected completion date	Jul 2018
Estimated size	175
Requestor Location	Adrienne Minerick Chemical Sciences and Engineering Building 203

https://s100.copyright.com/AppDispatchServlet   1/2

	1400 Townsend Drive
	HOUGHTON, MI 49931
	United States
	Attn: Adrienne Minerick
Billing Type	Invoice
Billing address	Adrienne Minerick
	Chemical Sciences and Engineering
	Office 202H
	1400 Townsend Drive
	HOUGHTON, MI 49931
	United States
	Attn: Adrienne Minerick
Total	0.00 USD

ORDER MORE   CLOSE WINDOW

184

C.7 Permission for Figure 2.2 d

SPRINGER NATURE LICENSE
TERMS AND CONDITIONS

Jul 02, 2018

This Agreement between Adrienne Minerick ("You") and Springer Nature ("Springer Nature") consists of your license details and the terms and conditions provided by Springer Nature and Copyright Clearance Center.

License Number	4377830657495
License date	Jun 28, 2018
Licensed Content Publisher	Springer Nature
Licensed Content Publication	Nature
Licensed Content Title	Control and detection of chemical reactions in microfluidic systems
Licensed Content Author	Andrew J. deMello
Licensed Content Date	Jul 26, 2006
Licensed Content Volume	442
Licensed Content Issue	7101
Type of Use	Thesis/Dissertation
Requestor type	academic/university or research institute
Format	print and electronic
Portion	figures/tables/illustrations
Number of figures/tables/illustrations	1
High-res required	no
Will you be translating?	no
Circulation/distribution	< 501
Author of this Springer Nature content	no
Title	Reverse Insulator Dielectrophoresis: Utilizing Droplet Microenvironments for Discerning Molecular Expressions on Cell Surfaces
Instructor name	n/a
Institution name	Michigan Technological University
Expected presentation date	Jul 2018
Portions	Figure 2
Requestor Location	Adrienne Minerick Chemical Sciences and Engineering Building 203 1400 Townsend Drive HOUGHTON, MI 49931 United States Attn: Adrienne Minerick
Billing Type	Invoice
Billing Address	Adrienne Minerick Chemical Sciences and Engineering Office 202H

185

1400 Townsend Drive
HOUGHTON, MI 49931
United States
Attn: Adrienne Minerick

Total   0.00 USD

Terms and Conditions

Springer Nature Terms and Conditions for RightsLink Permissions

Springer Customer Service Centre GmbH (the Licensor) hereby grants you a non-exclusive, world-wide licence to reproduce the material and for the purpose and requirements specified in the attached copy of your order form, and for no other use, subject to the conditions below:

1. The Licensor warrants that it has, to the best of its knowledge, the rights to license reuse of this material. However, you should ensure that the material you are requesting is original to the Licensor and does not carry the copyright of another entity (as credited in the published version).

   If the credit line on any part of the material you have requested indicates that it was reprinted or adapted with permission from another source, then you should also seek permission from that source to reuse the material.

2. Where **print only** permission has been granted for a fee, separate permission must be obtained for any additional electronic re-use.

3. Permission granted **free of charge** for material in print is also usually granted for any electronic version of that work, provided that the material is incidental to your work as a whole and that the electronic version is essentially equivalent to, or substitutes for, the print version.

4. A licence for 'post on a website' is valid for 12 months from the licence date. This licence does not cover use of full text articles on websites.

5. Where **'reuse in a dissertation/thesis'** has been selected the following terms apply: Print rights for up to 100 copies, electronic rights for use only on a personal website or institutional repository as defined by the Sherpa guideline (www.sherpa.ac.uk/romeo/).

6. Permission granted for books and journals is granted for the lifetime of the first edition and does not apply to second and subsequent editions (except where the first edition permission was granted free of charge or for signatories to the STM Permissions Guidelines http://www.stm-assoc.org/copyright-legal-affairs/permissions/permissions-guidelines/), and does not apply for editions in other languages unless additional translation rights have been granted separately in the licence.

7. Rights for additional components such as custom editions and derivatives require additional permission and may be subject to an additional fee. Please apply to Journalpermissions@springernature.com/bookpermissions@springernature.com for these rights.

8. The Licensor's permission must be acknowledged next to the licensed material in print. In electronic form, this acknowledgement must be visible at the same time as the figures/tables/illustrations or abstract, and must be hyperlinked to the journal/book's homepage. Our required acknowledgement format is in the Appendix below.

9. Use of the material for incidental promotional use, minor editing privileges (this does not include cropping, adapting, omitting material or any other changes that affect the meaning, intention or moral rights of the author) and copies for the disabled are permitted under this licence.

10. Minor adaptations of single figures (changes of format, colour and style) do not require the Licensor's approval. However, the adaptation should be credited as shown in Appendix below.

Appendix — Acknowledgements:

For Journal Content:
Reprinted by permission from [**the Licensor**]: [**Journal Publisher** (e.g.
Nature/Springer/Palgrave)] [**JOURNAL NAME**] [**REFERENCE CITATION**
(Article name, Author(s) Name), [**COPYRIGHT**] (year of publication)

For **Advance Online Publication papers**:
Reprinted by permission from [**the Licensor**]: [**Journal Publisher** (e.g.
Nature/Springer/Palgrave)] [**JOURNAL NAME**] [**REFERENCE CITATION**
(Article name, Author(s) Name), [**COPYRIGHT**] (year of publication), advance
online publication, day month year (doi: 10.1038/sj.[JOURNAL ACRONYM].)

For **Adaptations/Translations**:
Adapted/Translated by permission from [**the Licensor**]: [**Journal Publisher** (e.g.
Nature/Springer/Palgrave)] [**JOURNAL NAME**] [**REFERENCE CITATION**
(Article name, Author(s) Name), [**COPYRIGHT**] (year of publication)

Note: For any republication from the British Journal of Cancer, the following credit line style applies:

Reprinted/adapted/translated by permission from [**the Licensor**]: on behalf of Cancer
Research UK: : [**Journal Publisher** (e.g. Nature/Springer/Palgrave)] [**JOURNAL
NAME**] [**REFERENCE CITATION** (Article name, Author(s) Name),
[**COPYRIGHT**] (year of publication).

For **Advance Online Publication** papers:
Reprinted by permission from The [**the Licensor**]: on behalf of Cancer Research UK:
[**Journal Publisher** (e.g. Nature/Springer/Palgrave)] [**JOURNAL NAME**]
[**REFERENCE CITATION** (Article name, Author(s) Name), [**COPYRIGHT**] (year
of publication), advance online publication, day month year (doi: 10.1038/sj.
[JOURNAL ACRONYM])

For **Book content**:
Reprinted/adapted by permission from [**the Licensor**]: [**Book Publisher** (e.g.
Palgrave Macmillan, Springer etc) [**Book Title**] by [**Book author**(s)]
[**COPYRIGHT**] (year of publication)

Other Conditions:

Version 1.0

Questions? customercare@copyright.com or +1-855-239-3415 (toll free in the US) or
+1-978-646-2777.

187

C.8   Permission for Figure 2.4

Copyright Clearance Center

RightsLink®

Home   Create Account   Help

ACS Publications
Most Trusted. Most Cited. Most Read.

Title: Hysteresis in Multiphase Microfluidics at a T-Junction

Author: Michele Zagnoni, Jamie Anderson, Jonathan M. Cooper

Publication: Langmuir

Publisher: American Chemical Society

Date: Jun 1, 2010

Copyright © 2010, American Chemical Society

LOGIN

If you're a copyright.com user, you can login to RightsLink using your copyright.com credentials.

Already a **RightsLink user** or want to learn more?

PERMISSION/LICENSE IS GRANTED FOR YOUR ORDER AT NO CHARGE

This type of permission/license, instead of the standard Terms & Conditions, is sent to you because no fee is being charged for your order. Please note the following:

- Permission is granted for your request in both print and electronic formats, and translations.
- If figures and/or tables were requested, they may be adapted or used in part.
- Please print this page for your records and send a copy of it to your publisher/graduate school.
- Appropriate credit for the requested material should be given as follows: "Reprinted (adapted) with permission from (COMPLETE REFERENCE CITATION). Copyright (YEAR) American Chemical Society." Insert appropriate information in place of the capitalized words.
- One-time permission is granted only for the use specified in your request. No additional uses are granted (such as derivative works or other editions). For any other uses, please submit a new request.

If credit is given to another source for the material you requested, permission must be obtained from that source.

BACK   CLOSE WINDOW

C.9   Permission for Figure 2.7

ELSEVIER LICENSE
TERMS AND CONDITIONS

Jul 02, 2018

This Agreement between Adrienne Minerick ("You") and Elsevier ("Elsevier") consists of your license details and the terms and conditions provided by Elsevier and Copyright Clearance Center.

License Number	4377220115229
License date	Jun 27, 2018
Licensed Content Publisher	Elsevier
Licensed Content Publication	Biosensors and Bioelectronics
Licensed Content Title	Dielectrophoretic platforms for bio-microfluidic systems
Licensed Content Author	Khashayar Khoshmanesh,Saeid Nahavandi,Sara Baratchi,Arnan Mitchell,Kourosh Kalantar-zadeh
Licensed Content Date	Jan 15, 2011
Licensed Content Volume	26
Licensed Content Issue	5
Licensed Content Pages	15
Start Page	1800
End Page	1814
Type of Use	reuse in a thesis/dissertation
Intended publisher of new work	other
Portion	figures/tables/illustrations
Number of figures/tables/illustrations	1
Format	both print and electronic
Are you the author of this Elsevier article?	No
Will you be translating?	No
Original figure numbers	Figure 3
Title of your thesis/dissertation	Reverse Insulator Dielectrophoresis: Utilizing Droplet Microenvironments for Discerning Molecular Expressions on Cell Surfaces
Publisher of new work	Michigan Technological University
Expected completion date	Jul 2018
Estimated size (number of pages)	175
Requestor Location	Adrienne Minerick Chemical Sciences and Engineering Building 203 1400 Townsend Drive HOUGHTON, MI 49931 United States Attn: Adrienne Minerick

Publisher Tax ID   98-0397604

Total   0.00 USD

Terms and Conditions

INTRODUCTION

1. The publisher for this copyrighted material is Elsevier. By clicking "accept" in connection with completing this licensing transaction, you agree that the following terms and conditions apply to this transaction (along with the Billing and Payment terms and conditions established by Copyright Clearance Center, Inc. ("CCC"), at the time that you opened your Rightslink account and that are available at any time at http://myaccount.copyright.com).

GENERAL TERMS

2. Elsevier hereby grants you permission to reproduce the aforementioned material subject to the terms and conditions indicated.

3. Acknowledgement: If any part of the material to be used (for example, figures) has appeared in our publication with credit or acknowledgement to another source, permission must also be sought from that source. If such permission is not obtained then that material may not be included in your publication/copies. Suitable acknowledgement to the source must be made, either as a footnote or in a reference list at the end of your publication, as follows:

"Reprinted from Publication title, Vol /edition number, Author(s), Title of article / title of chapter, Pages No., Copyright (Year), with permission from Elsevier [OR APPLICABLE SOCIETY COPYRIGHT OWNER]." Also Lancet special credit - "Reprinted from The Lancet, Vol. number, Author(s), Title of article, Pages No., Copyright (Year), with permission from Elsevier."

4. Reproduction of this material is confined to the purpose and/or media for which permission is hereby given.

5. Altering/Modifying Material: Not Permitted. However figures and illustrations may be altered/adapted minimally to serve your work. Any other abbreviations, additions, deletions and/or any other alterations shall be made only with prior written authorization of Elsevier Ltd. (Please contact Elsevier at permissions@elsevier.com). No modifications can be made to any Lancet figures/tables and they must be reproduced in full.

6. If the permission fee for the requested use of our material is waived in this instance, please be advised that your future requests for Elsevier materials may attract a fee.

7. Reservation of Rights: Publisher reserves all rights not specifically granted in the combination of (i) the license details provided by you and accepted in the course of this licensing transaction, (ii) these terms and conditions and (iii) CCC's Billing and Payment terms and conditions.

8. License Contingent Upon Payment: While you may exercise the rights licensed immediately upon issuance of the license at the end of the licensing process for the transaction, provided that you have disclosed complete and accurate details of your proposed use, no license is finally effective unless and until full payment is received from you (either by publisher or by CCC) as provided in CCC's Billing and Payment terms and conditions. If full payment is not received on a timely basis, then any license preliminarily granted shall be deemed automatically revoked and shall be void as if never granted. Further, in the event that you breach any of these terms and conditions or any of CCC's Billing and Payment terms and conditions, the license is automatically revoked and shall be void as if never granted. Use of materials as described in a revoked license, as well as any use of the materials beyond the scope of an unrevoked license, may constitute copyright infringement and publisher reserves the right to take any and all action to protect its copyright in the materials.

9. Warranties: Publisher makes no representations or warranties with respect to the licensed material.

10. Indemnity: You hereby indemnify and agree to hold harmless publisher and CCC, and their respective officers, directors, employees and agents, from and against any and all

190

claims arising out of your use of the licensed material other than as specifically authorized pursuant to this license.

11. No Transfer of License: This license is personal to you and may not be sublicensed, assigned, or transferred by you to any other person without publisher's written permission.

12. No Amendment Except in Writing: This license may not be amended except in a writing signed by both parties (or, in the case of publisher, by CCC on publisher's behalf).

13. Objection to Contrary Terms: Publisher hereby objects to any terms contained in any purchase order, acknowledgment, check endorsement or other writing prepared by you, which terms are inconsistent with these terms and conditions or CCC's Billing and Payment terms and conditions. These terms and conditions, together with CCC's Billing and Payment terms and conditions (which are incorporated herein), comprise the entire agreement between you and publisher (and CCC) concerning this licensing transaction. In the event of any conflict between your obligations established by these terms and conditions and those established by CCC's Billing and Payment terms and conditions, these terms and conditions shall control.

14. Revocation: Elsevier or Copyright Clearance Center may deny the permissions described in this License at their sole discretion, for any reason or no reason, with a full refund payable to you. Notice of such denial will be made using the contact information provided by you. Failure to receive such notice will not alter or invalidate the denial. In no event will Elsevier or Copyright Clearance Center be responsible or liable for any costs, expenses or damage incurred by you as a result of a denial of your permission request, other than a refund of the amount(s) paid by you to Elsevier and/or Copyright Clearance Center for denied permissions.

LIMITED LICENSE

The following terms and conditions apply only to specific license types:

15. **Translation**: This permission is granted for non-exclusive world **English** rights only unless your license was granted for translation rights. If you licensed translation rights you may only translate this content into the languages you requested. A professional translator must perform all translations and reproduce the content word for word preserving the integrity of the article.

16. **Posting licensed content on any Website**: The following terms and conditions apply as follows: Licensing material from an Elsevier journal: All content posted to the web site must maintain the copyright information line on the bottom of each image; A hyper-text must be included to the Homepage of the journal from which you are licensing at http://www.sciencedirect.com/science/journal/xxxxx or the Elsevier homepage for books at http://www.elsevier.com; Central Storage: This license does not include permission for a scanned version of the material to be stored in a central repository such as that provided by Heron/XanEdu.

Licensing material from an Elsevier book: A hyper-text link must be included to the Elsevier homepage at http://www.elsevier.com . All content posted to the web site must maintain the copyright information line on the bottom of each image.

Posting licensed content on Electronic reserve: In addition to the above the following clauses are applicable: The web site must be password-protected and made available only to bona fide students registered on a relevant course. This permission is granted for 1 year only. You may obtain a new license for future website posting.

17. **For journal authors:** the following clauses are applicable in addition to the above:
Preprints:

A preprint is an author's own write-up of research results and analysis, it has not been peer-reviewed, nor has it had any other value added to it by a publisher (such as formatting, copyright, technical enhancement etc.).

Authors can share their preprints anywhere at any time. Preprints should not be added to or enhanced in any way in order to appear more like, or to substitute for, the final versions of

191

articles however authors can update their preprints on arXiv or RePEc with their Accepted Author Manuscript (see below).

If accepted for publication, we encourage authors to link from the preprint to their formal publication via its DOI. Millions of researchers have access to the formal publications on ScienceDirect, and so links will help users to find, access, cite and use the best available version. Please note that Cell Press, The Lancet and some society-owned have different preprint policies. Information on these policies is available on the journal homepage.

Accepted Author Manuscripts: An accepted author manuscript is the manuscript of an article that has been accepted for publication and which typically includes author-incorporated changes suggested during submission, peer review and editor-author communications.

Authors can share their accepted author manuscript:

- immediately
  - via their non-commercial person homepage or blog
  - by updating a preprint in arXiv or RePEc with the accepted manuscript
  - via their research institute or institutional repository for internal institutional uses or as part of an invitation-only research collaboration work-group
  - directly by providing copies to their students or to research collaborators for their personal use
  - for private scholarly sharing as part of an invitation-only work group on commercial sites with which Elsevier has an agreement
- After the embargo period
  - via non-commercial hosting platforms such as their institutional repository
  - via commercial sites with which Elsevier has an agreement

In all cases accepted manuscripts should:

- link to the formal publication via its DOI
- bear a CC-BY-NC-ND license - this is easy to do
- if aggregated with other manuscripts, for example in a repository or other site, be shared in alignment with our hosting policy not be added to or enhanced in any way to appear more like, or to substitute for, the published journal article.

Published journal article (JPA): A published journal article (PJA) is the definitive final record of published research that appears or will appear in the journal and embodies all value-adding publishing activities including peer review co-ordination, copy-editing, formatting, (if relevant) pagination and online enrichment.

Policies for sharing publishing journal articles differ for subscription and gold open access articles:

Subscription Articles: If you are an author, please share a link to your article rather than the full-text. Millions of researchers have access to the formal publications on ScienceDirect, and so links will help your users to find, access, cite, and use the best available version. Theses and dissertations which contain embedded PJAs as part of the formal submission can be posted publicly by the awarding institution with DOI links back to the formal publications on ScienceDirect.

If you are affiliated with a library that subscribes to ScienceDirect you have additional private sharing rights for others' research accessed under that agreement. This includes use for classroom teaching and internal training at the institution (including use in course packs and courseware programs), and inclusion of the article for grant funding purposes.

Gold Open Access Articles: May be shared according to the author-selected end-user license and should contain a CrossMark logo, the end user license, and a DOI link to the formal publication on ScienceDirect.

Please refer to Elsevier's posting policy for further information.

192

18. **For book authors** the following clauses are applicable in addition to the above: Authors are permitted to place a brief summary of their work online only. You are not allowed to download and post the published electronic version of your chapter, nor may you scan the printed edition to create an electronic version. **Posting to a repository:** Authors are permitted to post a summary of their chapter only in their institution's repository.

19. **Thesis/Dissertation**: If your license is for use in a thesis/dissertation your thesis may be submitted to your institution in either print or electronic form. Should your thesis be published commercially, please reapply for permission. These requirements include permission for the Library and Archives of Canada to supply single copies, on demand, of the complete thesis and include permission for Proquest/UMI to supply single copies, on demand, of the complete thesis. Should your thesis be published commercially, please reapply for permission. Theses and dissertations which contain embedded PJAs as part of the formal submission can be posted publicly by the awarding institution with DOI links back to the formal publications on ScienceDirect.

Elsevier Open Access Terms and Conditions

You can publish open access with Elsevier in hundreds of open access journals or in nearly 2000 established subscription journals that support open access publishing. Permitted third party re-use of these open access articles is defined by the author's choice of Creative Commons user license. See our open access license policy for more information.

Terms & Conditions applicable to all Open Access articles published with Elsevier:
Any reuse of the article must not represent the author as endorsing the adaptation of the article nor should the article be modified in such a way as to damage the author's honour or reputation. If any changes have been made, such changes must be clearly indicated.

The author(s) must be appropriately credited and we ask that you include the end user license and a DOI link to the formal publication on ScienceDirect.

If any part of the material to be used (for example, figures) has appeared in our publication with credit or acknowledgement to another source it is the responsibility of the user to ensure their reuse complies with the terms and conditions determined by the rights holder.

Additional Terms & Conditions applicable to each Creative Commons user license:
CC BY: The CC-BY license allows users to copy, to create extracts, abstracts and new works from the Article, to alter and revise the Article and to make commercial use of the Article (including reuse and/or resale of the Article by commercial entities), provided the user gives appropriate credit (with a link to the formal publication through the relevant DOI), provides a link to the license, indicates if changes were made and the licensor is not represented as endorsing the use made of the work. The full details of the license are available at http://creativecommons.org/licenses/by/4.0.

CC BY NC SA: The CC BY-NC-SA license allows users to copy, to create extracts, abstracts and new works from the Article, to alter and revise the Article, provided this is not done for commercial purposes, and that the user gives appropriate credit (with a link to the formal publication through the relevant DOI), provides a link to the license, indicates if changes were made and the licensor is not represented as endorsing the use made of the work. Further, any new works must be made available on the same conditions. The full details of the license are available at http://creativecommons.org/licenses/by-nc-sa/4.0.

CC BY NC ND: The CC BY-NC-ND license allows users to copy and distribute the Article, provided this is not done for commercial purposes and further does not permit distribution of the Article if it is changed or edited in any way, and provided the user gives appropriate credit (with a link to the formal publication through the relevant DOI), provides a link to the license, and that the licensor is not represented as endorsing the use made of the work. The full details of the license are available at http://creativecommons.org/licenses/by-nc-nd/4.0.

Any commercial reuse of Open Access articles published with a CC BY NC SA or CC BY NC ND license requires permission from Elsevier and will be subject to a fee.

Commercial reuse includes:

193

- Associating advertising with the full text of the Article
- Charging fees for document delivery or access
- Article aggregation
- Systematic distribution via e-mail lists or share buttons

Posting or linking by commercial companies for use by customers of those companies.

20. **Other Conditions**:

v1.9

Questions? customercare@copyright.com or **+1-855-239-3415 (toll free in the US) or +1-978-646-2777.**

194

C.10   Permission for Figure 2.8 a and b

This copyrighted material is owned by or exclusively licensed to John Wiley & Sons, Inc. or one of its group companies (each a"Wiley Company") or handled on behalf of a society with which a Wiley Company has exclusive publishing rights in relation to a particular work (collectively "WILEY"). By clicking "accept" in connection with completing this licensing transaction, you agree that the following terms and conditions apply to this transaction (along with the billing and payment terms and conditions established by the Copyright Clearance Center Inc., ("CCC's Billing and Payment terms and conditions"), at the time that you opened your RightsLink account (these are available at any time at http://myaccount.copyright.com).

Terms and Conditions

- The materials you have requested permission to reproduce or reuse (the "Wiley Materials") are protected by copyright.

- You are hereby granted a personal, non-exclusive, non-sub licensable (on a stand-alone basis), non-transferable, worldwide, limited license to reproduce the Wiley Materials for the purpose specified in the licensing process. This license, **and any CONTENT (PDF or image file) purchased as part of your order,** is for a one-time use only and limited to any maximum distribution number specified in the license. The first instance of republication or reuse granted by this license must be completed within two years of the date of the grant of this license (although copies prepared before the end date may be distributed thereafter). The Wiley Materials shall not be used in any other manner or for any other purpose, beyond what is granted in the license. Permission is granted subject to an appropriate acknowledgement given to the author, title of the material/book/journal and the publisher. You shall also duplicate the copyright notice that appears in the Wiley publication in your use of the Wiley Material. Permission is also granted on the understanding that nowhere in the text is a previously published source acknowledged for all or part of this Wiley Material. Any third party content is expressly excluded from this permission.

- With respect to the Wiley Materials, all rights are reserved. Except as expressly granted by the terms of the license, no part of the Wiley Materials may be copied, modified, adapted (except for minor reformatting required by the new Publication), translated, reproduced, transferred or distributed, in any form or by any means, and no derivative works may be made based on the Wiley Materials without the prior permission of the respective copyright owner.**For STM Signatory Publishers clearing permission under the terms of the STM Permissions Guidelines only, the terms of the license are extended to include subsequent editions and for editions in other languages, provided such editions are for the work as a whole in situ and does not involve the separate exploitation of the permitted figures or extracts,** You may not alter, remove or suppress in any manner any copyright, trademark or other notices displayed by the Wiley Materials. You may not license, rent, sell, loan, lease, pledge, offer as security, transfer or assign the Wiley Materials on a stand-alone basis, or any of the rights granted to you hereunder to any other person.

- The Wiley Materials and all of the intellectual property rights therein shall at all times remain the exclusive property of John Wiley & Sons Inc, the Wiley Companies, or their respective licensors, and your interest therein is only that of having possession of and the right to reproduce the Wiley Materials pursuant to Section 2 herein during the continuance of this Agreement. You agree that you own no right, title or interest in or to the Wiley Materials or any of the intellectual property rights therein. You shall have no rights hereunder other than the license as provided for above in Section 2. No right, license or interest to any trademark, trade name, service mark or other branding

196

("Marks") of WILEY or its licensors is granted hereunder, and you agree that you shall not assert any such right, license or interest with respect thereto

- NEITHER WILEY NOR ITS LICENSORS MAKES ANY WARRANTY OR REPRESENTATION OF ANY KIND TO YOU OR ANY THIRD PARTY, EXPRESS, IMPLIED OR STATUTORY, WITH RESPECT TO THE MATERIALS OR THE ACCURACY OF ANY INFORMATION CONTAINED IN THE MATERIALS, INCLUDING, WITHOUT LIMITATION, ANY IMPLIED WARRANTY OF MERCHANTABILITY, ACCURACY, SATISFACTORY QUALITY, FITNESS FOR A PARTICULAR PURPOSE, USABILITY, INTEGRATION OR NON-INFRINGEMENT AND ALL SUCH WARRANTIES ARE HEREBY EXCLUDED BY WILEY AND ITS LICENSORS AND WAIVED BY YOU.

- WILEY shall have the right to terminate this Agreement immediately upon breach of this Agreement by you.

- You shall indemnify, defend and hold harmless WILEY, its Licensors and their respective directors, officers, agents and employees, from and against any actual or threatened claims, demands, causes of action or proceedings arising from any breach of this Agreement by you.

- IN NO EVENT SHALL WILEY OR ITS LICENSORS BE LIABLE TO YOU OR ANY OTHER PARTY OR ANY OTHER PERSON OR ENTITY FOR ANY SPECIAL, CONSEQUENTIAL, INCIDENTAL, INDIRECT, EXEMPLARY OR PUNITIVE DAMAGES, HOWEVER CAUSED, ARISING OUT OF OR IN CONNECTION WITH THE DOWNLOADING, PROVISIONING, VIEWING OR USE OF THE MATERIALS REGARDLESS OF THE FORM OF ACTION, WHETHER FOR BREACH OF CONTRACT, BREACH OF WARRANTY, TORT, NEGLIGENCE, INFRINGEMENT OR OTHERWISE (INCLUDING, WITHOUT LIMITATION, DAMAGES BASED ON LOSS OF PROFITS, DATA, FILES, USE, BUSINESS OPPORTUNITY OR CLAIMS OF THIRD PARTIES), AND WHETHER OR NOT THE PARTY HAS BEEN ADVISED OF THE POSSIBILITY OF SUCH DAMAGES. THIS LIMITATION SHALL APPLY NOTWITHSTANDING ANY FAILURE OF ESSENTIAL PURPOSE OF ANY LIMITED REMEDY PROVIDED HEREIN.

- Should any provision of this Agreement be held by a court of competent jurisdiction to be illegal, invalid, or unenforceable, that provision shall be deemed amended to achieve as nearly as possible the same economic effect as the original provision, and the legality, validity and enforceability of the remaining provisions of this Agreement shall not be affected or impaired thereby.

- The failure of either party to enforce any term or condition of this Agreement shall not constitute a waiver of either party's right to enforce each and every term and condition of this Agreement. No breach under this agreement shall be deemed waived or excused by either party unless such waiver or consent is in writing signed by the party granting such waiver or consent. The waiver by or consent of a party to a breach of any provision of this Agreement shall not operate or be construed as a waiver of or consent to any other or subsequent breach by such other party.

- This Agreement may not be assigned (including by operation of law or otherwise) by you without WILEY's prior written consent.

197

- Any fee required for this permission shall be non-refundable after thirty (30) days from receipt by the CCC.

- These terms and conditions together with CCC's Billing and Payment terms and conditions (which are incorporated herein) form the entire agreement between you and WILEY concerning this licensing transaction and (in the absence of fraud) supersedes all prior agreements and representations of the parties, oral or written. This Agreement may not be amended except in writing signed by both parties. This Agreement shall be binding upon and inure to the benefit of the parties' successors, legal representatives, and authorized assigns.

- In the event of any conflict between your obligations established by these terms and conditions and those established by CCC's Billing and Payment terms and conditions, these terms and conditions shall prevail.

- WILEY expressly reserves all rights not specifically granted in the combination of (i) the license details provided by you and accepted in the course of this licensing transaction, (ii) these terms and conditions and (iii) CCC's Billing and Payment terms and conditions.

- This Agreement will be void if the Type of Use, Format, Circulation, or Requestor Type was misrepresented during the licensing process.

- This Agreement shall be governed by and construed in accordance with the laws of the State of New York, USA, without regards to such state's conflict of law rules. Any legal action, suit or proceeding arising out of or relating to these Terms and Conditions or the breach thereof shall be instituted in a court of competent jurisdiction in New York County in the State of New York in the United States of America and each party hereby consents and submits to the personal jurisdiction of such court, waives any objection to venue in such court and consents to service of process by registered or certified mail, return receipt requested, at the last known address of such party.

WILEY OPEN ACCESS TERMS AND CONDITIONS
Wiley Publishes Open Access Articles in fully Open Access Journals and in Subscription journals offering Online Open. Although most of the fully Open Access journals publish open access articles under the terms of the Creative Commons Attribution (CC BY) License only, the subscription journals and a few of the Open Access Journals offer a choice of Creative Commons Licenses. The license type is clearly identified on the article.
The Creative Commons Attribution License
The Creative Commons Attribution License (CC-BY) allows users to copy, distribute and transmit an article, adapt the article and make commercial use of the article. The CC-BY license permits commercial and non-
Creative Commons Attribution Non-Commercial License
The Creative Commons Attribution Non-Commercial (CC-BY-NC)License permits use, distribution and reproduction in any medium, provided the original work is properly cited and is not used for commercial purposes.(see below)

Creative Commons Attribution-Non-Commercial-NoDerivs License
The Creative Commons Attribution Non-Commercial-NoDerivs License (CC-BY-NC-ND) permits use, distribution and reproduction in any medium, provided the original work is properly cited, is not used for commercial purposes and no modifications or adaptations are made. (see below)
Use by commercial "for-profit" organizations

Use of Wiley Open Access articles for commercial, promotional, or marketing purposes requires further explicit permission from Wiley and will be subject to a fee. Further details can be found on Wiley Online Library http://olabout.wiley.com/WileyCDA/Section/id-410895.html

Other Terms and Conditions:

v1.10 Last updated September 2015

Questions? customercare@copyright.com **or +1-855-239-3415 (toll free in the US) or +1-978-646-2777.**

C.11　Permission for Figure 2.8 c and d

Copyright Clearance Center

Note: Copyright.com supplies permissions but not the copyrighted content itself.

1	2	3
PAYMENT	REVIEW	CONFIRMATION

Step 3: Order Confirmation

Thank you for your order! A confirmation for your order will be sent to your account email address. If you have questions about your order, you can call us 24 hrs/day, M-F at +1.855.239.3415 Toll Free, or write to us at info@copyright.com. This is not an invoice.

Confirmation Number: 11727096
Order Date: 06/28/2018

If you paid by credit card, your order will be finalized and your card will be charged within 24 hours. If you choose to be invoiced, you can change or cancel your order until the invoice is generated.

Payment Information

Adrienne Minerick
minerick@mtu.edu
+1 (906) 487-2796
Payment Method: n/a

Order Details

Journal of micromechanics and microengineering : structures, devices, and systems

Order detail ID:	71268476	**Permission Status:** ✅ Granted
Order License Id:	4377840243842	**Permission type:** Republish or display content
ISSN:	0960-1317	**Type of use:** Thesis/Dissertation
Publication Type:	Journal	View details
Volume:		
Issue:		
Start page:		
Publisher:	INSTITUTE OF PHYSICS PUBLISHING	
Author/Editor:	Institute of Physics (Great Britain) ; American Institute of Physics	

Note: This item will be invoiced or charged separately through CCC's **RightsLink** service. More info　　　**$ 0.00**

	This is not an invoice.	
Total order items: 1		**Order Total: 0.00 USD**

C.12   Permission for Figure 2.9

SPRINGER NATURE LICENSE
TERMS AND CONDITIONS

Jul 02, 2018

This Agreement between Adrienne Minerick ("You") and Springer Nature ("Springer Nature") consists of your license details and the terms and conditions provided by Springer Nature and Copyright Clearance Center.

License Number	4377210967978
License date	Jun 27, 2018
Licensed Content Publisher	Springer Nature
Licensed Content Publication	Analytical and Bioanalytical Chemistry
Licensed Content Title	DC insulator dielectrophoretic applications in microdevice technology: a review
Licensed Content Author	Soumya K. Srivastava, Aytug Gencoglu, Adrienne R. Minerick
Licensed Content Date	Jan 1, 2010
Licensed Content Volume	399
Licensed Content Issue	1
Type of Use	Thesis/Dissertation
Requestor type	academic/university or research institute
Format	print and electronic
Portion	figures/tables/illustrations
Number of figures/tables/illustrations	1
Will you be translating?	no
Circulation/distribution	< 501
Author of this Springer Nature content	no
Title	Reverse Insulator Dielectrophoresis: Utilizing Droplet Microenvironments for Discerning Molecular Expressions on Cell Surfaces
Instructor name	n/a
Institution name	Michigan Technological University
Expected presentation date	Jul 2018
Portions	Fig. 4
Requestor Location	Adrienne Minerick Chemical Sciences and Engineering Building 203 1400 Townsend Drive HOUGHTON, MI 49931 United States Attn: Adrienne Minerick
Billing Type	Invoice
Billing Address	Adrienne Minerick Chemical Sciences and Engineering Office 202H

201

1400 Townsend Drive
HOUGHTON, MI 49931
United States
Attn: Adrienne Minerick

Total   0.00 USD

Terms and Conditions

Springer Nature Terms and Conditions for RightsLink Permissions

Springer Customer Service Centre GmbH (the Licensor) hereby grants you a non-exclusive, world-wide licence to reproduce the material and for the purpose and requirements specified in the attached copy of your order form, and for no other use, subject to the conditions below:

1. The Licensor warrants that it has, to the best of its knowledge, the rights to license reuse of this material. However, you should ensure that the material you are requesting is original to the Licensor and does not carry the copyright of another entity (as credited in the published version).

   If the credit line on any part of the material you have requested indicates that it was reprinted or adapted with permission from another source, then you should also seek permission from that source to reuse the material.

2. Where **print only** permission has been granted for a fee, separate permission must be obtained for any additional electronic re-use.

3. Permission granted **free of charge** for material in print is also usually granted for any electronic version of that work, provided that the material is incidental to your work as a whole and that the electronic version is essentially equivalent to, or substitutes for, the print version.

4. A licence for 'post on a website' is valid for 12 months from the licence date. This licence does not cover use of full text articles on websites.

5. Where **'reuse in a dissertation/thesis'** has been selected the following terms apply: Print rights for up to 100 copies, electronic rights for use only on a personal website or institutional repository as defined by the Sherpa guideline (www.sherpa.ac.uk/romeo/).

6. Permission granted for books and journals is granted for the lifetime of the first edition and does not apply to second and subsequent editions (except where the first edition permission was granted free of charge or for signatories to the STM Permissions Guidelines http://www.stm-assoc.org/copyright-legal-affairs/permissions/permissions-guidelines/), and does not apply for editions in other languages unless additional translation rights have been granted separately in the licence.

7. Rights for additional components such as custom editions and derivatives require additional permission and may be subject to an additional fee. Please apply to Journalpermissions@springernature.com/bookpermissions@springernature.com for these rights.

8. The Licensor's permission must be acknowledged next to the licensed material in print. In electronic form, this acknowledgement must be visible at the same time as the figures/tables/illustrations or abstract, and must be hyperlinked to the journal/book's homepage. Our required acknowledgement format is in the Appendix below.

9. Use of the material for incidental promotional use, minor editing privileges (this does not include cropping, adapting, omitting material or any other changes that affect the meaning, intention or moral rights of the author) and copies for the disabled are permitted under this licence.

10. Minor adaptations of single figures (changes of format, colour and style) do not require the Licensor's approval. However, the adaptation should be credited as shown in Appendix below.

202

Appendix — Acknowledgements:

For Journal Content:
Reprinted by permission from [**the Licensor**]: [**Journal Publisher** (e.g. Nature/Springer/Palgrave)] [**JOURNAL NAME**] [**REFERENCE CITATION** (Article name, Author(s) Name), [**COPYRIGHT**] (year of publication)

For Advance Online Publication papers:
Reprinted by permission from [**the Licensor**]: [**Journal Publisher** (e.g. Nature/Springer/Palgrave)] [**JOURNAL NAME**] [**REFERENCE CITATION** (Article name, Author(s) Name), [**COPYRIGHT**] (year of publication), advance online publication, day month year (doi: 10.1038/sj.[JOURNAL ACRONYM].)

For Adaptations/Translations:
Adapted/Translated by permission from [**the Licensor**]: [**Journal Publisher** (e.g. Nature/Springer/Palgrave)] [**JOURNAL NAME**] [**REFERENCE CITATION** (Article name, Author(s) Name), [**COPYRIGHT**] (year of publication)

Note: For any republication from the British Journal of Cancer, the following credit line style applies:

Reprinted/adapted/translated by permission from [**the Licensor**]: on behalf of Cancer Research UK: : [**Journal Publisher** (e.g. Nature/Springer/Palgrave)] [**JOURNAL NAME**] [**REFERENCE CITATION** (Article name, Author(s) Name), [**COPYRIGHT**] (year of publication)

For **Advance Online Publication** papers:
Reprinted by permission from The [**the Licensor**]: on behalf of Cancer Research UK: [**Journal Publisher** (e.g. Nature/Springer/Palgrave)] [**JOURNAL NAME**] [**REFERENCE CITATION** (Article name, Author(s) Name), [**COPYRIGHT**] (year of publication), advance online publication, day month year (doi: 10.1038/sj. [JOURNAL ACRONYM])

For Book content:
Reprinted/adapted by permission from [**the Licensor**]: [**Book Publisher** (e.g. Palgrave Macmillan, Springer etc) [**Book Title**] by [**Book author**(s)] [**COPYRIGHT**] (year of publication)

Other Conditions:

Version 1.0

Questions? customercare@copyright.com or +1-855-239-3415 (toll free in the US) or +1-978-646-2777.

203

C.13   Permission for Figure 2.10 a and b

Copyright Clearance Center

RightsLink®

Home   Account Info   Help

ELECTROPHORESIS
11'17

Title: Droplet fusion by alternating current (AC) field electrocoalescence in microchannels

Author: Max Chabert, Kevin D. Dorfman, Jean-Louis Viovy

Publication: Electrophoresis

Publisher: John Wiley and Sons

Date: Sep 30, 2005

Copyright © 2005, John Wiley and Sons

Logged in as:
Adrienne Minerick
Account #:
3000694731

LOGOUT

Review Order

Please review the order details and the associated terms and conditions.

No royalties will be charged for this reuse request although you are required to obtain a license and comply with the license terms and conditions. To obtain the license, click the Accept button below.

Licensed Content Publisher	John Wiley and Sons
Licensed Content Publication	Electrophoresis
Licensed Content Title	Droplet fusion by alternating current (AC) field electrocoalescence in microchannels
Licensed Content Author	Max Chabert, Kevin D. Dorfman, Jean-Louis Viovy
Licensed Content Date	Sep 30, 2005
Licensed Content Volume	26
Licensed Content Issue	19
Licensed Content Pages	10
Type of use	Dissertation/Thesis
Requestor type	University/Academic
Format	Print and electronic
Portion	Figure/table
Number of figures/tables	1
Original Wiley figure/table number(s)	Figure 4
Will you be translating?	No
Title of your thesis / dissertation	Reverse Insulator Dielectrophoresis: Utilizing Droplet Microenvironments for Discerning Molecular Expressions on Cell Surfaces
Expected completion date	Jul 2018
Expected size (number of pages)	175
Requestor Location	Adrienne Minerick Chemical Sciences and Engineering Building 203 1400 Townsend Drive HOUGHTON, MI 49931 United States Attn: Adrienne Minerick
Publisher Tax ID	EU826007151
Total	0.00 USD

Edit Order Details

Edit Requestor Location   This location may be used to determine your tax liability.

☐ I agree to these terms and conditions.

☐ I understand this license is for reuse only and that no content is provided.

| Customer Code (if supplied) | | APPLY |

BACK   DECLINE   ACCEPT

Please click accept only once.

205

C.14 Permission for Figure 2.10 c, d, and e

**ROYAL SOCIETY OF CHEMISTRY LICENSE
TERMS AND CONDITIONS**

Jul 02, 2018

This Agreement between Adrienne Minerick ("You") and Royal Society of Chemistry ("Royal Society of Chemistry") consists of your license details and the terms and conditions provided by Royal Society of Chemistry and Copyright Clearance Center.

License Number	4377220628067
License date	Jun 27, 2018
Licensed Content Publisher	Royal Society of Chemistry
Licensed Content Publication	Lab on a Chip
Licensed Content Title	Dielectrowetting manipulation for digital microfluidics: creating, transporting, splitting, and merging of droplets
Licensed Content Author	Hongyao Geng,Jian Feng,Lisa Marie Stabryla,Sung Kwon Cho
Licensed Content Date	Feb 13, 2017
Licensed Content Volume	17
Licensed Content Issue	6
Type of Use	Thesis/Dissertation
Requestor type	academic/educational
Portion	figures/tables/images
Number of figures/tables/images	1
Format	print and electronic
Distribution quantity	10
Will you be translating?	no
Order reference number	
Title of the thesis/dissertation	Reverse Insulator Dielectrophoresis: Utilizing Droplet Microenvironments for Discerning Molecular Expressions on Cell Surfaces
Expected completion date	Jul 2018
Estimated size	175
Requestor Location	Adrienne Minerick Chemical Sciences and Engineering Building 203 1400 Townsend Drive HOUGHTON, MI 49931 United States Attn: Adrienne Minerick
Billing Type	Invoice
Billing Address	Adrienne Minerick Chemical Sciences and Engineering Office 202H 1400 Townsend Drive HOUGHTON, MI 49931 United States Attn: Adrienne Minerick

206

Total   0.00 USD

Terms and Conditions

This License Agreement is between {Requestor Name} ("You") and The Royal Society of Chemistry ("RSC") provided by the Copyright Clearance Center ("CCC"). The license consists of your order details, the terms and conditions provided by the Royal Society of Chemistry, and the payment terms and conditions.

RSC / TERMS AND CONDITIONS

INTRODUCTION

The publisher for this copyrighted material is The Royal Society of Chemistry. By clicking "accept" in connection with completing this licensing transaction, you agree that the following terms and conditions apply to this transaction (along with the Billing and Payment terms and conditions established by CCC, at the time that you opened your RightsLink account and that are available at any time at .

LICENSE GRANTED

The RSC hereby grants you a non-exclusive license to use the aforementioned material anywhere in the world subject to the terms and conditions indicated herein. Reproduction of the material is confined to the purpose and/or media for which permission is hereby given.

RESERVATION OF RIGHTS

The RSC reserves all rights not specifically granted in the combination of (i) the license details provided by your and accepted in the course of this licensing transaction; (ii) these terms and conditions; and (iii) CCC's Billing and Payment terms and conditions.

REVOCATION

The RSC reserves the right to revoke this license for any reason, including, but not limited to, advertising and promotional uses of RSC content, third party usage, and incorrect source figure attribution.

THIRD-PARTY MATERIAL DISCLAIMER

If part of the material to be used (for example, a figure) has appeared in the RSC publication with credit to another source, permission must also be sought from that source. If the other source is another RSC publication these details should be included in your RightsLink request. If the other source is a third party, permission must be obtained from the third party. The RSC disclaims any responsibility for the reproduction you make of items owned by a third party.

PAYMENT OF FEE

If the permission fee for the requested material is waived in this instance, please be advised that any future requests for the reproduction of RSC materials may attract a fee.

ACKNOWLEDGEMENT

The reproduction of the licensed material must be accompanied by the following acknowledgement:

Reproduced ("Adapted" or "in part") from {Reference Citation} (or Ref XX) with permission of The Royal Society of Chemistry.

If the licensed material is being reproduced from New Journal of Chemistry (NJC), Photochemical & Photobiological Sciences (PPS) or Physical Chemistry Chemical Physics (PCCP) you must include one of the following acknowledgements:

For figures originally published in NJC:

Reproduced ("Adapted" or "in part") from {Reference Citation} (or Ref XX) with permission of The Royal Society of Chemistry (RSC) on behalf of the European Society for Photobiology, the European Photochemistry Association and the RSC.

For figures originally published in PPS:

Reproduced ("Adapted" or "in part") from {Reference Citation} (or Ref XX) with permission of The Royal Society of Chemistry (RSC) on behalf of the Centre National de la Recherche Scientifique (CNRS) and the RSC.

For figures originally published in PCCP:

Reproduced ("Adapted" or "in part") from {Reference Citation} (or Ref XX) with permission of the PCCP Owner Societies.

HYPERTEXT LINKS

With any material which is being reproduced in electronic form, you must include a hypertext link to the original RSC article on the RSC's website. The recommended form for the hyperlink is http://dx.doi.org/10.1039/DOI suffix, for example in the link http://dx.doi.org/10.1039/b110420a the DOI suffix is 'b110420a'. To find the relevant DOI suffix for the RSC article in question, go to the Journals section of the website and locate the article in the list of papers for the volume and issue of your specific journal. You will find the DOI suffix quoted there.

LICENSE CONTINGENT ON PAYMENT

While you may exercise the rights licensed immediately upon issuance of the license at the end of the licensing process for the transaction, provided that you have disclosed complete and accurate details of your proposed use, no license is finally effective unless and until full payment is received from you (by CCC) as provided in CCC's Billing and Payment terms and conditions. If full payment is not received on a timely basis, then any license preliminarily granted shall be deemed automatically revoked and shall be void as if never granted. Further, in the event that you breach any of these terms and conditions or any of CCC's Billing and Payment terms and conditions, the license is automatically revoked and shall be void as if never granted. Use of materials as described in a revoked license, as well as any use of the materials beyond the scope of an unrevoked license, may constitute copyright infringement and the RSC reserves the right to take any and all action to protect its copyright in the materials.

WARRANTIES

The RSC makes no representations or warranties with respect to the licensed material.

INDEMNITY

You hereby indemnify and agree to hold harmless the RSC and the CCC, and their respective officers, directors, trustees, employees and agents, from and against any and all claims arising out of your use of the licensed material other than as specifically authorized pursuant to this licence.

NO TRANSFER OF LICENSE

This license is personal to you or your publisher and may not be sublicensed, assigned, or transferred by you to any other person without the RSC's written permission.

NO AMENDMENT EXCEPT IN WRITING

This license may not be amended except in a writing signed by both parties (or, in the case of "Other Conditions, v1.2", by CCC on the RSC's behalf).

OBJECTION TO CONTRARY TERMS

You hereby acknowledge and agree that these terms and conditions, together with CCC's Billing and Payment terms and conditions (which are incorporated herein), comprise the entire agreement between you and the RSC (and CCC) concerning this licensing transaction, to the exclusion of all other terms and conditions, written or verbal, express or implied (including any terms contained in any purchase order, acknowledgment, check endorsement or other writing prepared by you). In the event of any conflict between your obligations established by these terms and conditions and those established by CCC's Billing and Payment terms and conditions, these terms and conditions shall control.

JURISDICTION

This license transaction shall be governed by and construed in accordance with the laws of the District of Columbia. You hereby agree to submit to the jurisdiction of the courts located in the District of Columbia for purposes of resolving any disputes that may arise in connection with this licensing transaction.

LIMITED LICENSE

The following terms and conditions apply to specific license types:

Translation

This permission is granted for non-exclusive world English rights only unless your license was granted for translation rights. If you licensed translation rights you may only translate

208

this content into the languages you requested. A professional translator must perform all translations and reproduce the content word for word preserving the integrity of the article.
Intranet
If the licensed material is being posted on an Intranet, the Intranet is to be password-protected and made available only to bona fide students or employees only. All content posted to the Intranet must maintain the copyright information line on the bottom of each image. You must also fully reference the material and include a hypertext link as specified above.
Copies of Whole Articles
All copies of whole articles must maintain, if available, the copyright information line on the bottom of each page.
Other Conditions
v1.2
Gratis licenses (referencing $0 in the Total field) are free. Please retain this printable license for your reference. No payment is required.
If you would like to pay for this license now, please remit this license along with yourpayment made payable to "COPYRIGHT CLEARANCE CENTER" otherwise you will be invoiced within 48 hours of the license date. Payment should be in the form of a check or money order referencing your account number and this invoice number {Invoice Number}. Once you receive your invoice for this order, you may pay your invoice by credit card. Please follow instructions provided at that time.
Make Payment To:
Copyright Clearance Center
29118 Network Place
Chicago, IL 60673-1291
For suggestions or comments regarding this order, contact Rightslink Customer Support: customercare@copyright.com or +1-855-239-3415 (toll free in the US) or +1-978-646-2777.

Questions? customercare@copyright.com **or +1-855-239-3415 (toll free in the US) or +1-978-646-2777.**

209